Title

The impact of stellar feedback on galaxies and dark matter halos

Permalink

https://escholarship.org/uc/item/41t1b1kn

Author

Chan, Tsang Keung

Publication Date

2019

Peer reviewed|Thesis/dissertation

UNIVERSITY OF CALIFORNIA SAN DIEGO

The impact of stellar feedback on galaxies and dark matter halos

A dissertation submitted in partial satisfaction of the
requirements for the degree
Doctor of Philosophy

in

Physics

by

Tsang Keung Chan

Committee in charge:

Professor Dusan Keres, Chair
Professor Patrick Diamond
Professor George Fuller
Professor Philip E. Gill
Professor Michael Norman

2019

The dissertation of Tsang Keung Chan is approved, and it is acceptable in quality and form for publication on microfilm and electronically:

Chair

University of California San Diego

2019

DEDICATION

For my parents and my sisters.

EPIGRAPH

We do not ask for what useful purpose the birds do sing,
for song is their pleasure since they were created for singing.
Similarly, we ought not to ask why the human mind troubles
to fathom the secrets of the heavens.
The diversity of the phenomena of nature is so great
and the treasures hidden in the heavens so rich precisely
in order that the human mind shall never be lacking in fresh nourishment.

—Johannes Kepler

TABLE OF CONTENTS

LIST OF FIGURES

LIST OF TABLES

LIST OF ABBREVIATIONS

DM	Dark Matter
CDM	Cold Dark Matter
WDM	Warm Dark Matter
SIDM	Self-Interacting Dark Matter
MW	Milky Way
TBTF	Too Big To Fail
LSBG	Low Surface Brightness Galaxy
HSBG	High Surface Brightness Galaxy
GC	Globular Cluster
UDG	Ultra Diffuse Galaxy
CR	Cosmic Rays
ISM	Interstellar Medium
CGM	Circumgalactic Medium

ACKNOWLEDGEMENTS

I am greatly indebted to my PhD advisor, Professor Dusan Keres, for his teaching, guidance, and support. Dusan leads me to the field of galaxy simulation, sets the stage for my research, and provides me invaluable advice and resources. Without him, I could not succeed in my current research.

I would like to thank my fellow doctoral students, Bili Dong, Nathan Butcher, Caleb Choban, Cameron Trapp, and Stella Zhang. They help me a lot with my research, especially Bili with his programming skills. They show me that research group is not only about research, but also about mutual support and connection.

My research would have been impossible without the aid and support of my collaborators, Philip Hopkins, Eliot Quataert, Claude-André Faucher-Giguère, Alexander Muratov, Andrew Wetzel, Shea Garrison-Kimmel, Kareem El-Badry, Christopher Hayward, Kung-Yi Su, and Jose Oñorbe.

I appreciate the help from the UCSD faculty and my committee members. I gain my plasma physics knowledge from Patrick Diamond, which aids me on my cosmic ray research. Michael Norman taught me parallel computing and numerical techniques. I benefited from discussing with George Fuller on dark matter physics. I was a teaching assistant for Karin Sandstrom's class. She demonstrated how to be a good teacher and helped me to develop my teaching skills.

Chapter 2, in full, is a reformatted reprint of the material as it appears in *Monthly Notices of the Royal Astronomical Society*, Chan, Tsang Keung; Kereš, Dušan ; Oñorbe, Jose; Hopkins, Philip F. ; Muratov, Alexander L.; Faucher-Giguère, Claude-André; Quataert, Eliot, Volume 454, Issue 3, 11 December 2015, Pages 2981-3001. The dissertation author was the primary investigator and author of this paper.

Chapter 3, in full, is a reformatted reprint of the material as it appears in *Monthly Notices of the Royal Astronoical Society*, Chan, Tsang Keung; Kereš, Dušan; Wetzel, Andrew; Hopkins,

Philip F.; Faucher-Giguère, Claude-André; El-Badry, Kareem; Garrison-Kimmel, Shea; Boylan-Kolchin, Michael, Volume 478, Issue 1, July 2018, Pages 906-925. The dissertation author was the primary investigator and author of this paper.

Chapter 4, in full, is a reformatted reprint of the material as it will appear in *Monthly Notices of the Royal Astronomical Society*, Chan, Tsang Keung; Kereš, Dušan; Hopkins, Philip F.; Quataert, Eliot; Su, Kung-Yi ; Hayward, Christopher C.; Faucher-Giguère, Claude-André, Volume 488, Issue 3, September 2019, Pages 3716-3744. The dissertation author was the primary investigator and author of this paper.

VITA

2011	B. S. in Physics, Chinese University of Hong Kong, Hong Kong
2013	M.Phil. in Physics, Chinese University of Hong Kong, Hong Kong
2019	Ph.D. in Physics, University of California, San Diego

ABSTRACT OF THE DISSERTATION

The impact of stellar feedback on galaxies and dark matter halos

by

Tsang Keung Chan

Doctor of Philosophy in Physics

University of California San Diego, 2019

Professor Dusan Keres, Chair

In Chapter 2, we study the inner dark matter profiles of galaxies with halo masses ($M_\mathrm{h} \sim 10^{9-12}\mathrm{M}_\odot$) and stellar masses ($M_* \sim 10^{4-11}\mathrm{M}_\odot$) in the "Feedback In Realistic Environment" (FIRE) cosmological simulations. We find repeated episodes of feedback-driven outflows can transfer energy to DM and flatten the inner DM profiles. $\sim$ kpc-size DM cores form in galaxies with $M_\mathrm{h} \sim 10^{11}\mathrm{M}_\odot$, since feedback energy is sufficient to reduce inner DM density. At $M_\mathrm{h} \sim 10^{12}\mathrm{M}_\odot$, baryonic infall into halo center can contract DM halos, which effectively cancel the effect from feedback, producing DM profiles close to the Navarro-Frenk-White (NFW) profile.

In Chapter 3, we study the formation mechanism of the ultra diffuse galaxies (UDGs) with galaxies with the z=0 stellar mass $M_* \sim 10^{4-11}\mathrm{M}_\odot$ in the cosmological FIRE simulations.

We show dwarf galaxies with $M_* \sim 10^8 \mathrm{M}_\odot$, expanded by stellar feedback, quenched, and then passively evolving in galaxy clusters, can reproduce the properties of “red” UDGs. We find if those dwarf galaxies are not quenched, they produce blue diffuse galaxies, which could be prevalent in the field environment.

In Chapter 4, we present the first implementation of the cosmic ray (CR) feedback in the FIRE simulation. We study non cosmological simulations of dwarf, dwarf starburst, and $L\star$ galaxies with CR feedback, including advection, isotropic/anisotropic diffusion, and/or streaming. We constrain CR propagation models by comparing the simulated star formation rate and GeV γ-ray emission with the observed nearby and starburst galaxies. We find the “effective” isotropic diffusion coefficients to be around $3 \times 10^{29} \mathrm{cm}^2/\mathrm{s}$ to match the observations.

Chapter 1

General introduction

1.1 Stellar feedback

The main focus of my graduate research is stellar feedback, a term used to describe processes related to stellar evolution that inject energy and momentum into the interstellar medium (ISM) and circumgalactic medium (CGM). These processes play a central role in galaxy formation and evolution, since they control the formation of stars, gas and metal flows, and even modify the structures of dark matter halos and galaxies. In the following, we will illustrate the importance of stellar feedback and lay the foundation for the related research topics.

1.1.1 The role of stellar feedback in Galaxy Formation Theory

One of the biggest triumphs in modern astronomy is the highly successful, cold dark matter model with a cosmological constant (ΛCDM). It states 70-75 % of the energy density of the Universe in dark energy (corresponding to the cosmological constant, leading to the accelerated expansion of the universe), 20 % in cold dark matter (CDM), and 5% in baryonic matter (most of which can be measured with electromagnetic radiations). It successfully explains the temperature fluctuations in the cosmic microwave background (CMB) (Planck Collaboration et al., 2014) and

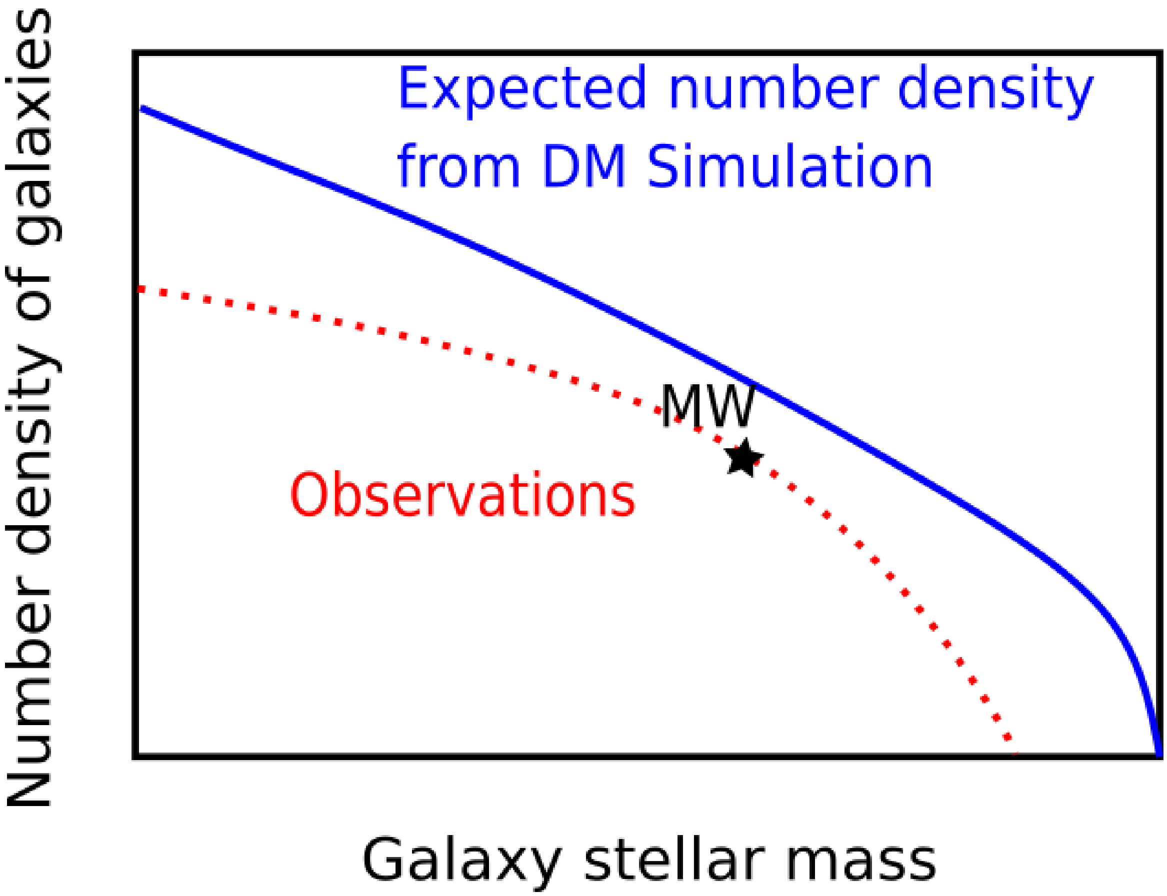

Figure 1.1: A schematic diagram illustrating the discrepancy between observations and a hierarchical galaxy formation theory, which assumes all gas in DM halos collapses and form stars. The x axis shows the stellar mass of the galaxies and the y axis shows the number density of the galaxies at that stellar mass. There are significantly fewer galaxies with masses much greater or smaller than the Milky Way (MW), compared to the theory.

the cosmic variance from the large scale structure formation (Springel et al., 2005).

ΛCDM naturally leads to hierarchical galaxy formation. The initial small density perturbations are amplified by gravitationally instabilities and then collapse into small DM halos. Those halos subsequently merge and hierarchically build up larger structures. Gas within the DM halos condenses at the center and forms galaxies(White & Frenk, 1991). During the collapses of halos one expects the fraction of baryons in halos to be the same as the ratio of baryon density to dark matter density on larger scales. If all such available baryons manage to cool and form stars, then the galaxy mass function (the number density of galaxies at a given stellar mass) should follow the DM mass function (the number density of DM halos at a given halo mass). However, observations show a significant mismatch of the galaxy mass function with the predicted DM mass function, which we have illustrate in Fig. 1.1[1]. Specifically, stellar masses are suppressed at low (dwarf galaxies) and high halo masses (galaxy clusters), while most of the stars are hosted in Milky Way mass galaxies, since the observed stellar mass function shows that only in Milky-Way mass galaxies baryons convert to stars with relatively high efficiency(Kereš et al., 2009a).

This discrepancy can be studied with two major approaches in galaxy formation theory, semi-analytic models and cosmological galaxy simulations (see Somerville & Davé 2015 for a review). Semi-analytic modelling is an approach to study the statistics and properties of galaxies with approximate analytic techniques. It approximates various physical processes with theoretical arguments, empirical relations from observations, and results from simulations. Its major advantage is a relatively low computational cost.

Cosmological galaxy simulations, on the other hand, are numerical models that incorporate the full complexity of various physics, and thus attempt to derive properties of galaxies from first principles. They follow galaxy formation from high redshift with a given cosmology, and self-consistently model collapse of density fluctuations into large scale structure and halos. At the same time they model gas cooling and star formation processes within the hierarchically growing

---

[1] In practice, we can only infer galaxy mass from its luminosity at multiple wavelengths.

structure. Therefore, they require greater computational power than semi-analytic models, so they typically run on supercomputers.

Both approaches suggest, in order to suppress the conversion of halo gas to stars, gas needs to be expelled from galaxies or gas accretion onto galaxies has to be suppressed. Possible processes include stellar feedback, e.g. supernova explosion, stellar winds, and radiation. At galaxy cluster scale, energy from stellar feedback is weaker than the gravitational energy, so other mechanisms, e.g. cooling inefficiency, active galactic nuclei feedback, or non thermal pressure, might be required.

The “Feedback in Realistic Environment” (FIRE) simulations are modern cosmological galaxy simulations that incorporate comprehensive physics, including stellar feedback and star formation (Hopkins et al., 2014, 2018b). It has been shown to reproduce many observed relations, e.g. the stellar-to-halo mass relation (and thus the galaxy mass function)(Hopkins et al., 2014), strong galactic outflows(Muratov et al., 2015), the stellar-mass-metallicity relation(Ma et al., 2016), the Kennicutt-Schmidt relation(Orr et al., 2018), etc.

Therefore, we will use the FIRE simulation to investigate many important aspects of stellar feedback on galaxies and DM halos. In Chapter 2, we will demonstrate that stellar feedback is able to modify the underlying structures of DM halos, which can alleviate or even resolve some small scale (especially in dwarf galaxies) issues with ΛCDM. In Chapter 3, we will explain the formation of the Ultra Diffuse Galaxies with stellar feedback. In Chapter 4, we will describe one important type of stellar feedback, cosmic ray feedback, which has only recently introduced to galaxy simulation, and explore its consequences.

In the following, we will introduce the basic issue related to these topics and leave detailed solutions and analysis based on the FIRE simulations for the next few Chapters.

1.1.2 Dark matter halo structures

Motivated by the success of ΛCDM in explaining larger scale structure, the model has also been applied to understanding the inner structures of DM halos. According to the results from CDM only simulations (i.e. simulations without baryons), DM halo density profiles at all of the halo masses can be well approximated by the NFW profiles (Navarro et al., 1997):

$$\rho_{\mathrm{DM}} = \frac{4\rho_0}{r/r_s(1+r/r_s)^2}, \tag{1.1}$$

where r_s is the scale radius and ρ_0 is the normalization constant. The profile is often parameterized by the halo mass M_{vir} and the halo concentration $c = r_{vir}/r_{\mathrm{s}}$, where r_{vir} is the halo (virial) radius. We note that the central density profile is cuspy with $\rho \propto 1/r$ (which corresponds to a log-slope α of -1) and the density drops more steeply with a log-slope of -3 at $r \gg r_s$. Cosmological CDM only simulations show c is a function of M_{vir}, redshift, and formation time. Early formed halos are usually more concentrated, since they form at a higher mean density of the universe.

However, recent observations of dwarf galaxies, including isolated and satellite galaxies, pose serious challenges to the ΛCDM paradigm based on the CDM simulations without baryonic physics (for a review, see Bullock & Boylan-Kolchin 2017). The first issue is the cusp/core problem. Eq. 1.1 indicates that inner DM profiles should be cuspy with a log slope of -1, but recent observations, e.g. (Oh et al., 2015), show that nearby dwarf and low surface brightness galaxies have a inner DM profile flatter than the NFW profiles.

A related issue is the excessive baryonic contraction. Gas can collapse and fall into centers of DM halos, which gravitationally contracts the DM halo(Blumenthal et al., 1986). The resultant inner DM profiles are expected to be even steeper than the NFW profiles. These steep profiles (and the higher central masses) lead to higher galactic rotation curves than those from the NFW halos, in tension with the observed empirical relation between the luminosity of galaxies and the flat part of the rotation curve, i.e. the Tully Fisher relation (Tully & Fisher, 1977). This issue is more prominent in galaxies with a larger amount of baryons (i.e. Milky-Way mass or above).

Another issue is the Too Big to Fail (TBTF) problem(Boylan-Kolchin et al., 2011). When comparing the CDM only simulations with the observations of satellite galaxies, we assign observed satellite galaxies to simulated subhalos according to their luminosity and mass, i.e. the most luminous galaxies are matched with the most massive subhalos. While this approach gives the correct numbers of satellite galaxies (if small subhalos are not forming galaxies), the observed central masses of satellite galaxies are found to be systematically lower than the predictions from the CDM only simulations.

These issues motivate various modifications of the CDM theory, e.g. self interacting dark matter (SIDM) and warm dark matter (WDM). The SIDM model introduces self interactions between dark matter (but only gravitational interaction with baryons). This model can significantly flatten central DM density profiles, easing the cusp/core problem (Yoshida et al., 2000). Another proposal is to consider DM with higher effective temperature (have faster streaming speed) than cold dark matter, namely the WDM model (Abazajian, 2006), which erases the small scale structures by free streaming. It inhibits formations of small DM halos (e.g. satellite galaxies), which may be helpful in explaining the TBTF problem.

Galaxy simulations demonstrate that stellar feedback is able to address the above issues. Stellar feedback, e.g. supernova feedback, can drive strong outflows, remove significant amounts of gas from DM halo centers, rapidly reduce the central gravitational potential and expand DM orbits. Repeated episodes of outflows can create DM cores upto order kpc sizes(Pontzen & Governato, 2012). This also effectively cancels effects from the baryonic contraction in Milky-Way mass galaxies.

Since stellar feedback reduces the central masses of DM halos hosting satellite galaxies, the TBTF problem can also be alleviated. In Chapter 2, we will analyze a suite of high resolution cosmological galaxy simulations, ranging from faint dwarf to Milky Way-mass galaxies, to explore the stellar feedback-driven core formation scenario and compare with observations.

1.1.3 Ultra Diffuse Galaxies

One of the biggest challenges in astronomy is to observe a complete sample of galaxy population and categorize them according to their color, magnitude, luminosity, morphology, and many other properties. Mapping out the whole galaxy population would help us understand galaxy formation, galaxy evolution, and cosmology.

However, current surveys of galaxies are still far from complete. Due to finite sensitivity of the instruments and contamination from sky background, there are surface brightness limits below which galaxies cannot be detected. Thus, surveys preferentially select high surface brightness galaxies (HSBGs), while, hard-to-detect low surface brightness galaxies (LSBGs) have central surface brightness below 23 $\mathrm{mag/arcsec^2}$ in B band (for a review on LSBG, see Impey & Bothun 1997). Recently, due to technological advances, e.g. CCD , astronomers have discovered a diverse population of LSBGs down to at least 25 $\mathrm{mag/arcsec^2}$ in B band . These discoveries change our understanding of galaxy theories previous based on mostly HSBGs.

These discoveries allow more accurate determinations of the galaxy mass function, which are central to observational cosmology. LSBGs can be as numerous as HSBGs at the lower end, so they can affect the low mass end slope of the galaxy mass function. LSBGs have higher HI mass contents (twice more gas rich than HSBGs with the same luminosity) and also higher mass-to-light ratios(Zwaan et al., 1995). These facts, combined with their high number density, imply LSBGs are responsible for significant baryonic and dark matter masses, which are missed in the surveys of HSBGs.

LSBGs are also important in galaxy formation theories. Observing that LSBGs are predominately disky, Dalcanton et al. (1997) proposed that LSBGs are hosted in high angular momentum halos. They inferred that a significant number of disky galaxies are LSBGs, which have not been detected.

Recently, Roberto Abraham and Pieter van Dokkum designed the Dragonfly Array, which is a multi-lens array for detecting low surface brightness galaxies. It makes use of Canon 400mm lenses with nano-fabricated coatings and subwavelength structure on optical glasses. It also reduces unwanted light by imaging a galaxy through multiple lenses at the same time.

With this novel instrument, van Dokkum et al. (2015a) discovered a number of extremely low surface brightnes galaxies in a galaxy cluster that they termed "Ultra Diffuse Galaxies". They have galaxy sizes comparable to the Milky Way, while their luminosities are similar to dwarf galaxies, so they are a hundred times dimmer than the Milky Way. Subsequent observations find numerous UDGs in other galaxy clusters and groups(Beasley et al., 2016) , as well as in isolated environments. Their prevalent existence might pose a challenge to galaxy formation theory and could be an important arena for new physics.

The UDGs in clusters have many peculiar properties. They are predominately red. Their stellar velocity dispersion is also higher than the "normal" galaxies with similar luminosity, i.e. their mass-to-light ratios are abnormally high. They host larger numbers of globular clusters (GCs) than normal galaxies with similar luminosity, but their GC numbers are close to galaxies with similar velocity dispersion. Unlike LSBGs in isolated environments, cluster UDGs predominately appear spheroidal.

Some of these properties seem to imply some of the cluster UDGs reside in DM halos as massive as the Milky Way's. van Dokkum suggested that cluster UDGs are failed Milky-Way mass galaxies that got quenched at high redshift. The rest of the cluster UDGs are observed to have lower dynamical masses, which could be failed dwarf galaxies(Beasley et al., 2016).

Similar to the classical LSBGs, their low surface brightnesses could stem from their high angular momenta. For example, Amorisco & Loeb (2016) proposed UDGs reside in high spin tails of dark matter halos. However, this scenario cannot explain the spherical appearance of cluster UDGs, since high spin galaxies should be predominately disky.

Another possible formation scenario is that they form through star formation driven outflow. Supernova explosions and other stellar feedback remove significant amounts of gas from the center of galaxies (outflow), which reduces the gravitational potential. This leads to the relaxation of stellar orbits and the expansion of galaxies (El-Badry et al., 2016). Multiple episodes of these expansions could result in galaxies with surface brightness as low as UDGs (see Di Cintio et al. 2017, for UDGs in the field).

However, these studies do not incorporate the potential effect of star formation quenching for UDGs in galaxy clusters and do not reproduce the properties of cluster UDGs. In Chapter 3, we will discuss how to incorporate the outflow and quenching mechanisms to explain various peculiarities of cluster UDGs.

1.1.4 Cosmic Rays and their effects on galaxies

Cosmic rays (CR) are highly energetic charged particles which originate outside the Earth. Their exterrestrial nature was first discovered by Hess through a balloon flight measurement(Hess, 1912). Satellite and balloon flight measurements have revealed the components of CRs: 90% protons, 10% helium nuclei, 2% electrons, other heavy elements and positrons. Most of cosmic ray energy is in 1 GeV CR protons (see Grenier et al. 2015 for a summary of CR observations).

CRs in the Milky Way are mainly generated through diffusive shock acceleration (CRs scatter back and forth between converging upstream and downstream shocks) in supernova remnants, where 5%-30% of the supernova mechanical energy is injected to CRs (Bell, 1978; Blandford & Ostriker, 1978).

While CRs can travel at nearly speed of light in empty space, they are confined strongly within the Milky Way, as evidenced by (1) the GeV cosmic ray distribution observed on Earth is very isotropic, one part of 10^4, despite their sources should be anisotropically distributed; (2) the time that CRs reside in the Milky Way is $\sim 10^7$ years (orders of magnitude longer than light crossing time over the Milky Way), as inferred from the ratio between unstable and stable isotropic species (and a standard propagation model)(Zweibel, 2013).

The strong confinement of CRs is through the interactions with galactic magnetic fields. First, CRs gyrate around turbulent magnetic field lines, so CRs perform random walk motions with short mean free paths across the Milky Way. Second, CRs can amplify pre-existing Alfven waves (one kind of plasma waves) through gyro-resonant interactions, named streaming instability. This instability limits the bulk transport velocity of CRs to be around Alfven speed (in steady state) and dissipate the remaining energy and momentum into thermal gas. Regardless of the exact microscopic confinement mechanisms, CR propagation can be effectively modelled by an advection-diffusion equation with the possible addition of streaming(Trotta et al., 2011).

Propagating across the ISM, CRs constantly bombard ISM nuclei and generate pions, including neutral pions that decay into GeV γ rays. CRs can also dissipate their energy through Coulomb interactions with ambient ionized gas (Schlickeiser, 2002).

The rest of the CRs either escape from the Milky Way or build up an extended CR halo a few kpc in height, as inferred from synchrotron emission. The midplane energy density of CRs at the solar neighborhood is observed to be around 1 $\mathrm{eV/cm^3}$ (Webber et al., 2003), roughly in equi-partition with magnetic field and turbulence energies (Draine, 2011).

Since CRs have substantial pressure in the ISM and above the midplane, they could have significant effects on the galaxy evolution. Unlike other stellar feedback mechanisms that act locally around young massive stars, CRs can provide pressure and affect gas far from their sources. Analytic calculations and simulations suggest that CR pressure can drive winds and regulate star formation (Breitschwerdt et al., 1991; Mao & Ostriker, 2018). As CRs couple with most of the gas via magnetic field perturbations (except perhaps completely neutral gas in the cores of molecular clouds), CR driven winds are multi-phase, with most of the outflowing gas at a temperature of 10^4 K (Booth et al., 2013; Salem & Bryan, 2014). This is in sharp contrast with the thermal driven winds, which are dominated by 10^6 K hot diffuse gas.

These studies also show the ability for CRs to regulate star formation and drive winds depends on the CR propagation model (Uhlig et al., 2012; Ruszkowski et al., 2017), which has to be inferred from observations. In Chapter 4, we will constrain the CR propagation model by comparing our simulated and observed high energy γ ray luminosity, which results from the hadronic interactions of CRs with the ISM. In this chapter, we will also describe the numerical method to simulate CR propagation. This fast and accurate numerical method allows us to study the CR effect on the ISM, the halo gas (i.e. the circum-galactic medium), and the overall evolution of galaxies.

My dissertation research is documented in three publications Chan et al. (2015, 2018, 2019) as listed in the reference sections.

Chapter 2

The Impact of Baryonic Physics on the Structure of Dark Matter Halos: the View from the FIRE Cosmological Simulations

2.1 abstract

We study the distribution of cold dark matter (CDM) in cosmological simulations from the FIRE (Feedback In Realistic Environments) project, for $M_* \sim 10^{4-11} M_\odot$ galaxies in $M_\mathrm{h} \sim 10^{9-12} M_\odot$ halos. FIRE incorporates explicit stellar feedback in the multi-phase ISM, with energetics from stellar population models. We find that stellar feedback, without "fine-tuned" parameters, greatly alleviates small-scale problems in CDM. Feedback causes bursts of star formation and outflows, altering the DM distribution. As a result, the inner slope of the DM halo profile (α) shows a strong mass dependence: profiles are shallow at $M_\mathrm{h} \sim 10^{10} - 10^{11} M_\odot$ and steepen at higher/lower masses. The resulting core sizes and slopes are consistent with observations. This is broadly consistent with previous work using simpler feedback schemes, but we find steeper mass dependence of α, and relatively late growth of cores. Because the star

formation efficiency M_*/M_h is strongly halo mass dependent, a rapid change in α occurs around $M_\mathrm{h} \sim 10^{10} M_\odot$ ($M_* \sim 10^6 - 10^7 M_\odot$), as sufficient feedback energy becomes available to perturb the DM. Large cores are not established during the period of rapid growth of halos because of ongoing DM mass accumulation. Instead, cores require several bursts of star formation after the rapid buildup has completed. Stellar feedback dramatically reduces circular velocities in the inner kpc of massive dwarfs; this could be sufficient to explain the “Too Big To Fail” problem without invoking non-standard DM. Finally, feedback and baryonic contraction in Milky Way-mass halos produce DM profiles slightly shallower than the Navarro-Frenk-White profile, consistent with the normalization of the observed Tully-Fisher relation.

2.2 Introduction

Cold Dark Matter with a cosmological constant (ΛCDM) is a successful cosmological model that can simultaneously explain large scale fluctuations in the cosmic microwave background and the large-scale structure of the universe that forms out of these fluctuations at much later time (Spergel et al., 2007; Springel et al., 2005). However, on much smaller scales, within dark matter halos that host observed galaxies, there are indications that the distribution of dark matter is inconsistent with the simplest prediction of the cold dark matter paradigm. The most obvious and most studied disagreement is in density profiles of dark matter halos inferred from observations of dwarf and low surface-brightness galaxies. While observed slopes are relatively flat (central density slope $\alpha \sim 0$, where central density $\propto r^\alpha$) (Salucci & Burkert, 2000; Swaters et al., 2003; Gentile et al., 2004; Spekkens et al., 2005; Walter et al., 2008; de Blok et al., 2008; Oh et al., 2011) simulated cold dark matter halos are cuspy ($\alpha \sim -1$) (Flores & Primack, 1994; Moore, 1994; Navarro et al., 1997). This problem is known as the *cusp/core* problem.

To address this problem, various modifications of dark matter properties have been proposed to erase the steep central regions and produce a core-like density profile. Examples include warm dark matter (WDM), whose free streaming can suppress the small scale structure (Abazajian, 2006; Dunstan et al., 2011; Lovell et al., 2012) and self-interacting dark matter (SIDM) whose interaction can substantially affect the central density profile of halos (e.g. Yoshida et al., 2000; Burkert, 2000; Kochanek & White, 2000; Davé et al., 2001; Elbert et al., 2015). There is still no consensus on whether these modifications can solve the problem and satisfy all observational constraints: these modifications can produce serious problems on their own. For example Macciò et al. (2012a) found that in order to produce dark matter cores as large as those seen in observed dwarf galaxies, the warm dark matter would also prevent the formation of dwarf galaxies. Simple SIDM models (Carlson et al., 1992; Machacek et al., 1993; de Laix et al., 1995) were shown to violate observations of central regions of galaxy clusters (Miralda-Escudé, 2002; Yoshida et al., 2000) that are found to be denser and more elliptical than SIDM would predict. However, recent SIDM models that take into account more accurate observational constraints and the effects of baryons offer promising explanation of the problem without violating any known observational constraints (Rocha et al., 2013; Peter et al., 2013; Kaplinghat et al., 2014; Elbert et al., 2015).

Initial problems with the SIDM have motivated more complex models such as velocity-dependent SIDM (Yoshida et al., 2000; Loeb & Weiner, 2011; Macciò et al., 2012a). However, SIDM with a simple power-law velocity dependence will not be able to create a core and, at the same time, produce stable halos of dwarf galaxies over a Hubble time (Gnedin & Ostriker, 2001). Loeb & Weiner (2011) proposed SIDM with a Yukawa potential, which has a nontrivial velocity-dependence that is effective at producing cores in dwarf galaxies without adverse effects on clusters of galaxies. Cosmological simulation of a Milky Way-mass halo with this SIDM showed that realistic cores can be formed in sub-halos expected to host dwarf galaxies (Vogelsberger et al., 2012b). However, this model requires more free parameters for the velocity dependence and it is not yet known whether it can reproduce the correct halo abundance and mass distribution.

Before concluding that simple cold dark matter models must be modified,, we must also examine the effects of baryons on the distribution of dark matter within halos. Baryons are not only what is actually observed in galaxies, but baryonic effects at the halo center can, in principle, also play a role in shaping the dark matter profiles (Blumenthal et al., 1986; Navarro et al., 1996; El-Zant et al., 2001; Gnedin et al., 2004; Read & Gilmore, 2005; Governato et al., 2010; Peñarrubia et al., 2012; Governato et al., 2012; Pontzen & Governato, 2012; Macciò et al., 2012b; Teyssier et al., 2013; Di Cintio et al., 2014; Pontzen & Governato, 2014).

Navarro et al. (1996) and Read & Gilmore (2005) used N-body simulations to model a sudden removal of a large baryonic component via supernova-driven winds (represented as a change in the external potential) in a dwarf galaxy with an initially cuspy dark matter halo. They showed that such mass removal leads to formation of a dark matter core. An alternative mechanism was proposed by Mashchenko et al. (2006), who showed that bulk motion of gas within forming galaxies leads to significant gravitational potential changes which can also redistribute dark matter and reduce its central density. Dynamical effects between baryons and dark matter during the halo formation were also suggested as a mechanism that could modify dark matter density profiles (e.g. El-Zant et al., 2001; Tonini et al., 2006; Romano-Díaz et al., 2008; Del Popolo, 2009).

Recently Governato et al. (2010, 2012) used cosmological "zoom-in simulations" with baryons, cooling, star formation and supernovae feedback to show that outflow episodes in dwarf galaxies can turn the central dark matter cusps into cores. Strong supernova-driven outflows from clustered star formation in the inhomogeneous interstellar medium (ISM) resulted in a decrease of the dark matter density within central kiloparsec to less than half of what it would otherwise be in a halo of this mass ($m_{\mathrm{dm}} \approx 10^{10}\mathrm{M}_{\odot}$). Pontzen & Governato (2012) further clarified this density flattening mechanism: a quick change in gravitational potential due to gas outflow can effectively inject energy into dark matter orbits and (typically after many outflow episodes) flatten the central dark matter profile. They showed that the repeated changes of gravitational potential on timescales shorter than t_{dyn} during $2 < z < 4$ can significantly flatten cuspy dark matter profiles.

Brook et al. (2012) showed that a large fraction of the gas that is expelled returns via a large-scale galactic fountain (see also Oppenheimer et al., 2010) to form stars at later times: this greatly increases the chance of outflows from the inner regions and further helps in core formation. Other, non-cosmological simulations with strong SNe feedback also showed that it is possible to form cores in dwarf galaxies owing to bursty star formation that removes large quantities of gas during bursts (Teyssier et al., 2013).

On the other hand, idealized simulations by Gnedin & Zhao (2002),Ogiya & Mori (2011), and Garrison-Kimmel et al. (2013) focused on time evolution, supernovae energy requirements and mass ejection frequency in idealized models and argued that SNe driven feedback is not efficient enough to form cores at the observed level. However, recent cosmological simulations have had more success. Madau et al. (2014) suggest that earlier mass removal can lower the energy requirements for core formation and Oñorbe et al. (2015) showed that late star formation, after the early epoch of cusp building, is particularly efficient at utilizing stellar feedback to remove dark matter.

There are two other related “problems” with structural properties of CDM halos. One is the lack of very steep central profiles in relatively massive disk galaxies. Cuspy NFW profiles (Navarro et al., 1997) are expected to be even steeper within baryon dominated galaxies owing to the contraction of dark matter caused by the central concentration of baryons (Blumenthal et al., 1986). The distribution of matter in galaxies effectively determines the Tully-Fisher relation (e.g. Tully & Fisher, 1976; Dutton et al., 2007). However, given the observed distribution of baryons, contraction of an NFW halo would result in circular velocities too high at a given luminosity/mass. This motivated several authors to suggest that dark matter does not undergo contraction or is perhaps even expanded from the original cuspy NFW profile (Dutton et al., 2007). While this could be interpreted as suggesting a problem with the currently favored CDM model, stellar feedback is also able to effectively “expand” the dark matter distribution even in Milky-Way mass halos (Macciò et al., 2012b).

The second problem is the so called “Too Big To Fail" problem (Boylan-Kolchin et al., 2011). In the Milky Way, satellites have significantly lower dark matter densities in the inner few hundred parsecs than the corresponding sub-halos in CDM only simulations without baryons. Alternatively, massive sub-halos whose inner densities are high, never formed galaxies. Similar problems also exist in other dwarf galaxies in the Local Group (Garrison-Kimmel et al., 2014; Papastergis et al., 2015). There are hints that feedback can help solve this issue along with the cusp/core problem (Madau et al., 2014; Brooks & Zolotov, 2014; Oñorbe et al., 2015), although proper statistics are still lacking.

It is becoming clear that the bursty nature of stellar feedback in galaxies can modify the inner regions of dark matter halos. However, in general, most simulations used to study this problem so far used crude and often unphysical implementations of stellar feedback. One might worry that this could impact the effect of stellar feedback. Most of the cosmological simulations used to address the cusp/core issue simply turn off cooling from the gas heated by supernovae ejecta until such gas escapes galaxies (Governato et al., 2010, 2012; Pontzen & Governato, 2012; Macciò et al., 2012b; Di Cintio et al., 2014). The delayed cooling is unphysically long and results from a misinterpretation of the standard supernova remnant results (Martizzi et al., 2015). In addition, most simulations include only supernovae feedback while other stellar feedback mechanisms are ignored or implemented crudely: e.g. radiation pressure, cosmic rays, and photo-heating are often approximated with pure thermal energy input and additional freely-adjustable parameters (Macciò et al., 2012b; Di Cintio et al., 2014).

Furthermore, the particle mass resolution used in some previous studies was insufficient to properly resolve the observed core sizes. Low resolution may hinder the investigation of central density profiles on small scales owing to two-body relaxation effects (Power et al., 2003). In Appendix 2.A, we show the relation between the convergence radius and particle mass that should be used to estimate resolved scales in different simulations.

To study the *cusp/core* problem in a complex cosmological environment we use simulations from the Feedback in Realistic Environments (FIRE) project (Hopkins et al., 2014)[1] (H14), supplemented by four new dwarf galaxy simulations. Our simulations use physically motivated stellar feedback, in which energy and momentum input are based on stellar population synthesis models alone, with no adjusted parameters. In additions to supernovae energy and momentum we include radiation pressure, stellar winds, photo-ionization and photo-electric heating processes. In H14 we show that the M_*-$M_{\rm h}$ relation in FIRE is in reasonable agreement with observations, for galaxies residing in halo masses $M \lesssim 10^{12}{\rm M}_{\odot}$. This result is sensitive to the feedback physics: simulations with supernovae alone fail to reproduce the correct relation, unless additional feedback processes are also incorporated. Overall, stellar feedback in FIRE simulations results in bursty star formation histories followed by strong outflow episodes (Muratov et al., 2015) that can affect matter distribution within galaxies.

Our simulations are among the highest resolution cosmological “zoom-in" simulations to date evolved down to $z = 0$ with full baryonic physics. In addition to the advantages in implemented physics and resolution, we adopt the P-SPH “pressure-entropy” formulation of SPH (Hopkins, 2013), which includes a large number of numerical improvements relative to previous SPH studies, which together significantly improve the treatment of cooling and multi-phase fluid mixing, and reduce the well-known discrepancies between SPH and grid-based codes.

In this paper we study halos with masses $10^9 < M_{\rm h}/{\rm M}_{\odot} < 10^{12}$ with full feedback and their dark matter only analogs, which enables us to directly compare their dark matter distributions. We find results in broad agreement with previous work, but with some important differences. We find that stellar feedback affects all of the systems we study but large cores develop only in the halo mass range of $\sim 10^{10}{\rm M}_{\odot}$ to a few $\times 10^{11}{\rm M}_{\odot}$. Furthermore we show that cores change over time, and that progenitors of massive galaxies once had more prominent cores. We demonstrate how bursty star formation and related feedback correlate with changes in dark matter halos and show that feedback effectively cancels the effects of adiabatic contraction. Finally we discuss

---

[1] Project website: http://fire.northwestern.edu/

consequences of our results for the cusp/core issue, the Tully-Fisher relation, the “Too Big To Fail" problem and indirect dark matter detection.

We find encouraging trends that have the potential to solve most of the apparent small scale problems of the CDM paradigm.

The paper is organized as follows: §2.3 includes a brief description of the code and implemented stellar feedback as well as the set-up of the simulations. In §2.4, we show the dark matter density profiles and their time evolution. In §2.5 we study the effects of stellar feedback on the expected contraction of dark matter and on the Tully-Fisher relation. In §2.6, we compare our results with previous work, discuss the implications and propose directions for further investigation.

2.3 Simulations

2.3.1 Simulation Code

The simulations in this work were run with the newly developed GIZMO code (Hopkins, 2014) in a fully conservative, pressure-entropy based smoothed particle hydrodynamic (P-SPH) mode (Hopkins, 2013). P-SPH eliminates artificial surface tension at contact discontinuities that affects traditional density based SPH (Agertz et al., 2007; Saitoh & Makino, 2013; Sijacki et al., 2012). We use the artificial viscosity algorithm with a switch from Cullen & Dehnen (2010) which reduces viscosity to close to zero away from shocks and enables accurate shock capturing. The same higher-order dissipation switch is used to trigger entropy mixing at the kernel scale following Price (2008). Time-stepping is controlled by the limiter from Durier & Dalla Vecchia (2012), which limits the difference in time-steps between neighboring particles, further reducing numerical errors. The gravity solver of the GIZMO code is an updated version of the PM+Tree algorithm from Gadget-3 (Springel, 2005) and uses fully conservative adaptive gravitational softening for gas (Price & Monaghan, 2007). GIZMO’s softening kernel represents the exact solution of the particle mass distributed over the SPH smoothing kernel (Barnes, 2012).

The code performs well on standard strong shock, Kelvin-Helmholtz and Rayleigh-Taylor instabilities, and subsonic turbulence tests (for more details see Hopkins, 2013). In cosmological “zoom-in" simulations of a Milky Way size halo without outflows, the code eliminates most of the artificial fragmentation of halo gas seen in traditional SPH simulations (Kaufmann et al., 2006; Sommer-Larsen, 2006; Kereš & Hernquist, 2009) and increases cooling from the hot halo gas at late times (e.g. Kereš et al., 2005), when compared to the classical SPH (Kereš et al., in preparation). Overall, the resulting halo gas properties are similar to the results from adaptive-mesh and moving-mesh simulations (Agertz et al., 2009; Kereš et al., 2012; Vogelsberger et al., 2012a; Nelson et al., 2013).

2.3.2 Baryonic Physics

Our simulations incorporate cooling, star formation and physical stellar feedback processes that are observed to be relevant in the inter-stellar medium. Here we briefly review these components, for detailed description please see H14.

Gas follows an ionized+atomic+molecular cooling curve from $10 - 10^{10}$ K, including metallicity-dependent fine-structure and molecular cooling at low temperatures, and at high-temperatures ($> 10^4$ K) metal-line cooling followed species-by-species for 11 separately tracked species. At all times, we tabulate the appropriate ionization states and cooling rates from a compilation of CLOUDY runs, including the effect of the photo-ionizing background. We use global ultraviolet background model from Faucher-Giguère et al. (2009) that heats and ionizes the gas in an ionization equilibrium approximation. We apply on-the-fly ionization corrections in denser gas to account for the self-shielding based on the local Jeans-length approximation (to determine the surface density), which provides an excellent match to a full ionization radiative transfer calculation (Faucher-Giguère et al., 2010; Rahmati et al., 2013; Faucher-Giguère et al., 2015b).

Star formation is allowed only in dense, molecular, self-gravitating regions above $n > 10-100\ \mathrm{cm}^{-3}$. This threshold is much higher than that adopted in most “zoom-in" simulations of galaxy formation (the high value allows us to capture highly clustered star formation). We follow Krumholz & Gnedin (2011) to calculate the molecular fraction f_{H2} in dense gas as a function of local column density and metallicity. We allow SF only from the locally self-gravitating molecular gas using the efficiency of 100% per free fall time (the actual SF efficiency is feedback regulated).

Our stellar feedback model includes a comprehensive set of physical mechanisms: radiation pressure, supernovae (with appropriate momentum and thermal energy input), stellar winds, photo-ionization and photo-electric heating as described in H14. We do not tune any feedback model parameters but instead directly use the energy, momentum, mass and metal return based on the output of the STARBURST99 stellar population synthesis model (Leitherer et al., 1999). Our feedback model is implemented within the densest interstellar-medium material, yet we do not resort to turning off cooling of supernova heated gas at any time.

2.3.3 Initial conditions and zoom-in method

We adopted a ‘standard’ flat ΛCDM cosmology with $\Omega_0 \approx 0.27$, $\Lambda \approx 0.73$, $\Omega_b \approx 0.045$, $h \approx 0.7$ for all runs. In order to reach the high-resolution necessary to resolve a multi-phase ISM and to properly incorporate our feedback model we use the “zoom-in” technique. This places maximum baryonic and dark matter resolution around the halo of interest in a lower resolution, collisionless box (Porter, 1985; Katz & White, 1993).

We consider halos with mass from 10^9 to $10^{12}\mathrm{M}_\odot$ at $z = 0$ from the FIRE project (Hopkins et al., 2014). Initial conditions of those halos are listed in Tab. 2.1. The simulations **m09** and **m10** are constructed using the methods from Oñorbe et al. (2014); they are isolated dwarfs. Simulations **m11**, **m12q** and **m12i** are chosen to match a subset of initial conditions from the AGORA project (Kim et al., 2014a) while **m12v** uses initial conditions from Faucher-Giguère &

Table 2.1: Simulation details. M_{h}^{0} and M_{*}^{0} are the total mass and stellar mass of the largest halo in the simulation at $z = 0$. $R_{1/2}$ is the radius of the region where half of the stellar mass is enclosed. m_{b} is the mass of a gas particle in the simulation; m_{dm} is the mass of a dark matter particle in the simulation. ε_{b} is the minimum gravitational smoothing length of gas; $\varepsilon_{\mathrm{dm}}$ is the Plummer equivalent gravitational smoothing length of dark matter. The simulation name convention is as follows, "mXX" refers to the halo mass $\sim 10^{XX}\mathrm{M}_{\odot}$. **d** are the corresponding dark matter only simulations, e.g. **dm09** corresponds to **m09**. DM only and hydrodynamical simulations have the same initial conditions, except that the gas particles are absorbed into the dark matter particles in DM only simulations. **m09**, **m10**, **m11**, **m12v**, **m12i** and **m12q** are from H14, whereas **m10h1297**, **m10h1146**, **m10h573** and **m11h383** are new simulations first presented in this work.

Name	M_{h}^{0} $[M_{\odot}]$	M_{*}^{0} $[M_{\odot}]$	R_{vir} [kpc]	$R_{1/2}$ [kpc]	m_{b} $[M_{\odot}]$	ε_{b} [pc]	m_{dm} $[M_{\odot}]$	$\varepsilon_{\mathrm{dm}}$ [pc]
m09	2.6e9	4.6e4	36	0.49	2.6e2	2.0	1.3e3	29
m10	7.9e9	2.3e6	50	0.51	2.6e2	2.9	1.3e3	29
m11	1.4e11	2.4e9	1.4e2	6.9	7.1e3	7.1	3.5e4	71
m12v	6.3e11	2.9e10	2.2e2	1.8	3.9e4	21	2.0e5	2.9e2
m12i	1.1e12	6.1e10	2.7e2	4.3	5.7e4	20	2.8e5	1.4e2
m12q	1.2e12	2.1e10	2.8e2	3.6	7.1e3	20	2.8e5	2.1e2
dm09	3.3e9	-	39	-	-	-	1.6e3	29
dm10	9.3e9	-	54	-	-	-	1.6e3	29
dm11	1.6e11	-	1.4e2	-	-	-	4.3e4	71
dm12v	7.7e11	-	2.4e2	-	-	-	2.4e5	2.9e2
dm12i	1.1e12	-	2.9e2	-	-	-	3.4e5	1.4e2
dm12q	1.4e12	-	3.0e2	-	-	-	3.4e5	2.1e2
m10h1297	1.3e10	1.7e7	62	1.8	1.5e3	4.3	7.3e3	43
m10h1146	1.6e10	7.9e7	65	2.5	1.5e3	4.3	7.3e3	43
m10h573	4.0e10	3.2e8	88	3.4	1.5e3	10	7.3e3	1.0e2
m11h383	1.6e11	4.0e9	1.4e2	7.2	1.2e4	10	5.9e4	1.0e2
dm10h1297	1.6e10	-	66	-	-	-	8.8e3	43
dm10h1146	1.8e10	-	68	-	-	-	8.8e3	43
dm10h573	4.2e10	-	91	-	-	-	8.8e3	1e2
dm11h383	1.7e11	-	1.4e2	-	-	-	7.1e4	1.0e2

Kereš (2011) (higher resolution versions of the run first presented in Kereš & Hernquist, 2009). In addition, we re-simulated all of these initial conditions using dark matter only N-body simulations with the same Ω_m to have a matched set of simulations with and without baryonic physics for a direct comparison.

To improve halo mass coverage in the regime where cores are prominent, $M_\mathrm{h} \sim 10^{10} - 10^{11}\mathrm{M}_\odot$, we have also simulated additional four halos with the same FIRE code, also listed in Table 2.1. These additional simulations are first time presented in this work. Initial conditions were generated using the MUSIC code (Hahn & Abel, 2011). We randomly selected halos with small Lagrangian regions for resimulation from a 40 h^{-1} Mpc box. All particles within $3R_\mathrm{vir}$ at $z = 0$ are enclosed by the Lagrangian region to reduce contamination (Oñorbe et al., 2014). Halos **m10h1297**, **m10h1146** and **m10h573** have masses between **m10** and **m11**, while **m11h383** is slightly more massive. They are all isolated field dwarfs.

2.3.4 Convergence Radius

We adopted the method described in Power et al. (2003) to calculate a conservative limit for the convergence radius of the dark matter profiles in the N-body only simulations. They found that effective resolution is related to radius where the two-body relaxation time, t_relax, becomes shorter than the age of the universe t_0. They verified this with N-body simulations and found out that for this particular problem, well resolved regions of halos require $t_\mathrm{relax} > 0.6t_0$. At smaller radii, even if the dynamics are locally well resolved, small N-body effects can, over a long integration time, artificially turn cusps into cores. Given the enclosed number of particles N and the average density of the enclosed region $\bar{\rho}$ one can show that:

$$\frac{t_\mathrm{relax}(r)}{t_0} = \frac{\sqrt{200}}{8}\frac{N}{\ln N}\left(\frac{\bar{\rho}}{\rho_\mathrm{crit}}\right)^{-1/2}, \tag{2.1}$$

where $\rho_{\rm crit}$ is the critical density. We define $r_{\rm Pow}$ as the smallest radius that fulfills $t_{\rm relax} > 0.6 t_0$ for the dark matter only simulations and use $r_{\rm Pow}$ to conservatively estimate where DM profiles are converged. We show the minimum particle mass required for converged profiles at $0.3 - 3\% R_{\rm vir}$ in Appendix 2.A and discuss implications and limitations of this convergence criterion in § 2.6.1.

2.3.5 Halo Finding

We identify halos and estimate their masses and radii using the Amiga Halo Finder (AHF) (Knollmann & Knebe, 2009)[2]. AHF uses an adaptive mesh refinement hierarchy to locate the prospective halo center (Knebe et al., 2001). We use the Bryan & Norman (1998) formulae to determine the virial over-density and virial radius, $R_{\rm vir}$, and quote the halo mass as the mass enclosed within the virial radius. We follow the main progenitor of a halo using the merger tree code included in AHF and check the growth history of each individual halo, making sure that we follow the same main progenitor. We use the histories of the main progenitors to study the time evolution of the density profile. Occasionally, AHF misidentifies the main progenitor of the halo, so sometimes $R_{\rm vir}$ temporarily decreases. We avoid this problem by searching for another halo with larger $R_{\rm vir}$ and its center within 50 kpc of the center of the main progenitor in the previous snapshot.

During ongoing mergers and for galaxies with large clumps of stars and gas, AHF adaptive centering on the highest overall density might quickly change over time and might not center on the stars. This is especially important in halos with shallow dark matter profiles and relatively shallow distributions of stars. To avoid this issue and have a consistent centering on the stellar component, we use two-step procedure to identify the center. First we use AHF to define $R_{\rm vir}$ and an approximate center. Within $0.1 R_{\rm vir}$ around this center we place the stellar mass volume density on a grid. We search for progressively higher overdensities which we enclose in an iso-density ellipsoid. Once this ellipsoid includes less than one quarter of the total galaxy stellar mass we

---

[2] http://popia.ft.uam.es/AHF/Download.html

stop the procedure. The center of the ellipsoid is our new halo center. This ensures consistent centering of all profiles on the galactic stellar distribution. We tested this procedure and found that our newly defined center is closer to the DM density peak than the original AHF for cases with shallow central cores and shows less stochastic variations of the central density slope over time.

2.4 Dark matter profiles and their time evolution

The focus of this paper is the effect of stellar feedback on the dark matter distribution in our simulated halos. There are three major areas we explore: the relation between the halo mass and the central dark matter profile, the time evolution of the inner dark matter density, and the changes to galaxy structure caused by the effects of stellar feedback.

2.4.1 Dark matter profiles

Figure 2.1 shows spherically averaged dark matter density profiles of six simulated halos at $z = 0$. We focus on the inner regions of halos, 0.002-0.2$R_{\rm vir}$ where galaxies reside and where effects of feedback are expected to be measurable. We show both the profiles from DM only simulations as well as DM profiles from simulations with baryonic physics. DM only profiles are re-normalized to account for the lower global $\Omega_{\rm DM}$ in simulations with baryons. Effects of the baryonic physics are visible in most halos to a different degree and are the largest in **m11** and **m12v** simulations. In **m09** the DM density profile is almost the same in simulations with and without baryons, while in **m10**, a small, resolved core forms in the central region. The density profile in **m11** has the largest core and the lowest central DM density. In **m12v**, central density starts increasing again and the relative core size decreases, but differences in profiles are present all the way to several percent of $R_{\rm vir}$. In the two most massive halos we analyze, **m12i** and **m12q**, differences in central region are even smaller, although profiles are still shallower than what is

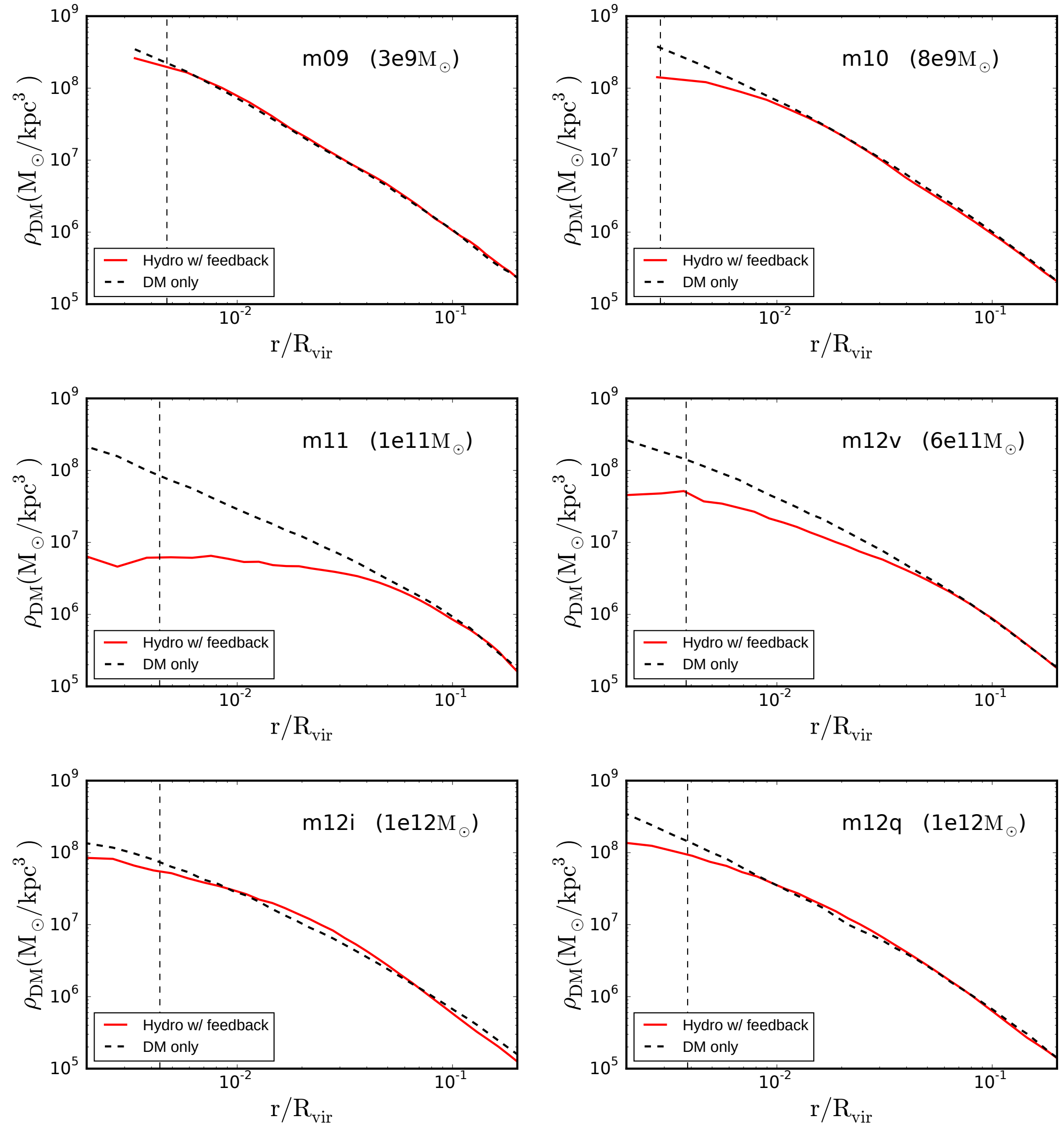

Figure 2.1: Dark matter density profiles of halos at $z = 0$. Black dashed lines represent collisionless dark matter only simulations; red solid lines represent simulations with baryons and stellar feedback. The Power radius $r_{\rm Pow}$, within which N-body relaxation effects can become important, is shown with vertical black dashed lines. The halo masses are shown in the brackets. Baryonic feedback reduces the central DM density, especially at around $M_{\rm h} \sim 10^{11}{\rm M}_\odot$.

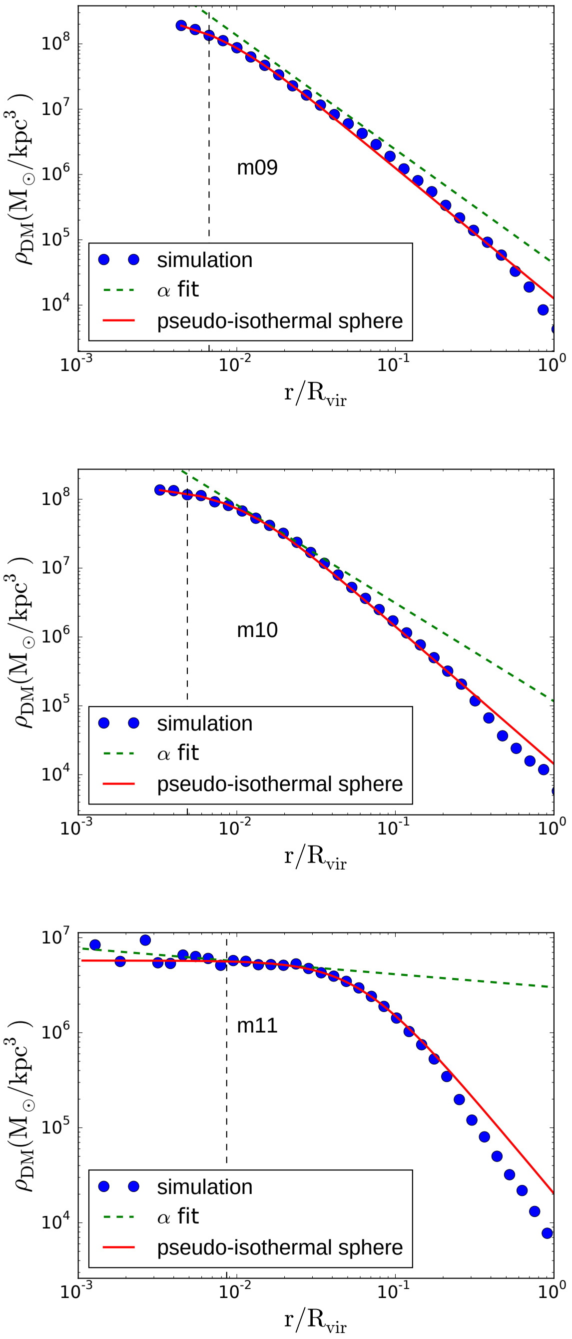

Figure 2.2: Dark matter density profiles of halos at $z = 0$ from hydrodynamic simulations (blue solid circles), fits with the pseudo-isothermal sphere (black solid line) and fit with a power-law model ($\propto r^{\alpha}$) at 1-2 $\%R_{\mathrm{vir}}$ (green dashed line). The black vertical line shows the convergent radius according to the Power criterion. The pseudo-isothermal sphere is a good fit to the central regions of the simulated halos and provides a good estimate of the core sizes.

expected based on N-body simulations. However in § 2.4.4, we show that the effect of feedback in these halos is significant and largely cancels out the gravitational influence of baryons that is expected to steepen the profile seen in dark matter only case. We note that all of the plotted range is resolved with many gravitational softenings of the dark matter particles. We also show the more conservative Power convergence criterion which is typically a fraction of a percent of $R_{\rm vir}$ for all of our halos.

We quantify the effect of feedback on dark matter distribution using two parameters that are frequently estimated from observations: the central slope α of the dark matter density profile ($\rho_{DM} \propto r^{\alpha}$) and the core radius $r_{\rm core}$ of the pseudo-isothermal sphere (see Eq. 2.2). Examples of the fits are shown in Figure 2.2.

2.4.2 Inner slopes of dark matter halo profiles

We estimate the slope α of the dark matter density profile by fitting a power law relation $\rho_{DM} \propto r^{\alpha}$ in the $1-2\% R_{\rm vir}$ interval. This range is well resolved for all of our main halos at z=0 and it is physically meaningful as it shows the relative profile change at a fixed fraction of the halo size. For dwarf galaxies, this is close to the region where observations indicate shallow and core-like profiles in low-mass galaxies (typically measured at a few hundred pc; see Oh et al., 2011, 2015; Walter et al., 2008; Hunter et al., 2012). We also show slopes at $0.5-1\% R_{\rm vir}$ for comparison. Example of the fit for α are shown in Figure 2.2. We have also measured α in the fitting ranges of $0.3-0.7$kpc and $1-2$kpc. In Appendix 2.B we discuss limitations of these alternative fitting ranges and show that general trends of α with halo mass are similar to our default fitting choice.

Figure 2.3 shows α as a function of the halo virial mass, $M_{\rm h}$, at different redshifts. We only show main halos with more than 10^5 DM particles and remove all sub-halos and halos with more than 1% contamination by more massive DM particles within the inner $0.1 R_{\rm vir}$ [3]. The

---

[3] Note that in most runs we use a "padding region" around our zoom in region where mass resolution is lower

hollow circles represent α whose fitting range contain regions smaller than 0.5 $r_{\rm Pow}$ and/or larger than 1/3 r_s, where $r_{\rm s}$ is the scale radius of the NFW profiles. [4]

We focus on $z \leq 2$ when profiles of halos start to stabilize as rapid halo growth subsides. At $z = 0$, the simulated halos show a clear tendency to form shallow central profiles at $M_{\rm h} \sim 10^{10} - 10^{11}{\rm M}_{\odot}$. All of the profiles in this range are significantly shallower than the NFW profile. More accurate estimate of the halo mass and stellar mass ranges where feedback flattens central slopes will require a larger number of simulations as our statistic are currently limited. When profiles are measured at even smaller radii, 0.5-1% of $R_{\rm vir}$, profiles are typically even more shallow. At z=2 we see that the scaling with mass shows much larger dispersion, which owes to very bursty star formation and central halo regions that are just coming out of the fast growth stage. We later show that in intermediate mass halos at a fixed physical radius, DM profiles get shallower with time.

It is interesting to notice that low mass dwarfs with $M_{\rm h} \ll 10^{10}{\rm M}_{\odot}$ do not develop density cores even at 1% of $R_{\rm vir}$ (which is typically only several hundreds of parsecs). As we discuss later, only a small fraction of baryons are converted to stars in these halos, owing to efficient feedback and effects of the UV background. The energy available from a small number of SNe is not sufficient to dramatically modify the dark matter distribution. Around $M_{\rm h} = 10^{10}{\rm M}_{\odot}$, the slope of the inner density profile increases rapidly with mass, indicating the development of DM cores. This seems to be a "threshold" halo mass needed to develop large cores. As discussed in Oñorbe et al. (2015), small differences in star formation histories in halos close to this threshold can result in the substantial difference in central slopes of the dark matter distribution.

Finally, in halos with mass comparable to the Milky Way (**m12v** and **m12i**) profiles steepen again and are only slightly shallower than NFW. These halos have deep potential wells that can retain a large fraction of available baryons and convert them into stars. Baryons are

---

only by factor of 8. Mild contamination with such particles can sometimes occur within $R_{\rm vir}$ but typically has no consequence on the evolution of halo gas or central slopes.

[4] We estimate $r_{\rm s}$ from the concentration $c = R_{\rm vir}/r_{\rm s}$ at a given mass, from the concentration-mass relation of Dutton & Macciò (2014).

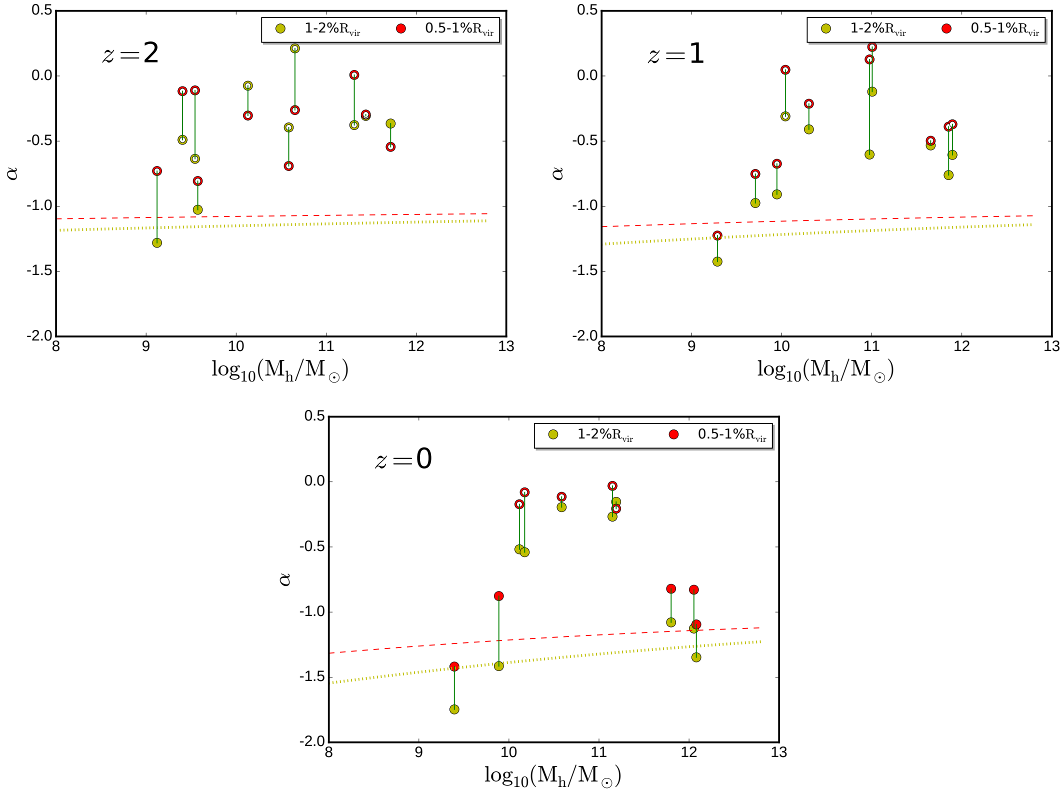

Figure 2.3: Slopes of dark matter density α as a function of halo mass at different redshifts. The green dotted and red dashed lines represent the expected α for the NFW profiles measured at 1-2% and 0.5-1%R_{vir} respectively. The concentration of the NFW profiles is evolved with redshift as in Dutton & Macciò (2014). Filled circles represent α for simulated halos in which the fitting range is larger than 0.5 r_{Pow} and smaller than one third of r_{s}. Hollow circles represent the slopes in halos in which at least one of these criteria is not satisfied (see the main text for other selection criteria) At $M_{\mathrm{h}} \sim 10^{10} - 10^{11}\mathrm{M}_{\odot}$, baryonic effects lead to profiles significantly shallower than the corresponding NFW profiles from N-body simulations.

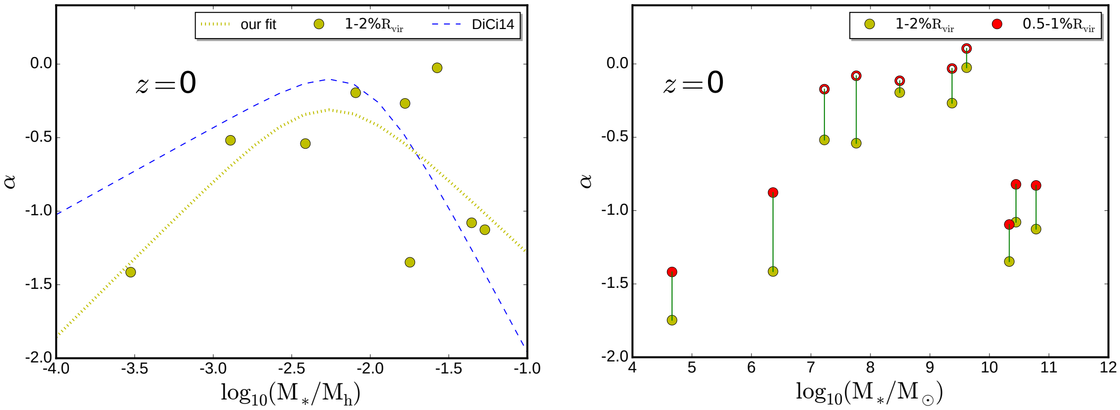

Figure 2.4: (*Upper*) Relation between α and ratio between M_* and M_h. The blue dashed line show the fit from Di Cintio et al. (2014) whereas the yellow dotted line shows the same fitting for our data. (*Lower*) Relation between α and M_*. The symbols are explained in Figure 2.3. The DM profiles near halo centers are cuspy at the lowest and highest masses, and shallowest at $M_* \sim 10^8 - 10^9 \mathrm{M}_\odot$ and $M_*/M_\mathrm{h} \sim 0.01$.

actually expected to steepen the DM profiles to $\alpha < -1$ owing to adiabatic contraction of dark matter. However, bursty feedback largely cancels and in some cases even overcomes this expected effect of contraction, resulting in slopes $\alpha \gtrsim -1$. The interplay between baryonic contraction and stellar feedback will be discussed in Section 2.4.4.

Figure 2.4 shows the scaling of profile slope with galaxy stellar mass (lower panel) and M_*/M_h (upper panel). In terms of stellar mass, feedback significantly modifies DM slopes in the $M_* \sim 10^7 - 5\times10^9 \mathrm{M}_\odot$ range, with a fast transition from cusps to cores occurring at a few $\times 10^6 - 10^7 \mathrm{M}_\odot$. Overall trends of α with M_h in Figure 2.3 are similar to the result of Governato et al. (2012) and Di Cintio et al. (2014) (see also a recently submitted work by Tollet et al., 2016). However, we stress that both of these simulations simply suppress cooling in dense gas after supernovae explosions rather than explicitly treat most of the feedback processes around young stars. Furthermore the spatial and mass resolution is typically better in our simulations, by about a factor of ten in mass. This leads to some differences in the slopes of dark matter halos that are illustrated in the upper panel of Figure 2.4. In general, profile slopes increase faster with M_*/M_h compared to the previous “subgrid” models, suggesting faster transition from cusps to cores. We caution that a small number of simulated halos in both samples could also be responsible for some of the differences. In addition we find that the central slope relation is different for the inner 1% or inner 2% of $R_{\rm vir}$, which means that the fitting formula in Di Cintio et al. (2014) is not generally applicable. We compare our result with observations in §4.5.2.

2.4.3 Core radii

In addition to the inner slope, we also examine another parameter, the core radius $r_{\rm core}$ of the halo. We quantify the core size using the the pseudo-isothermal sphere fit that is frequently used to describe dark matter density profiles (e.g. Begeman 1987; Broeils 1992; de Blok & McGaugh 1997; Verheijen 1997; another popular fit is the Burkert profile, e.g. Salucci & Burkert 2000). Density profile is given by

$$\rho(r) = \rho_0 \left[1 + \left(\frac{r}{r_{\rm core}}\right)^2\right]^{-1}, \tag{2.2}$$

where ρ_0 is the central dark matter density. We use Eq. 2.2 to fit the spherically averaged dark matter density profiles of the simulated halos. The two free parameters, $r_{\rm core}$ and ρ_0, were determined through a χ^2 minimization fitting procedure starting at $r = 0.1$kpc and ending at $r = \min[{\rm R_{vir}}, 100{\rm kpc}]$. Table 2.2 lists $r_{\rm core}$ for all halos analyzed in this work. Examples of our fits are shown in Figure 2.2. In general fits agree well (to better than few tens of percent within $0.1R_{\rm vir}$) with the DM density profiles for all halos with $M_{\rm h} < 10^{12}{\rm M}_{\odot}$. For **m12q** and **m12i** pseudo-isothermal profiles deviate significantly from the DM distribution. Evidence of cores is present in all halos. The core size is smallest (relative to $R_{\rm vir}$) in the **m09** run ($< 0.5\% R_{\rm vir}$) and largest in **m11h383** and **m10h573** ($> 4\% R_{\rm vir}$) , where we also find the shallowest central slope. Cores of the size of $> 0.005 R_{\rm vir}$ are present even in Milky Way mass halos, albeit with higher central DM density and less shallow central slopes than at $M_{\rm h} \sim 10^{11}{\rm M}_{\odot}$. We compare the core radii from our simulations to observations in § 2.5.1.

Table 2.2: The core radii of the best fitted pseudo-isothermal spheres (Eq. 2.2) of the simulated halos at $z = 0$. Large cores of 3-4% $R_{\rm vir}$ form at $M_{\rm h} \sim 10^{10} - 10^{11}{\rm M}_{\odot}$.

$z = 0$	$r_{\rm core}$ (kpc)	$r_{\rm core}/R_{\rm vir}$
m09	0.17	0.0048
m10	0.38	0.0073
m11	4.7	0.034
m12v	1.4	0.0061
m12i	2.0	0.0073
m12q	1.2	0.0043
m10h1297	2.0	0.032
m10h1146	2.1	0.033
m10h573	3.6	0.041
m11h383	5.7	0.041

Time Evolution of α

Next, we investigate the time evolution of the central slope of the dark matter distribution, for five representative halos from our sample. Left panels of Figure 2.5 show the time evolution of α measured at $1-2\%$ of the halo virial radius at $z = 0$ ($R_{\rm v0}$). For each halo, this radius is kept fixed in physical units at all times. [5] In **m10**, $\alpha < -1$ at all times, which is consistent with its relatively small core size, below $1\% R_{\rm vir}$. In **m10h1297**, α is steadily rising from -1 at $z \gtrsim 1$ to ~ -0.5 at $z = 0$. In **m11**, $\alpha \sim -1$ early on, increasing to $\alpha \sim 0$ around $z \sim 1$ and stays quite flat until late times.[6] In **m12i** and **m12v** central DM profiles are flattened to $\alpha \sim -0.7$ at $z \simeq 1$ but steepen afterwards such that central dark matter slope is $\alpha \sim -1$ at the present time.

The right panels show the time evolution of the enclosed mass within $0.02R_{\rm v0}$ and the star

---

[5] We have also analyzed the results within a fixed fraction of the time dependent virial radius ($R_{\rm vir}$ instead of $R_{\rm v0}$) but the correlation between stellar feedback and the enclosed DM mass is difficult to interpret because enclosed DM mass increases with $R_{\rm vir}$.

[6] At late times $z < 0.5$, this halo undergoes several episodes of very fast central slope variations. We examined this system closely and found that these are caused by close passages of a substructure in an ongoing merger. Vertical lines in Figure 2.5 indicate the times of closest passages: they correlate well with temporary drop and strong oscillations in central slope. The close passages can affect the accuracy of locating center of the galaxy in AHF, which further motivates our two-step center finding procedure described in §2.3.5.

formation rate within $0.1R_{v0}$ averaged over 0.2 Gyr. [7] [8] A dense central concentration of dark matter builds up early in **m10**, with some fluctuations during the bursty star formation epoch at $2 < z < 4$, but as star formation subsides the amount of dark matter in the central region remains almost unchanged until the present time. The correlation between star formation and strong outflows of gas that follow the burst (Muratov et al., 2015) and the decrease of dark matter in the central region is clearly visible in the **m10h1297** and **m11** panels. Removal of DM mass occurs after strong bursts of star formation. We examine this more closely in §2.6.1. While some of the dark matter gets re-accreted, the central concentration of dark matter remains lower after the burst for at least several Gyrs.

Each strong burst of star formation reduces central density of DM, so the final slope and core size are a consequence of several burst episodes over a Hubble time. The overall effect is small in **m10**, because the star formation rate decreases to very low values at $z < 4$. From the comparison of DM only and feedback simulations it is clear that a small difference in central DM concentration was established early on and stays largely unchanged until late times.

A small, fluctuating and early decrease in the DM concentration is also seen in more massive halos, e.g. **m10h1297** and **m11**. However, the amount of dark matter in a central region only decreases significantly once the central region finishes rapid growth, at $z \sim 1$ in **m10h1297** and $z \sim 3$ in **m11**. After this stage, DM only simulations show an approximately constant amount of dark matter in the central region while baryonic simulations successfully evacuate a large amount of dark matter from the center. Unlike **m10**, they have several ongoing bursts of star formation after the rapid-buildup stage, each of which removes a significant amount of dark matter. It appears that having strong bursts of star formation and outflows *after* the inner halo buildup slows down is the key to produce a long lasting shallow DM density profile. At early times, during the fast buildup stage, shallow profiles are not fully established as showed in Figure

---

[7] Newly formed stellar particles can move quickly between simulation outputs during the star formation burst, owing to feedback induced mass redistribution, so we integrate star formation within this larger radius.

[8] Results averaged over 0.1Gyr or shorter time-scales are qualitatively similar but show more rapid fluctuations in sub-components of longer bursts so we selected 0.2Gyr for the sake of clarity.

2.5.

In **m12i** and **m12v**, removal of DM after the peaks of star formation is also seen at $z > 1$ when fluctuations are large. After $z \sim 1$, the star formation continues at modest level without rapid bursts. At the same time, the enclosed DM mass grows slowly. In these massive halos re-accretion of dark matter in the center occurs when the star formation rate is low and hierarchical assembly is slow. To explain this we followed the central accumulation of baryonic material and found out that in both halos baryons start to dominate central mass at $z \sim 1.5$. As a consequence dark matter gets contracted, increasing the amount in the inner halo (see § 2.5). This effect is stronger in the **m12i** simulation that is more baryon dominated, and accumulates baryons faster at late times. [9]

The core forms after multiple starbursts rather than one single blow-out, which is consistent with the mechanism discussed in Pontzen & Governato (2012) (see also Ogiya & Mori, 2014). After a blow-out some re-accretion of DM does occur but even after several Gyrs the amount of DM enclosed in central region does not return to the pre-burst level, indicating that the effect on DM is long lived. These trends are the most obvious at $M_\mathrm{h} \sim 10^{11}\mathrm{M}_\odot$, i.e. in **m11**. However, in more massive systems we see that cuspier profiles are re-built at later times. While star formation proceeds to late times, it is often spread throughout the disk. In a companion paper (Muratov et al., 2015) we show that at late times the star formation activity is not able to eject large quantities of material from galaxies, which is why this continuous star formation does not "heat" and remove DM from the center. Even if the assembly of central regions of the dark matter halos slows down at relatively early times, increase in central concentration of baryons at late times can rebuilt DM cusps via adiabatic contraction. Our simulations suggest that the contribution of minor mergers to the re-growth of cusps (e.g. Dekel et al., 2003; Laporte & Peñarrubia, 2015) at late times is likely sub-dominant or negligible, but a larger number of halos is needed to confirm this for halos with diverse growth histories.

---

[9] In **m12v** the star formation rate is low and the amount of baryons in the central region changes very slowly in the final several Gyrs. The enclosed dark matter at those times is also affected by ongoing minor mergers, that cross very close to the center and are later disrupted causing variations in the enclosed density.

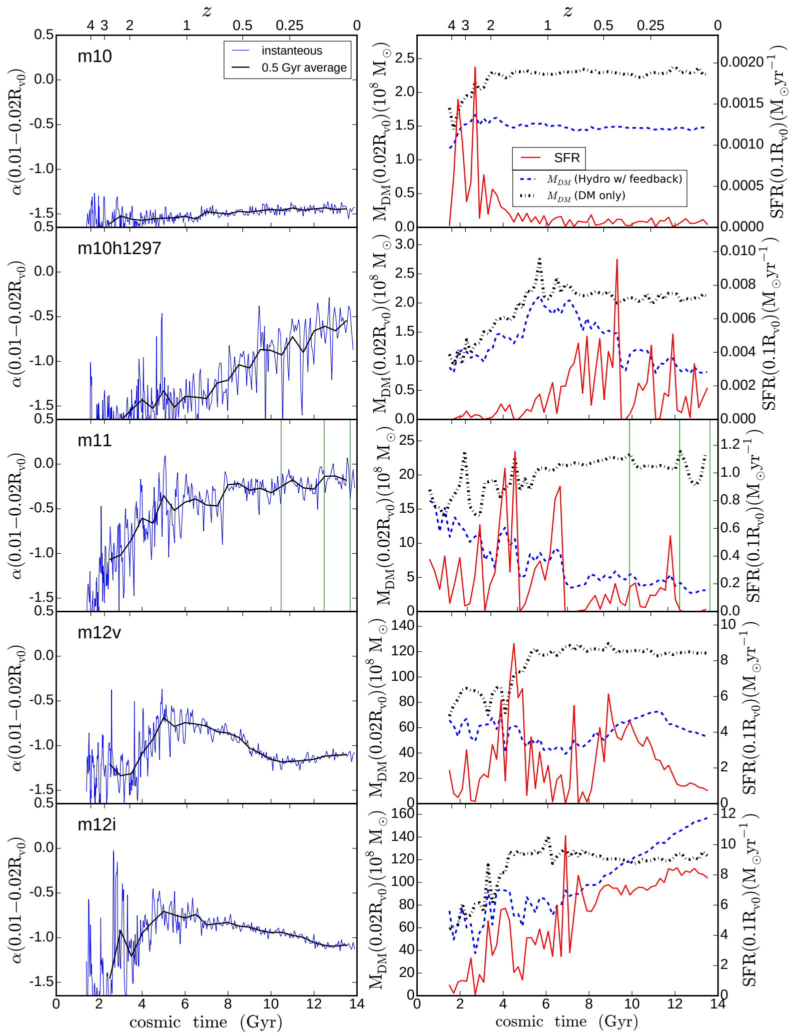

Figure 2.5: (*Left*) Dark matter density slope, α, within $1-2\% R_{\rm vir}(z=0)$, $R_{\rm v0}$, as a function of redshift/cosmic time in **m10**, **m10h1297**, **m11**, **m12v** and **m12i** respectively (from top to bottom). The slope is measured at fixed physical radius at all times. Blue lines shows the variations on the time scale of our simulation output (typically 20-30 Myrs) while the black lines show the average values over 0.5Gyr. (*Right*) Time evolution of the enclosed dark matter mass within $0.02R_{\rm v0}$ for DM only (black dash-dotted) and hydrodynamical simulations with feedback (blue, dashed) and star formation rate within $0.1R_{\rm v0}$ (red solid), all averaged over 0.2Gyr. Green vertical lines in **m11** panels show the times of close passages of a subhalo. Cores form when the central DM accretion stops but the star formation is still bursty, as seen in **m10h1297** and **m11**.

We have already seen that core formation depends strongly on halo mass but also on the presence of significant star formation episodes after the central region stops accreting dark matter. This is critical at halo masses where large cores start to develop. We showed this directly by using the initial condition of **m10**, simulated with a slightly different local feedback coupling scheme that increases late time star formation and its burstiness: the outcome is a larger DM density core and a shallower center slope compared to the original FIRE **m10** simulation analyzed here (see Oñorbe et al., 2015) This means that if there are bursts of star formation activity occurring in dwarf galaxies/halos around this mass at late times they could result in shallow density profiles by present time.

The star formation history of **m10** is significantly different from **m10h1297**. It forms most of the stars before $z = 2$ and becomes passive at late time whereas other halos remain actively star forming at present. From the observations of dwarf galaxies in the Local Group, Weisz et al. (2014) show that a large fraction of dwarf galaxies have active late time star formations, especially for field galaxies and galaxies with $M_* > 10^6 \mathrm{M}_\odot$. Therefore, the star formation histories of our simulated galaxies are well within the observed range. Our limited statistics suggest that at $M_* \sim 10^6 - 10^7 \mathrm{M}_\odot$ SFR history is closely linked to formations of large cores (see also Oñorbe et al., 2015).

2.4.4 Halo Expansion or Baryonic Contraction?

In the previous section, we investigated the shapes of profiles of our simulated halos. Here we examine the effect of a central concentration of baryons on the dark matter profiles.

First, we examine the net effect of halo expansion via feedback and halo contraction owing to central concentration of baryons. Feedback is dominant in shaping flatter profiles in lower mass halos, but baryonic contraction largely cancels the feedback effect in Milky Way mass halos, such that their final profiles are only slightly shallower than the NFW profile.

In order to estimate the effect of baryonic contraction on the dark matter profiles, we follow Blumenthal et al. (1986) to calculate the final dark matter mass distribution M_x, given the final baryon mass distribution $m_{\rm b}$ and the initial total mass distribution M_i:

$$r[m_{\rm b}(r)+M_x(r)] = r_i M_i(r_i) = r_i M_x(r)/(1-F_b), \tag{2.3}$$

where F_b is the fraction of dissipational baryons, r_i and r are initial and final orbital radii respectively. We follow the simple semi-analytic model (Dutton et al., 2007), and assume that initial total halo density profile is the one from our DM only simulation, and use the final distribution of baryons (stars and gas) in the full physics simulation to estimate the contraction. Therefore, we use $m_{\rm b}$ from hydrodynamical simulations with stellar feedback, and M_i is the halo mass from dark matter only simulations. [10]

Figure 2.6 shows density profiles from collisionless simulations, full feedback simulations, and from models with a contracted DM halo. Left panels show three different DM profiles for each halo and baryon density profiles from feedback simulations for reference. Right panels show the total density profiles including DM and baryons (gas and stars).

In **m10**, the estimated effect of adiabatic contraction is very small because the fraction of baryons in the center of **m10** is small. The baryon density is less than one tenth of dark matter density near the center. However, the feedback slightly expands the DM and forms a small core.

In **m10h1297** and **m11**, stellar feedback strongly affects dark matter distribution, making it much shallower than in the corresponding collisionless run. It is interesting that in **m10h1297**, feedback significantly flattens the DM profile, creating a large core, but the halo remains dark matter dominated at all radii. In **m11**, the baryon density is a slightly larger fraction of the total, but still significantly lower than the corresponding dark matter density in the collisionless simulation. The contracted profiles for both of these halos are therefore very similar to the dark

---

[10] We also tried to account for the loss of baryons due to feedback but the mass loss is much smaller than the total mass, especially in **m12** series. The difference in circular velocity with or without the missing baryons is less than a few percent in **m11** and negligible at higher masses.

matter profiles from the corresponding collisionless simulations.

In more massive halos, the **m12** series, baryonic contraction is expected to significantly steepen the DM profiles, because their central regions are baryon dominated. While **m12v** shows a strong effect of feedback, the profile of **m12i** is relatively steep in the center, similar to the NFW profile. However, when compared to the expectations of baryonic contraction we see that the resulting profile is much shallower than contracted NFW halo for all of the plotted simulations. This demonstrates that even in these massive halos, feedback has a strong effect on shaping the final dark matter profiles, and largely cancels out the effect of contraction. In general the expansion of the halo by the stellar feedback causes an order of magnitude difference in the density profiles around 1 kpc in $10^{11-12}\mathrm{M}_\odot$ halos when compared to expectations of a simple baryonic contraction model.

While feedback effects on the DM distribution are substantial even in **m12** series halos, in those halos baryons completely dominate the central few kpc at z=0. This is why the differences between the total matter density profiles in simulations with feedback and profiles expected from the contracted original DM halo are relatively small (right panels). We will return to these total matter profiles shortly and show that even this small effect has measurable consequences in the circular velocity curves of galaxies. It is interesting to note that the total matter distribution in the inner 20% of the R_{vir} of **m12** series is well approximated by the isothermal density profile ($\rho \propto 1/r^2$).

The results from our **m12v** simulation are consistent with the strong feedback run in Macciò et al. (2012b) who showed core formation in a $7 \times 10^{11}\mathrm{M}_\odot$ halo. We do however find slightly higher central density of dark matter than reported in Macciò et al. (2012b). While this might be just a matter of small number statistics, our simulation results should give more accurate predictions for the central profiles both because of more realistically implemented stellar feedback and because of the higher resolution. At masses similar to the Milky Way ($M_{\mathrm{h}} \sim 10^{12}\mathrm{M}_\odot$), the dark matter density distribution in the center is only slightly shallower that the NFW profile as strong feedback effects and adiabatic contraction of such expanded halo nearly cancel out.

2.5 Observable consequences

The following subsections show how our simulations with stellar feedback can alleviate the tensions between previous simulations and observations, including the "lack" of baryonic contraction, the "Too Big To Fail" and *cusp/core* problems.

2.5.1 Rotation curves and the Tully-Fisher normalization

The distribution of matter in galaxies can be measured with the rotation curves. For disk galaxies, there is a tight relation between their luminosity (or mass) and their circular velocity, so called the Tully-Fisher (Tully & Fisher, 1976) relation (TFR). Here we examine the effect of stellar feedback and baryonic contraction on rotation curves.

Figure 2.7 shows the rotation curves of halos from simulations and baryonic contraction calculations for **m11**, **m12v** and **m12i**. Here $V_c = \sqrt{GM(r)/r}$. The rotation curves of simulated galaxies do not show profiles expected from the NFW halos affected by adiabatic contraction. Instead, galaxies have lower mass concentrations in the centers, resulting in lower circular velocities. Therefore feedback effectively prevents buildup of high densities expected from strong adiabatic contraction. As expected, the rotation curves in the **m12** series are approximately flat at radii larger than several kpc, while for the massive dwarf **m11** the rotation curve is rising.

The effect of feedback, which cancels the effect of baryonic contraction, turns out to be very important for the normalization of the TFR. We do not perform a detailed comparison with observations, which would require mimicking observational measurements of the rotational velocity and luminosity. We plan to study this in future work. Here, instead, we focus on the relative effect of the feedback on dark matter profiles that determine the normalization of TFR. To show this effect and compare our simulated galaxies with the observed TFR, we measure the

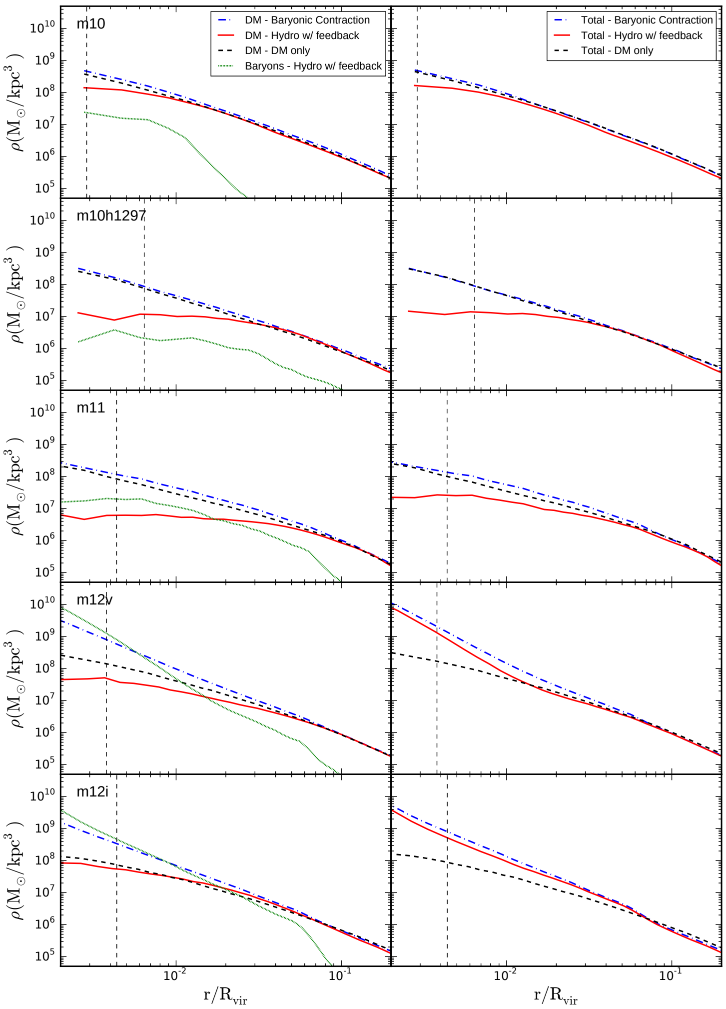

Figure 2.6: (*Left*) Dark matter density profiles of **m10**, **m10h1297**, **m11**, **m12v** and **m12i** at $z = 0$. Different line colors show the expected DM profile in simulations with baryons and feedback (solid; red), in collisionless simulations (dashed; black) and in calculations including baryonic contraction (dot-dashed; blue). The green dotted line shows the total baryon density, including both gas and stars, in feedback runs. (*Right*) Total density profiles of the same halos, including both dark matter and baryons. The Power convergence radii are shown as dashed vertical lines. In halos where baryons dominate in the central regions, total and dark matter densities based on the simple baryonic contraction model are higher than the actual densities in our simulations with baryonic feedback. Feedback effectively cancels the effect of baryonic contraction.

circular velocity of the halo $V_c = \sqrt{GM(r)/r}$. We measure circular velocity at 2.2 'disk scale length' $V_{2.2}$, approximately mimicking frequent observational approach (Dutton et al., 2010). We first measure the half mass radius of the stellar distribution $r_{1/2}$ and use the relation between half mass radius and scale radius of an exponential disk to define disk scale length as $r_d = r_{1/2}/1.67$.

Figure 2.8 shows the TFR of main galaxies with $10^9 < M_*/M_\odot < 10^{11}$, and the best fit of the observed TFR from Dutton et al. (2010). They derived the TFR using the data from Courteau et al. (2007) and with the best fit:

$$\log_{10}\frac{V_{2.2}}{[\mathrm{km\,s^{-1}}]} = 2.064 + 0.259\left(\log_{10}\frac{M_*}{[10^{10}\mathrm{M_\odot}]}\right). \tag{2.4}$$

This relation was derived for relatively massive galaxies, most with $\log \mathrm{V_c[km/s]} > 1.8$. Similar relations were found for dwarfs, however with significantly enlarged scatter and non-uniform way of measuring V_c (e.g. Ferrero et al., 2012). We therefore limit discussion here to galaxies with $M_* > 10^9\mathrm{M_\odot}$.

It is clear that the strong feedback which reduces the effect of adiabatic contraction is a necessary ingredient in reproducing and explaining the TFR in massive galaxies with $M_* > 10^{10}\mathrm{M_\odot}$. While there are direct effects of feedback on the distribution of baryons within galaxies feedback effect on the distribution of dark matter is also an important ingredient in establishing the TFR. Simulated galaxies appear to better match the observed TFR than our model with baryonic contraction. The circular velocities in baryonic contraction calculations are higher by a factor of 1.2-1.5 than V_c in simulations.

Our findings confirm previous conclusions that the lack of effective contraction is necessary to explain the Tully-Fisher relation (Dutton et al., 2007; Macciò et al., 2012b). This also explains why previous generations of simulations without efficient feedback had trouble matching the normalization of TFR (e.g. Steinmetz & Navarro, 2000). In these models too much gas collapsed to the center exerting strong contraction of DM halo without previously affecting the DM distribution.

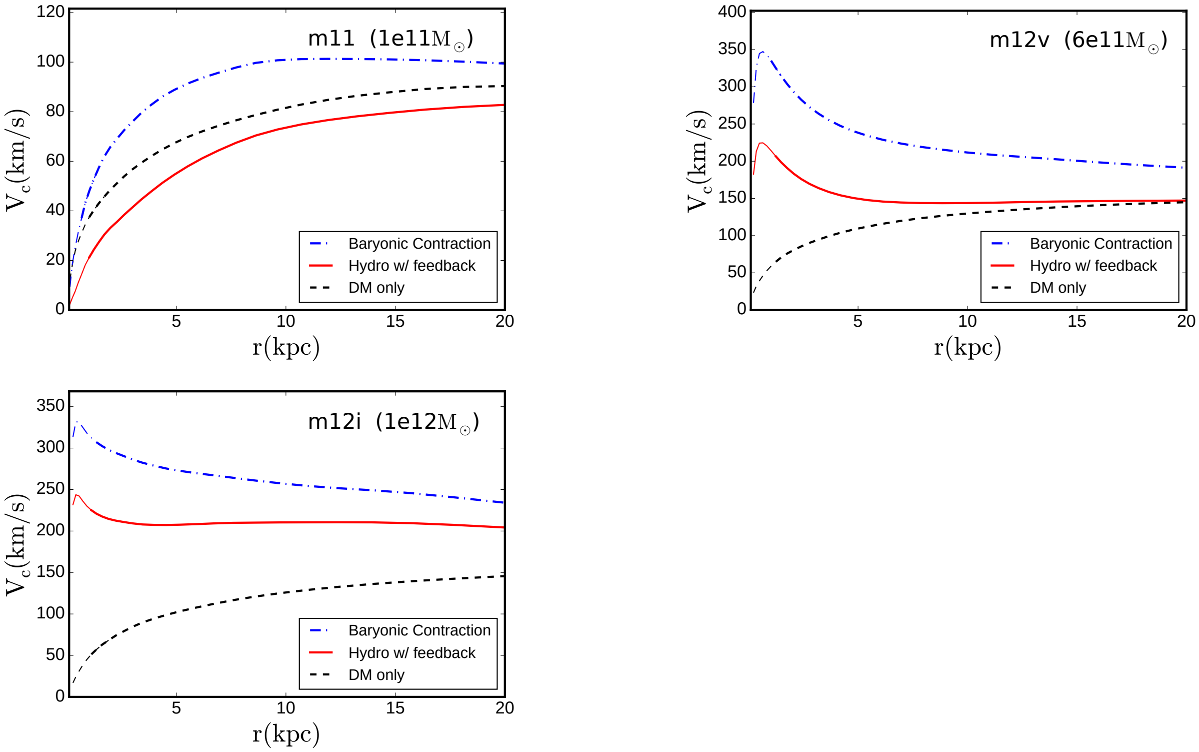

Figure 2.7: Rotation curves of halos, including **m11**, **m12v** and **m12i**. Red solid lines represent rotation curves from simulation with feedback, black dashed lines show results from DM only simulations, whereas blue dot-dashed lines represent rotation curves with baryonic contraction. Dashed lines show the region within the Power radius. Their halo masses are shown in the brackets. The rotation curves in simulations with baryonic feedback are lower than in a simple baryonic contraction model. The simulated Milky Way-mass halos show flat rotation curves, while the large dwarf galaxy **m11** shows a rising rotation curve.

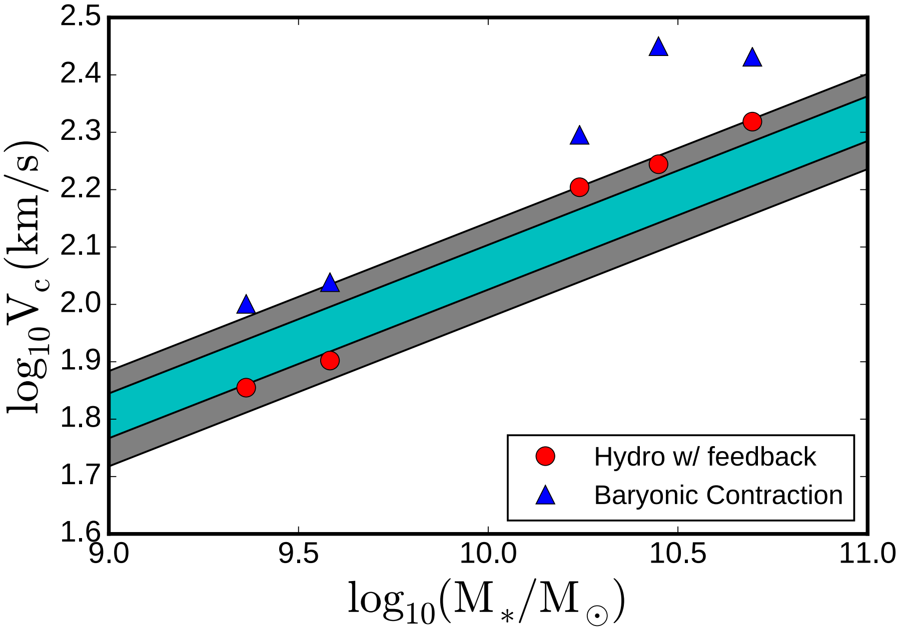

Figure 2.8: Stellar mass — Tully-Fisher relation for observed galaxies (Eq. 2.4) and for the simulated halos (**m11h383**, **m11**, **m12v**, **m12q** and **m12i**). The y-axis is the rotation velocity measured at 2.2 disk scale length. The shaded regions show Eq. 2.4 with one sigma uncertainty ($\sigma = 0.039$)(cyan) and two sigma uncertainty on the zero-point (grey) respectively. Stellar feedback, which counteracts the effects of adiabatic contraction, appears necessary to establish the observed normalization of the Tully-Fisher relation.

Implication for the ‘Too Big To Fail’ problem

In addition to the cusp/core problem, cold dark matter simulations are also challenged by another problem, the so called “Too Big to Fail” problem (Boylan-Kolchin et al., 2011; Garrison-Kimmel et al., 2013). The simplest version of this problem is that the observed Milky Way’s satellite galaxies have much lower central circular velocities than sub-halos from cosmological collisionless cold dark matter simulations. This either means that massive sub-halos do not have corresponding match in observed satellite galaxies or that central regions of predicted cold dark matter sub-halos are too dense compared to observed halos. This seems to be generic problem, independent of the halo formation history as similar effects are also observed in the Local Group and for dwarf galaxies in general (Ferrero et al., 2012; Garrison-Kimmel et al., 2014; Papastergis et al., 2015) including non-satellite galaxies.

We have already shown that stellar feedback can reduce the central dark matter density, which could potentially resolve this discrepancy, without invoking different a type of dark matter. In Figure 2.9, we show the circular velocity profiles of the central kpc of **m10**, **m10h1297** and **m10h1146** at z=0 along with their corresponding dark matter only simulations. These are our best resolved systems with galaxy stellar mass $\sim 2\times10^{6}-8\times10^{7}\mathrm{M}_{\odot}$ at z=0, which are close to the stellar masses of the galaxies for which the “Too Big to Fail” problem was demonstrated (Boylan-Kolchin et al., 2011; Garrison-Kimmel et al., 2013). For comparison we also include the observational data from Milky Way satellite galaxies (Strigari et al., 2007; Walker et al., 2009; Wolf et al., 2010) and Local Group field galaxies (Kirby et al., 2014). It is clear that feedback strongly reduces circular velocities in the central few hundred pc with respect to collisionless cold matter simulations, in some cases by a large factor. Such reduced circular velocity implies that observed dwarf galaxies (including satellite galaxies) should not be associated with halos and sub-halos from DM only simulations with the same circular velocity, instead these should be connected to the predicted higher circular velocity analogs, whose circular velocity is now reduced owing to feedback. Our results strongly suggest that this effect would dramatically reduce the number of “massive failures” and can alleviate or potentially solve the “Too Big to Fail” problem. Our findings qualitatively agree with hints in previous work (Brook & Di Cintio, 2015).

It is interesting that the high stellar mass dwarf galaxies (e.g. **m10h1146** and **m10h1297**) have more significant reductions in central rotation velocities (and thus dynamical masses) compared to low stellar mass dwarf galaxies (e.g. **m10**). This causes the rank order of V_c at small radius (e.g. 500pc) not to correspond to the rank order of their V_{max} or their stellar mass, as illustrated in the middle and lower panels of Figure 2.9. Direct comparison between dark matter only simulations and simulations with baryons is even more complex, and rank order matching of V_c, or V_{peak} from measurements at small radii might lead to incorrect physical interpretations.

Our results only indirectly address the “Too Big To Fail” problem in satellite galaxies, because the galaxies we consider here are not satellites but field galaxies. Satellite galaxies of relevant mass in our **m12** simulations do not have sufficient mass resolution to study their dark matter distributions at the galaxy centers. The effect of host galaxies on satellites, e.g. tidal stripping, could also modify the structure of DM halos (Zolotov et al., 2012; Brooks & Zolotov, 2014). However, the effect of lowering the circular velocity of galaxies is generic in the range of stellar masses $2 \times 10^6 - 3 \times 10^9 \mathrm{M}_\odot$ and we therefore believe that satellite galaxies in this mass range will be affected in the same systematic way.

Central Slopes and Core sizes

Oh et al. (2011) and Oh et al. (2015) measured detailed density profiles of field dwarf galaxies, and found flat DM profiles near the center, in contrast with the cuspy NFW profiles, predicted from N-body simulations. In massive galaxies, such as the Milky Way, baryons dominate in the central few kpc (e.g. Courteau & Dutton, 2015) making measurements of central dark matter properties extremely difficult. We therefore focus on lower mass galaxies/halos with reliably measured central DM profiles.

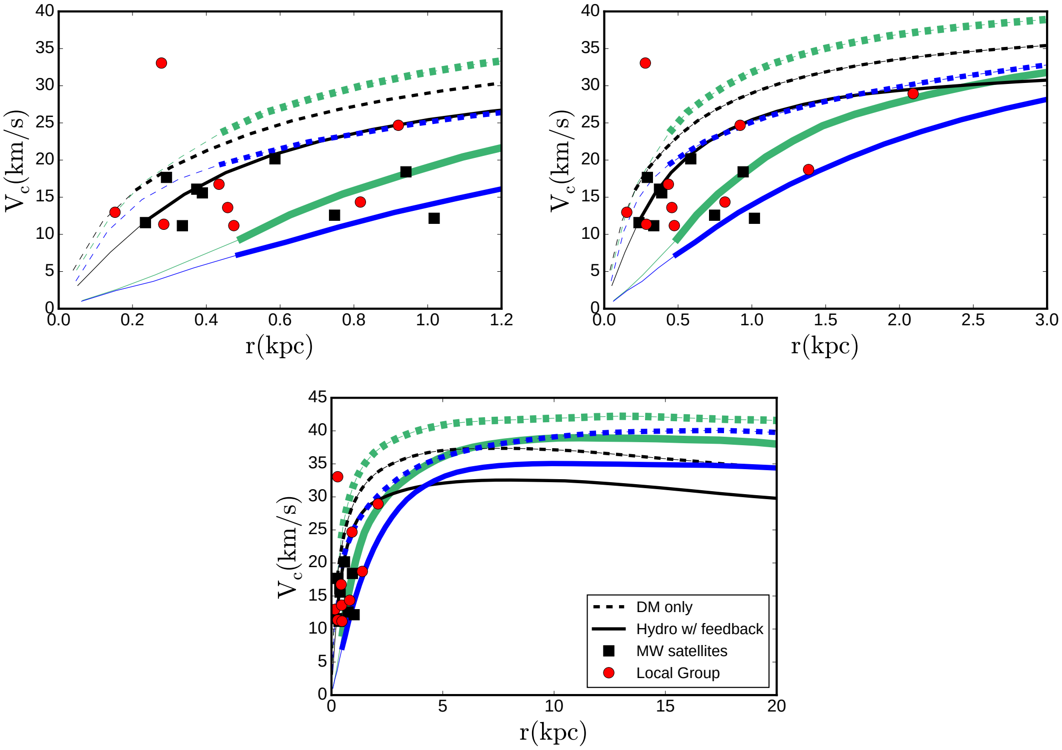

Figure 2.9: Rotation curves illustrating the TBTF problem, plotted over a range of radial scales. We have included halos **m10** ($M_* = 2.3 \times 10^6 M_\odot$; black, thin), **m10h1297** ($M_* = 1.7 \times 10^7 M_\odot$; blue, normal) and **m10h1146** ($M_* = 7.9 \times 10^7 M_\odot$; green, thick) and their corresponding DM only simulations. Thick dashed lines represent the halos from the collisionless simulations while thick solid lines represent the halos from the hydrodynamical simulations with feedback. The thin lines show the velocity curves at radius smaller than the Power convergence radius. Black squares show the data from Milky Way bright satellite galaxies (Strigari et al., 2007; Walker et al., 2009; Wolf et al., 2010), while red circles show the isolated dwarf galaxies in the Local Group (Kirby et al., 2014). The panels show three different scales of the same plot to illustrate that the order of rotation curves at small scales may not imply the order of halo masses. Stellar feedback reduces the central circular velocity such that the rotation curves can match the observed dwarfs, suggesting that baryonic feedback may solve the "Too Big To Fail" problem. Observational errors are typically smaller than a few km/s (not shown for clarity).

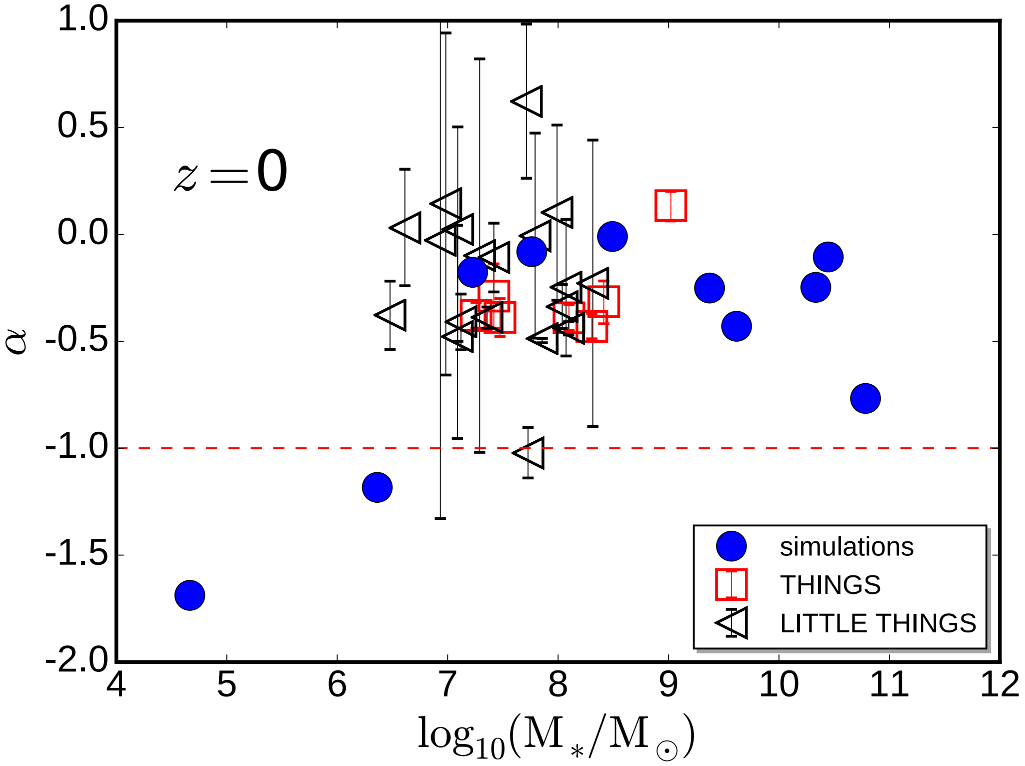

Figure 2.10: Slope of dark matter density profile, α, from our simulations (measured at $r = 0.3 - 0.7$kpc) compared with α from observations (typically measured at a few hundred pc). Blue solid circles represent the simulated halos at $z = 0$. Red hollow squares represent the observed dwarf galaxies from THINGS (Oh et al., 2011; Walter et al., 2008), whereas black hollow triangles represent the dwarf galaxies from LITTLE THINGS (Oh et al., 2015; Hunter et al., 2012). In the overlapping mass range, the simulated dwarf galaxies have central DM profile slopes in good agreement with the observed dwarfs.

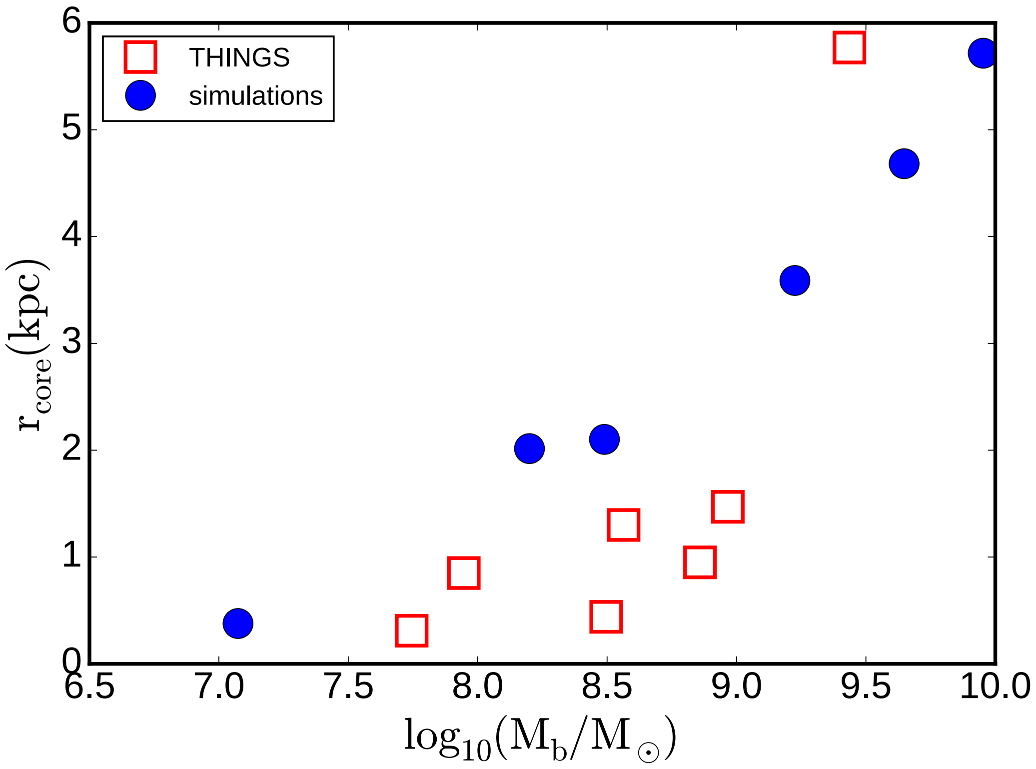

Figure 2.11: Comparison between the core radii of THINGS dwarf galaxies and our simulations as a function of baryonic mass m_{b} (see footnote 11) at $z = 0$. Red hollow squares show the observed core radii (Walter et al., 2008; Oh et al., 2011) while blue circles show the core radii from our simulations. Within the plot range, the core size increases with baryonic mass, which is largely consistent with the observed cores. A larger number of observed and simulated dwarfs is necessary to draw stronger conclusions.

In Figure 2.10, we show that FIRE halos at $z = 0$ are in good agreement with the observed slopes of central DM density profiles (see also Governato et al., 2012). This suggests that the inclusion of stellar feedback in our simulations helps resolve so called “cusp/core” problem observed in low mass galaxies. However, the observed scatter is large and number of simulated objects is limited in the observed mass range. It is therefore clear that much larger sample of model galaxies/halos as well as more detailed accounting for methodology and selection used in observations are needed to test our model in detail.

Figure 2.11 shows the DM core radii of our simulated galaxies as a function of their baryonic masses and compares them to observations from Walter et al. (2008). In general, for

$m_\mathrm{b} \sim 10^7 - 10^{10} M_\odot$ [11] , core radius increases with baryonic mass. There is a broad agreement with observed core sizes. A more detailed comparison will require a larger number of halos and more detailed modeling of the methodology used to calculate the core sizes in observed galaxies.

2.6 Discussion

We use the FIRE suite of high-resolution cosmological "zoom-in" simulations with physical feedback models to study the properties of the central regions of dark matter halos. Our simulations have higher resolution (in most cases the highest resolution to date at a given halo mass), and more explicit and comprehensive implementation of stellar feedback than simulations used previously to study baryonic effects on DM profiles. Critically our models contain no "freely adjusted" parameters tuned to any particular results. We characterize the evolution of halo properties and correlation with galaxy and halo mass and explore the effects of star formation driven feedback and adiabatic contraction on the slopes, cores size and circular velocity profiles of galactic halos.

We find that at $z = 0$ the central slopes of DM density profiles measured at $\sim 1\% R_\mathrm{vir}$ are shallow in halos $M_\mathrm{h} \sim 10^{10} - 10^{11}\mathrm{M}_\odot$, but the slopes are cuspier at lower and higher masses. We see a sharp transition around $M_\mathrm{h} \sim 10^{10}\mathrm{M}_\odot$ from cuspier profiles at lower masses to shallow, core-like profiles at higher masses. Efficient feedback continues to at least $M_\mathrm{h} \sim 10^{12}\mathrm{M}_\odot$ where the core-like profiles that form during earlier evolution are contracted by baryons at late times into steeper profiles. Final profiles are similar or flatter than NFW, and therefore significantly flatter than expectations for a contracted NFW halo.

Our results are in broad agreement with others found in the literature. For example we find that feedback is efficient in forming large cores at halo masses $\sim 10^{10}\mathrm{M}_\odot$- few $\times 10^{11}\mathrm{M}_\odot$ which is similar to previous findings (Governato et al., 2012; Di Cintio et al., 2014; Pontzen

---

[11] m_b is defined as the total baryonic mass within 20% R_vir of the halo.

& Governato, 2014). It appears that simulations with bursty star formation and outflows, but different small scale feedback implementations, affect dark matter profiles in a qualitatively similar way. However we also found some interesting differences. This is not surprising, given that our simulations are in most cases higher resolution and have explicit treatment of feedback on small scales. For example we find that in the halos with large cores, cores are established at around $z \sim 1$ and can grow even at low redshift while other authors find that cores formed very early already at $z = 2 - 3$ (e.g. Madau et al., 2014). This could be a consequence of different star formation histories that can change core formation (Oñorbe et al., 2015). For example, these authors note that earlier simulations or dwarf galaxies with "sub-grid" feedback models produced too many stars at a given halo mass. Alternatively, these differences could indicate that different treatments of material affected by feedback (cooling prevention vs. explicit model) cause differences in DM profiles.

We also find cuspier DM profiles at around $6 - 7 \times 10^{11}\mathrm{M}_{\odot}$ than the one reported in Macciò et al. (2012b) and therefore weaker halo expansion and somewhat steeper dependence of slope on M_{*}/M_{h} than the relation presented in Di Cintio et al. (2014). Overall, better statistics from a larger number of simulated halos are needed for a more robust analysis of these differences.

Energetics

Given that the efficiency of conversion of halo gas into stars increases from dwarf galaxies to massive galaxies, it is natural to connect feedback effects to the energy available from stellar feedback. We therefore compare the amount of energy available from feedback with the energy needed to overcome the gravitational potential and move dark matter outside of the central region. The simplest estimate is to calculate how much energy gets injected into the ISM from the SNe only, which represents a lower limit to the available energy budget.

Previously, Gnedin & Zhao (2002), Ogiya & Mori (2011) and Garrison-Kimmel et al. (2013) claimed that the total feedback energy released in SNe is insufficient to remove enough

Table 2.3: Comparison of the difference in gravitational potential energy ΔU of halos from dark matter only simulation and the same halos with constant density core of 1% of R_{vir} (left) or 3% of R_{vir} (middle), and their total supernova energy (E_{sn}, right), obtained from the corresponding simulations with feedback. Energy input from supernovae alone is sufficient to produce cores in **m10** and **m11**.

	ΔU (1% core) (erg)	ΔU (3% core) (erg)	E_{sn} (erg)
m09	5.85e52	6.45e53	2.68e53
m10	1.08e53	2.02e54	2.13e55
m11	3.43e55	6.46e56	2.22e58

dark matter to form large cores. In particular, Garrison-Kimmel et al. (2013) tested if stellar feedback can lower central densities to a degree needed to explain the “Too Big To Fail” problem. They simulated supernova feedback with time-varying potential and found the number of SNe needed to match observed profile of a halo hosting $M_* \sim 10^6 \mathrm{M}_\odot$ galaxy exceeds the number of SNe produced in most of the dwarf galaxies for the typical initial mass function. However, they did not consider the full growth history of the halo. The frequent mergers and star formation bursts at higher redshift could dynamically heat up more dark matter in the center, when halo was smaller. Furthermore, they assume mass loading of SNe driven winds smaller than we find for FIRE galaxies of comparable masses (Muratov et al., 2015). Finally their selected halo has a high concentration compared to a typical sub-halo that is expected to host observed dwarf galaxies. As we show below, there is a sufficient amount of energy available to couple to dark matter in the relevant halo and galaxy mass regime.

Table 2.3 shows the energy needed to create a constant density core with radius 1% or $3\% R_{\mathrm{vir}}$ in halos from our dark matter only simulations and the total supernova energy inferred from our hydrodynamic simulations by z=0. We constructed a constant density core in our “cuspy” DM only simulations by keeping the density profile outside the core unchanged and moving the excess mass within the core radius to infinity. Then we calculate the total potential energy for the initial and cored profiles with the formula below

$$U = -4\pi G \int_0^{R_{\rm vir}} M(r)\rho(r) r \mathrm{d}r, \tag{2.5}$$

and report the difference, ΔU, in Table 2.3.

To estimate the supernova energy, we assume the energy from one supernova $E_{\rm sn} = 10^{51}$erg, the fraction of massive stars which can produce supernovae $\xi(m_* > 8\mathrm{M}_\odot) = 0.0037$ (Kroupa, 2002), and the mean stellar mass $M_{\rm mean} = 0.4\mathrm{M}_\odot$. The total supernova energy of a halo is given by

$$E_{\rm SN}^{\rm tot} = M_*/(<m_*>) * \xi(m_* > 8\mathrm{M}_\odot) * E_{\rm sn}. \tag{2.6}$$

From Table 2.3 we see that for **m09**, the amount of SNe energy is not sufficient to create a large core at 3% $R_{\rm vir}$ even if it all couples (via secondary gravitational interactions) to the DM. Even creating 1% $R_{\rm vir}$ core is difficult as it requires that more than 20% of the available energy is coupled to dark matter, which is unlikely given the indirect connection via the change of gravitational potential and that a large fraction of this energy is in heavily mass loaded winds that move rapidly (Muratov et al., 2015).

However, for **m10**, a small core is energetically possible and even a 3%$R_{\rm vir}$ core requires less than 10% of the available energy. We see some signs of profile flattening within the inner 1% of $R_{\rm vir}$, but not a fully developed core. However, for the same halo mass Oñorbe et al. (2015) show that a slightly different star formation history can cause a much larger effect and form a central core with a radius of 1-2 %$R_{\rm vir}$.

In **m11**, the supernova energy is three orders of magnitude higher than what is needed to create a small core at 1 % of $R_{\rm vir}$ and even 3% of $R_{\rm vir}$ core can be created with few percents of coupling efficiency. It is therefore not surprising that this halo indeed hosts a large core. Even though the depth of the potential well increases in more massive halos, the amount of stellar mass is a steep function of halo mass, which provides sufficient energy to affect central dark matter profiles. This is why we see a relatively sharp transition at $\sim 10^{10}\mathrm{M}_{\odot}$ from low mass cuspy halos to core-like halos at higher masses.

2.6.1 Correlation with star formation

Here we show a simple connection between bursts of star formation that cause strong gas ejection episodes, and the change in the amount of dark matter in the central part of halos. In Figure 2.12, we plot the change in the enclosed dark matter mass as a function of the peak star formation rate in **m11**, the halo in which the effect of feedback on dark matter is one of the strongest in our sample. We focus on bursts with high peaks of star formation and neglect low star formation rate episodes as they typically do not show strong outflows (Muratov et al., 2015). In Figure 2.12 we plot the rate of change in the central amount of dark matter as a function of the peak star formation rate. The star formation rate and mass change are measured as averages over 0.2 Gyr. The rate of change of the DM mass is

$$\frac{\Delta M}{\Delta t}(t) = \frac{m_{\rm dm}(t+0.2\mathrm{Gyr}) - \mathrm{m_{dm}(t)}}{0.2\mathrm{Gyr}}, \tag{2.7}$$

where $m_{\rm dm}(t)$ is the enclosed DM mass within $2\%R_{\rm v0}$ (the virial radius at $z=0$) averaged over 0.2Gyr and t is the beginning time of the interval. We measure star formation between $t-0.2$Gyr and t, within a larger radius of 0.1 $R_{\rm v0}$ to make sure to include stars that move out of the very center between the two time intervals. [12]

A significant decrease of mass enclosed in the central $2\%R_{\rm v0}$ occurs just after a strong starburst when a large amount of dark matter is "heated" and effectively pushed out of the central region. At the corresponding times DM only simulation does not show negative mass change,

---

[12] We have also tried to average SFR over 0.1 Gyr and considered the delay of 0.1 Gyr. The enclosed DM mass drops 0.1 Gyr after the peak SFR in a way similar to Figure 12 (i.e. it is negative), but with the larger scatter and greater changes in DM mass. We note that this simple measurement cannot use much longer intervals for averaging of SF and for time delay because on large time scales the SFR bursts would be "washed out" and we could have multiple burst episodes within a long delay time interval.

except in the case of the largest burst which is triggered by the close passage during a merger (as indicated in Figure 2.5), i.e. the merger dynamically alters the profile. Hence we conclude that there is a correlation between mass removal from the center and star formation rate.

This correlation suggests that a strong burst of star formation can provide sufficient feedback to remove a significant amount of baryons, which then cause a decrease in the central potential and lower the concentration of DM. This scenario is consistent with the mechanism suggested in Pontzen & Governato (2012) in which repeated changes of central gravitational potential transfer energy to the orbits of DM particles causing a central density decrease.

Some fraction of the removed DM does return, i.e. cores get partially rebuilt, however when large cores are present this is a relatively small effect. When cores are established after the period of rapid early halo growth, they survive largely intact for at least several Gyrs, before a new major bursts of star formation and gas expulsion sets in (see § 2.4.3). In more massive halos (**m12**), shallow profiles that form at higher redshift steepen by redshift zero significantly. In these halos we see continuous late time star formation without significant galactic wind episodes (Muratov et al., 2015) which continuously increases central density of baryons that dominate the central potential. As a consequence dark matter halos are pulled inward by adiabatic contraction changing shallow profiles into cusps.

While a burst-driven core formation mechanism is consistent with our findings, we cannot exclude a contribution of other dynamical mechanisms, such as the motion of dense baryonic clumps within galaxies with respect to the halo centers. On the other hand, core formation via enhanced dynamical friction from the dense infalling sub-structure (e.g. El-Zant et al., 2001) is unlikely to play a significant role for the halo mass range probed here, because feedback lowers the density of infalling sub-halos relative to their DM-only counterparts (see Figure 2.6; all of the infalling sub-halos in our sample have $M_{\rm h} \lesssim 10^{11} {\rm M}_{\odot}$).

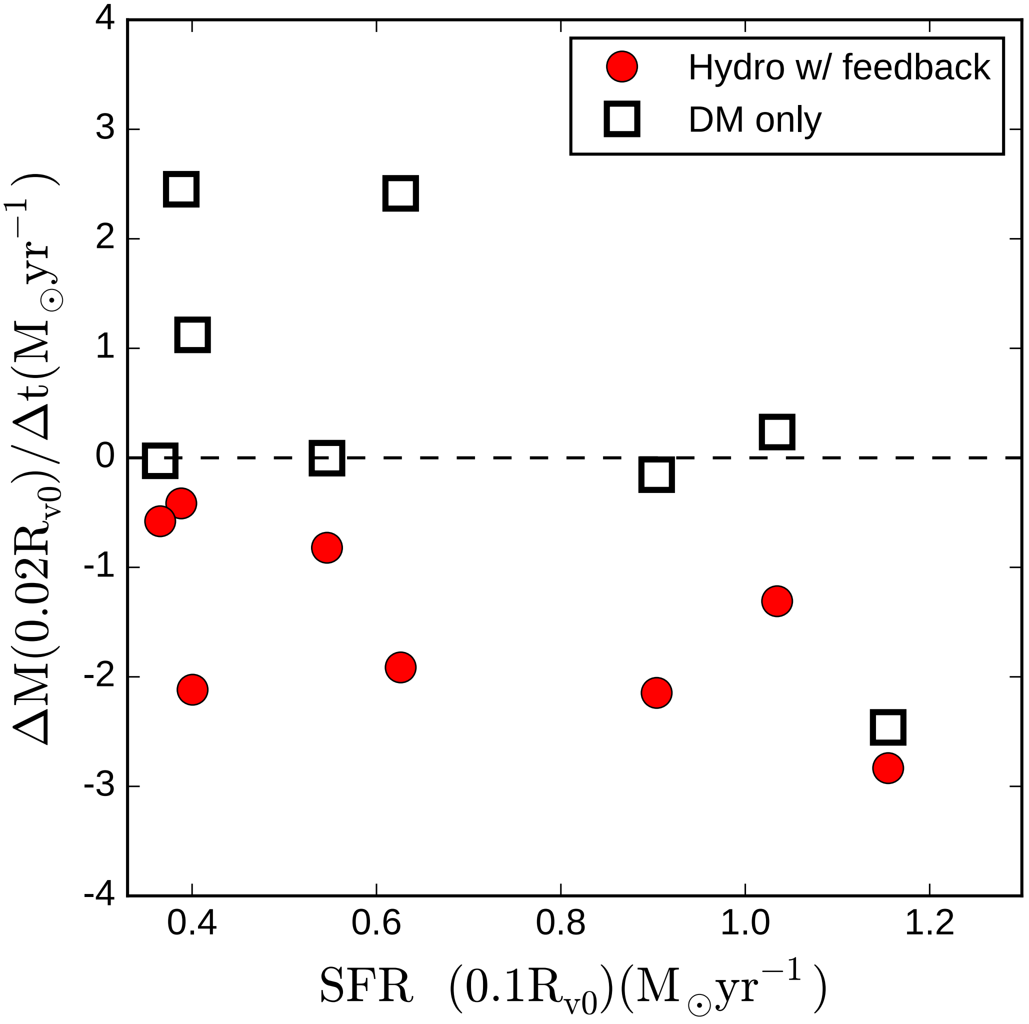

Figure 2.12: The rate of change of enclosed dark matter mass within 2% of R_{v0} as a function of peak star formation rate within $10\% R_{v0}$ in **m11** (red circles) and **dm11** (black hollow squares) simulations, both averaged over 0.2 Gyr. In both cases we plot the SFR from the corresponding feedback simulations at the same cosmic time. The star formation rate is measured 0.2 Gyr ahead of the rate of change of enclosed dark matter mass. Strong bursts of star formation are followed by a reduction in the enclosed DM mass in the simulation with feedback.

Significance for the dark matter detection

The dark matter profile in the Milk Way is important in studies of indirect detection of dark matter particles from annihilation or decay signals. Recently, extended emission in gamma rays from the galactic center has been reported based on the data from the Large Area Telescope aboard the Fermi Gamma Ray Space Telescope (e.g. Hooper & Goodenough, 2011). To interpret this signal as a consequence of annihilation of dark matter particles or to constrain its contribution it would be extremely useful to know the central dark matter profile (Abazajian et al., 2014). The signal is consistent with the annihilation rate of thermally produced weakly interacting massive particle dark matter (Goodenough & Hooper, 2009; Hooper & Goodenough, 2011; Hooper & Linden, 2011; Boyarsky et al., 2011; Abazajian & Kaplinghat, 2012; Gordon & Macías, 2013; Macias & Gordon, 2014; Abazajian et al., 2014) although other possibilities remain valid alternatives (Abazajian, 2011).

While we have a small number of objects at the relevant mass, one robust finding from our simulations is that central density of cold dark matter will not correspond to contracted NFW profiles in Milky Way-mass halos. This helps constrain the range of values used in the modeling of the observed signatures. We find values of $\alpha \sim -1$ to -1.4 at $1-2\%R_{\rm vir}$ which is consistent with the best fit in Abazajian et al. (2014). However our results from **m12** halos suggests that deeper in the halo, the DM profile is likely shallower $\alpha \sim -0.7$ to -1.1 at $< 1\%R_{\rm vir}$. Given the slight differences of the central slope definition and fitting procedures it would be interesting to test if the profiles shown here provide a good match for the observed signal. We defer such more detailed comparison for future work.

Limitations

There are some clear limitations in our study of dark matter halo properties. The number of simulated halos in our sample is limited because such high-resolution simulations are very time-consuming. In the future we plan to simulate a much larger number of halos to be able to extract direct statistical predictions and to compare to observed values, including the scatter in observations and theoretical predictions.

Further limitation comes from the finite resolution. Our simulations are amongst the highest resolution cosmological simulations at z=0 to date and our **m09 and m10** simulations can robustly resolve dark matter profiles on < 200 pc scales. However detailed comparison to observations requires converged results and the ability to exactly integrate circular orbits over a Hubble time without N-body effects within 300 pc in $M_{\rm h} \sim 10^{10-11}{\rm M}_{\odot}(M_{*} \sim 10^{7-9}{\rm M}_{\odot})$ halos (Walter et al., 2008). In our **m10h1297**, **m10h1146** and **m11** simulations, this is larger than many gravitational softening lengths, however the more stringent Power convergence criterion §2.3.4 (Power et al., 2003) requires a further factor of several improvement in mass resolution to reach this limit.

Resolution requirements can be even more dramatic if one wants to directly study the inner density profiles of small dwarfs that form within sub-halos of large spiral galaxies (e.g. to directly address TBTF problem). Such study would require simulating $M_{\rm h} = 10^{12}{\rm M}_{\odot}$ halos with $> 10^9$ particles within the virial radius. We have shown, however, that many of the CDM "problems" can be explained by baryonic feedback in isolated, well resolved, dwarf galaxies suggesting a similar solution for satellite galaxies.

We caution that the Power convergence criterion was derived for different time-stepping algorithm, different force accuracy and different softening values. Based on the DM profiles in Figure 2.1 we see that steep central slope in DM only simulations continue to at least factor of ~ 2 smaller radii than what is estimated by Power convergence radius. More importantly, direct resolution tests confirm the convergence in DM cusp profiles down to a factor $\sim 2-3$ smaller radii for our fiducial resolution. This suggests that this convergence criterion might be too conservative for our simulation setup.

We did not study **m13** halo ($M_{\rm h} \sim 10^{13}{\rm M}_{\odot}$) from the FIRE project sample because the star formation rate of this halo, at low redshift, is higher than the observed rates in observed galaxies of the same mass (H14). Some additional physics, e.g. active galactic nucleus (AGN) feedback, is needed to explain the observations. Yet, the investigation of the profiles of these high mass halos is highly intriguing both observationally and theoretically. Observationally, gravitational lensing provides an accurate measurement of the enclosed mass of those halos (Bolton et al., 2008), though dark matter only constitutes a minor fraction of the mass.

Nevertheless, stellar kinematics and strong lensing do suggest cores in galaxy clusters with $\alpha \sim -0.5$ (Newman et al., 2013b,a). It is not clear if a single mechanism can explain such shallow slopes over a large range. Mechanisms ranging from more frequent major mergers as well as processes such as AGN feedback, magnetic fields, anisotropic conduction, and cosmic rays, that are not yet incorporated in our simulations may be important in regulating late time star formation and affecting the core formation in massive halos (e.g. Peirani et al., 2008; Martizzi et al., 2013).

AGN feedback in particular might even affect halos with masses similar to our **m12** simulations, e.g. Velliscig et al. (2014) showed that AGN feedback can have a non-negligible impact on the halo properties (i.e. mass and profile) down to $M_{\rm h} \sim 5 \times 10^{11} {\rm M}_{\odot}$. These results suggest that the effect of AGN feedback, in addition to stellar feedback, could further lower the central density of the most massive halos in our sample. We note that regardless of the dominant feedback mechanism, the overall efficiency of feedback must be similar to what is seen in our simulations, as this efficiency is constrained by the observed $M_* - M_{\rm h}$ relation. Our simulations provide a clean test for the effects of stellar feedback alone on the DM distribution.

Dependence on star formation history

Oñorbe et al. (2015) compared our **m10** simulation from H14 with the one with a slightly different supernova feedback coupling at smaller scales. In our default case, energy deposition is volume weighted while in the other version it was mass weighted. This creates slight differences in the feedback and changes late time star formation. A 1-kpc core was formed in a halo with more prominent late time star formation, while our default **m10** simulation shows a core at < 400pc and much higher central density of dark matter. It is likely that this strong sensitivity is caused by this halo mass being at the transition region from smaller to larger cores.

This then suggests that when a large sample of simulated halos is available, comparison to the observations around this mass scale will potentially help distinguish between feedback models by analyzing their star formation histories and properties of their dark matter halos (Fitts et al., in preparation). For slightly more massive halos we see core formations in all cases we explored, regardless of their detailed SF history and the details of their feedback implementations.

2.7 Conclusions

We have explored cold dark matter profiles in simulations with stellar feedback. We used the FIRE suite of hydrodynamic simulations initially discussed in H14 and supplement these with 4 new dwarf galaxy simulations. We also run collisionless counterparts for all of these simulations. We show that baryonic simulations can successfully produce results consistent with observations and alleviate or solve several so called "problems" of the CDM: "cusp-core", the lack of adiabatic contraction or "halo expansion" and the "Too Big To Fail", without any fine turning or introduction of adjustable parameters. Our main results are:

1. The baryons have little influence on halos with $M_{\mathrm{h}} \ll 10^{10}\mathrm{M}_{\odot}$ because only a small fraction of available baryons are converted to stars, owing to feedback and the UV background that suppress their star formation after the reionization (Oñorbe et al., 2015; Wheeler et al., 2015). The smallest halos are therefore perfect places for testing various theories of dark matter.

2. The central slopes of dark matter density profiles are governed by halo mass and stellar mass. Profiles are shallow with relatively large cores for $M_{\mathrm{h}} \sim 10^{10}-$ few $\times 10^{11}\mathrm{M}_{\odot}$ and $M_{*} \sim 10^{7}-$ few $\times 10^{9}\mathrm{M}_{\odot}$, where $\alpha \sim -0.5-0$ and cores are $r_{\mathrm{core}} > 1$ kpc. Small central cores can also form at slightly lower masses $M_{*} \sim 10^{6}\mathrm{M}_{\odot}$. This result is consistent with the

observations of dwarf galaxies and can explain the “cusp-core" problem.

3. Bursts of star formation and feedback start forming cores at early times but the cores are established typically at later times, e.g. in our **m11** simulation core is still growing at $z < 1$. Stable cores are established once central regions of halos stop their rapid growth. After this time ($z \lesssim 2$) removal of mass from the central region leaves a long term effect on the halo profile. We show that strong bursts of star formation are correlated with dark matter expansion.

4. The total supernova energy in halos with $M_{\rm h} > 10^{10}{\rm M}_{\odot}$ is sufficient to produce a core with radius $3\% R_{\rm vir}$, but not sufficient to make large cores in lower mass halos. In practice only a few percent of the available energy is transferred into evacuation of dark matter from the central region.

5. Baryonic contraction of dark matter halos becomes significant when central regions of halos are clearly dominated by baryons, which in our simulations occurs for $M_{\rm h} > 5 \times 10^{11}{\rm M}_{\odot}$. However feedback in the progenitors of these massive galaxies significantly lowered central DM density at $z \sim 1 - 1.5$. The cumulative effect of feedback and contraction is then a profile that in our **m12** runs is slightly shallower than NFW. This explains why the normalization of the Tully-Fisher relation requires no contraction or halo expansion with respect to the collisionless NFW profile.

6. Stellar feedback in galaxies with $M_{*} \sim$ few $\times 10^{6} - 10^{8}{\rm M}_{\odot}$ lowers the central density of DM when compared to dark matter only simulations and significantly reduces the rotational velocity near the center. This means that relatively low circular velocities of observed galaxies should correspond to much higher maximum circular velocities or virial velocities of halos or sub-halos in collisionless CDM simulation. This can solve or at least substantially alleviate the “Too Big To Fail" problem.

Table 2.4: The coefficients in Eq. (2.8) for different resolutions.

$r_{\rm res}/R_{\rm vir}$	a	b
0.3%	0.94	-6.2
1%	0.95	-5.0
2%	0.95	-4.3
3%	0.96	-3.9

2.A Convergence limits

We use the Power convergence criterion (Power et al., 2003) to derive empirical formulae for the minimum particle mass needed to quantify cusps down to $0.2-3\%R_{\rm vir}$. We consider DM only simulations and assume their profiles can be fitted with an NFW profile. The ratio between the scale radius $r_{\rm s}$ and the virial radius $R_{\rm vir}$ is determined through a concentration-mass relation from Dutton & Macciò (2014), and we use the virial overdensity from Bryan & Norman (1998). Then we calculate the enclosed number of particles and density within $0.3-3\%R_{\rm vir}$ as well as 300 and 700 pc. From Eq. 2.1, we estimate the minimum radius such that $t_{\rm relax}/t_0 < 0.6$ and plot the relation between the required particle mass to meet this criteria at the desired radius, and the total halo mass in Figure 2.13.

The data can be fitted with a linear relation,

$$\log_{10}(m_{\rm dm}/{\rm M}_\odot) = a\log_{10}(M_{\rm h}/{\rm M}_\odot) + b \tag{2.8}$$

where a and b are list in Table 2.4

Oh et al. (2011) measured α between 300-700 pc in dwarf galaxies with M_* between $10^6-10^9M_\odot$ and found cored profiles in those galaxies. In order to match this observational result, the minimum resolved radius in the simulations should be around 300 pc. For a fixed physical radius this turns into a requirement in particle mass that is almost independent of the halo mass, owing to higher concentration in lower mass halos.The maximum mass of dark matter particles needs to be slightly smaller than $10^4M_\odot$ to converge at 300 pc and smaller than $10^5M_\odot$

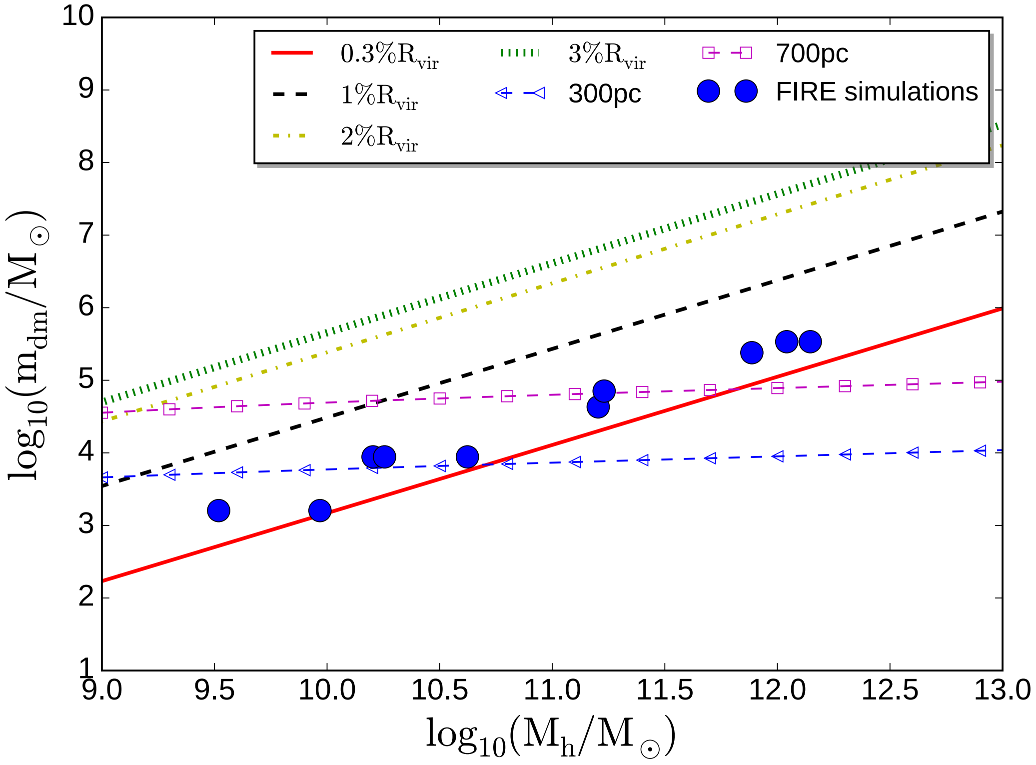

Figure 2.13: The virial mass of a halo as a function of the maximum particle mass allowed in order to reach convergent profiles at $0.3, 1, 2, 3\% R_{\rm vir}$, 300 pc and 700 pc. Small circles represent the corresponding values from dark matter only simulation listed in Table 2.1. (Our full physics simulations have the same DM particle numbers.)

to converge within 700 pc. Our **m09** and **m10** are clearly converged at both of these radii.

Our slightly more massive halos **m10h1297**, **m10h1146** and **m10h573** are marginally converged at 300 pc, but fully converged at 700 pc. Figure 2.13 assumes an NFW profile and implicitly assumes that the central region has close to a Hubble time to undergo relaxation processes. As discussed in the main text, it is not clear what the appropriate convergence criterion should be once large cores are formed and the central density is reduced. This likely depends on the core formation time as well as details of the gravitational softening of multiple particle species and their time-stepping algorithms.

It is important to note that our DM force softening is typically a factor of five smaller than the corresponding Power convergence criterion. Furthermore, we have also tested if the force softening of the baryonic component influences dark matter profiles: e.g. we increased the baryonic softening from 2.0 to 25 pc in the slightly modified version of **m10** run in Oñorbe et al. (2015) and found that the dark matter profile was only mildly changed (the core size was actually larger in run with smaller softening). While two-body relaxation effects are important in estimating central DM profiles, in H14 (Appendix C) we have used idealized runs to show that our standard resolution in **m12** runs is also sufficient to reliably determine other relevant quantities, e.g. SFR, wind mass-loading and gas phase distribution. All are consistent to within a factor of ~ 2 even with ~ 50 times better mass resolution. This indicates that the general properties of dark matter profiles on resolved scales in our simulations are numerically robust.

2.B Choice of α

We investigate the effect of different fitting ranges on α in this appendix. We consider three different fitting ranges, 1-2 kpc, 0.3-0.7 kpc, and $1-2\% R_{\rm v0}$. Figure 2.14 shows α that corresponds to those ranges. In general, 0.3-0.7 kpc includes some overlap below the Power radius for halos with mass larger than $10^{11}{\rm M}_{\odot}$ but α in this range can be directly compared with

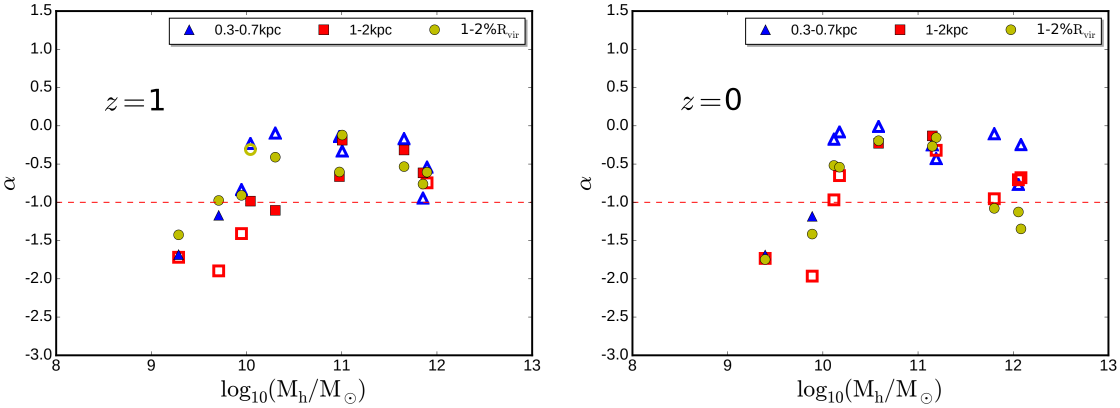

Figure 2.14: DM profile slope α inferred from different criteria plotted as a function of the halo mass. “0.3-0.7kpc” is the dark matter density slope interpolated within 0.3-0.7 kpc from the center. “$1-2\%R_{\rm vir}$” is α interpolated within $1-2\%R_{\rm vir}$. “1-2kpc” is α interpolated within 1-2 kpc. Filled circles show that the profile measurement range is larger than $0.5r_{\rm Pow}$ and smaller than a third of r_s. Open circles indicate that one of these criteria is not satisfied.

observations of dwarf galaxies. 1-2 kpc lies outside the central region ($> 1.3r_s$) in small dwarfs. $1-2\%R_{\rm vir}$ is well-resolved, lies inside the central region and physically meaningful, so we use this fitting range as our “default” choice in the main text. Overall all of the methods show very similar trends of the DM density profile slope with mass.

Chapter 2, in full, is a reformatted reformatted version of the published material in *Monthly Notices of the Royal Astronomical Society*, Chan, Tsang Keung; Kereš, Dušan ; Oñorbe, Jose; Hopkins, Philip F. ; Muratov, Alexander L.; Faucher-Giguère, Claude-André; Quataert, Eliot, Volume 454, Issue 3, 11 December 2015, Pages 2981-3001. The dissertation author was the primary investigator and author of this paper.

Chapter 3

Origin of ultra diffuse galaxies: stellar feedback and quenching

3.1 abstract

We test if the cosmological zoom-in simulations of isolated galaxies from the FIRE project reproduce the properties of ultra diffuse galaxies (UDGs). We show that outflows that dynamically heat galactic stars, together with a passively aging stellar population after imposed quenching, naturally reproduce the observed population of red UDGs, without the need for high spin halos, or dynamical influence from their host cluster. We reproduce the range of surface brightness, radius and absolute magnitude of the observed red UDGs by quenching simulated galaxies at a range of different times. They represent a mostly uniform population of dark matter-dominated dwarf galaxies with $M_* \sim 10^8\,\mathrm{M}_\odot$, low metallicity and a broad range of ages; the more massive the UDGs, the older they are. The most massive red UDG in our sample ($M_* \sim 3\times10^8\mathrm{M}_\odot$) requires quenching at $z \sim 3$ when its halo reached $M_\mathrm{h} \sim 10^{11}\,\mathrm{M}_\odot$. Our simulated UDGs form with normal stellar-to-halo ratios and match the central enclosed masses and the velocity dispersions of the observed UDGs. Enclosed masses remain largely fixed across a broad range of quenching times

because the central regions of their dark matter halos complete their growth early. If our simulated dwarfs are not quenched, they evolve into bluer low-surface brightness galaxies with M/L similar to observed field dwarfs. While our simulation sample covers a limited range of formation histories and halo masses, we predict that UDG is a common, and perhaps even dominant, galaxy type around $M_* \sim 10^8\,\mathrm{M}_\odot$, both in the field and in clusters.

3.2 Introduction

Low surface brightness galaxies (LSBs) with large effective radii were detected and studied by many authors over the past several decades (Impey et al., 1988; Bothun et al., 1991; Dalcanton et al., 1997; Caldwell, 2006; McConnachie et al., 2008). van Dokkum et al. (2015a) sparked a recent interest in LSBs by finding many LSBs in the Coma cluster, named ultra diffuse galaxies (UDGs), with absolute magnitudes comparable to those of dwarf galaxies ($M_g \sim -14$), but with effective radii as large as the Milky Way (MW) ($\sim 4\,\mathrm{kpc}$) and surface brightnesses of $\sim 25\,\mathrm{mag/arcsec^2}$. They appear spheroidal and red, indicating old stellar populations.

Since then, a large number of UDGs have been discovered in the Coma cluster (Koda et al., 2015), the Virgo cluster (Caldwell, 2006; Mihos et al., 2015), the Fornax cluster (Muñoz et al., 2015), clusters with $z \sim 0.044 - 0.063$ (van der Burg et al., 2016), the Abell 2744 cluster (Janssens et al., 2017), the Abell S1063 clusters (Lee et al., 2017), the Pisces–Perseus Supercluster (Martínez-Delgado et al., 2016), the M77 group (Trujillo et al., 2017), the elliptical galaxy NGC 5485 (Merritt et al., 2016), three nearby isolated groups (Román & Trujillo, 2017b) and the Hickson Compact Group 95 (Shi et al., 2017).

Because of their large effective radii and low inferred stellar masses, van Dokkum et al. (2015a) proposed that UDGs are "failed" L$\star$ galaxies initially forming in relatively massive halos that were quenched at $z \sim 2$. This hypothesis is supported by the stellar velocity dispersion and the number of globular clusters (GCs) of a massive UDG, Dragonfly 44, in the Coma cluster for which van Dokkum et al. (2016, 2017) inferred a total halo mass $\sim 10^{12}\mathrm{M}_\odot$.

However, from recent observations of the GC systems of other UDGs, Beasley et al. (2016); Beasley & Trujillo (2016); Peng & Lim (2016) argued that the UDGs are "failed" dwarf galaxies. By measuring the velocity dispersion of the GC system in a UDG (VCC 1287 in Virgo Cluster), Beasley et al. (2016) inferred a dynamical mass of $4.5 \times 10^9\mathrm{M}_\odot$ within 8.1 kpc. By comparing its dynamical mass with numerical simulations, they estimated its halo mass $M_{200} = (8 \pm 4) \times 10^{10}\mathrm{M}_\odot$, comparable to a dwarf galaxy halo. By measuring the number of GCs in Coma UDGs and assuming the correlation between GC number and halo mass, Amorisco et al. (2018) found most of the Coma UDGs reside in dwarf halos. Similar conclusions were reached with measurements of GC specific frequencies of UDGs (Beasley et al., 2016; Beasley & Trujillo, 2016; Peng & Lim, 2016). Furthermore, Román & Trujillo (2017a) revealed that the spatial distribution of UDGs in a galaxy cluster resembles the distribution of dwarf galaxies rather than $L\star$ galaxies. Based on these measurements, Beasley & Trujillo (2016) argued that UDGs are quenched galaxies that inhabit Large Magellanic Cloud (LMC)-sized halos and quench their star formation at $z \sim 3$. In this scenario, cluster UDGs have to be quenched for more than 10 Gyr. Sifón et al. (2018) used weak gravitational lensing to show that the average virial mass of 784 UDGs in 18 clusters is $m_{200} \leq 10^{11.80}\mathrm{M}_\odot$, consistent with dwarf halo masses but leaving a possibility of the most massive UDGs to be hosted in MW-mass halos.

Yozin & Bekki (2015) similarly argued that UDGs have dwarf progenitors, but they quenched at much later times. They simulated interactions between a cluster and an infalling diffuse dwarf galaxy at $z \sim 2$, and showed that the harsh cluster environment can rapidly halt any ongoing star formation. Their initial conditions assumed the infalling dwarf was hosted in a high spin halo, allowing the galaxy to be much more diffuse than normal galaxies even before interacting with the host cluster. Following this line of thought, Amorisco & Loeb (2016) proposed that UDGs are the high spin tail of the dwarf galaxy population, so they are diffuse even without interacting with the cluster. They predicted there should also be a field population of UDGs but with possibly different morphologies and colors. Rong et al. (2017) supported this hypothesis by finding that UDGs in their cosmological simulations reside in high spin halos.

Upon finding UDGs with bluer color far from clusters, Román & Trujillo (2017b) and Trujillo et al. (2017) suggested that red UDGs in clusters might be initially low surface brightness diffuse dwarf galaxies born in the field that are later processed in groups and ultimately accreted into galaxy clusters.

In this paper, we use cosmological zoom-in simulations from the FIRE simulation to study the effects of stellar feedback and quenching on the progenitors of UDGs. Stellar feedback is known to shape dark matter (DM) profiles, creating large cores in the DM distribution of dwarf galaxy halos (Navarro et al., 1996; El-Zant et al., 2001; Gnedin et al., 2004; Read & Gilmore, 2005; Governato et al., 2010; Peñarrubia et al., 2012; Governato et al., 2012; Pontzen & Governato, 2012; Macciò et al., 2012b; Teyssier et al., 2013; Di Cintio et al., 2014; Pontzen & Governato, 2014; Chan et al., 2015; Tollet et al., 2016). Feedback can also drive significant radial migrations of stars via two processes: (1) inflowing/outgoing gas clouds can form stars that inherit the velocities of the gas clouds and continue migrating within their first 100Myr; (2) Feedback-driven gas outflows modify central gravitational potential and transfer energy to stars non adiabatically (in the same manner as in DM core creation; see El-Badry et al. 2016). Through these processes, feedback expands galaxies into diffuse spheroids, producing large effective radii (El-Badry et al., 2016) and large axis ratios (Wheeler et al., 2017) simultaneously. Effects of stellar feedback on both DM and stellar distributions peak at $M_{*} \sim 10^{8}\mathrm{M}_{\odot}$, which is also a typical mass of the observed UDGs.

Using cosmological simulations of isolated galaxies with stellar feedback, Di Cintio et al. (2017) recently also showed that feedback can produce extended stellar profiles similar to observed UDGs. Our study differs both in the stellar feedback model and in the inclusion of the effect of quenching, which has significant effects on the formation of red UDGs (see § 3.5.4 for a comparison of their findings with our work).

Table 3.1: Simulation details. $M_{\rm h}^0$ and M_*^0 are the halo mass and stellar mass (within $0.2R_{\rm vir}$) of the largest halo in the zoom-in region at $z = 0$; $R_{\rm vir}$ is the virial radius; $m_{\rm b}$ is the mass of a gas particle in the simulation; $m_{\rm dm}$ is the mass of a DM particle in the simulation. ε_b is the minimum gravitational softening of a gas particle; $\varepsilon_{\rm dm}$ is the Plummer equivalent gravitational softening of a DM particle. All simulations are a part of the FIRE-2 simulation suite (Hopkins et al., 2018b). The initial conditions for **m11q** are from Kim et al. (2014b), while **m11z** and **m11c** are from Chan et al. (2015). **m11a**, **m11b** and **m11f** are newly targeted halos in the mass range relevant for UDGs. Note that Hopkins et al. (2018b) presented higher resolution runs of **m10z** and **m11c**, which we discuss in Appendix 3.C.

Name	$M_{\rm h}^0$ [$M_\odot$]	M_*^0 [$M_\odot$]	$R_{\rm vir}$ [kpc]	$m_{\rm b}$ [$M_\odot$]	$\varepsilon_{\rm b}$ [pc]	$m_{\rm dm}$ [$M_\odot$]	$\varepsilon_{\rm dm}$ [pc]
m10z	3.5e10	5.3e7	85	2.1e3	0.43	1.0e4	43
m11a	4.1e10	1.2e8	90	2.1e3	0.43	1.0e4	43
m11b	4.4e10	1.1e8	92	2.1e3	0.43	1.0e4	43
m11q	1.2e11	1.0e9	1.4e2	7.1e3	0.42	3.5e4	14
m11c	1.5e11	2.0e9	1.4e2	1.7e4	0.86	8.3e4	86
m11f	4.9e11	2.7e10	2.1e2	1.7e4	0.86	8.3e4	86

In § 3.3 we describe the simulation methodology, the suite of simulations used in this paper and the method for mock observations with GALFIT. In § 3.4, we show how radius, surface brightness and other properties of simulated galaxies change with quenching time. In § 3.5 we discuss the structural properties of our dwarfs, the connections to the formation scenarios discussed in the literature as well as the implications for the properties of field dwarf galaxies. Finally we present our conclusions in § 3.6.

3.3 Method

3.3.1 Simulation code and setup

Our simulations utilize the GIZMO[1] code (Hopkins, 2015a) in the mesh-free Lagrangian finite mass (MFM) mode for hydrodynamics. GIZMO uses an updated version of the PM+Tree algorithm from Gadget-3 (Springel, 2005) to calculate gravity and adopts fully conservative

---

[1] http://www.tapir.caltech.edu/∼phopkins/Site/GIZMO

adaptive gravitational softening for gas (Price & Monaghan, 2007). We employ the zoom-in technique to reach high resolutions in a cosmological environment and evolve simulations from $z = 99$ to $z = 0$.

Gas cooling is calculated with the tabulated cooling rates from CLOUDY (Ferland et al., 2013) for $T = 10 - 10^{10}$ K, including atomic, metal-line, and molecular cooling. We apply the redshift-dependent ultraviolet background model from Faucher-Giguère et al. (2009) that ionizes and heats gas in an optically thin approximation and use an approximate prescription to account for self-shielding of dense gas.

Star formation and stellar feedback are implemented using the FIRE-2 algorithm (Hopkins et al., 2018b), which is an updated version of the FIRE feedback scheme from Hopkins et al. (2014). Briefly, stars form in self-gravitating molecular gas at densities $n_{\rm H} \geq 1000\,{\rm cm}^{-3}$, with 100% instantaneous efficiency per free fall time. Stellar feedback physics implemented includes stellar winds, radiation pressure from young stars, Type II and Type Ia supernovae, photoelectric heating, and photoheating from ionizing radiation. We calculate the energy, momentum, mass and metal return according to the STARBURST99 stellar population synthesis model (Leitherer et al., 1999) and Kroupa IMF (Kroupa, 2002). Full details of the implementation of gas and gravitational physics are provided in Hopkins et al. (2018b).

All simulations analyzed in this work are a part of the FIRE-2 simulation suite of the FIRE project[2]. Most are based on the initial conditions previously explored with FIRE-1 models in Hopkins et al. (2014) and Chan et al. (2015)[3][4], while several additional galaxies were specifically simulated to explore the relevant mass scale of UDGs. Our sample includes all FIRE-2 galaxies with $z = 0$ stellar mass $5 \times 10^7 - 2 \times 10^9 {\rm M}_\odot$ and one additional higher mass galaxy, **m11f**, selected to explore the UDG formation with quenching at high redshift. All satisfy the absolute

---

[2] http://fire.northwestern.edu

[3] The FIRE-1 runs corresponding to **m10z**, **m11q** and **m11c** were named as **m10h573**, **m11** and **m11h383** respectively.

[4] We note that our values of $m_{\rm b}$ and $m_{\rm dm}$ for the runs included in Chan et al. (2015) differ from values in Table 1 in that paper owing to their omission of the factor of $h = 0.7$. This omission did not affect any of the results quoted in that paper.

magnitude range of the observed UDGs in at least one simulation snapshot in the redshift interval $z = 0-3$ when post-processed with our mock-observations. Here we focus on properties of stellar population in our simulations; their gas properties were explored in El-Badry et al. (2018). Parameters of the simulated galaxies are listed in Table 3.1.

The galaxies we examine are isolated field dwarfs with $M_{\mathrm{h}} \sim 10^{10-11}\mathrm{M}_{\odot}$ at $z = 0$, where the effects of stellar feedback on the underlying density distributions are *large* (see e.g. Chan et al., 2015, El-Badry et al., 2016, Tollet et al., 2016; but also Oñorbe et al., 2015 and Fitts et al., 2017 for the effect in lower mass halos). Our simulations were run in a 'standard' flat ΛCDM cosmology with the following cosmological parameters: $\Omega_0 \approx 0.27$, $\Lambda \approx 0.73$, $\Omega_b \approx 0.045$ and $h \approx 0.7$.

We note that our simulated halos have a normal distribution of spin parameters. We measured the spin parameters of our DM halos (in default runs with full hydrodynamics and feedback) and found that at $z = 0$ all except one are within 1σ of the measured spin parameter distribution from Macciò et al. (2008) with values $\lambda \sim 0.02-0.035$. The exception is **m11b** whose spin parameter is about 2σ above the mean with spin parameter $\lambda = 0.077$.

3.3.2 Simulation analysis and mock observations

All of our isolated dwarf galaxies remain gas-rich and star-forming until $z = 0$. This is in contrast to UDGs observed in galaxy clusters, many of which are quenched, likely because of the environmental effect of the clusters. To mimic the quenching of star formation that likely occurs during the infall into the cluster environment, we artificially stop each galaxy's star formation at the assumed quenching time $t = t_{\mathrm{q}}$ (measured as cosmic time starting from the Big-Bang) and passively evolve its stellar populations to $z = 0$. The minimum t_{q} we consider is 2 Gyr (i.e. $z \sim 3.5$) since all of the simulated galaxies in this work have sizes smaller than ∼1 kpc at earlier times and would therefore not satisfy our observationally motivated UDG selection (see § 3.4).

We assume that stellar morphology has not changed since t_{q}. Even if quenching processes

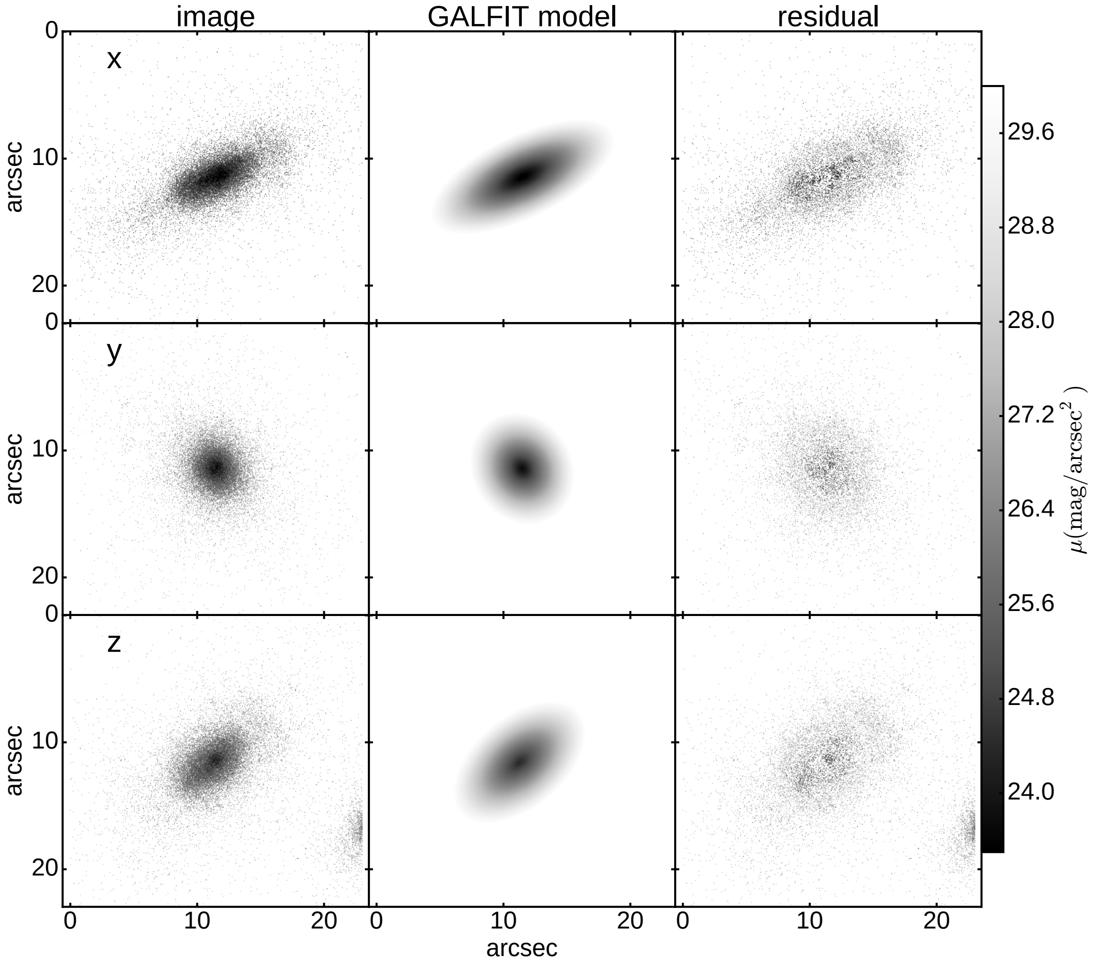

Figure 3.1: The mock g-band image of **m11b** ($M_* \sim 10^8 \mathrm{M}_\odot$) quenched at a cosmic time $t_\mathrm{q} = 6$ Gyr and passively aged stellar population from t_q to $z = 0$, the best-fitting GALFIT model and the residuals from the fit. Each panel spans 16 kpc × 16 kpc ($23'' \times 23''$ if we place the galaxy at the distance of the Coma cluster) and is shaded according to surface brightness. The top, middle and bottom panels show images viewed along x, y and z direction, respectively.

remove galactic gas (e.g. via ram pressure), this is a reasonable assumption as long as the galaxy is DM-dominated and stays far from the cluster center where cluster tidal interactions are important. In Appendix 3.B we study dynamical effects of gas removal and show that they tend to slightly decrease surface brightness but do not affect any of our conclusions. We do not attempt to account for other possible cluster interactions (e.g. tidal disruptions, galaxy harassment, etc.), which would require a full scale galaxy cluster simulation that is beyond the scope of our paper. In other words, our UDG candidates are simulated dwarf galaxies at $t_{\rm q}$, but with their stellar populations artificially aged to $z = 0$.

In order to compare our simulated galaxies with observations, we produce mock images at $z = 0$ for $t_{\rm q} \sim 2 - 14$ Gyr ($z_{\rm q} \sim 3.4 - 0$) with passively evolved stellar populations and perform mock observations to estimate their g-band surface brightnesses $\mu(g)$, effective radii $r_{\rm eff}$, and g-i colors. We follow the steps in van Dokkum et al. (2015a) closely for a more direct comparison. The galaxy images are initially centered on the halos of their main progenitors identified with the Amiga Halo Finder (AHF) (Knollmann & Knebe, 2009), which uses an adaptive mesh refinement hierarchy (Knebe et al., 2001) to define centers. Halo centers may not coincide with galaxy centers during ongoing mergers or instabilities, however, so we relocated centers with a χ^2 minimization on galaxy images with GALFIT (Peng et al., 2002). To calculate enclosed masses (e.g. in Figures 3.6 and 3.7), we applied the two-step procedure described in Chan et al. (2015) to center on the stellar distribution of the galaxy. We use AHF and virial overdensities from Bryan & Norman (1998) to calculate virial mass $M_{\rm h}$, virial radius $R_{\rm vir}$ and M_*, the total stellar mass enclosed within $0.2R_{\rm vir}$.

van Dokkum et al. (2015a) inferred axis ratios and effective radii from combined g+i band images, and surface brightnesses from g-band images. To follow their procedure, we generated a table of SDSS (Sloan Digital Sky Survey) g and i band luminosities for stellar populations of different ages and metallicities[5] with the Flexible Stellar Population Synthesis model (FSPS)

---

[5] Although we do not use the Canada-France-Hawaii Telescope (CFHT) MegaCam filters, which the observations in van Dokkum et al. (2015a) are performed with, the difference between the SDSS and CFHT filters are negligible

(Conroy et al., 2009), assuming the latest Padova stellar evolution model (Marigo & Girardi, 2007; Marigo et al., 2008) and the Kroupa initial mass function (Kroupa, 2002). The luminosity of each stellar particle is interpolated from the table according to their stellar ages, masses and metallicities. Then, for each simulation output we project the g + i band luminosities over a 40 kpc × 40 kpc (60 kpc × 60 kpc for **m11f**) region onto 1000^2 uniform mesh, and generate mock galaxy images. We explore the effects of lowering the image resolution (down to 100x larger pixels, i.e. 100x100 pixels per image) in Appendix 3.D and found that this does not significantly affect our results[6].

We also generate images with g-band luminosities to estimate g-band surface brightness. We do not account for any dust attenuation because we assume all gas is removed immediately after the infall (we briefly discuss the dust attenuation effects at $z = 0$ in § 3.5.4). The left panel of Figure 3.1 shows the processed g+i band image of **m11b** at $z = 0$ with $t_{\mathrm{q}} = 6$ Gyr (i.e. passively evolved from $z = 1$), viewed along three perpendicular directions.

To estimate structural parameters from the mock images, we fit them with the Sersic profiles using GALFIT (Peng et al., 2002, 2010), similar to the techniques used in other UDG observations (e.g. Koda et al., 2015; Mihos et al., 2015). We allow n_s to vary in our fits to increase convergence (Koda et al., 2015; Mihos et al., 2015). Our galaxies have $n_s = 0.8 \pm 0.4$, close to the $n_s = 1$ profiles, used in van Dokkum et al. (2015a). We have compared central surface brightness of our galaxies obtained with the $n_s = 1$ fits to those with variable n_s and found only minor differences. Our fits do not account for sky noise: we have tested adding sky noise to our images in Appendix 3.A and again found very little difference in the inferred properties of our galaxies (see Figure 3.10). The middle panels of Figure 3.1 show the GALFIT models and the right panels show the residuals.

---

and would not affect our main results.

[6] This is because GALFIT attempts to fit for average surface brightness within each elliptical ring.

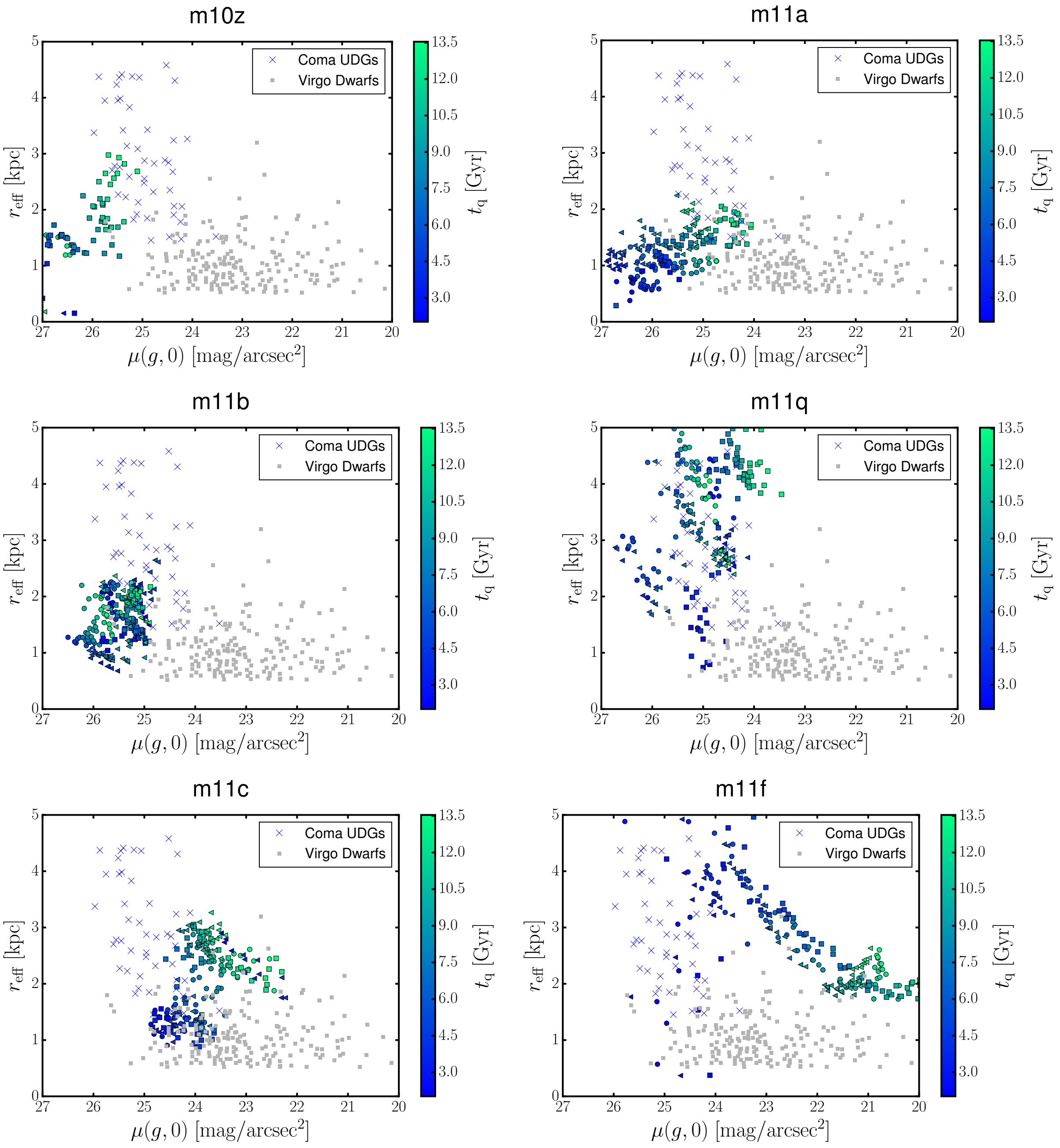

Figure 3.2: Central g-band surface brightness of our simulated galaxies plotted against their effective radius. The colors of points represent quenching times, at which we artificially stop their star formation and passively evolve their stellar population to $z = 0$ according to FSPS. The styles show different viewing angles (*squares*: along x axis; *triangles* : along y axis; *circles*: along z axis). Each panel represents a single simulated galaxy. We also show the observed values of early-type galaxies in the Virgo cluster (Gavazzi et al., 2005) and UDGs in the Coma cluster (van Dokkum et al., 2015a). We find that all of these simulated galaxies have sizes and surface brightnesses that are consistent with observed UDGs, depending on the quenching time that we assume.

3.4 Results

3.4.1 Effective Radius and Surface Brightness

We first define UDGs based on the van Dokkum et al. (2015a) sample: (1) $\mu(g) \gtrsim 23.5\,\mathrm{mag/arcsec^2}$; (2) $r_{\rm eff} \gtrsim 1.25$kpc. This definition is also similar to the selection criteria in Román & Trujillo (2017a). Koda et al. (2015) and Mihos et al. (2015) also use the similar $r_{\rm eff}$ limit to define UDGs, but require different μ cutoffs according to the bands they use[7].

Figure 3.2 shows the central g-band surface brightness $\mu(g,0)$, defined as the surface brightness of the fitted Sersic profile at the center, as a function of the effective radius of our galaxies, compared to the observed red UDGs and dwarf galaxies associated with galaxy clusters. We "observe" each galaxy along three perpendicular viewing angles for different assumed quenching times, and label the results with different symbols accordingly in Figure 3.2 and 3.3. The choice of viewing angle only mildly affects the results, consistent with expectations for roughly spheroidal geometries. The differences in surface brightness between different viewing angles are in general smaller than 1 mag/arcsec^2, except for very irregular geometries during mergers.

In Figure 3.2 we show that μ and $r_{\rm eff}$ of **m10z**, **m11a**, **m11b**, and **m11q** are a good match to the observed red UDGs for $t_{\rm q} \sim 6-13$ Gyr. Later quenching times allow these galaxies to form more stars, while strong stellar feedback increases their $r_{\rm eff}$. **m11c** and **m11f** agree with the red UDGs in van Dokkum et al. (2015a) only for very early quenching times ($t_{\rm q} \sim 2-4$ Gyr) but have much higher surface brightness if their star formation proceeds to later times. For early quenching times these two galaxies are therefore valid progenitors of UDGs according to our criteria stated in § 3.4.1. If we, in addition to our standard criteria, consider the absolute magnitude range of van Dokkum et al. (2015a), **m11f**, can only reproduce the bright end of the UDGs for $t_{\rm q} \lesssim 2.5$ Gyr, owing to its large g-band magnitude if quenched much later (see Figure

---

[7] Although our UDG definition does not include limits on the total magnitude, we may impose magnitude cuts to match specific observation samples in the following, e.g. Table 3.2.

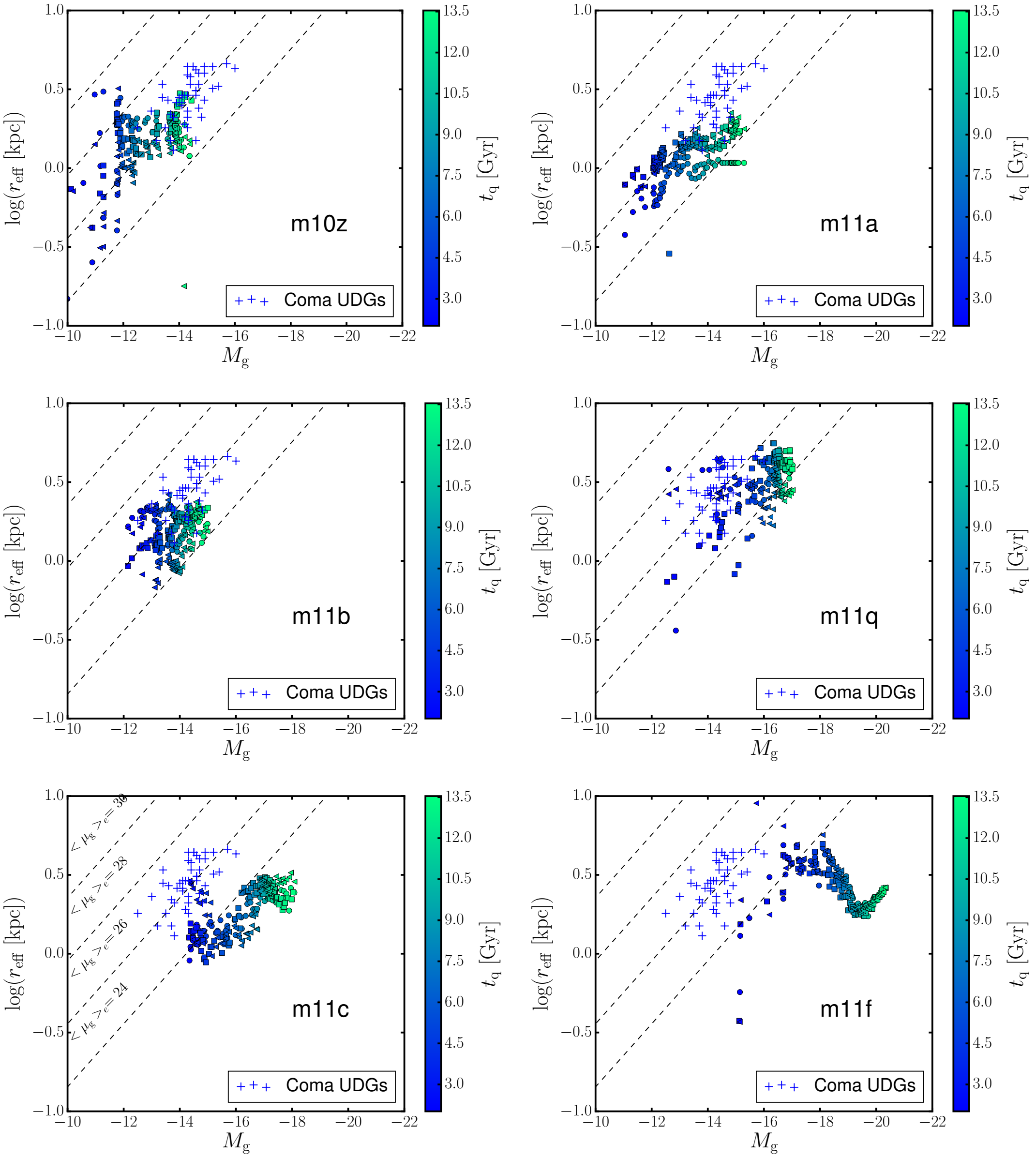

Figure 3.3: Absolute g-band magnitude (in AB) plotted against effective radius. Dashed lines show constant g-band surface brightnesses within effective radii, $\langle \mu_g \rangle_e$ [mag/arcsec^2]. The color of each point represents the assumed quenching time, whereas point styles show different orientations, as in Figure 3.2. Cross symbols represent the observed UDGs from van Dokkum et al. (2015a). Our simulated galaxies can match the range of observed surface brightness and magnitudes at some quenching times, but more massive UDGs have to quench very early to match the range of observed magnitudes.

3.3 and 3.4). Overall, the luminosities, effective radii, and colors of stellar populations formed by $z \sim 0-3$ in dwarfs simulated with the FIRE-2 model are consistent with those of observed UDGs, but galaxies forming in more massive halos (at $z = 0$) require earlier quenching times.

Figure 3.3 shows effective radius, $r_{\rm eff}$, as a function of absolute g-band magnitude, $M_{\rm g}$, for the FIRE-2 dwarfs and the observed red UDGs from van Dokkum et al. (2015a). We also show lines indicating the average surface brightness within the effective radius[8].

All galaxies can roughly match the parameter space of the observed UDGs for a wide range of quenching times, except **m11c** and **m11f**, our two most massive systems. These galaxies meet our UDG criteria only for snapshots with $t_{\rm q} < 3\,{\rm Gyr}$ (excluding some occasional contraction periods and minor mergers) and represent more massive UDGs. At larger $t_{\rm q}$, their surface brightnesses are higher than the observed UDGs in the van Dokkum et al. (2015a) sample.

3.4.2 Effects of Quenching Time

In this section, we explore how properties of our simulated galaxies at $z = 0$ depend on quenching time. We explore the range of the allowed quenching times by matching the observed properties of our simulated UDGs, e.g. $r_{\rm eff}$, $M_{\rm g}$ and $\mu_{\rm g}$, to the observations.

We plot the properties of our galaxies as a function of quenching time in Figure 3.4 and compare them with the median values from the observations (van Dokkum et al., 2015a), shown with horizontal dashed lines. The gray regions show the minimum and maximum observed values for $r_{\rm eff}$, $M_{\rm g}$ and $\mu_{\rm g}$. We also show the evolution of axis ratio, g-i color, stellar mass M_*, stellar age Age$_*$, and metallicity [Fe/H].

Absolute g-band magnitudes and mass weighted stellar ages drop with quenching time for all galaxies because later quenching implies a shorter passive evolution period and a longer time during which a galaxy can form stars. The typical axis ratios of our simulated galaxies are ~ 0.8

---

[8] Note that the difference between average surface brightness within $r_{\rm eff}$ and central surface brightness, $\langle\mu_g\rangle_e - \mu(g,0)$, is generally small because of relatively flat profiles, but it can occasionally reach up to ~ 0.5mag.

Table 3.2: Characteristic properties of simulated UDGs. The properties of the simulated galaxies are extracted for quenching times when they satisfy UDG selection criteria from § 3.4.1 and when, in addition, their $M_{\rm g}$ falls within the observed range of red UDGs in van Dokkum et al. (2015a), $M_{\rm g}$=[-16.0, -12.5]. The values presented in large numbers are determined at the $t_{\rm q}$ for which the g-band magnitude is the closest to the median observed magnitude $M_g = -14.3$, while the small numbers show the maximum and minimum during the range of t_q described above. Effective radius, $r_{\rm eff}$ and central surface brightness, $\mu(g,0)$ are determined by GALFIT. The absolute magnitude, M_g and color, $g-i$, are determined directly from star particles. Stellar age and metallicity are mass weighted. Stellar mass is measured within $0.2R_{\rm vir}$. Next, we show the range of halo masses, $M_{\rm h,q}$, and the stellar-to-halo mass ratio, $M_*/M_{\rm h,q}$. $M_{1/2,\rm obs}$ is the total stellar plus DM mass within de-projected half-light radius ($r_{1/2} = r_{\rm eff} \times \sqrt{b/a} \times 4/3$, where b/a is axis ratio from GALFIT), whereas $M_{1/2}$ is the total stellar plus DM mass within 3D half stellar mass radius. In addition, we show the ratio of the stellar mass to stellar plus DM mass, $f_{1/2,*}$, within the de-projected half light radius $r_{1/2}$. All of the masses and mass ratios are measured at $t_{\rm q}$ (i.e. we assume that structural properties of galaxies and halos remain fixed after $t_{\rm q}$). The second column ("Observed") shows properties of observed UDGs. Given the constraints on effective radius, surface brightness and g-band luminosity/magnitude, we predict colors, ages, metallicities and stellar-to-halo mass ratios. All quantities are measured as viewed along x axis.

	Observed		**m10z**		**m11a**		**m11b**		**m11q**		**m11c**		**m11f**	
$t_{\rm q}$[Gyr]	-		13.4	13.5 8.2	10.4	13.5 5.7	10.7	13.5 2.6	2.7	6.0 2.3	2.0	6.5 2.0	2.2	2.4 2.2
$r_{\rm eff}$[kpc]	2.8	4.6 1.5	2.9	3.2 1.4	1.4	1.4 1.3	2.0	2.0 1.3	1.7	4.0 1.3	1.3	1.5 1.3	1.6	2.5 1.6
μ(g, 0)	25.0	26.5 23.5	25.67	25.67 26.3	24.42	23.76 25.96	25.14	24.92 25.77	25.98	25.47 26.01	23.74	23.4 23.74	26.24	24.87 26.24
$M_{\rm g}$[AB]	-14.3	−16.0 −12.5	−14.3	−14.4 −12.5	−14.3	−15.2 −12.5	−14.3	−15.0 −12.7	−14.3	−16.0 −13.8	−14.3	−16.0 −14.3	−15.2	−16.0 −15.2
$g-i$	0.8	0.7 0.9	0.54	0.51 0.77	0.72	0.59 0.79	0.76	0.59 0.79	0.81	0.85 0.8	0.84	0.86 0.84	0.83	0.83 0.83
Age$_*$[Gyr]	-		5.4	5.4 9.3	6.8	5.1 11.0	8.7	7.2 12.2	11.6	9.9 11.8	12.6	9.9 12.6	12.1	11.9 12.1
[Fe/H]	-		−1.41	−1.41 −1.67	−1.26	−1.1 −1.7	−1.28	−1.17 −1.77	−1.54	−1.15 −1.71	−1.39	−1.02 −1.39	−1.45	−1.37 −1.45
$M_*[10^8 {\rm M}_\odot]$	-		0.53	0.55 0.19	0.8	1.22 0.21	0.94	1.16 0.26	1.2	5.58 0.74	1.36	5.76 1.36	2.77	6.12 2.77
$M_{\rm h,q}[10^{10} {\rm M}_\odot]$	-		3.5	3.5 3.4	3.8	4.1 2.9	4.0	4.4 1.3	3.4	9.3 3.1	2.2	11.4 2.2	5.5	9.7 5.5
$10^3 M_*/M_{\rm h,q}$	-		1.53	1.59 0.55	2.04	2.94 0.72	2.36	2.65 1.92	3.75	6.09 1.71	6.14	4.93 6.14	4.91	5.94 4.91
$M_{1/2,\rm obs}[10^8 {\rm M}_\odot]$	-		4.28	4.98 2.29	3.41	2.5 2.16	7.65	9.3 2.6	2.1	21.54 1.55	3.68	3.0 3.68	13.66	14.25 13.66
$M_{1/2}[10^8 {\rm M}_\odot]$	-		8.83	9.53 4.67	4.76	4.66 2.82	7.68	9.92 4.87	20.48	32.83 52.56	10.06	30.13 10.06	25.1	26.0 25.1
$10 \times f_{1/2,*}$	-		0.39	0.4 0.26	0.86	1.2 0.37	0.6	0.58 0.32	0.27	0.99 0.05	0.91	0.73 0.91	0.64	0.83 0.64

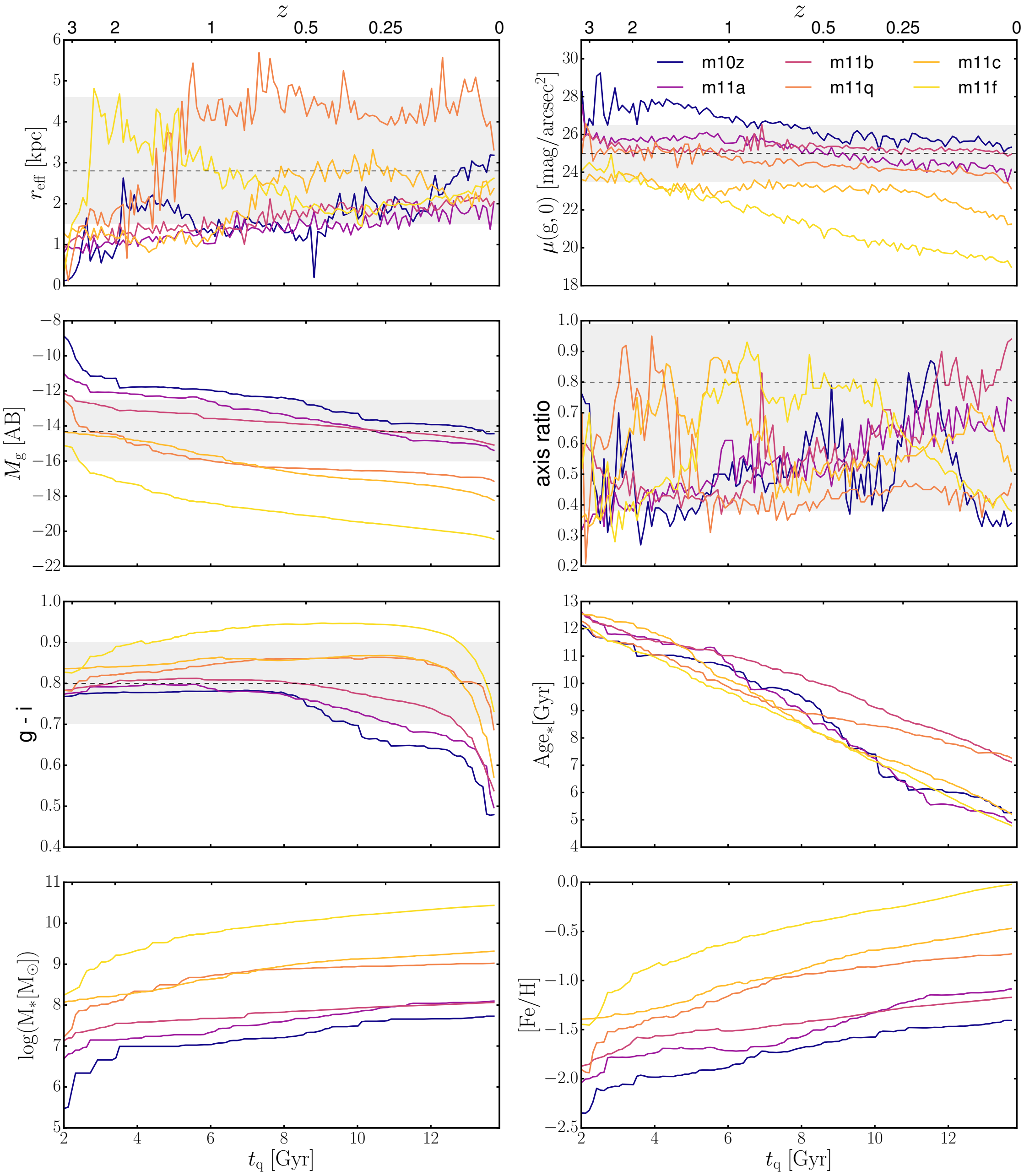

Figure 3.4: Effective radius $r_{\rm eff}$, central g-band surface brightness $\mu(g,0)$, absolute g-band magnitude $M_{\rm g}$, axis ratio, g - i color, (mass-weighed) stellar age Age$_*$, stellar mass within $0.2R_{\rm vir}$, M_*, as functions of quenching time. We use GALFIT to determine central surface brightness from the g-band images and effective radii and axis ratios from g + i images. All other quantities are obtained directly from star particles without using a fit. All quantities are measured as viewed along x axis. Horizontal dashed lines show the median values of the observed UDGs (van Dokkum et al., 2015a) while horizontal shaded regions show their ranges.

since our galaxies are usually spheroidal owing to continuous stellar feedback, which prevents formations of prominent disks in dwarfs (Wheeler et al., 2017; El-Badry et al., 2018). Our most massive galaxy builds a stellar disk at late times, which shows as a fast drop in axis ratio.

Finally, the g-i colors of all but our most massive dwarfs are approximately $0.75-0.85$ for $t_\mathrm{q} \lesssim 10-11\,\mathrm{Gyr}$, consistent with observations of UDGs. The slow change in colors is caused by the interplay between increasing metallicities and decreasing mean stellar ages as we increase t_q. These competing effects mostly cancel out and prevent strong changes in the overall colors of the galaxies until $t_\mathrm{q} \sim 10\,\mathrm{Gyr}$ for lower mass dwarfs and $t_\mathrm{q} \sim 12\,\mathrm{Gyr}$ for our higher mass dwarfs. This implies that mean stellar ages and metallicities of UDGs cannot be determined with g-i colors alone.

Although we cannot infer precise quenching times of observed UDGs from their g-i colors only, effective radius, surface brightness, and g-band magnitude can provide tighter constraints. **m10z**, **m11a** and **m11b** correspond to red UDGs if $t_\mathrm{q} \gtrsim 5\,\mathrm{Gyr}$. The more massive dwarfs **m11q** and **m11c** must have $t_\mathrm{q} \lesssim 6\,\mathrm{Gyr}$ and $t_\mathrm{q} \lesssim 3\,\mathrm{Gyr}$, respectively, in order to match the g-band magnitude of the sample in van Dokkum et al. (2015a).

Stellar age and metallicity measurements also give useful constraints on quenching time. Kadowaki et al. (2017) found low stellar metallicity ($[\mathrm{Fe/H}] \lesssim -1.5$) from the stacked spectrum of Coma UDGs. Gu et al. (2017) analyzed the optical spectra of three of the brightest Coma UDGs and found they are metal poor ($[\mathrm{Fe/H}] = -0.8^{+0.5}_{-0.5} - 1.3^{+0.4}_{-0.4}$) and old ($7.9^{+3.6}_{-2.5} - 9.1^{+3.9}_{-5.5}$ Gyr). Using optical through near infrared SED fitting, Pandya et al. (2018) inferred a UDG in the Virgo cluster (VCC 1287) to be metal poor ($[\mathrm{Fe/H}] \lesssim -1.0$) and old ($\gtrsim$ 9 Gyr). These data and Figure 3.4 together imply an early quenching scenario for cluster UDGs ($t_\mathrm{q} \lesssim 6\,\mathrm{Gyr}$).

3.4.3 Characteristic properties of simulated red UDGs

Table 3.2 lists the properties of our simulated galaxies, for a range of quenching times during which they match the observed range of r_eff and $\mu(g,0)$. We also list the median values of the observed UDGs (van Dokkum et al., 2015a). When the g-band magnitude of our simulated galaxy matches the median of the observed sample at a certain quenching time, the galaxy also yields a close match in effective radius, central surface brightness, and color, suggesting that our simulated galaxies are good analogs of the observed UDGs. While our galaxies are slightly less spheroidal than UDGs, we expect they would be rounder if the dynamical effect of gas removal were taken into account (shown in Appendix 3.B). Simulated and observed UDGs have similar stellar masses, largely determined by the absolute magnitude selection of the sample, since old stars have approximately constant stellar mass-to-light ratios.

With earlier quenching times, stars are older at $z = 0$ and have lower metallicities because of the evolution of the galaxy mass-metallicity relation (e.g. Zahid et al., 2013; Ma et al., 2016). Metallicities of UDGs could potentially be used to constrain quenching times of UDGs. However, for our simulated sample, typical metallicities grow very slowly with later quenching times because the metallicity evolution is offset by larger stellar masses of the galaxies that satisfy the UDG selection for early quenching times (typically galaxies with $z = 0$ halo mass $\gtrsim 10^{11}\mathrm{M}_{\odot}$). A larger sample of simulated galaxies is needed to explore the metallicity trends in detail.

Observationally, long exposure spectroscopic studies combined with stellar population modeling are necessary to determine dynamical masses, stellar ages and metallicities of UDGs and potentially constrain their origin and quenching times (e.g. Makarov et al., 2015; Kadowaki et al., 2017; Gu et al., 2017; Pandya et al., 2018). Low surface brightness sensitive instruments such as the Keck Cosmic Web Imager (Martin et al., 2010) should be helpful in extending such studies to a larger number of objects. Overall, for the observed range of surface brightnesses and magnitudes of UDGs, our model predicts a uniform population of galaxies in terms of their stellar masses and g-i colors but with a broad range of average stellar ages.

3.4.4 UDGs and their halos

The M_*/M_h row in Table 3.2 shows the stellar-to-halo mass ratios measured at the range of quenching times when these galaxies satisfy red UDG criteria. The upper panel of Figure 3.5 shows the ratios as a function of quenching time. While the ratios are small, they do not deviate much from the dwarfs with similar masses in the Local Group (LG, McConnachie 2012). It is reasonable to expect that DM halos of UDGs cannot grow significantly after t_q due to cluster influence. Furthermore, the outskirts of UDG halos will likely be stripped or modified following the infall into a cluster. Stellar to total mass (stellar+DM) ratio within effective radius, given in the last row of Table 3.2, is thus a more robust quantity. This ratio shows that for quenching times when our galaxies are analogs to UDGs, their central regions are strongly DM dominated.

Recently, Beasley et al. (2016) claimed that one of the UDGs in the Virgo cluster, VCC 1287, has a stellar fraction $\sim 3.5 \times 10^{-4}$, much lower than "normal" dwarf galaxies of similar masses whose stellar fractions are $\sim 10^{-2} - 10^{-3}$. They estimated its total halo mass using the velocity dispersion and the number of GCs. While at face value this is lower than the stellar fractions of our simulated dwarfs, they do not directly measure the mass at the virial radius; instead, they infer it assuming a density profile, which introduces significant uncertainty. However, their observations do directly constrain the mass within 8.1 kpc with the "trace mass estimator" (Watkins et al., 2010) using GCs as tracers; we therefore compare their estimate to the enclosed masses of our simulated galaxies measured at this radius.

Figure 3.6 shows the enclosed stellar and DM mass within 8.1 kpc at different t_q. We do not include the gas mass as we are comparing to a red cluster UDG that has likely lost its interstellar gas. The enclosed masses of our simulated dwarfs are roughly constant over 10 Gyr, and our lower mass halos **m10z, m11a and m11b** can match the measured enclosed mass in VCC 1287, while having normal stellar fractions. Therefore, our simulated red UDGs formed as regular dwarf galaxies. However, their growths stopped at early times while outskirt of isolated halos can continue growing until much later. We may wrongly infer much larger masses of their host halos

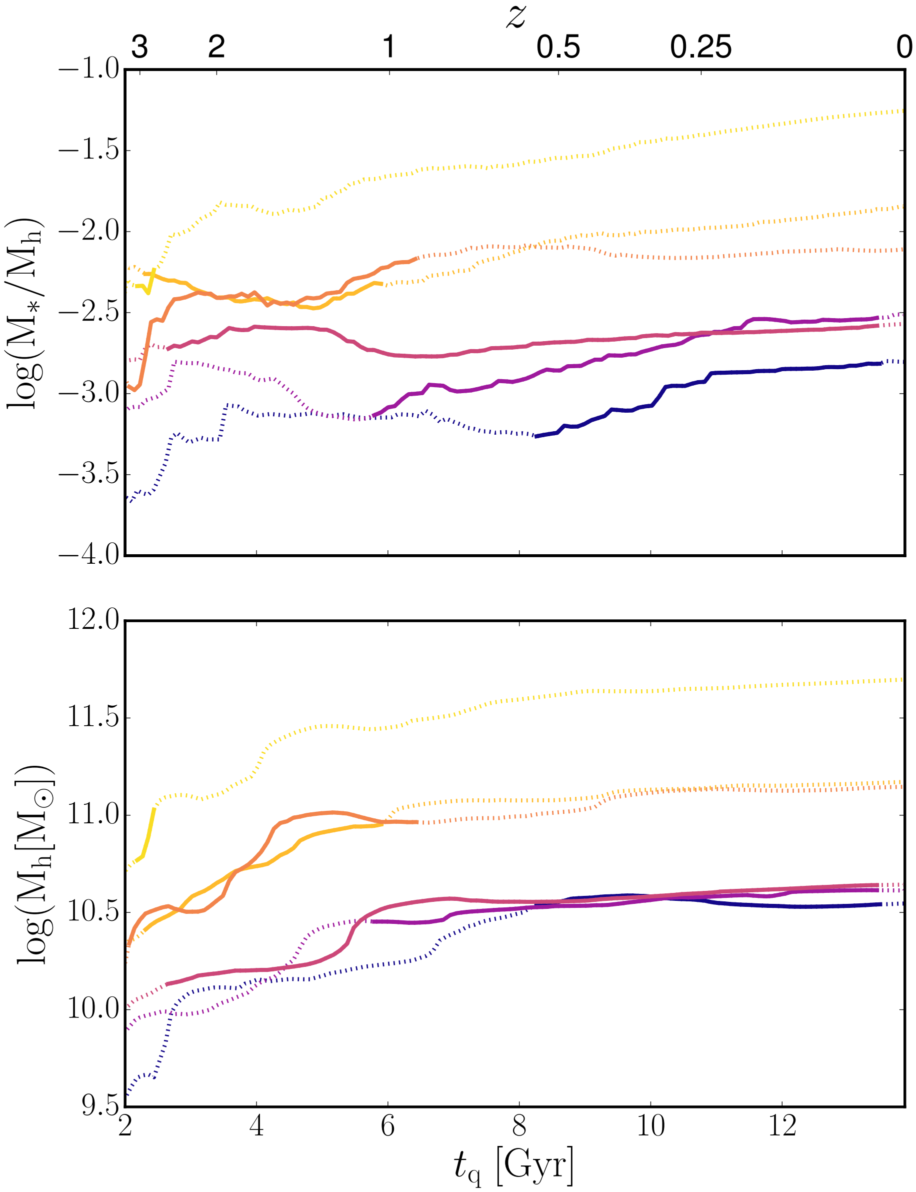

Figure 3.5: (*Upper*) stellar fraction and (*lower*) halo mass as functions of quenching time for our sample of simulated galaxies. Solid lines show the quenching times when they satisfy the UDG criteria and dotted lines when they do not. The color scheme follows Figure 3.4. Our UDGs have "normal" stellar fraction for they stellar and halo mass range ($\sim 10^{-2} - 10^{-3}$).

from the measurements of the central regions of UDGs and the mass profiles of isolated halos.

The enclosed masses within the inner 8.1 kpc of several of our dwarfs match the value for VCC 1287 for long periods of time, during which their total halo masses change significantly. For example, the halo mass of **m10z** grew by a factor of six (see Figure 3.5) while the mass within 8.1 kpc remained consistent with VCC 1287. This constancy (lack of growth) of the inner DM profile is typical in ΛCDM: most "growth" in low-mass halos at late cosmic times occurs because of a drop in the reference density, not because of a change in the mass enclosed within a fixed physical radius ("pseudo-evolution", Diemer et al. 2013; van den Bosch et al. 2014; Wetzel et al. 2015). The exception is **m11f**, which forms the most massive halo in our sample and whose stellar mass grew rapidly at late times, contributing a significant fraction of mass within 8.1 kpc and contracting the underlying DM profile (see e.g. Chan et al., 2015), although the overall effect is small as shown in Figure 3.6.

Given the board range of possible quenching times and the constancy of inner halo mass, one cannot accurately estimate their total halo mass and stellar-to-halo mass ratios from their enclosed masses without knowing their quenching times. If we determine their total halo mass by comparing their inner mass and the $z = 0$ halo mass profile of an isolated halo, the estimated halo mass may be several times larger than the true value.

3.5 Discussion

3.5.1 UDG mass estimates

While recent observations have constrained the masses of the inner halos of several UDGs, the fraction of known UDGs with accurate measurements for the inner halo mass is very small. For those few systems with their inner masses measured, moreover, one must assume a density profile and extrapolate to infer a total halo mass. Together, these complications have led to two different views for the characteristic mass of UDG host halos.

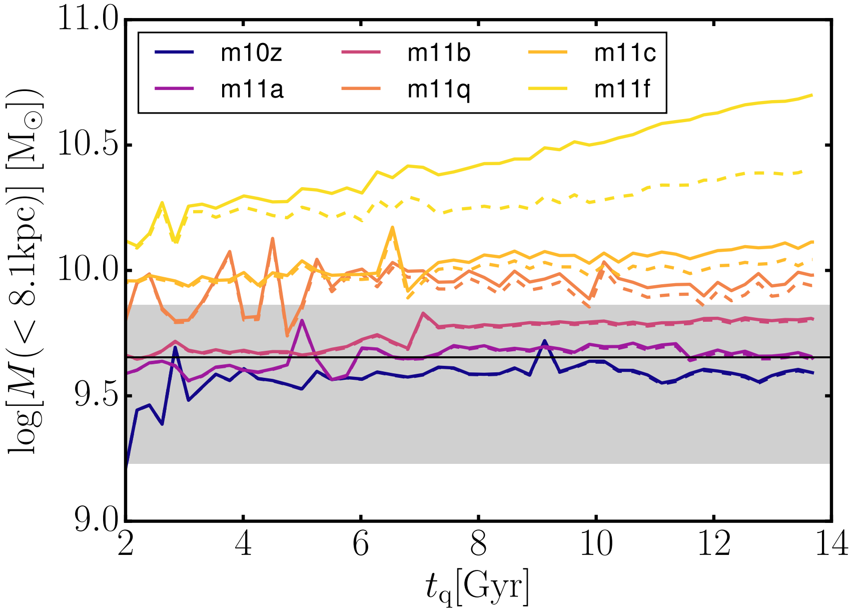

Figure 3.6: Enclosed stellar plus DM (solid) and DM only (dashed) masses of our simulated halos within 8.1 kpc as a function of t_q compared to VCC 1287 (Beasley et al., 2016) (black horizontal line; shaded region indicates the uncertainties in the observation). The colors follow Figure 3.4. The enclosed masses of **m10z**, **m11a** and **m11b** roughly match the observed value for a broad range of t_q.

van Dokkum et al. (2015a, 2016) suggested that UDGs are “failed” L$\star$ galaxies, whereas Yozin & Bekki (2015), Amorisco & Loeb (2016), Beasley et al. (2016), Beasley & Trujillo (2016) and Peng & Lim (2016) argued they are “failed” *dwarf* galaxies, based on the inferred ratios of stellar-to-halo mass. Both camps support their claims with the enclosed masses of UDGs inferred from velocity dispersions and the numbers of globular clusters (GCs).

In the previous section, we showed that simulated UDGs can form in halos with $M_{\rm h} \sim 3-15\times10^{10}{\rm M}_\odot$ and that their central enclosed masses alone are not be a good indicator of their host halo mass at the time of quenching. Here we compare the velocity dispersions and masses of our simulated UDGs to the several observed examples and critically examine the methodology used to infer masses from observations.

In Table 3.3 we show the range of velocity dispersion as seen along three perpendicular directions and the average values of each of our UDG analogs. The line-of-sight velocity dispersion of our galaxies ranges from $\sim 20-50$km/s. Our intermediate mass dwarfs provide a good match to $\langle\sigma\rangle = 33^{+16}_{-10}$km/s measured for VCC 1287 (Beasley et al., 2016) and our most massive UDG provides a match to $\langle\sigma\rangle = 47^{+8}_{-6}$km/s measured for Dragonfly 44 (van Dokkum et al., 2016).

With the measured velocity dispersion and effective radius, van Dokkum et al. (2016); Beasley et al. (2016) and Beasley & Trujillo (2016) inferred the enclosed mass within stellar half-light radius using an equation first presented in Wolf et al. (2010):

$$M_{1/2} \simeq 9.3\times10^5\left(\frac{\langle\sigma^2_{\rm los}\rangle}{{\rm km}^2/{\rm s}^2}\right)\left(\frac{r_{\rm eff}}{\rm kpc}\right){\rm M}_\odot, \tag{3.1}$$

where $M_{1/2}$ is the total mass within the 3D half light radius and $\langle\sigma^2_{\rm los}\rangle$ is the square of the line-of-sight velocity dispersion. Strictly speaking this relation is only valid for velocity dispersion dominated spherically symmetric systems but in practice, it is applied to estimate masses of a variety of dwarf galaxies (see discussions in González-Samaniego et al. 2017 for details).

We have applied this equation to the line-of-sight velocity dispersion and circularized $r_{\rm eff}$ for our dwarf galaxies and compared them to the actual enclosed mass within the 3D half-light radii. [9] When used directly with $r_{\rm eff}$ from GALFIT, this approach tends to over-predict the mass within the 3D effective radius and it shows large variations between different sight-lines. We get a better agreement and no systematic offset when we use the same approach after the gas removal and subsequent relaxation (see the Appendix 3.B), which tends to make galaxies smoother. Furthermore, when we apply this equation to the actual 2D half-mass radii (instead of half-light) we recover the actual enclosed mass within the 3D half-mass radius to within 15% when averaged over three orthogonal projections (consistent with the tests of this mass estimator on a lower mass FIRE-2 simulations by González-Samaniego et al. 2017). We therefore conclude that velocity dispersion and effective radius can indeed provide reasonable estimate of the enclosed mass but a larger number of measured systems are needed to reach a robust measure of the typical enclosed masses of UDGs.

In Figure 3.7 we present the enclosed mass profiles of our simulated halos, including their stellar and DM components[10]. Profiles are compared to the inferred values from the observations of Beasley et al. (2016); van Dokkum et al. (2016). The outer point from Beasley et al. (2016), already studied in Figure 3.6, is well matched by several of our lower mass dwarf galaxies suggesting that it is indeed a "quenched dwarf".

The innermost point of VCC 1287 was calculated by the same authors with Equation 3.1, with an additional assumption that GC velocity dispersion represents stellar velocity dispersion. This suggests a higher halo mass and it can be matched by four of our highest mass halos **m11b**, **m11q**, **m11c** and **m11f**. We note that using GC velocity dispersion instead of stellar velocity dispersion could be problematic because they only used 7 GCs, one of which is $r \gtrsim 3r_{\rm eff}$ away from the galactic center. However, even with this limitation our **m11b** galaxy (with a $z = 0$ halo

---

[9] To get the 3D half-light radius we follow the observational approach and estimate it from the circularized, de-projected effective radius, $r_{1/2} = r_{\rm eff} \times \sqrt{b/a} \times 4/3$, where $r_{\rm eff}$ and the axis ratio, b/a, are calculated by GALFIT.

[10] While gas can be a non-negligible component in our galaxies, we leave it out of the enclosed mass calculation as we are comparing to red UDGs in clusters.

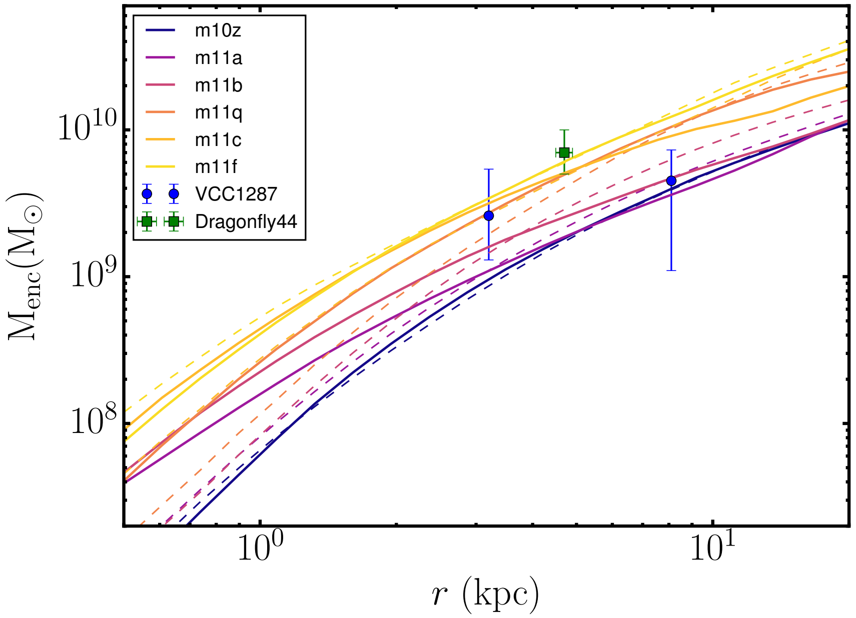

Figure 3.7: Cumulative mass profiles of our simulated halos including stars and DM, compared to the observations of VCC 1287 (*blue circle*) (Beasley et al., 2016) and Dragonfly 44 (*green square*) (van Dokkum et al., 2016). Solid (dashed) lines show the mass profiles at the earliest (latest) quenching time when simulated galaxies match the UDG selection criteria and the range of absolute magnitudes from van Dokkum et al. (2015a) (see Table 3.2). While our dwarf galaxies/halos match the outer measurement of VCC 1287, our most massive galaxy/halo **m11f** in the sample is a good match for Dragonfly 44.

mass of $4.4 \times 10^{10} \mathrm{M}_{\odot}$) can match both mass measurements, suggesting that VCC 1287 formed in a dwarf mass halo. Future spectroscopic studies with long integration times are needed to constrain its actual stellar kinematics.

The mass measurement of Dragonfly 44 came directly from stellar kinematics and Equation 3.1, and it is matched by the largest galaxy in our sample, **m11f**. **m11c**'s mass profile provides a marginal match, but only for the latest quenching time for which it is still identified as a UDG. At the quenching times when this galaxy satisfies the UDG criteria, its halo mass is only $\sim 0.5 - 1 \times 10^{11} \mathrm{M}_{\odot}$, implying its total mass today $\sim 1 \times 10^{11} \mathrm{M}_{\odot}$, assuming that its growth is insignificant after its infall.

The number of GCs in Dragonfly 44 is 94^{+25}_{-20}, much higher than inferred from its stellar mass and luminosity (van Dokkum et al., 2016). Interestingly, according to relations in Harris et al. (2013), halos with ~ 94 GCs have masses similar to that of **m11f** at $z = 0$. If all of the GCs in this system formed at very early times and the galaxy's stellar mass growth was stopped at high redshifts, one should actually expect a very high number of GCs despite its low stellar and halo mass at quenching. This is because galaxies used for the Harris et al. (2013) relation continue growing their stellar and halo masses to much later times, unlike quenched UDGs. This may also explain the finding of Amorisco et al. (2018) that the ratios between the number of GCs and stellar mass are much higher in some UDGs than the galaxies studied in Harris et al. (2013).

We have also checked the more massive galaxies presented in Hopkins et al. (2018b), **m12z**, **m12i** and **m12c**, with $z = 0$ halo masses 8.7×10^{11}, 1.3×10^{12} and $1.4 \times 10^{12} \mathrm{M}_{\odot}$ respectively. They can only match the absolute magnitude and effective radius of Dragonfly 44 for $t_{\mathrm{q}} \lesssim 2\,\mathrm{Gyr}$, i.e. $z_{\mathrm{q}} \gtrsim 3.3$. At those times, their halo masses were around $10^{11} \mathrm{M}_{\odot}$ and their inner masses matched Dragonfly 44. Hence, Dragonfly 44 can form in a halo similar to the MW's progenitor, but it has to be quenched very early. This means that at the time of quenching, Dragonfly 44 is not hosted by a highly "over-massive" DM halo. Its central halo mass, which appears unusually high for its estimated stellar mass, can be explained by its early formation time.

While forming a massive UDG requires very early quenching, we note that the Coma cluster was not fully formed so early in the structure formation process: the Coma cluster progenitor at $t = 2$ Gyr is expected to have less than 5% of its present-day halo mass (Li et al., 2007). However, it is possible that the most massive UDGs ($M_{\star} \gtrsim 2 \times 10^{8}\mathrm{M}_{\odot}$) were quenched in group-mass progenitors that existed at high redshift. Indeed, semi-empirical constraints suggest that the majority of quiescent low-mass satellites in galaxy clusters today quenched in a group (Wetzel et al., 2013). The exact mechanism and the feasibility of such a scenario have to be explored with cosmological simulations that follow formations of galaxy groups or clusters.

Relatively early quenching of massive UDGs is also suggested by spectroscopic observations (Makarov et al., 2015; Kadowaki et al., 2017; Gu et al., 2017). In particular, Gu et al. (2017) inferred the stellar age and metallicity of Dragonfly 44 to be $8.9^{+4.3}_{-3.3}$ Gyr and $[\mathrm{Fe/H}] = -1.3^{+0.4}_{-0.4}$, respectively. Our **m11f** simulation has similar metallicity at t_{q} when it is a UDG but our age estimate is close to the upper range suggested by observations (see Table 3.2). More massive simulated halos result in even older stellar ages for the allowed range of quenching times. However, we stress that uncertainties in age measurement are too large for an accurate determination of the quenching time of Dragonfly 44.

Our analysis therefore suggests that galaxies like Dragonfly 44 formed early ($z \sim 3$), in $\sim 10^{11}\mathrm{M}_{\odot}$ halos and stopped growing after their infall into a cluster. These objects could continue accreting mass, forming stars and reaching much higher luminosities and halo masses by $z = 0$ if they did not fall into a cluster. But due to the cluster influence, they should have stellar and halo masses significantly lower than those hosting L$\star$ galaxies at $z = 0$, since their formation and quenching likely took place in much lower mass halos. Overall, our simulations suggest that a majority of UDGs in clusters form in halos that span a relatively broad range of halo masses (a few $\times\ 10^{10-11}\mathrm{M}_{\odot}$), with more massive UDGs forming in more massive halos.

Table 3.3: Line-of-sight velocity dispersion $\langle\sigma\rangle\,(=\sqrt{\langle\sigma^2_{\mathrm{los}}\rangle})$ calculated at t_{q} when galaxies satisfy the UDG criteria and their g-band absolute magnitude is closest to $M_{\mathrm{g}} \sim -14.3$, the average absolute magnitude of UDGs in van Dokkum et al. (2015a). Velocity dispersions are measured in a cylindrical aperture with radius of 20 kpc, that includes vast majority of stars of each simulated UDG. The larger fonts show values averaged over three perpendicular directions, whereas the smaller fonts represent the maximum and minimum values of velocity dispersion as measured from three different perpendicular directions. For reference, $\langle\sigma\rangle$ of VCC 1287 is $33^{+16}_{-10}\mathrm{km/s}$ (Beasley et al., 2016) and of Dragonfly 44 is $47^{+8}_{-6}\mathrm{km/s}$ (van Dokkum et al., 2016).

	m10z		**m11a**		**m11b**		**m11q**		**m11c**		**m11f**	
$\langle\sigma\rangle$ [km/s]	21.4	22.6 20.1	21.6	24.4 19.5	23.8	24.1 23.1	31.2	36.6 27.0	29.5	33.4 27.2	47.7	54.2 39.0

3.5.2 Galaxy Expansion

One of the distinctive features of UDGs is their diffuseness. While we have already shown that stellar feedback leads to large effective radii and quenching of star formation can redden their colors, a large number of UDGs have been discovered in clusters, leading to a natural question: can satellite galaxies be further puffed-up with tidal heating and ram-pressure stripping? We explore the dynamical effects of gas removal in the Appendix 3.B and show that this mildly increases the size and reduces the surface brightness further.

Without invoking clusters, Yozin & Bekki (2015), Amorisco & Loeb (2016) and Rong et al. (2017) proposed that UDGs are diffuse because their progenitors have larger angular momenta compared to normal galaxies. In other words, they are the *high spin tail* of the galaxy population. Yet, high spin galaxies are also more likely to resemble disk-like (Yozin & Bekki, 2015) rather than spheroidal structures as observed in UDGs[11]. We note (as discussed in § 3.3.1) that most of our simulated UDGs have normal spin parameters and we find no clear differences between the UDGs forming in low and high spin halos [12].

Observations also seem to contradict the "high spin tail" scenario. For example van Dokkum et al. (2016) showed that Dragonfly 44 is dispersion-dominated with no evidence of

---

[11] Yozin & Bekki (2015) found their galaxies have high axis ratios but they only considered face-on images.

[12] We note that unlike Dragonfly 44, two of our galaxies **m11b** and **m11f** do develop clear stellar disks at late times (without quenching). However, at those times they are not identified as red UDGs.

rotation and radial variations in the velocity dispersion. Similarly, Burkert (2017) argued that from their axis ratios, UDGs are unlikely puffed-up disk galaxies, but are instead similar to dwarf spheroidal galaxies.

Tidal stirring provides a possible pathway from gas rich dwarf irregulars with rotational support to gas free dwarf spheroidals through repeated tidal interactions with a massive host galaxy (Mayer et al., 2001; Klimentowski et al., 2007, 2009; Łokas et al., 2015). But this mechanism may not explain the abundance of UDGs with high axis ratios observed in a variety of environments, from cluster, cluster outskirt, and group, e.g Martínez-Delgado et al. (2016); van der Burg et al. (2016, 2017); Román & Trujillo (2017a,b). Furthermore such mechanism might not be needed to transform most of the dwarf irregulars as a large fraction of the isolated dwarfs are likely dispersion dominated (Wheeler et al., 2017).

Stellar feedback can produce diffuse and spheroidal stellar distribution independent of host interactions. Through stellar migration and dynamical heating, feedback can decrease both the surface brightness and ellipticity of a dwarf galaxy while simultaneously increasing its effective radius (Chan et al., 2015; El-Badry et al., 2016). One generic effect of stellar feedback in dwarfs with $M_{\rm h} \sim 10^{10-11}{\rm M}_{\odot}$ is a cored stellar profile (Read & Gilmore, 2005; Stinson et al., 2013; El-Badry et al., 2016), implying a flat central light profile and low Sersic index[13]. A flat surface brightness profile has been observed in one of the biggest UDGs in the Coma cluster (van Dokkum et al., 2015b) and low Sersic indices ($\sim 0.8-0.9$) in UDGs were reported in various observations (e.g. Koda et al., 2015; Román & Trujillo, 2017b).

If feedback is the major driver of their diffuseness, it is very natural to expect an abundant population of diffuse galaxies far from cluster centers and even in the field, which we will discuss in § 3.5.4. Román & Trujillo (2017a) and Martínez-Delgado et al. (2016) found galaxies with large $r_{\rm eff}$ and low surface brightness even in under-dense regions, so cluster interactions are likely not an essential factor for their diffuseness, consistent with the scenario where feedback plays the

---

[13] The average Sersic indexes of our galaxies are 0.8 ± 0.4.

dominant role in shaping the UDGs.

Furthermore, for feedback-driven radial migration, old stars experienced more feedback episodes than young stars, so older stars will migrate outside and young stars remain near the center. We should therefore expect mixed or even inverted age gradients in UDGs (El-Badry et al., 2016), i.e. stars far from the center might be older than the stars at the center, which could be observed in the future.

3.5.3 Gas Removal and Quenching

In order to quench dwarf galaxies, their gas supply needs to be truncated and their ISM gas also needs to be largely removed (or consumed) in order to stop their star formation. But the exact mechanism of gas removal from UDGs is still an open question. Tidal stripping is one possible mechanism, but it tends to remove weakly bound stars near the edges and reduce the sizes of the galaxies, making them more compact rather than more diffuse (e.g. Read et al., 2006). Mowla et al. (2017) did not find any signature of tidal stripping out to 4 r_{eff} in the Coma UDGs. However, Venhola et al. (2017) found elongated and distorted shapes of the largest UDGs ($r_{\mathrm{eff}} > 3$kpc) in the Fornax cluster, which may indicate the effect of tidal stripping, but the total contribution is unclear. Simulating the interaction between a cluster and a high spin dwarf galaxy, Yozin & Bekki (2015) showed ram pressure stripping can efficiently remove the gas and quench the dwarf galaxy if it falls in at $z \sim 2$.

Our model does not specify the gas removal mechanism but assumes that feedback-expanded dwarfs have their gas reservoir removed along with the truncation of their gas supply (so called "strangulation") as they fall into clusters, enabling them to quench their star formation and turn into red UDGs. This can occur because hot cluster environment shuts down gas accretion in infalling satellite galaxies (e.g. Kereš et al. 2005, 2009b; Simha et al. 2009; van de Voort et al. 2017) while their gas reservoir can be either removed by ram pressure of hot gas or by a feedback episode shortly after infall. Exact nature of gas removal and prevention of further gas accretion will be explored in future work.

In both the major text and Appendix 3.B, we assume instant quenching, since we expect a short quenching time scale in the cluster environments. Yozin & Bekki (2015) showed the cluster can quench the dwarf galaxy within 2 Gyr with ram pressure stripping. Wetzel et al. (2015) and Fillingham et al. (2015) constrained the quenching times of similarly low-mass ($M_* \sim 10^8 \mathrm{M}_\odot$) LG satellites to be $\lesssim 3$ Gyr. Quenching in more massive clusters should occur even faster and more efficiently.

3.5.4 Implications for blue dwarf galaxies

Without accounting for quenching, none of our simulated galaxies end up as red UDGs at the present. However, even without quenching, at $z = 0$ three of our simulated galaxies with $M_* \sim 10^8 \mathrm{M}_\odot$ (**m10z, m11a, m11b**) have large effective radii, low surface brightnesses and $M_g > -16$ (as shown in Figure 3.4), i.e. they satisfy most of the UDG criteria. These diffuse galaxies are much bluer than the red UDGs in van Dokkum et al. (2015a) ($g - i < 0.7$). This implies that there should be a significant population of blue UDG-like dwarfs in the field and at the cluster outskirts with $\mu(g,0) > 23.5$ mag/arcsec^2 and $r_{\mathrm{eff}} > 1$ kpc. According to Figure 3.4, these blue UDGs have young stellar ages and are spheroidal (axis ratio ~ 0.6) and typically dispersion supported (as shown in El-Badry et al. 2018).

Indeed, there are ‘blue’ UDGs observed far from galaxy clusters or even in groups, e.g. Martínez-Delgado et al. (2016), Merritt et al. (2016), Román & Trujillo (2017b), Trujillo et al. (2017) and Shi et al. (2017). Pandya et al. (2018) studied one of the UDGs in the sample of Martínez-Delgado et al. (2016) and found younger stellar populations (~ 3 Gyr) and higher metallicity ($[\mathrm{Z}/\mathrm{Z}_\odot] \sim -0.6$) than UDGs in cluster environments (e.g. Gu et al. 2017).

A similar population of bluer UDGs was recently observed by Román & Trujillo (2017a) outside of the over dense region of the galaxy cluster Abell 168. Compared to UDGs near cluster centers, UDGs in lower density regions have similar effective radii and surface brightnesses, but

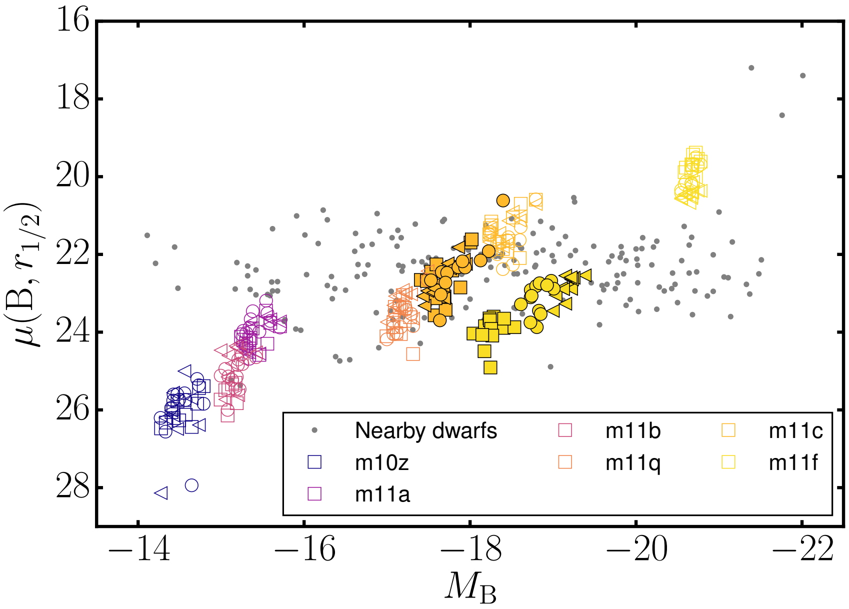

Figure 3.8: B-band surface brightness, $\mu(\mathrm{B}, r_{1/2})$, at a half light radius $r_{1/2}$ as a function of B-band absolute magnitude, M_B, of our simulated galaxies for a number of simulation output times in the redshift range $z \sim 0-0.1$, compared to nearby galaxies from Jansen et al. (2000). Empty symbols represent unattenuated values whereas solid symbols represent attenuated values. We show different lines of sight with different symbols, in the same manner as Figure 3.2.

higher luminosities, bluer colors, and slightly higher stellar masses. Based on these properties, Román & Trujillo (2017a) suggested that blue UDGs could be a low surface brightness extension of regular dwarf galaxies. These observations also showed that unlike other low redshift galaxies, the stellar mass distribution of UDGs peaks at $10^8\mathrm{M}_\odot$, coincident with the mass range of the most efficient dynamical effect of stellar feedback (e.g. Governato et al. 2012; Di Cintio et al. 2014; Chan et al. 2015; El-Badry et al. 2016; Tollet et al. 2016) and in a good agreement with our predictions for the properties of field UDGs. It is therefore clear that a large population of galaxies can remain diffuse in the field, owing to the effects of stellar feedback (also suggested in Di Cintio et al. 2017).

Galaxies that, without quenching, reach much higher stellar masses by $z = 0$ (e.g. **m11q**, **m11c** and **m11f**) are too bright to be included in van Dokkum et al. (2015a) sample. However one of them, **m11q**, is still relatively diffuse at $z = 0$ and could be an example of a more massive but more rare population of UDGs with $M_{\rm g} < -16$, $\mu(g,0) \sim 23-23.5$, $r_{\rm eff} \sim 1-5$ kpc and $g-i < 0.8$. Indeed, several observations, e.g. Mihos et al. (2015); Román & Trujillo (2017b), found brighter examples of UDGs.

Finally, all of our galaxies are simulated as field dwarfs in cosmological simulations without the influence of a cluster, so at $z = 0$ they should resemble field dwarf galaxies. El-Badry et al. (2016) showed that the effective radii of galaxies in FIRE simulations agree with those of the observed galaxies in NASA-Sloan Atlas (Blanton et al., 2011), resembling both the trend and scatter of the sample. In Figure 3.8 we compare properties of our simulated galaxies with the sample of nearby field dwarfs from Jansen et al. (2000). We consider our galaxies at $z \sim 0-0.1$ (to account for the star formation and feedback driven size variations) without passive aging, and, following the observations, measure their surface brightnesses $\mu({\rm B}, r_{1/2})$ at 2D half light radii $r_{1/2}$ in B-band.

Given that the observations are in B band, we calculate both the attenuated and unattenuated luminosities of star particles and estimate galactic luminosity, effective radii and surface brightness for both cases[14] and show results in Figure 3.8. For low-mass dwarfs, attenuated and unattenuated values are almost the same so we only show attenuated values for our higher mass dwarfs, $M_* \sim 10^9\,{\rm M}_\odot$, where differences are significant. The figure shows that our galaxies provide a reasonable match to the observed nearby field dwarfs, although simulated $M_* \sim 10^8{\rm M}_\odot$ dwarfs tend to be lower surface brightness than the dimmest dwarfs in the observed sample. We note that potential complex selection effects in the observed sample are not taken into account. Jansen et al. (2000) noted that the relative completeness at a given luminosity of their sample, especially at low surface brightness, is not well characterized, leaving out a potentially large population of low-surface brightness dwarfs such as the ones in our simulations. Much lower

---

[14] We assume the gas to dust ratio from Bouchet et al. (1985) scaled by metallicity, the SMC-like dust extinction curves from Pei (1992) and use the method from Hopkins et al. (2005) to calculate the dust attenuation of stellar light.

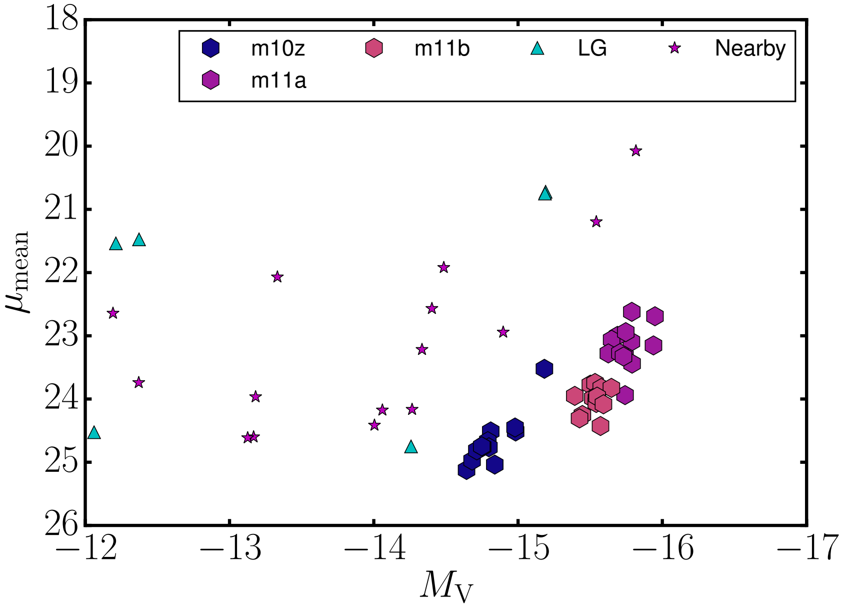

Figure 3.9: Mean V-band surface brightness within the effective radius, $\mu_{\rm mean}$, viewed along x direction as a function of V-band absolute magnitude $M_{\rm V}$ for three of our simulated galaxies at $z \sim 0-0.1$, compared to the LG and nearby galaxies from McConnachie (2012). The nearby galaxies are defined as isolated galaxies that do not belong to any major galaxy grouping but are still within 3 Mpc of the Sun.

surface brightness galaxies indeed exist in the under-dense environment near clusters (e.g. Román & Trujillo, 2017a).

In Figure 3.9, we compare simulated dwarf galaxies with observed dwarfs in the Local Group and nearby regions (McConnachie, 2012), who use different photometric bands and probe galaxies to lower magnitudes than the Jansen et al. (2000) sample. Following McConnachie (2012), we measure the mean surface brightness within the circular isophote defined by the half light radius. We do not consider passive aging and attenuation, and show the results at $z = 0-0.1$ to account for the occasional bursts of star formation. The figure shows three of our simulated galaxies whose absolute magnitude overlaps with McConnachie (2012) sample. Our galaxies resemble the trend of the higher mass end of the nearby dwarfs, although simulated galaxies have somewhat lower surface brightnesses. Field dwarfs are slightly higher surface brightness (i.e. more compact) than UDGs of the same absolute magnitude. At V-band magnitude $M_{\rm V} \sim -14.5$ to -15.5, most of the field dwarfs are diffuse with $r_{\rm eff} \gtrsim 1\,{\rm kpc}$ and have V-band effective surface brightnesses $<\mu_{\rm V}>_e \sim 21-23.5\,{\rm mag/arcsec^2}$, while our simulated dwarfs have $<\mu_{\rm V}>_e \sim 22.5-25\,{\rm mag/arcsec^2}$.

While our current sample is too small for a detailed statistical comparison, it does not produce any high-surface brightness analogues in the relevant mass range $M_* \sim 10^7-10^9{\rm M_\odot}$, which could indicate excessive expansion by feedback. We note, however, that the observational sample is limited by the small survey volume and multiple examples of isolated galaxies with much lower surface-brightness (typically by 2-3 ${\rm mag/arcsec^2}$) than the McConnachie (2012) sample exist (e.g. Dalcanton et al., 1997; Román & Trujillo, 2017b; Bellazzini et al., 2017) outside of LG. In the nearby universe, deep optical follow-ups of HI detected objects (already tested in e.g. Tollerud et al. 2015) or hostless transients due to novae or SNe (Conroy & Bullock, 2015), or a large CCD survey (e.g. Dalcanton et al., 1997) could be used to uncover an even larger number of blue UDGs.

Our results suggest that UDG-type surface brightness is the dominant outcome of galaxy formation in low-mass halos that host galaxies with stellar masses $\lesssim 10^8{\rm M_\odot}$ ($M_{\rm h} \lesssim 5\times10^{10}{\rm M_\odot}$), with a caveat that our simulated sample currently contains only a small number of galaxies. While our lower mass examples appear to have lower surface brightness than local observed dwarfs, we note that the full population of low redshift field galaxies has not yet been properly characterized at very low surface brightness, and that typical observed samples are biased toward high surface brightness. For example, Huang et al. (2012) found that about half of the HI selected dwarf galaxies in their survey, which have typically low surface brightness, do not have a counterpart in the SDSS spectroscopic survey, suggesting that current surveys miss a significant fraction of such objects. More careful analysis of these sources revealed that a large fraction of these galaxies have properties similar to blue UDGs (Leisman et al., 2017). Our simulated galaxies that remain diffuse at $z=0$ with $\mu(g,0) > 23.5\,{\rm mag/arsec^2}$, (**m10z**, **m11a** and **m11b**), are all gas rich with corresponding gas fractions, $f_{\text{gas}} = m_{\text{HI}}/(m_{\text{HI}} + m_*)$, of 0.57, 0.55 and 0.9, respectively and could represent such HI-rich UDGs.

Di Cintio et al. (2017) proposed a formation scenario for field UDGs very similar to ours: feedback-driven gas outflows affect stellar profiles in the central regions in the same way as DM core formation, and produce diffuse low surface brightness dwarf galaxies. They considered isolated galaxies in cosmological simulations in the Numerical Investigation of a Hundred Astrophysical Objects (NIHAO) project (Wang et al., 2015), showing that their dwarf galaxies with $M_{\text{h}} \sim 10^{10-11}\text{M}_{\odot}$ at $z = 0$ can match the surface brightness of observed UDGs, similar to our finding for the field UDG population, despite differences in stellar feedback models and hydrodynamical methods[15].

Given the burstiness of star formation and resulting outflows in FIRE simulations of dwarf galaxies (Muratov et al., 2015), our simulations make specific predictions for blue UDGs formed by stellar feedback. They should have: (a) a range of sizes at fixed stellar mass depending on where they are in their burst cycles, (b) mixed or even inverted age and metallicity gradients (El-Badry et al., 2016), and (c) sizes and velocity dispersions that correlate with their recent star formation history (El-Badry et al., 2017).

3.6 Conclusions

We study the origin of UDGs using FIRE-2 cosmological simulations of field dwarf galaxies with halo masses $M_{\text{h}}(z = 0) \sim 10^{10-11}\text{M}_{\odot}$. Our earlier work with the FIRE simulations (El-Badry et al., 2016; Chan et al., 2015) showed that in this halo mass range, stellar feedback and associated changes in the gravitational potential are the most effective in dispersing both DM and stellar populations in the inner halo. In addition, newly-formed stars can inherit the velocity of

---

[15] While Di Cintio et al. (2017) only studied blue field UDGs with simulated isolated or central galaxies fully evolved to $z = 0$, we also account for the effects of quenching, which enables us to more directly address the formation mechanism of red UDGs, commonly observed in clusters.

the star forming gas cloud pushed by an outflow episode and further expand the stellar population. Here we show that these mechanisms lead to a diffuse quasi-spherical stellar distribution with surface brightness and overall properties comparable to observed UDGs.

We then assume that star formation and growth of progenitors of UDGs stop (i.e. galaxies "quench") during infall into a cluster of galaxies as a combination of tidal and gas stripping processes prevents fresh gas supply and removes the existing gas. To mimic this quenching, we artificially stop star formations of UDG progenitors at a cosmic time t_q and passively evolve their stars to $z \sim 0$ according to a stellar population synthesis model (FSPS; Conroy et al. 2009). Finally we generate synthetic images and use GALFIT (Peng et al., 2002) to estimate their central surface brightness and effective radii. Our main findings are summarized below:

•All of our simulated galaxies with $M_{*} \sim 10^{7} - 10^{8}\,\mathrm{M}_{\odot}$ are diffuse and spatially extended ($\mu(g) \gtrsim 23.5\,\mathrm{mag/arcsec^{2}}$ and $r_\mathrm{eff} \gtrsim 1.25\,\mathrm{kpc}$). These galaxies are typically hosted in halos with $M_\mathrm{h} \sim 3 \times 10^{10} - 1 \times 10^{11}\,\mathrm{M}_{\odot}$ at their quenching times.

•The dynamical effects of stellar feedback produce UDGs even without taking into account cluster influence. Gas removal can help to further expand the galaxies, as shown in Appendix 3.B but this effect is likely of secondary importance.

•DM halos of our simulated galaxies have a typical distribution of spin parameters, suggesting that formation of UDGs does not require high spin halos.

•Red UDGs require quenching of star formation. Our simulations indicate that typical UDGs are dwarf galaxies quenched over a wide range of times ($t_\mathrm{q} > 3$ Gyr). Simulated analogs of observed red UDGs that form in halos $M_\mathrm{h} \sim 2 \times 10^{10} - 1 \times 10^{11}\mathrm{M}_{\odot}$ halos can be quenched over a broad time interval $t_\mathrm{q} \sim 5 - 11$ Gyr, i.e. redshift range $z \sim 0.3 - 2$.

•The most massive red UDGs ($M_{\star} \gtrsim 2 \times 10^{8}\mathrm{M}_{\odot}$) in our simulations require earliest quenching. Our higher mass halos can host red UDGs if their star formation and growth is quenched at very early times, $t_\mathrm{q} \sim 3 - 5$ Gyr, i.e. at $z_\mathrm{q} \sim 2 - 3$. At the time of quenching, the host halo mass of our most massive simulated UDG, similar to e.g. Dragonfly 44, is around $10^{11}\mathrm{M}_{\odot}$.

•Colors of red UDGs are approximately independent of quenching time as galaxies quenched later (i.e. with a younger stellar population) typically have higher metallicity. This prevents an accurate estimation of quenching time from $g-i$ color.

•Galaxies with $M_* \lesssim 10^8 \mathrm{M}_\odot$ remain diffuse even at $z=0$ but have relatively blue colors. We predict that diffuse galaxies with bluer colors ($g-i<0.8$) are prevalent in the field. Our galaxies at $z=0$ match the magnitude-surface brightness relations of some samples of nearby galaxies, but have lower surface brightness than the LG sample from McConnachie (2012). While our sample is small and statistics are limited, this raises an interesting prospect that there is a large number of undiscovered low surface brightness galaxies in the Universe.

•Given the UDG formation process in our simulations, the size and velocity dispersion of 'blue' UDGs at a fixed mass should correlate with their recent star formation history.

•Our galaxies are not hosted in over-massive halos ($M_*/M_\mathrm{h} \lesssim 10^{-4}$) at quenching, but instead have a stellar-to-halo mass ratios similar to observed dwarfs, $M_*/M_\mathrm{h} \sim 10^{-3}$.

•The enclosed masses of our simulated galaxies can match the measured masses of observed UDGs in clusters, if we assume that the growth of their central enclosed mass stopped when they were quenched. Even if such halos had evolved in isolation outside of clusters, we showed that in most cases their enclosed DM mass on these scales would remain unchanged, owing to halo growth largely by "pseudoevolution". Owing to a broad range of formation times of these objects, inferred halo masses at z=0 can therefore lead to misleading conclusions about their host halo masses. This is especially important for the most massive UDGs whose dense central regions formed at very early times.

3.7 ACKNOWLEDGEMETS

We thank Aaron Romanowsky, Arianna Di Cintio, Timothy Carleton, and Viraj Pandya for helpful discussions. TKC was supported by NSF grant AST-1412153. DK was supported by

NSF grants AST-1412153 and AST-1715101 and the Cottrell Scholar Award from the Research Corporation for Science Advancement. AW was supported by a Caltech-Carnegie Fellowship, in part through the Moore Center for Theoretical Cosmology and Physics at Caltech, and by NASA through grants HST-GO-14734 and HST-AR-15057 from STScI. Support for PFH was provided by an Alfred P. Sloan Research Fellowship, NASA ATP Grant NNX14AH35G, and NSF Collaborative Research Grant #1411920 and CAREER grant #1455342. CAFG was supported by NSF through grants AST-1412836, AST-1517491, AST-1715216, and CAREER award AST-1652522, and by NASA through grant NNX15AB22G. KE was supported by a Berkeley graduate fellowship, a Hellman award for graduate study, and an NSF graduate research fellowship. Support for SGK was provided by NASA through Einstein Postdoctoral Fellowship grant number PF5-160136 awarded by the Chandra X-ray Center, which is operated by the Smithsonian Astrophysical Observatory for NASA under contract NAS8-03060. MBK acknowledges support from NSF grant AST-1517226 and from NASA grants NNX17AG29G and HST-AR-13888, HST-AR-13896, and HST-AR-14282 from the Space Telescope Science Institute, which is operated by AURA, Inc., under NASA contract NAS5-26555. The simulation presented here used computational resources granted by the Extreme Science and Engineering Discovery Environment (XSEDE), which is supported by National Science Foundation grant no. OCI-1053575, specifically allocation TG-AST120025.

3.A GALFIT with sky background

Realistic galaxy image contains sky background in addition to galactic light, so a sky subtraction is required. A proper subtraction is not trivial for galaxies with surface brightnesses comparable to the background, e.g. UDGs. To gauge the potential impact of sky background on the estimated properties of UDGs, we generate simulated galaxy images along with stochastic sky backgrounds whose average surface brightness is $\sim 26\,\mathrm{mag}/\mathrm{arcsec}^2$. Then we estimate their central surface brightness and effective radius with a two-component fit, assuming Sersic profiles for galaxies and tilted flat planes for sky backgrounds. Figure 3.10 shows that the differences in central surface brightness and effective radius with and without sky backgrounds are small, even when the sky is, on average, brighter than the galaxy, illustrating the robustness of the fitting. The fitted r_{eff} differs from Figure 3.4 because here we use g-band instead of $g + i$ images.

3.B Dynamical effect of Gas Removal

Most of the observed red UDGs are detected in galaxy clusters and were probably quenched through interactions with the host cluster. They do not show signatures of tidal interaction (Mowla et al., 2017) but it is possible that their gas was removed by ram pressure stripping. To simulate the effect of gas removal on a dwarf galaxy, we test a simple toy model introduced in El-Badry et al. (2017): all gas particles instantaneously receive 1000 km/s velocity boosts at a given infall/stripping time. Then we evolve the galaxy to $z = 0$ (by continuing the run in a fully cosmological environment) and estimate its properties with GALFIT as described in the main text.

Since the gas velocity after the kick is much higher than the escape velocity, all of the gas is quickly removed and the galaxy is quenched after around 100Myr. El-Badry et al. (2016) tested this method and concluded that the effect is almost identical to instantaneously taking out all of the gas particles. Fast moving particles also affect the surrounding gas so the galaxy can never accrete new gas and gets quenched. While in our default approach we only passively quench star formation and do not allow star particles to move after quenching, here they can freely move and adapt to a new and shallower gravitational potential.

Figure 3.11 shows that the effect of gas removal is small, since dynamical relaxation after gas stripping induces only a slight increase in size and a slight drop in central surface brightness, while there is no clear systematic effect on the axis ratio. The additional dynamical effects of gas

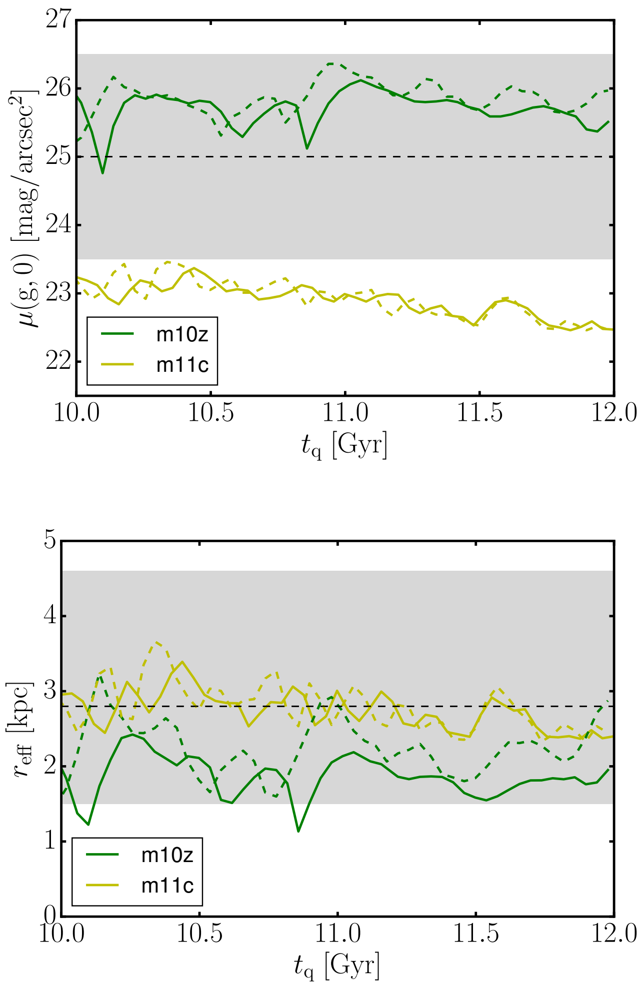

Figure 3.10: Time evolution of central g-band surface brightnesses $\mu(g,0)$ and effective radii of two of our simulated galaxies with a sky background (dashed) and without (solid) in their g-band images. The sky background is a random noise with the averaged surface brightness around 26 mag/arcsec^2. $\mu(g,0)$ is obtained with GALFIT. Sky background and galaxy are fitted simultaneously. Stars are passively aged to $z=0$ and dust attenuation is not considered. Including a typical sky background has only a small effect on the estimated values.

stripping (compared to the fiducial model) therefore only help making our simulated galaxies slightly more diffuse in the relevant mass range. These results also show that galaxy sizes do not evolve much after ram pressure stripping and remain largely "frozen" in time motivating our approach of passively evolving galaxies after the quenching time. Overall both galaxies stay within or outside of the observational range of UDGs even when gas stripping is applied.

Relatively weak effect of gas removal is not entirely surprising given that galaxies are already largely spheroidal and dark matter dominated. While the gas dominates baryonic component, its gravitational influence is much weaker than that from the dark matter. This is illustrated in Figure 3.12 where we show the enclosed mass profiles for stars, gas and dark matter in the inner halo for the two galaxies for which we apply quenching. Profiles are shown at characteristic times for which passively evolved counterparts correspond to the observed red UDGs. Dark matter dominates at all radii.

3.C Effect of resolution

To evaluate the effect of resolution, we compare two of our galaxies, **m10z** and **m11c**, with their higher resolution versions, presented in Hopkins et al. (2018b) (these have particle masses $m_{gas} = 260\mathrm{M}_{\odot}$ and $m_{gas} = 2.1 \times 10^{3}\mathrm{M}_{\odot}$, respectively). The high resolution versions have particle masses eight times smaller and softening lengths twice shorter than those shown in Table 3.1. While their halo masses do not change with resolution, their stellar masses at $z = 0$ drop by 40% and 60% in **m10z** and **m11c** respectively.

Figure 3.13 shows the difference in central surface brightness, effective radius and g-band magnitude between two resolutions. The sizes of the galaxies are not sensitive to resolution, but their g-band magnitudes decrease by ~ 1, as expected from their smaller stellar masses. Their surface brightness also drops accordingly. These changes are consistent with what we expect from stellar mass difference between lower and higher resolution galaxies. We therefore conclude

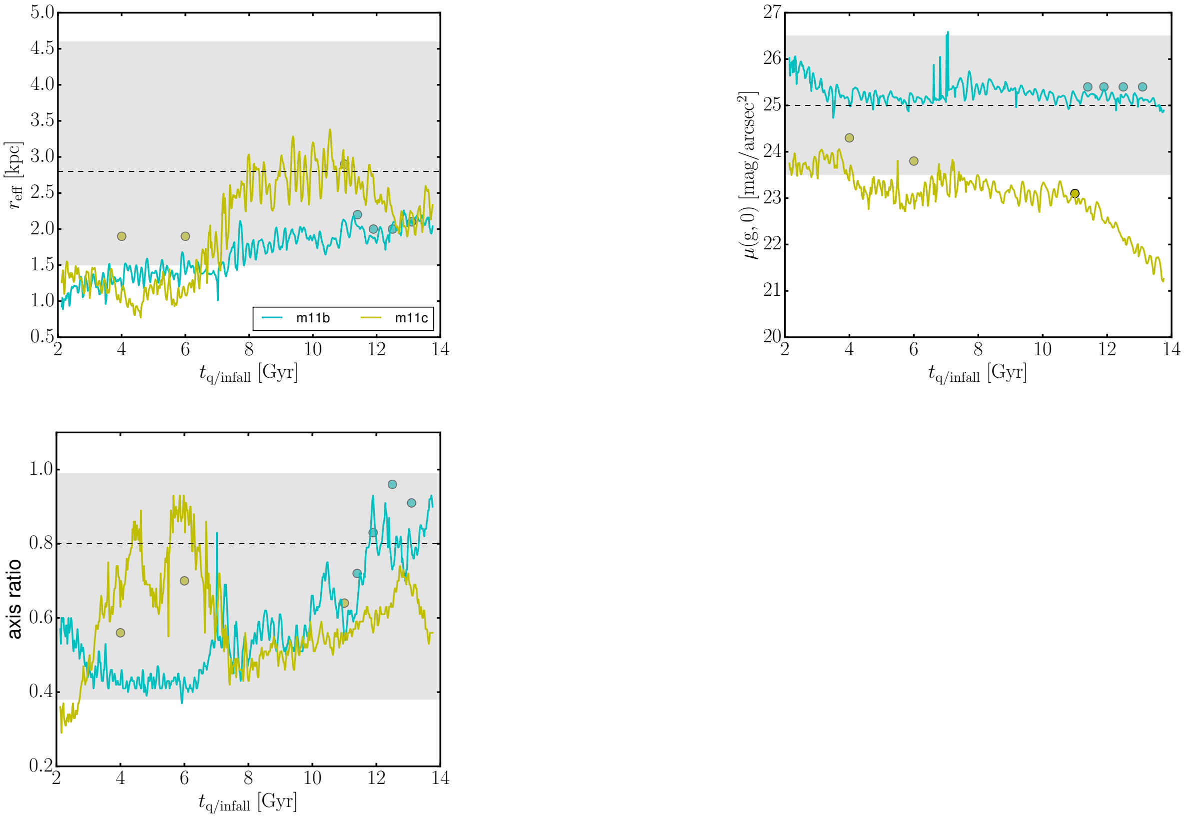

Figure 3.11: Evolution of the effective radius, central surface brightness and axis ratio for two of our simulated galaxies. Lines show values from passive evolution scenario described in the main text, whereas points show values from gas-stripped **m11b** and **m11c** dynamically evolved to $z = 0$. Lines are functions of quenching time t_q, while individual points indicate several different times for which we apply our ram pressure approximation, mimicking the effect of hot cluster gas during the infall. Galaxies are typically quenched shortly ($\sim$ 100Myr) after gas stripping.

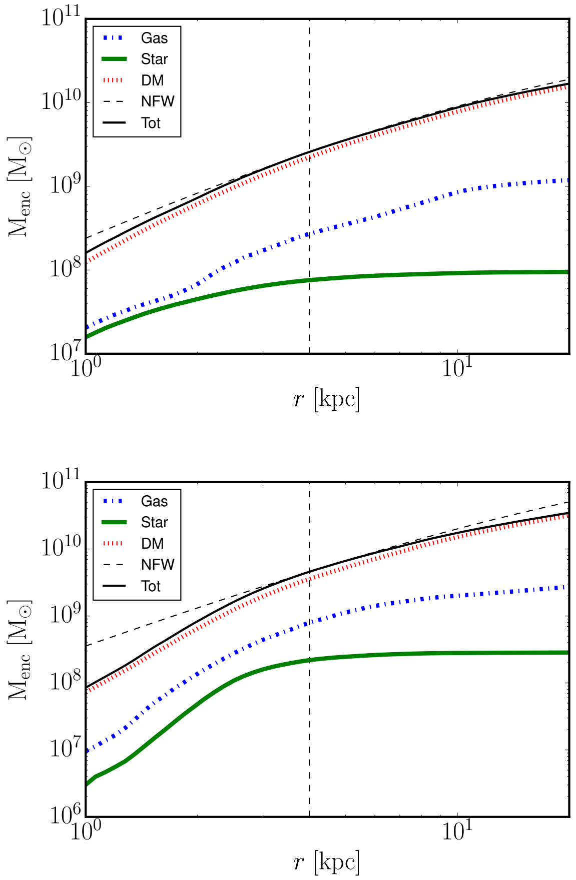

Figure 3.12: Cumulative gas (blue;dash-dotted), star (green;solid), DM (red;dotted) and total (black;solid) mass profiles of **m11b** at t=11 Gyr (Upper) and **m11c** at t=5 Gyr. Dashed vertical lines show the effective radii and black dashed curved lines show the NFW profiles whose enclosed masses within the effective radii match our halos. DM dominates enclosed mass throughout the halo for both galaxies.

that while resolution can affect the stellar masses of our simulated galaxies, the surface brightness and size at a given stellar mass are largely not affected by resolution.

3.D GALFIT modeling with different resolution images

Stellar particles in simulated galaxies have well determined positions and represent a population of stars with "radii" (i.e. gravitational softening) that is typically much finer than typical resolution from observations. To mimic a range of point spread functions (PSF) of different telescopes and a range of distances at which one observes UDGs, we vary the pixel size of our GALFIT images (i.e. the resolution of the 2-D projection of stellar properties) of our **m11b** galaxy from 40 pc to 400 pc, and show results in Figure 3.14. This approximately spans the range of PSF between the Hubble Space Telescope and the Canada-France-Hawaii Telescope (CFHT) at the distance of the Coma cluster (i.e. 0.08 to 0.8 arcsec for the assumed distance of 100 Mpc). For the tested range, there is a small systematic increase in effective radii and a slight decrease in surface brightness in low resolution images, but the change is smaller than the short term time variations of these properties.

Chapter 3, in full, is a reformatted reprint of the material as it appears in *Monthly Notices of the Royal Astronoical Society*, Chan, Tsang Keung; Kereš, Dušan; Wetzel, Andrew; Hopkins, Philip F.; Faucher-Giguère, Claude-André; El-Badry, Kareem; Garrison-Kimmel, Shea; Boylan-Kolchin, Michael, Volume 478, Issue 1, July 2018, Pages 906-925. The dissertation author was the primary investigator and author of this paper.

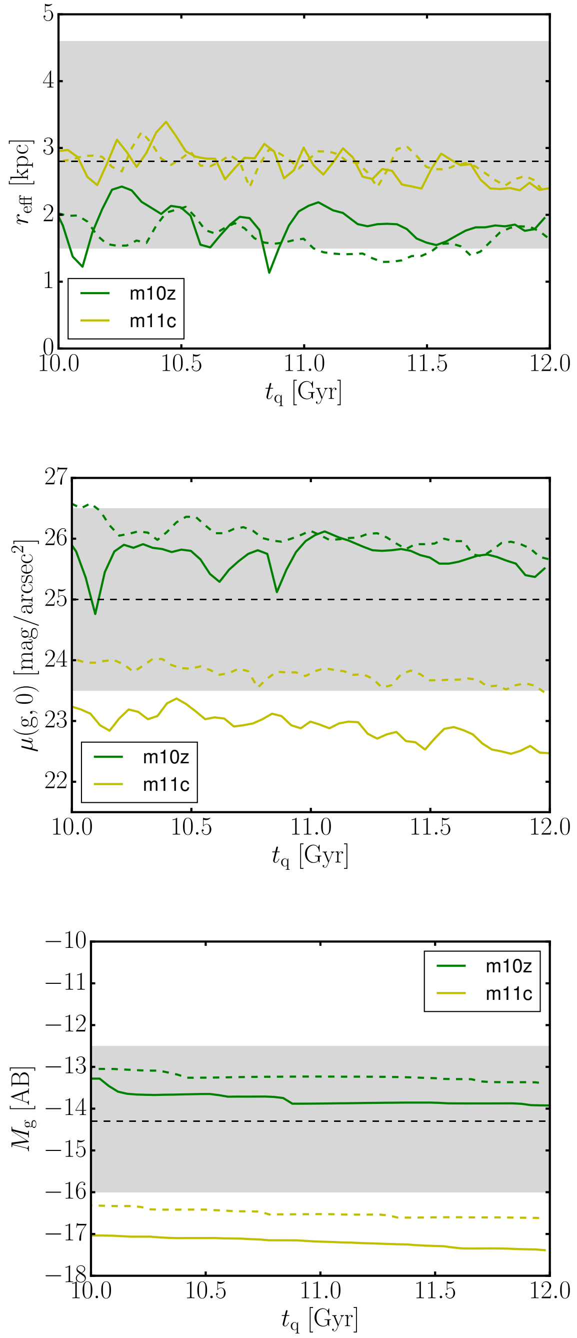

Figure 3.13: Time evolution of central g-band surface brightness $\mu(g,0)$ and effective radius for the two simulated galaxies with a higher resolution (dashed) and with the fiducial resolution (solid). Values are obtained from g-band images using GALFIT.

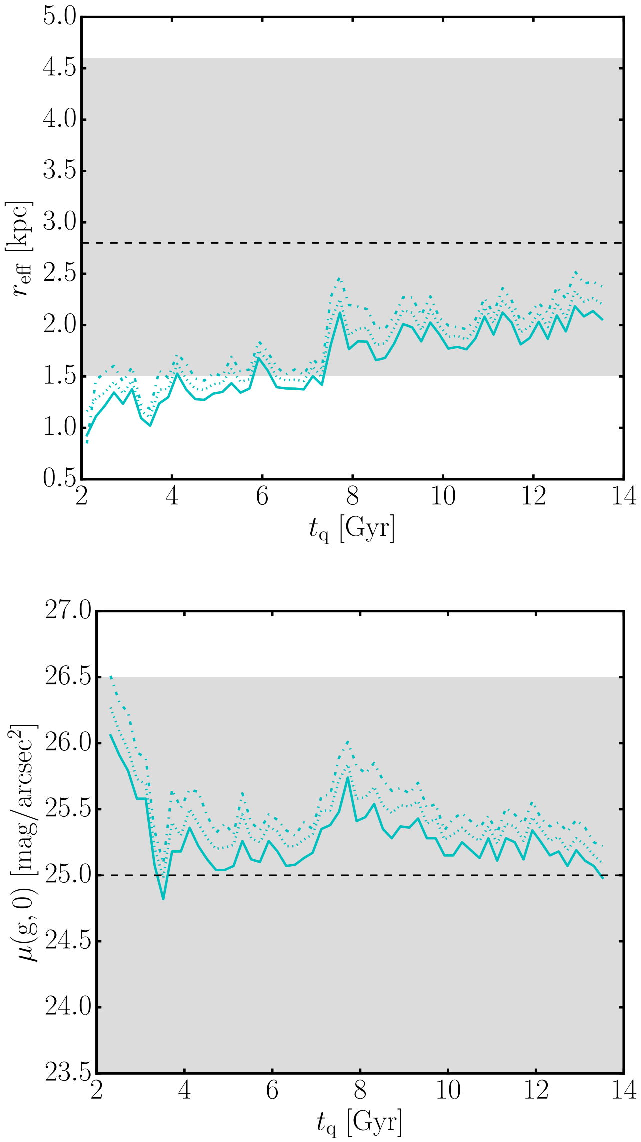

Figure 3.14: Time evolutions of the effective radius and surface brightness of **m11b** as calculated by GALFIT from 40 kpc x 40 kpc g band images with uniform-size pixels each with 400 pc (dashdot), 200 pc (dot) and 40 pc (solid) on a side (i.e. 100x100, 500x500 and 1000x1000 pixels).

Chapter 4

Cosmic ray feedback in the FIRE simulations: constraining cosmic ray propagation with GeV gamma ray emission

4.1 abstract

We present the implementation and the first results of cosmic ray (CR) feedback in the Feedback In Realistic Environments (FIRE) simulations. We investigate CR feedback in non-cosmological simulations of dwarf, sub-$L\star$ starburst, and $L\star$ galaxies with different propagation models, including advection, isotropic and anisotropic diffusion, and streaming along field lines with different transport coefficients. We simulate CR diffusion and streaming simultaneously in galaxies with high resolution, using a two moment method. We forward-model and compare to observations of γ-ray emission from nearby and starburst galaxies. We reproduce the γ-ray observations of dwarf and $L\star$ galaxies with constant isotropic diffusion coefficient $\kappa \sim$

$3\times10^{29}\,\mathrm{cm^2\,s^{-1}}$. Advection-only and streaming-only models produce order-of-magnitude too large γ-ray luminosities in dwarf and $L\star$ galaxies. We show that in models that match the γ-ray observations, most CRs escape low-gas-density galaxies (e.g. dwarfs) before significant collisional losses, while starburst galaxies are CR proton calorimeters. While adiabatic losses can be significant, they occur only after CRs escape galaxies, so they are only of secondary importance for γ-ray emissivities. Models where CRs are "trapped" in the star-forming disk have lower star formation efficiency, but these models are ruled out by γ-ray observations. For models with constant κ that match the γ-ray observations, CRs form extended halos with scale heights of several kpc to several tens of kpc.

4.2 Introduction

Cosmic rays (CRs) are charged particles moving with relativistic speeds, mainly generated through shock acceleration of supernova remnants (SNRs) (Bell, 2004) (and possibly also in active galactic nuclei in massive galaxies). Unlike thermal energy, they can propagate through the galactic interstellar medium (ISM) rapidly via advection, diffusion and streaming (Strong et al., 2007; Zweibel, 2013; Grenier et al., 2015), and transfer energy to gas via Coulombic and hadronic interactions (Mannheim & Schlickeiser, 1994; Enßlin et al., 2007; Guo & Oh, 2008). Their energy density is comparable to thermal and magnetic energies in the solar neighborhood (Ginzburg & Ptuskin, 1985; Boulares & Cox, 1990), so CRs are believed to be dynamically important in galaxy evolution.

The impacts of CRs on galaxy evolution have been studied with analytic models (Ipavich, 1975; Breitschwerdt et al., 1991, 1993; Zirakashvili et al., 1996; Socrates et al., 2008; Everett et al., 2008; Dorfi & Breitschwerdt, 2012; Mao & Ostriker, 2018) and idealized and cosmological simulations (e.g. Jubelgas et al. 2008; Uhlig et al. 2012; Booth et al. 2013; Wiener et al. 2013; Hanasz et al. 2013; Salem & Bryan 2014; Salem et al. 2014; Chen et al. 2016; Simpson et al. 2016;

Girichidis et al. 2016; Pakmor et al. 2016; Salem et al. 2016; Wiener et al. 2017; Ruszkowski et al. 2017; Butsky & Quinn 2018; Farber et al. 2018; Jacob et al. 2018; Girichidis et al. 2018). These studies show CRs can drive multiphase winds, reduce star formation rates in low mass galaxies, thicken gaseous disks, and modify the phase structure of the circum-galactic medium (CGM). It has also been suggested that CRs may play an important role in the galactic dynamo (Parker, 1992; Hanasz et al., 2009; Kulpa-Dybeł et al., 2011, 2015).

Despite its importance, the details of CR propagation are uncertain. The most popular CR propagation models are self confinement and extrinsic turbulence (Zweibel 2013, and reference herein). In the former picture, CRs interact with a series of Alfven waves, which results in random scattering in pitch angles. The waves are then amplified via the streaming instability of CRs, increasing the scattering and trapping CRs in a background medium. These "self confinement" interactions effectively transfer energy from the CRs to thermal plasma. In the extrinsic turbulence model, CRs propagate through random magnetic field lines and are scattered by the background turbulent magnetic fields. This mechanism is especially important for high energy CRs, since there are too few high energy CRs amplifying the Alfven waves and the self-confinement mechanism fails (Zweibel, 2013). These two mechanisms confine and isotropise the CR distribution explaining the remarkably low CR anisotropy observed from the Earth (see, e.g. Hillas & Ouldridge 1975) and the long residence time ($> 10^7$ yr) inferred from the ratios between stable primary and secondary nuclei (Strong et al., 2007). Their long confinement time and small anisotropy imply that CRs have short mean free paths ($\sim$ pc) and their propagation can therefore be approximated by a random walk, so CRs can be well described as a diffusive fluid, obeying an advection diffusion equation (see, e.g. Zweibel 2017, for arguments for the CR fluid theory).

Most of the studies of CR propagation have focused on an approximate picture of the Milky Way described by the flat halo diffusion model (Ginzburg & Ptuskin, 1976). This model consists of a cylindrical gaseous halo with a radius around 20 kpc and a height larger than 1 kpc, and a thinner yet more dense cylindrical internal disk with CR sources. CRs are assumed to diffuse isotropically (averaged over the scale of hundreds of pc) with a spatially constant but energy dependent diffusion coefficient, and "escape" through the halo boundaries to intergalactic space. Extensions of this model are commonly used in numerical CR propagation codes, e.g. GALPROP[1], which attempt to synthesize observational constraints on the MW gas density distribution, CR abundances and spectra, γ-ray and radio emission, and theoretical models for e.g. galactic winds and diffusive re-acceleration (Strong & Moskalenko, 1998, 2001). These models are commonly used to constrain the "effective" isotropic-equivalent diffusion coefficient of CRs averaged over the whole MW disk (e.g. Strong et al., 2007; Trotta et al., 2011). However, there are still large uncertainties in the role of gas dynamics and small-scale gas density fluctuations ("clumpiness"), magnetic field geometries on small scales, the spatial and temporal distribution of CR sources, the size and mass distribution of the gaseous galactic halo, and the CR propagation model. To make progress, self-consistent modeling of galaxy evolution that includes CR propagation together with hydrodynamics or magneto-hydrodynamics is required.

In addition to the CR energy density and abundance of nuclei, high energy γ-ray emission can serve as an independent constraint on CR propagation (Ackermann et al., 2012b; Strong et al., 2000, 2004). High energy ($>$ GeV) CRs collide with nuclei in the interstellar medium (ISM) and produce pions, which decay into GeV γ-rays. Since pionic γ-ray luminosity is proportional to CR density and most of the energy density of the CRs is at energies around GeV (from the direct CR observations, e.g. in AMS Collaboration et al. 2002), CR distribution and propagation can be constrained with high energy γ-ray observations.

Recently, γ-ray emission was observed from Local Group (Abdo et al., 2010d,c,b) and starburst galaxies (Acero et al., 2009; VERITAS Collaboration et al., 2009; Abdo et al., 2010a; H. E. S. S. Collaboration et al., 2018), which can be used as a probe of CRs beyond the solar system and the Milky Way (MW). Abdo et al. (2010c) found a correlation between γ-ray emission

---

[1] `https://galprop.stanford.edu/`

and star formation rate (SFR) with a steeper than linear drop at low SFRs ($E_\gamma \propto \mathrm{SFR}^{1.4\pm0.3}$; summarized in Ackermann et al. 2012a).

To explain this correlation, Lacki et al. (2011) (hereafter L11) constructed one-zone leaky box model of galaxies where a fixed fraction of SN energy is injected as CRs. They assume CRs escape with an energy dependent escape time and that the CR energy density and spectral distribution are in a steady state (the injections and losses are balanced). Constrained with the observed CR abundances and the far infrared (FIR)-radio correlation (Lacki et al., 2010), the model was used to estimate pionic γ-ray luminosities of galaxies. They found that in order to explain the correlation between γ-ray emission and SFR, in starburst galaxies, most CR protons are required to lose their energy via collisions with the ISM (i.e. that starbursts are "CR proton calorimeters", as in the earlier calculations of Thompson et al. 2007; see also Abramowski et al. 2012; Yoast-Hull et al. 2013; Wang & Fields 2018), while in dwarf galaxies, most of CR protons should escape. The main drivers of this effect are that SFR drops with decreasing gas surface density (Kennicutt, 1998), and that lower gas densities enable CRs to escape before heavy pionic losses. Subsequent observational studies have reached the same conclusion regarding efficient escape in galaxies like the MW, Andromeda (M31), the Large and Small Magellanic Clouds (LMC, SMC; see, e.g. Lopez et al. 2018).

In this study, we investigate the impact of CRs on dwarf, sub-$L\star$ starburst, and $L_\star$ galaxies, using idealized simulations of galaxy evolution. We run galaxy simulations with both CR diffusion and streaming with high spatial resolution and diffusivity thanks to the newly developed two-moment method (similar to Jiang & Oh, 2018). We also couple explicit CR transport and losses to an explicit, local stellar feedback model which time-resolves *individual* SNe explosions, as well as stellar mass-loss and radiative feedback, which together enable self-consistent generation of galactic winds and a turbulent, multi-phase ISM, critical for understanding CR transport and emission in that same ISM. Specifically, our CR implementation in the code GIZMO is coupled to the FIRE-2 (Feedback In Realistic Environments 2) algorithm for star formation and stellar feedback (Hopkins et al., 2018b,c).[2] Cosmological simulations with these physics (without explicit CR transport) have been shown to successfully reproduce many observed galaxy properties including stellar masses (Hopkins et al., 2018b), galactic winds (Muratov et al., 2015; Anglés-Alcázar et al., 2017; Hafen et al., 2019), cored central dark matter profiles (Oñorbe et al., 2015; Chan et al., 2015; Wetzel et al., 2016; Fitts et al., 2017), the mass-metallicity relation (Ma et al., 2016) and spatial distribution of gas and metals within galaxies and the CGM (Faucher-Giguère et al., 2015a, 2016; Ma et al., 2017; Muratov et al., 2017; Hafen et al., 2017), typical galaxy star formation rates and histories (Sparre et al., 2017), the Kennicutt-Schmidt law (Orr et al., 2018), and galactic magnetic field structure (Su et al., 2018).

In this, the first paper in a series, we introduce our implementation of the CR propagation model (including isotropic and anisotropic diffusion and streaming), simulate galaxies with several CR propagation models, and focus on constraining the model using the observations of $\sim$GeV γ-ray emission from galaxies (and compare our findings with previous theoretical studies). § 4.3 and § 4.4 discuss numerical methods, simulated physics, and initial conditions. In § 4.5.1, we investigate how CRs and their propagation influence galactic properties. In § 4.5.2 we calculate the γ-ray emission from CRs in our simulations and compare with observational data. In § 4.6, we compare our findings with the previous studies and analyze the relative importances of different CR energy gain and loss processes. We summarize our findings in § 4.7.

4.3 Method

4.3.1 Simulation code

All the physics and numerical details in this study, except for CRs, follow the FIRE-2 version of the FIRE algorithms presented in detail in Hopkins et al. (2018b), so we only briefly

---

[2] `http://fire.northwestern.edu/`

review them here. Our simulations use the GIZMO[3] code (Hopkins, 2015a) in its mesh-free Lagrangian finite mass (MFM) mode for (magneto)-hydrodynamics; extensive implementation details and tests of the MHD scheme are presented in Hopkins (2016); Hopkins & Raives (2016). GIZMO uses an updated version of the PM+Tree algorithm from Gadget-3 (Springel, 2005) to calculate gravity and adopts fully conservative adaptive gravitational softening for gas (Price & Monaghan, 2007). Gas cooling is calculated with tabulated cooling rates from $T = 10 - 10^{10}$ K, including atomic, metal-line, and molecular cooling. While our simulations are idealized and do not include cosmological environments, we do include the present-day ultraviolet background, from the Faucher-Giguère et al. (2009) model (accounting for local self-shielding). Stars form in locally self-gravitating, self-shielding, thermally Jeans-unstable gas[4] at densities $n_{\rm H} \geq 100\,{\rm cm}^{-3}$. Once formed, we calculate the energy, momentum, mass and metal return for each star according to the STARBURST99 stellar population synthesis model (Leitherer et al., 1999), for a Kroupa (2002) IMF, accounting for SNe Types Ia & II, O/B and AGB star mass-loss, and radiation (photo-electric and photo-ionization heating and radiation pressure with a five-band approximate radiation-hydrodynamics treatment). For details see Hopkins et al. (2018b,c,a).

4.3.2 Cosmic Rays

The implementation of CR physics in GIZMO includes fully-anisotropic cosmic ray transport with streaming and advection/diffusion, CR cooling (hadronic and Compton, adiabatic, and streaming losses), injection in SNe shocks, and CR-gas coupling. The CRs are treated as an ultra-relativistic fluid (adiabatic index $\gamma_{\rm cr} = 4/3$) in a “single bin” approximation.[5] Integrating over the CR distribution function and spectrum, the usual ideal-MHD equations solved for gas density ρ, velocity $\mathbf{v}$, magnetic field $\mathbf{B}$, and specific energy e, are extended with the equation for

---

[3] `http://www.tapir.caltech.edu/~phopkins/Site/GIZMO`

[4] We assume the strong coupling limit between gas and CRs, so the effective sound speed in the virial parameter includes both thermal and CR pressure. See Appendix C in Hopkins et al. 2018b.

[5] One can think of this as evolving only the CR energy density at the energies $\gtrsim$ GeV, which dominate the CR pressure, and approximating the CR energy spectrum as having a universal shape at all positions.

the CR energy density $e_{\rm cr}$ (McKenzie & Voelk, 1982):

$$\begin{aligned}
&\frac{\partial\rho}{\partial t}+\nabla\cdot(\rho\mathbf{v})=0,\\
&\frac{\partial\rho\mathbf{v}}{\partial t}+\nabla\cdot(\rho\mathbf{v}\otimes\mathbf{v}+P_T\mathbb{I}-\mathbf{B}\otimes\mathbf{B})=0,\\
&\frac{\partial\rho e}{\partial t}+\nabla\cdot[(\rho e+P_T)\mathbf{v}-(\mathbf{v}\cdot\mathbf{B})\mathbf{B}]\\
&\qquad=P_{\rm cr}\nabla\cdot\mathbf{v}+\Gamma_{\rm st}+S_{\rm g}-\Gamma_{\rm g},\\
&\frac{\partial\mathbf{B}}{\partial t}+\nabla\cdot(\mathbf{v}\otimes\mathbf{B}-\mathbf{B}\otimes\mathbf{v})=0,\\
&\frac{\partial e_{\rm cr}}{\partial t}+\nabla\cdot\mathbf{F}_{\rm cr}=\mathbf{v}\cdot\nabla P_{\rm cr}-\Gamma_{\rm st}+S_{\rm cr}-\Gamma_{\rm cr},
\end{aligned}\tag{4.1}$$

where $P_{\rm cr}=(\gamma_{\rm cr}-1)\,e_{\rm cr}$ is the CR pressure; P_T is the total (thermal+magnetic+CR) pressure; $\Gamma_{\rm st}=-\mathbf{v}_{\rm st}\cdot\nabla P_{\rm cr}$ is the CR "streaming loss term" discussed below; $S_{\rm g}$ and $S_{\rm cr}$ are gas and CR source terms (e.g. injection); $\Gamma_{\rm g}$ and $\Gamma_{\rm cr}$ are gas and CR sink/loss (or "cooling") terms; and $\mathbf{v}_{\rm st}$ is the CR streaming velocity. $\mathbf{F}_{\rm cr}$ is the CR energy flux, which can be written $\mathbf{F}_{\rm cr}=(e_{\rm cr}+P_{\rm cr})(\mathbf{v}+\mathbf{v}_{\rm st})+\mathbf{F}_{\rm di}$ where the first term represents advection and streaming, whereas the second term is a diffusive-like flux (e.g. given by $\mathbf{F}_{\rm di}=-\kappa\hat{\mathbf{B}}\otimes\hat{\mathbf{B}}\cdot\nabla e_{\rm cr}$ in the "pure diffusion" or "zeroth moment" approximation, but we explicitly evolve this; see §4.3.5).

For the gas equations-of-motion, note when solving the Riemann problem between neighboring fluid elements, P_T includes the CR pressure (i.e. we make the local strong-coupling approximation: CRs and gas strongly interact), and the effective sound speed of the two-fluid mixture is modified to $(c_s^2)_{\rm eff}=\partial P/\partial\rho=(c_s^2)_{\rm gas}+\gamma_{\rm cr}P_{\rm cr}/\rho$, but no other modifications to the MHD method is required.

4.3.3 CR Transport: Advection & Streaming

In our method, each mesh-generating point (which defines the gas resolution "elements") represents a finite-volume domain that moves with the fluid velocity $\mathbf{v}=\mathbf{v}_{\rm gas}$ in a quasi-Lagrangian fashion. After operator-splitting the source/injection and loss/cooling terms, it is convenient to re-write the advection and streaming terms in the following Lagrangian, finite-volume form (see e.g. Uhlig et al. 2012):

$$\frac{DE_{\rm cr}}{Dt} = -\int_{\Omega} d^3\mathbf{x} \left\{ P_{\rm cr}\,(\nabla\cdot\mathbf{v}) + \Gamma_{\rm st} + \nabla\cdot\tilde{\mathbf{F}}_{\rm cr} \right\} \tag{4.2}$$

where $D/Dt = \partial/\partial t + \mathbf{v}\cdot\nabla$ is the Lagrangian derivative co-moving with the gas, and $E^{i}_{\rm cr} = \int_{\Omega_i} e_{\rm cr}\, d^3\mathbf{x}$ is the conserved total CR energy in the finite-volume domain Ω_i belonging to element i. Here $\tilde{\mathbf{F}}_{\rm cr} \equiv \mathbf{F}_{\rm cr} - \mathbf{v}\,(e_{\rm cr} + P_{\rm cr}) = \mathbf{v}_{\rm st}\,(e_{\rm cr} + P_{\rm cr}) + \mathbf{F}_{\rm di}$. Pure advection with the gas is automatically handled in this description. In cosmological simulations, the Hubble flow is included in $\nabla\cdot\mathbf{v}$.

The $P_{\rm cr}(\nabla\cdot\mathbf{v})$ term represents adiabatic changes to the CR energy via compression/expansion (the "PdV work"), which exchanges energy with gas. We will refer to this as the "adiabatic" term throughout.[6], we have $\Delta E_{\rm cr} = -P_{\rm cr}\,\Delta V_i$. This is removed from the total energy equation after the hydrodynamic Riemann problem is solved to determine the total gas energy update.

The $\Gamma_{\rm st} = -\mathbf{v}_{\rm st}\cdot\nabla P_{\rm cr}$ term represents "streaming loss", which transfers energy to gas and is always positive because CRs always stream down the CR pressure gradient (see the next section). As CRs stream, instabilities excite high-frequency Alfven waves (frequency of order the gyro frequency, well below our simulation resolution limits; see e.g. Wentzel 1968; Kulsrud & Pearce 1969) which are damped and thermalize their energy effectively instantly (compared to our simulation timescales).[7]

Finally, the $\int_{\Omega} d^3\mathbf{x}\,\nabla\cdot\tilde{\mathbf{F}}_{\rm cr}$ term does not change the total CR energy, but represents flux of energy between resolution elements, caused by CR streaming and diffusion. This can be transformed via Stokes's law into a surface integral, $\int_{\partial\Omega} d\mathbf{A}\cdot\tilde{\mathbf{F}}_{\rm cr}$, which is then solved via our

---

[6] To ensure manifest energy conservation, this is solved when the mesh positions are updated. Calculating the volume changes $\Delta V_i = \int dt \int_{\Omega_i} d^3\mathbf{x}\,(\nabla\cdot\mathbf{v})$ with the kernel-weighted divergence of the *fluid* velocity field (which is the *exact* discrete change in the domain volume as defined in Hopkins 2015a)

[7] With the streaming velocity defined below, the streaming loss term can be written $DE_{\rm cr}/Dt = -E_{\rm cr}/\tau_{\rm st}$ with $\tau_{\rm st}^{-1} = (\gamma_{\rm cr} - 1)\,|\hat{\mathbf{B}}\cdot\hat{\nabla} e_{\rm cr}|^2\,|v_{\rm st}\,\nabla e_{\rm cr}|/e_{\rm cr}$. When this is updated the resulting energy lost $\Delta E_{\rm cr} = \int dt\,\tau_{\rm st}^{-1}\,E_{\rm cr}$ is added to the gas thermal energy.

usual second order-accurate, finite-volume Godunov MFM method (in a manner identical to the hydrodynamic equations, see Hopkins 2015a for details).

We explicitly evolve the conserved quantities $E_{\rm cr}$ and total gas energy $E_{\rm gas}$ which are exchanged (either between gas elements or one another), ensuring manifest total energy conservation.[8]

4.3.4 The Streaming Velocity

CRs stream at some speed $v_{\rm st}$ down the local CR phase-space density gradient (which is equivalent in our single-bin approximation to CR pressure or energy density gradient), projected along the magnetic field lines, i.e. $\mathbf{v}_{\rm st} \equiv -v_{\rm st}\,\hat{\mathbf{B}}\,(\hat{\mathbf{B}}\cdot\hat{\nabla}P_{\rm cr})$ where $\hat{\nabla}P_{\rm cr} = \hat{\nabla}e_{\rm cr} = (\nabla P_{\rm cr})/|\nabla P_{\rm cr}| = (\nabla e_{\rm cr})/|\nabla e_{\rm cr}|$ is the direction of the CR pressure/energy density gradient.

It is generally believed that micro-scale instabilities limit the streaming velocity to Alfven speed $v_{\rm A}\,(=B/\sqrt{4\pi\rho}\,)$ in the low-β limit (see Skilling 1971; Holman et al. 1979, or more recently Kulsrud 2005; Yan & Lazarian 2008; Enßlin et al. 2011), so we adopt a fiducial value $v_{\rm st} = v_{\rm A}$.

But in the weak-field, plasma $\beta \gg 1$, regime, the streaming velocity can be boosted by significant wave damping (see discussion in Enßlin et al., 2011; Wiener et al., 2013; Ruszkowski et al., 2017), so we have also tested various streaming speeds in Appendix 4.A. Although the streaming velocity can in principle exceed v_A by a large factor, Wiener et al. (2013) and Ruszkowski et al. (2017) argued that the streaming loss $\Gamma_{\rm st}$ should be still limited by $\Gamma_{\rm st} = -\mathbf{v}_{\rm A}\cdot\nabla P_{\rm cr}$, because this term is mediated by the excitation of Alfven waves. Therefore, regardless of streaming velocities, we set the streaming loss to $-\mathbf{v}_{\rm A}\cdot\nabla P_{\rm cr}$. When streaming is disabled we simply eliminate terms relevant to streaming.

---

[8] Because we do not evolve a total energy equation, if we use adaptive timesteps, total energy conservation is formally exact at integration-error level rather than machine-accurate. However we have verified that the errors are typically small (percents-level over hundreds of millions of years evolution, although in the most extreme case we find the cumulative amount over 500 Myr can be $\lesssim 20\%$ of the injection), and negligible compared to physical non-conservative terms (e.g. collisional/radiative losses, injection).

4.3.5 Diffusive Transport Terms: Two-moment Method

It is common in the literature to treat $\mathbf{F}_{\rm di}$ in the "zero-th moment" expansion, i.e. approximate it as an anisotropic scalar diffusion with $\mathbf{F}_{\rm di} = -\kappa \hat{\mathbf{B}}\,(\hat{\mathbf{B}} \cdot \nabla e_{\rm cr})$, where κ is the effective diffusion coefficient, which parameterizes the unresolved CR physics. However at high resolution this is problematic for several reasons: (1) it imposes a quadratic timestep criterion (if evaluated with an explicit scheme: $\Delta t < C_{\rm cour}\,\Delta x^2/\kappa$, where Δx is the resolution and $C_{\rm cour}$ the Courant factor) which becomes very small; (2) it implies unphysical super-luminal CR transport when the gradient-scale length $e_{\rm cr}/|\nabla e_{\rm cr}|$ becomes smaller than $\kappa/c \sim 3\,{\rm pc}\,(\kappa/3\times 10^{29}\,{\rm cm^2\,s^{-1}})$ (resolution often reached for simulations in this paper); (3) it cannot smoothly handle the transition between streaming and diffusion-dominated regimes; (4) it will develop spurious numerical oscillations near extrema when handling streaming (Sharma et al., 2010); and (5) it encounters the usual difficulties with anisotropic diffusion operators in moving-mesh codes described in Hopkins (2017) (including e.g. difficulty if CRs are "trapped" at local maxima).

Hence, we adopt a simple two-moment approximation for CR diffusion and streaming, independently developed for this work but similar in concept to the recently-presented implementations in Jiang & Oh (2018) and Thomas & Pfrommer (2019) (although the concept and use in CR dynamics are well-established; see Snodin et al. 2006 for examples). Rather than set $\tilde{\mathbf{F}}_{\rm cr} = -\kappa \nabla e_{\rm cr}$, we explicitly evolve the flux equation:

$$\frac{1}{\tilde{c}^2}\left[\frac{\partial \tilde{\mathbf{F}}_{\rm cr}}{\partial t} + \nabla \cdot \left(\mathbf{v} \otimes \tilde{\mathbf{F}}_{\rm cr}\right)\right] + \nabla_{\parallel} P_{\rm cr} = -\frac{(\gamma_{\rm cr}-1)}{\kappa^*}\,\tilde{\mathbf{F}}_{\rm cr}, \tag{4.3}$$

where $\tilde{\mathbf{F}}_{\rm cr}$ is the CR flux measured in the frame comoving with the fluid, $\nabla_{\parallel} P_{\rm cr} \equiv \hat{\mathbf{B}} \otimes \hat{\mathbf{B}} \cdot \nabla P_{\rm cr}$, $\tilde{c}$ is the (reduced) speed of light, and κ^* is the composite parallel (magnetic field-aligned) diffusion coefficient in the rest frame of the fluid,

$$\kappa^* = \kappa + \frac{v_{\rm st}(e_{\rm cr} + P_{\rm cr})}{|\hat{\mathbf{B}} \cdot \nabla e_{\rm cr}|}, \tag{4.4}$$

where the second term includes the CR streaming with the streaming velocity specified above.

For the numerical implementation of CR energy and flux, we follow the treatment of diffusion operators in MFM, outlined in Section 2 in Hopkins (2017) with a few modifications.

We solve a general evolution equation of conserved quantities $(V\mathbf{U})_i$ of cell i (e.g. CR energy) with a volume V by summing over all adjacent cells j:

$$\frac{\mathrm{d}}{\mathrm{d}t}(V\mathbf{U})_i = -\sum_j \mathbf{F}^*_{\mathrm{diff,ij}} \cdot \mathbf{A}_{i,j}, \tag{4.5}$$

where V is the cell volume and $\mathbf{F}^*_{\mathrm{diff,ij}}$ is the interface value of the flux and $\mathbf{A}_{i,j}$ is the effective face area defined in Hopkins (2015b), in the following steps:

1. We calculate all relevant coefficients, using the standard gradient estimator in GIZMO for MFM to estimate gradients, e.g. ∇P_{cr} and ∇e_{cr}, as described in Hopkins (2015b);
2. We estimate the values on the left and right sides of the face from the values of cells i and j through a linear reconstruction and use them to solve the Riemann problem;
3. We compute the interface face value of the flux $\mathbf{F}^*_{\mathrm{diff,ij}}$ by solving the Riemann problem (RP) through the Harten et al. (1983) (HLL) method, using a MINMOD slope limiter, in an operator split manner from the pure MHD.
4. Finally, the source term in Eq. 4.3 (not considered in Hopkins 2017) is added implicitly to ensure stability.

We differ from Hopkins (2017) since (1) we explicitly evolve the CR flux (instead of calculating it from the CR energy gradient) and (2) in the Riemann solver, we consider the fastest wavespeed to be generally $\tilde{c}$ (since we choose $\tilde{c}$ to be faster than other physical processes).

Unlike Jiang & Oh (2018), we do not modify the momentum transfer from CRs to gas, i.e. the second line of Eq. 4.1, since we assume the strong coupling limit between gas and CRs throughout the paper. This, however, will over-estimate the momentum transfer from CRs to gas when the strong coupling assumption breaks down, i.e. in regimes where the CR and gas coupling is weak and the CR mean free paths are long. In all of our simulations, the mean free paths $\sim (1\,\mathrm{pc})(\kappa/10^{29}\mathrm{cm}^2/\mathrm{s})$ are smaller than the resolved length-scales, so the strong coupling assumption is probably relevant in most of the situations.[9]

We stress that while the flux equation can be generically obtained by integrating the first moment of the Vlasov equation (with some model for closure of higher moments, equation-of-state, and scattering terms), one should not take Eq. 4.3 to represent a physical two-moment expansion of the relativistic Vlasov equation for CRs. Doing so requires making a number of additional assumptions about e.g. the CR phase space distribution function, ratio of gyro radii to resolved scales, and order of truncation in terms $O(v/c)$. We discuss some of the subtle differences that can arise in Eq. 4.3 as a result, in Appendix 4.B.5, but stress that on large and/or long time scales these vanish, and so they have no effect on our conclusions in this paper. For our purposes here, it is better to think of it as a generic two-moment numerical expansion of the anisotropic diffusion + streaming equation which eliminates all of the numerical pathologies (1)-(5) above. In future work, it will be interesting to explore more detailed physically-derived transport models that include these higher-order terms, and attempt to actually predict the coefficients κ and $v_{\rm st}$ on physical grounds (see e.g. Zweibel, 2017; Thomas & Pfrommer, 2019).

For now, if we ignore streaming, we see that in steady-state and/or when $\tilde{c}$ is large, or $\Delta t \gg \kappa/\tilde{c}^2$ (or on spatial scales $\gg \kappa/\tilde{c}$), this equation becomes $\mathbf{F}_{\rm cr} \approx -\kappa\hat{\mathbf{B}}\,(\hat{\mathbf{B}}\cdot\nabla e_{\rm cr})$, and we recover the usual diffusion equation (see Appendix 4.B.6 for a comparison between the pure diffusion and two-moment methods). However, the two-moment method smoothly limits the maximum bulk transport velocity of the CRs to $\tilde{c}$, and makes the timestep criterion $\Delta t < C_{\rm cour}\,\Delta x/\tilde{c}$,[10] which is only first-order, instead of quadratic, in Δx.

---

[9] The formulation in Jiang & Oh (2018) will also over-estimate the momentum transfer in the weakly coupling regime if the “reduced speed of light” approximation is introduced (see below and § 5.2 in Jiang & Oh 2018).

[10] We adopt $C_{\rm cour} = 0.4$ throughout, and have validated stability (as expected) for this value. Δx in the Courant condition is defined in the same manner as Hopkins et al. (2018b) as the local mean inter-particle separation (i.e. the equivalent of the grid spacing in a regular-grid code), $\Delta x \equiv (m/\rho)^{1/3}$.

Table 4.1: Simulation parameters. $M_{\rm vir}$ is the virial mass; c is the halo concentration;$M_{*,\rm disk}$ is the mass of stellar disk; $M_{*,\rm bulge}$ is the mass of stellar bulge; $M_{\rm g,disk}$ is the mass of gas disk; $M_{\rm g,halo}$ is the mass of gas halo; $d_{*,\rm disk}$ is the stellar disk radial scale length; $h_{*,\rm disk}$ is the thickness of stellar disk; $d_{\rm g,disk}$ is the gas disk radial scale length; $m_{\rm b}$ is the gas particle mass.

Name	$M_{\rm vir}$ $[10^{10}{\rm M}_\odot]$	$R_{\rm vir}$ [10 kpc]	c	$M_{*,\rm disk}$ $[10^{10}{\rm M}_\odot]$	$M_{*,\rm bulge}$ $[10^{10}{\rm M}_\odot]$	$M_{\rm g,disk}$ $[10^{10}{\rm M}_\odot]$	$M_{\rm g,halo}$ $[10^{10}{\rm M}_\odot]$	$d_{*,\rm disk}$ [kpc]	$h_{*,\rm disk}$ [kpc]	$d_{\rm g,disk}$ [kpc]	$m_{\rm b}$ $[10^{3}{\rm M}_\odot]$
Dwarf	2.9	63	15	0.019	0.0014	0.1	0.01	1.0	0.2	5	3.3
Starburst	21	121	11	0.57	0.14	4.0	1.0	1.0	0.2	15.0	20.0
$L\star$ **Galaxy**	150	234	12	4.7	1.5	0.9	0.1	3.2	0.24	6.4	2.6

For true micro-physical CR motion, however, $\tilde{c} \approx c$, the speed of light, which still requires a impractically small timestep. Fortunately, for our purposes in these simulations – where we only capture bulk CR properties in the fluid limit – it is more convenient to consider $\tilde{c} \ll c$ (namely the "*reduced speed of light*" approximation), since galaxy properties should still converge, regardless of $\tilde{c}$, provided it is set to some value faster than other relevant physical processes, e.g. the CR cooling or the *actual* bulk flow speeds realized in our simulations. We have experimented extensively with this and find that, for the simulations here, values $\tilde{c} \sim 500-2000\,{\rm km\,s^{-1}}$ are sufficient to give converged results, e.g. SFR and γ-ray emission (see Appendix 4.B.6).

In Appendix 4.B.3, we compare the results using the simpler pure-diffusion (zeroth-moment) approximation: we then simply assume $\mathbf{F}_{\rm di} \rightarrow -\kappa\hat{\mathbf{B}}\,(\hat{\mathbf{B}}\cdot\nabla e_{\rm cr})$ and solve the anisotropic diffusion equation (with the stricter Courant condition) as described in Hopkins (2017). This is equivalent to adopting $\tilde{c} \rightarrow \infty$, in our Eq. 4.3. For the same κ_*, this gives nearly-identical results to our default Eq. 4.3 in our galaxy simulations, demonstrating that the form of the CR flux equation is not a significant source of uncertainty here. We also find an excellent agreement between the zeroth- and two-moment methods in a pure diffusion test given a high enough reduced speed of light.

It is worth noting that our CR treatment is akin to the first-moment or "M1" moment-based method for radiation hydrodynamics (with different closure relations and the scattering terms), with the "reduced speed of light" $\tilde{c}$ (Levermore, 1984), while the "pure diffusion" approximation is akin to flux-limited diffusion (without the limiter).

Table 4.2: Different propagation models of CRs. Each column gives the name of our simulation models, while rows list the physics/parameters of the propagation model. The "MHD" column row indicates whether magnetic fields are included. The "Streaming" column indicates whether CR streaming is considered. κ gives the isotropic/parallel CR diffusion coefficient (CRs will diffuse isotropically if MHD is off, while CRs will diffuse along magnetic fields if MHD is on). $\tilde{c}$ is the "reduced speed of light" in the two-moment method (see § 4.3.5).

	Hydro no CR	**MHD no CR**	**Advection**	$\kappa = 3e27$	$\kappa = 3\mathrm{e}28$	$\kappa = 3\mathrm{e}29$	**MHD Streaming**	**MHD** $\kappa = 3\mathrm{e}28$	**MHD** $\kappa = 3\mathrm{e}28$ **Streaming**
MHD	Off	On	Off	Off	Off	Off	On	On	On
Streaming	Off	Off	Off	Off	Off	Off	On	Off	On
κ [cm^2/s]	-	-	0	3×10^{27}	3×10^{28}	3×10^{29}	0	3×10^{28}	3×10^{28}
$\tilde{c}$ [km/s]	-	-	-	500	1000	2000	1000	1000	1000

4.3.6 The Diffusion Coefficient

The only remaining unspecified parameter in the CR treatment is the effective diffusion coefficient κ[11]. However, there is still substantial uncertainty on its value from a theoretical or observational perspective. In the self confinement picture, it depends on wave damping mechanisms, which are currently not well constrained (Wiener et al., 2013; Zweibel, 2013). In the extrinsic turbulence picture, CRs are scattered through turbulent magnetic fields, but we have limited knowledge of the small scale magnetic fluctuations and the coupling between magnetic field turbulence and CRs (Enßlin, 2003; Enßlin et al., 2007).

Fortunately, there are some empirical constraints on the effective diffusion coefficients, i.e., the diffusion coefficients that broadly reproduce observations of cosmic rays in the Milky Way (even though it is possible that the microscopic model of diffusion is not the correct one for cosmic-ray transport).

For example, Trotta et al. (2011) constrained the *isotropically-averaged* diffusivity κ to be $\sim 6 \times 10^{28} \mathrm{cm}^2/\mathrm{s}$ to within a factor of a few, at ~GeV energy with GALPROP, using the measured energy spectra and abundances of nuclei species in CRs, and adopting a flat halo diffusion model (Ginzburg & Ptuskin 1976; see Introduction for a brief description). Implicitly, these abundances

---

[11] We do not attempt to calculate the diffusion coefficients from microphysics, but treat them as empirical parameters to be varied/constrained.

depend on the residence time of CRs in the Galaxy, so there is a degeneracy between κ and the CR halo height $z_{\rm h}$ (typically 1-10 kpc), out of which CRs can freely propagate (see Figure 3 in Trotta et al. 2011 or Figure 10 in Linden et al. 2010; this issue was also discussed in Ginzburg & Ptuskin 1976). Even in this model, it is possible to match the observational data with a significantly larger κ (up to factors of several) if a larger halo size is adopted.[12]

There are other substantial uncertainties in the estimates of κ, as these empirical constraints usually neglect e.g. local variations in κ or magnetic field structure, the role of advection, halo density profiles (in addition to sizes), small-scale gas density variations ("clumpiness"), and the complicated spatial and temporal distributions of CR sources. The value of κ is even more poorly constrained outside the MW.

Given these uncertainties, we do not attempt a self-consistent calculation of the diffusion coefficient. Instead, we simply assume a constant κ, which is a common approach in the literature (e.g. Booth et al., 2013; Salem & Bryan, 2014; Pakmor et al., 2016; Pfrommer et al., 2017b; Wiener et al., 2017), and test a wide range of κ.

Unlike a flat halo or "leaky box"-type diffusion model, where CRs simply freely escape after crossing the boundary of the halo, we assume CR diffusion with constant κ *everywhere*, even at large heights above the disk. It is therefore likely that our simulations will require a larger κ than the value from a flat halo model with a small halo size.

We will also consider anisotropic CR diffusion with a constant parallel diffusivity. Because the above estimate is isotropically-averaged, if magnetic fields are tangled or toroidal, the equivalent anistropic diffusion coefficient κ would be factor $\gtrsim 3$ larger.

---

[12] For example, Fig. 10 in Linden et al. (2010) shows isotropically-averaged $\kappa \sim 3 \times 10^{28}{\rm cm}^2/{\rm s}$ with $z_{\rm h} \sim 3$ kpc but $\kappa \sim 10^{29}{\rm cm}^2/{\rm s}$ with a larger $z_{\rm h} \sim 5$ kpc).

4.3.7 Sources & Injection

We assume CR injection from SNe (including Type Ia and Type II), with a fixed fraction $\epsilon_{\rm cr}$ ($= 0.1$, as our default value) of the initial ejecta energy ($\Delta E_{\rm cr} = \epsilon_{\rm cr} E_{\rm SNe}$ with $E_{\rm SNe} \approx 10^{51}$ erg) of every SNe explosion going into CRs. SNe explosions inject thermal and kinetic energy into neighboring gas resolution elements according to the algorithm described in detail in Hopkins et al. (2018c); we therefore reduce the coupled energy by $1 - \epsilon_{\rm cr}$ and inject the remaining $\epsilon_{\rm cr}$ energy alongside the metals, mass, and thermal+kinetic energy using the same relative "weights" to determine the CR energy assigned to each neighbor. Likewise the CR flux is updated assuming the CRs free-stream at injection ($\mathbf{F}_{\rm cr} \rightarrow \mathbf{F}_{\rm cr} + \Delta\mathbf{F}_{\rm cr}$ with $\Delta\mathbf{F}_{\rm cr} = \Delta e_{\rm cr}\, \tilde{c}\, \hat{\mathbf{r}}$ from the source, where $\hat{\mathbf{r}}$ is a unit vector pointing outwards from the source). The injection is therefore operator-split and solved discretely (associated with each SNe).

4.3.8 Hadronic & Coulomb Losses ("Cooling")

We adopt the estimate for combined hadronic ($\tilde{\Lambda}_{\rm cr,had}$) plus Coulomb ($\tilde{\Lambda}_{\rm cr,\,Cou}$) losses, $\Gamma_{\rm cr}$, from Völk et al. (1996) and Ensslin et al. (1997) as synthesized and updated in Guo & Oh (2008):

$$\begin{aligned}\Gamma_{\rm cr} &= \tilde{\Lambda}_{\rm cr}\, e_{\rm cr}\, n_{\rm n} = (\tilde{\Lambda}_{\rm cr,had} + \tilde{\Lambda}_{\rm cr,\,Cou})\, e_{\rm cr}\, n_{\rm n} \\ &= 5.8 \times 10^{-16}\, (1 + 0.28\, x_e) \left(\frac{e_{\rm cr}}{\rm erg\,cm^{-3}}\right) \left(\frac{n_{\rm n}}{\rm cm^{-3}}\right) {\rm erg\,cm^{-3}\,s^{-1}}\end{aligned} \tag{4.6}$$

where $n_{\rm n}$ is the number density of nucleons and x_e is the number of free electrons per nucleon. Following Guo & Oh (2008) we assume $\sim 1/6$ of the hadronic losses and all Coulomb losses are thermalized, adding a volumetric gas heating term

$$\begin{aligned}S_{\rm gas} = 0.98 \times 10^{-16}\, (1 + 1.7\, x_e) \left(\frac{e_{\rm cr}}{\rm erg\,cm^{-3}}\right) \times \\ \left(\frac{n_{\rm n}}{\rm cm^{-3}}\right) {\rm erg\,cm^{-3}\,s^{-1}}\end{aligned} \tag{4.7}$$

The remaining CR losses are assumed to escape in the form of γ-rays and other products to which the gas is optically thin.

Due to the hadronic and Coulomb losses, we have to consider the Boltzmann equation with a weak collision term, instead of the Vlasov equation. Since the collision term affects both CR energy density and flux, in the two moment method, we also update the CR flux as $\mathbf{F}_{\rm cr} \rightarrow \mathbf{F}_{\rm cr}(1-\tilde{\Lambda}_{\rm cr}\, n_{\rm n}\Delta t)$.

The loss and heating terms are operator-split and solved together with all other gas heating/cooling terms with our usual fully-implicit cooling scheme described in Hopkins et al. (2018b).

4.3.9 "Isotropic" Runs

By default, we solve the CR equations coupled to the ideal MHD equations, and treat the CR transport (streaming and advection/diffusion) fully anisotropically. However in many of the tests below we consider isotropic CR diffusion without MHD and streaming, so we simply solve the hydrodynamic equations, remove the terms relevant to streaming, and replace $\hat{\mathbf{B}}$ wherever it appears above (representing projection of motion along field lines) with $\hat{\nabla} P_{\rm cr}$.

4.4 Simulation setup

Initial conditions

We study the impact of CRs on three characteristic types of galaxies, dwarf (**Dwarf**), sub-$L\star$ starburst (**Starburst**) and $L\star$ (**$L\star$ Galaxy**) galaxies, whose details are listed in Table 4.1.

All of the runs have exponential stellar and gas disks with scale radii $d_{*,\rm disk}$ and $d_{\rm g,disk}$ respectively. We also include small stellar bulges with Hernquist profiles (Hernquist, 1990) and gas halos with beta profiles (beta=2). The latter enable CRs to diffuse far from the galaxies, since CRs cannot diffuse without the presence of neighboring gas particles in our numerical scheme.

Halo spin parameters (which determine the rotation of the halo gas and dark matter) are set to be 0.033, close to the median value of simulated halos in Bullock et al. (2001), and the initial Toomre Q is set to one uniformly in the gas and stellar disks. We set the metallicity of all star and gas particles in our initial conditions (ICs) in **Dwarf**, **Starburst** and $L\star$ **Galaxy** to be 0.1, 0.3, and 1.0 $Z_\odot$ respectively. Ages of stars present in our ICs are set to > 10 Gyr to avoid excessive SNe from old stellar populations when the simulation begins, which could significantly affect the early evolution of our simulations.

In all $L\star$ **Galaxy** and **Dwarf** runs, we delay turning on the CRs because of initial instabilities from settling of the ICs and to allow magnetic fields to first amplify to a steady-state strength. We enable CRs after initial evolution of 150 Myr in $L\star$ **Galaxy** and 300 Myr in **Dwarf**. In the runs with magnetic fields we start with a seed magnetic field with $10^{-2}\mu$G uniformly (over all gas particles) pointing along the direction of disk angular momentum. The magnetic fields rapidly amplify to $\sim \mu$G in dense gas and develop toroidal morphologies with significant turbulent structure, by around a hundred Myr (see Su et al. 2017, 2018). In the following, we define $t = 0$ at the time when CRs are turned on.

Starburst is designed to mimic dwarf galaxies with high gas surface density ($\sim 0.1\ \mathrm{g/cm^2}$) and SFR ($\sim 5\ \mathrm{M_\odot/yr}$) (e.g. M82 or NGC253). We set up a massive gas reservoir with the extended disk and halo such that gas can continuously accrete to the galaxy and trigger intense star formation for an extended period of time. In **Starburst** runs, we inject CRs immediately at the beginning of the run, since we want to study the transient phenomena (namely, the starburst).

For a subset of our runs we have performed resolution studies and show (see Appendix 4.B.8) that global quantities of interest are robust at our default resolution indicated in Table 4.1, and that main qualitative effects of CRs on galaxies can be captured at this resolution.

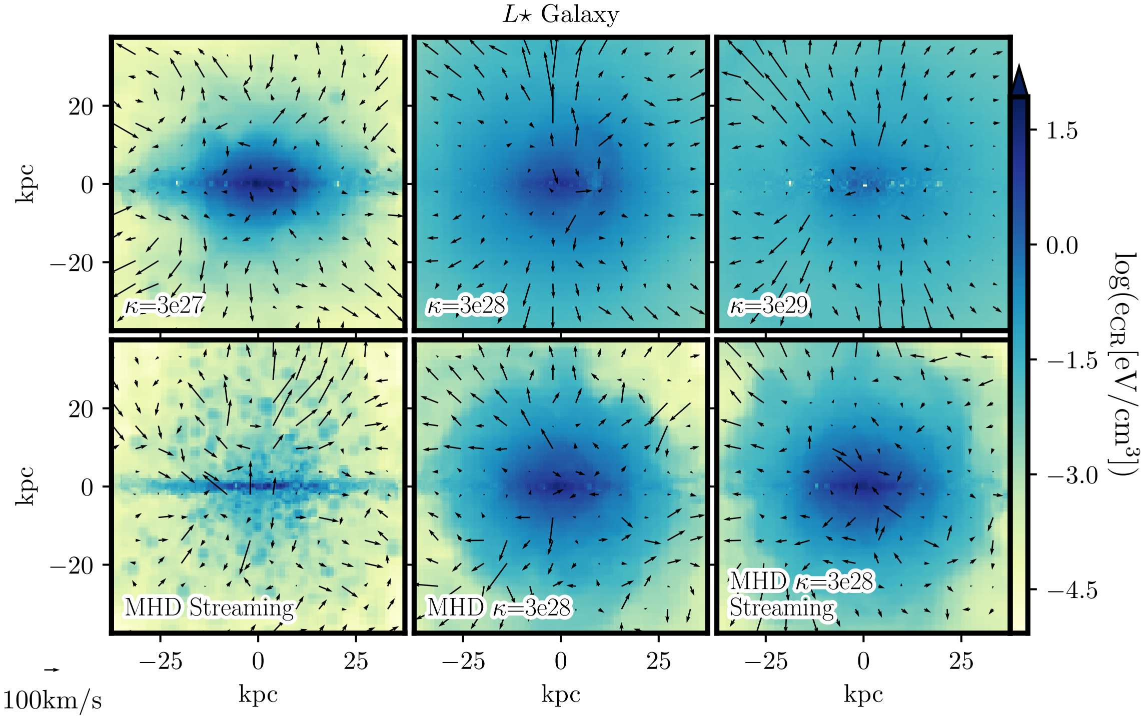

Figure 4.1: Slice plots of CR energy density e_{cr} (in a plane perpendicular to the galactic disk), in runs (of our $L\star$ galaxy model) with different CR transport assumptions (Table 4.2), after 500 Myr of evolution (in quasi-steady-state). Arrows show gas velocities parallel to the slices. CR halos are more extended with larger κ, somewhat smaller with magnetic fields included (owing to suppression of perpendicular diffusion), and somewhat larger again with streaming also included.

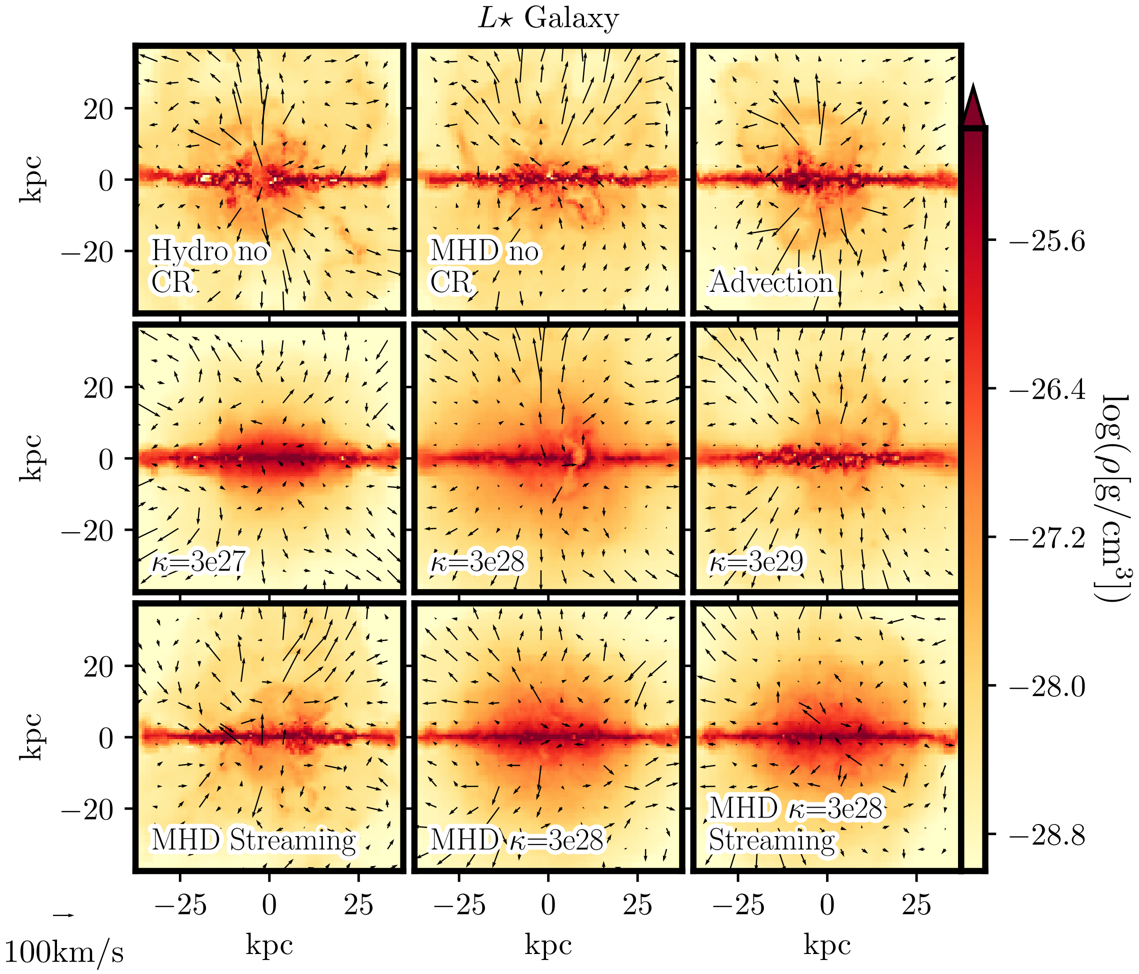

Figure 4.2: Slice plots of gas density and velocity, for the same runs (and in the same style as) Fig. 4.1. The gaseous halo responds more weakly to changes in CR assumptions: gas disks are thicker with CRs at low diffusivity (because CRs are trapped), but outflows more ordered at large scales with high diffusivity.

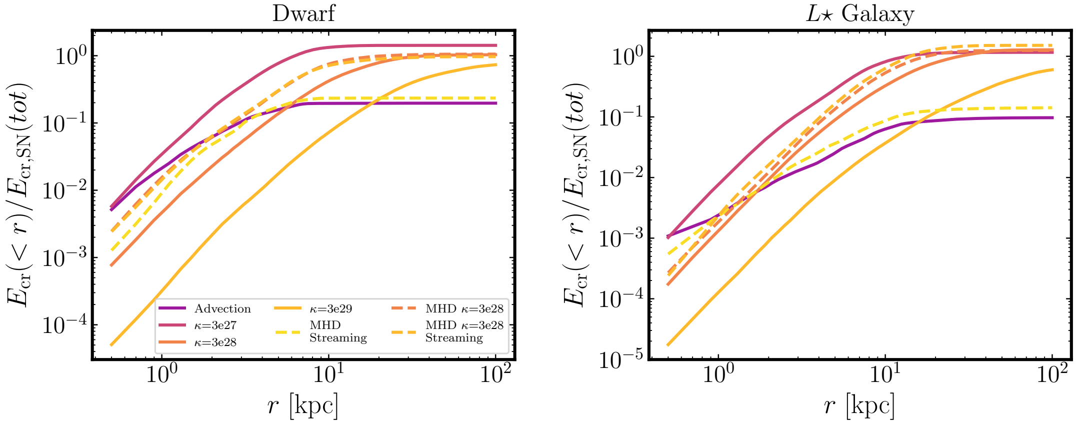

Figure 4.3: Cumulative CR energy as a function of radius from the galaxy center (at $t =$ 500 Myr), normalized by the total CR energy injected by SNe since $t = 0$, in our **Dwarf** (*left*) and $L\star$ galaxy models (*right*), from Table 4.1, with different CR propagation models (Table 4.2). Higher-κ leads to larger CR scale radii and lower CR densities at a given radius, as expected.

4.4.1 Cosmic Ray Propagation Models

We consider several different CR propagation models, and a range of diffusion coefficients. All models are listed in Table 4.2. In particular, we consider diffusion coefficients up to ten times higher and lower than the common inferred isotropically-averaged MW values, sampling a range $\kappa = 3\times10^{27}{\rm cm}^2/{\rm s} - 3\times10^{29}{\rm cm}^2/{\rm s}$.

The most complete (and potentially the most realistic) CR propagation model we test includes fully anisotropic diffusion with MHD and streaming. However, given the uncertainties in the magnetic field configuration on small scales as well as uncertainties in the streaming parameters, we evolve a range of simulations with isotropic diffusion without streaming. This model also enables straightforward comparison with other work as it is the most prevalent propagation model in the literature (see e.g. Strong & Moskalenko, 1998; Jubelgas et al., 2008; Lacki et al., 2010).

We apply the newly developed two-moment method (§ 4.3.5) to both streaming and diffusion with a reduced speed of light, $\tilde{c}$. In Appendix 4.B.6 we test different choices for this parameter and demonstrate that physical properties, e.g. SFR or γ-ray emission, are not affected

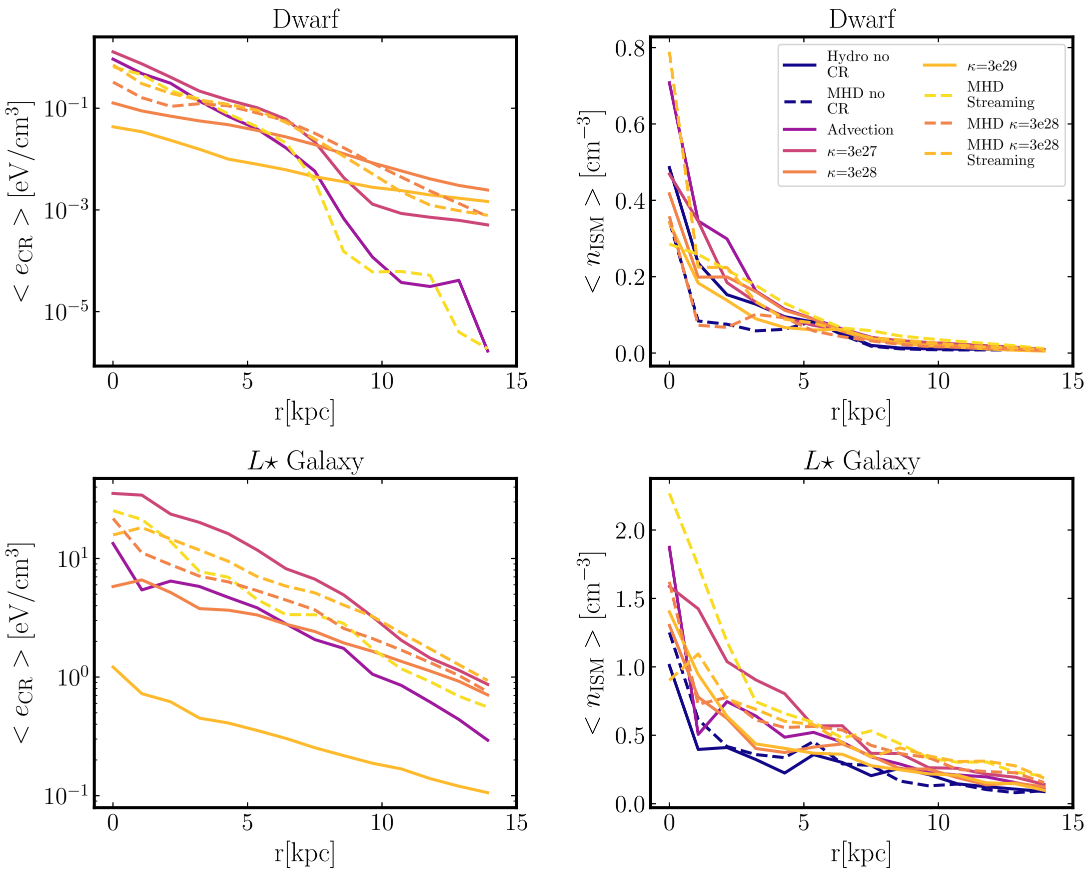

Figure 4.4: *Left:* Mid-plane value of CR energy density (averaged in a 200 pc-thick slab) at 500 Myr, for **Dwarf** and $L\star$ galaxies. *Right:* Mid-plane gas density. The gas density does not have an obvious dependence on the CR propagation models, as the latter influences both the midplane pressure and the gas flows from/onto the gas disk.

by the choice of $\tilde{c}$ as long as it is equal to or larger than the values listed in Table 4.2.

4.5 Results

4.5.1 Distribution of cosmic rays and the effects on galactic properties

Dwarf and $L\star$ galaxies

We begin with a brief overview of the evolution of the gas, CRs and magnetic fields in our $L\star$ **Galaxy** simulations with different CR propagation models. Once initial transients are

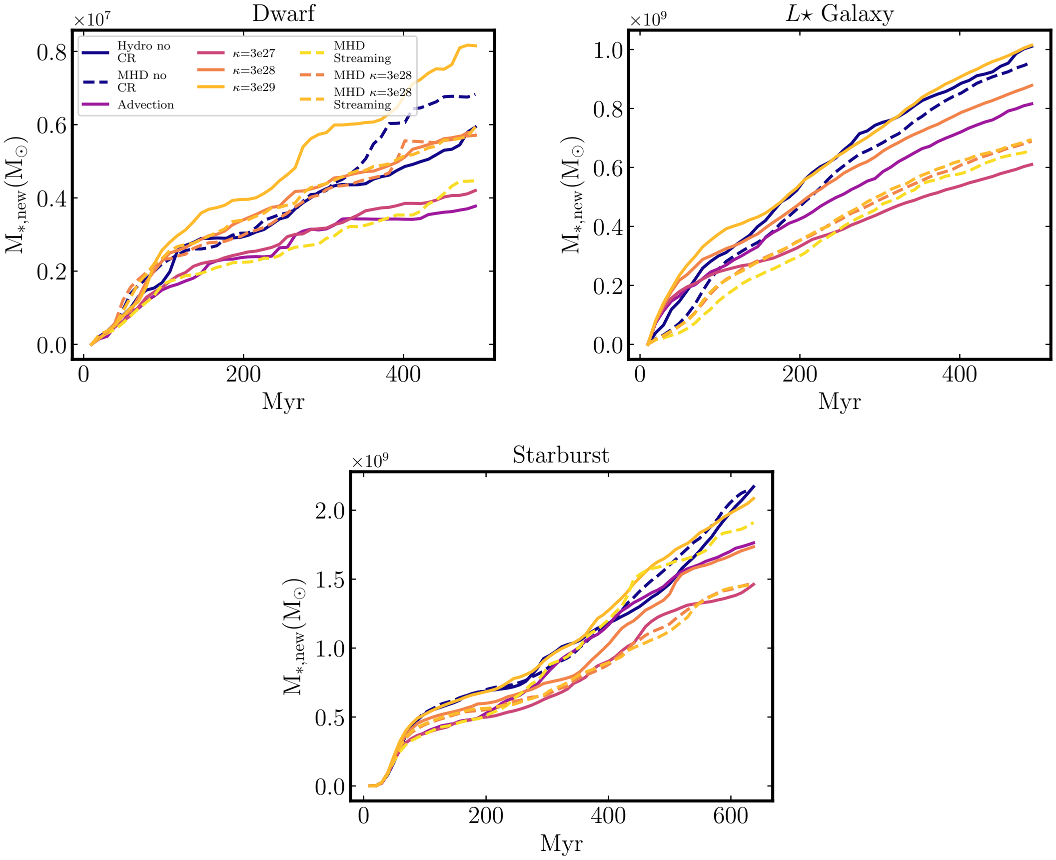

Figure 4.5: Cumulative mass of stars formed (after CRs are "turned on"), in different galaxies (labeled) with different CR propagation models (Table 4.2). CRs with very low diffusivity (e.g. $\kappa = 3e27$, "MHD Streaming" or "Advection" models) can modestly suppress star formation (by factors ~ 1.5 relative to models without CRs), while models with larger diffusivity have no effect (or even slightly enhance SFRs).

damped away, the galaxy has a relativity steady, low SFR with weak galactic winds driven by SNe and other stellar feedback processes. The magnetic fields amplify and develop irregular yet roughly toroidal morphology through dynamo action (Su et al., 2018). After 150 Myr when we turn on CRs, the galaxy is in approximate steady state. SNe inject a fraction of energy into the surrounding gas as CRs, which is transported via advection, diffusion, or streaming. The timescale for CR hadronic and Coulomb losses is long enough that steady-state CR pressure support can arise within/around the galaxy. The total CR energy at any time roughly follows the CR injection from SNe, which is proportional to the total stellar mass formed (see Figure 4.5 and the related text). However, there are also other CR energy gain and loss processes, which we will investigate in § 4.6.1. But in all runs, the CR source distributions are much more concentrated than CR densities, as CRs move from their "birthplace".

Figure 4.1 shows the distribution of the CR energy density in a 60kpc×60kpc slice centered on our simulated $L\star$ **Galaxy**. Runs with higher diffusion coefficients result in lower CR energy density at the galaxy center but develop stronger CR pressure away from the disks. The strong CR pressure gradients continue accelerating gas out to a large radius in the radial direction, although stellar feedback without CRs can also drive winds. In Figure 4.2, we also show that galaxies with CR diffusion in general have the smoother CGM structure, and outflowing gas is present further from the galactic centers. The study of CR driven outflows, including a comparison with thermally-driven outflows and their effect on the CGM, will be presented in a companion paper (Chan et al., in preparation). Simulations with only streaming ($\kappa = 0$ but $v_{\rm st} \neq 0$) are similar to cases with very low diffusivity ($\kappa \lesssim 3 \times 10^{27}\,{\rm cm^2\,s^{-1}}$), where CRs are largely confined to the galaxy. From Figure 4.1 it is clear that combining streaming with diffusion lowers the concentration of CRs in the disk plane and spreads them to larger distances. In almost all of our runs with non-negligible diffusion ($\kappa \gtrsim 10^{27}\,{\rm cm^2\,s^{-1}}$), diffusion makes the CR energy distribution approximately spherical, as opposed to flattened (only the streaming-only and advection-only runs show strongly flattened $e_{\rm cr}$, as the CRs do not efficiently escape the star-forming disk).

These scalings are easy to qualitatively understand. In the ISM, bulk transport speed for streaming is typically, $v_{\rm st} \sim 10\,{\rm km\,s^{-1}}(B/\mu{\rm G})(n_{\rm ISM}/0.1\,{\rm cm^{-3}})^{-1/2}$ (see Su et al. 2018), giving a transport time through a gas halo with a radius ℓ of $t_{\rm st} \sim 100$ Myr $(\ell/{\rm kpc})(v_{\rm st}/10\,{\rm km\,s^{-1}})^{-1}$, while the corresponding diffusive transport velocity/time is $v_{\rm di} \sim 330\,{\rm km\,s^{-1}}(\kappa/10^{29}{\rm cm^2\,s^{-1}})(\ell/{\rm kpc})^{-1}$ and $t_{\rm di} \sim 3\,{\rm Myr}\,(\ell/{\rm kpc})^2(\kappa/10^{29}{\rm cm^2\,s^{-1}})^{-1}$. Thus even for quite low κ, the diffusive flux dominates transport on sub-kpc scales.

But because the diffusion time scales as $\sim \ell^2$, if the CRs establish a smooth profile with scale length $\gtrsim 1-10\,$kpc, then on the larger scales the diffusion time eventually could become larger than the streaming transport time, i.e. outside a scale $\ell \sim 30\,{\rm kpc}\,(\kappa/10^{29}{\rm cm^2\,s^{-1}})$ $(v_{\rm st}/10\,{\rm km\,s^{-1}})^{-1}$.

We quantify the above observations with Figure 4.3, which shows the cumulative distribution of CR energy in the **Dwarf** and $L\star$ **Galaxy** runs. CR energy density is most extended vertically in simulations with the largest diffusion coefficients and it is most concentrated in **Advection** simulations. We define the (3D) CR scale radius $r_{\rm cr,1/2}$ such that the sphere with $r_{\rm cr,1/2}$ encloses one half of the total CR energy. In the $L\star$ **Galaxy**, we find $r_{\rm cr,1/2}$ is around 3 kpc in run "$\kappa = 3$e27", but it increases to around 10 kpc in run "$\kappa = 3$e28" and 30 kpc in run "$\kappa = 3$e29." Similarly, the scale-height of the CR energy distribution also increases with increasing κ. Trends of the CR scale radius with κ can be understood with a diffusion model where the CR injection time ($E_{\rm cr}/\dot{E}_{\rm inj}$) is comparable to the CR diffusion escape time ($t_{\rm di} \sim r^2_{\rm cr,1/2}/\kappa$) where $\dot{E}_{\rm inj}$ is the CR energy injection rate. Assuming a similar injection time, we find that $r_{\rm cr,1/2}$ is roughly proportional to $\sqrt{\kappa}$, so a faster diffusion leads to a more extended CR distribution.

We show the CR and gas mid-plane densities for our $L\star$ **Galaxy** and **Dwarf** runs in Figure 4.4. For both galaxy types, CR density profiles are significantly "flatter" (more extended and less centrally-concentrated) with higher κ. Consequently, in runs with fast diffusion, CRs have smaller impact on the central region of galaxies, providing less pressure support to the central gas, but they can be more important in the CGM. Interestingly, the "**Advection**" runs have lower CR central densities than "$\kappa = 3e27$" because of the smaller adiabatic energy gain (a highly non-linear effect), which we will discuss in the next section and Figure 4.13. The gas midplane density depends rather weakly on CRs. Low-κ (or streaming/advection-only) runs have slightly higher midplane densities while higher-κ runs have midplane densities similar to "no CR" runs.

This is likely caused by additional pressure support from CRs trapped in the midplane in low-κ runs, which allows gas to reach higher densities before fragmenting and forming stars.

It is interesting to compare the CR energy density in our $L\star$ galaxy model with that observed near the solar circle ($e_{\rm cr} \sim 1$ eV/cm^3, see e.g. Grenier et al. 2015), but we must recall that the $L\star$ model was *not* constructed to be an exact MW analogue. For example, it has a more steeply-rising central gas density, without the gas deficiency that appears in the center of the MW (i.e. it does not have a "star-forming ring" and corresponding "hole" in the central few kpc), and the gas densities at $\sim 8\,$kpc from its center are lower than the $\sim 1\,{\rm cm}^{-3}$ in the solar neighborhood (Moskalenko et al., 2002; Cox, 2005).

Nevertheless, the model has a stellar mass, gas mass, and SFR similar to the MW. Our runs with isotropic $\kappa \leq 3\times10^{27}\,{\rm cm}^2\,{\rm s}^{-1}$ produce a mid-plane $e_{\rm cr}$ at $\sim 8\,$kpc from the galaxy center which is high relative to the observed value, those with isotropic $\kappa \geq 3\times10^{29}\,{\rm cm}^2\,{\rm s}^{-1}$ are lower, while those in-between are reasonably consistent. Turning on MHD (making the diffusion anisotropic) increases $e_{\rm cr}$ by factors $\sim 2-3$, consistent with the isotropically-averaged κ being lower by a similar factor (as expected), so values $\kappa \sim 1-3\times10^{29}\,{\rm cm}^2\,{\rm s}^{-1}$ are marginally more favored. Given the lack of a detailed match between our models and the MW, stronger constraints on CR propagation come from γ-ray emission in § 4.5.2.

Fig. 4.5 shows cumulative SF histories: akin to the disk midplane-pressure effects above, CR runs with very low κ suppress SF by modest factors $\sim 1.5-2$, an effect which vanishes at higher κ. Smaller variations ($\sim 10\%$-level) are generally dominated by stochastic run-to-run variations. Runs with MHD generally show slightly higher SFRs (all else equal), an effect

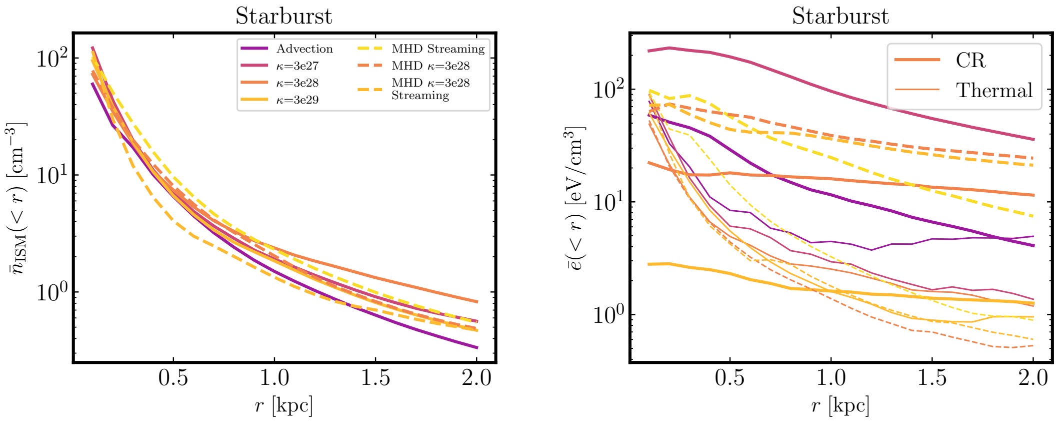

Figure 4.6: *Upper*: Gas densities averaged within a spherical radius r, in **Starburst**, in the snapshots when the central gas densities are the highest in each run. The high gas density is similar to that of observed starburst galaxies (to which we compare below). *Lower*: CR (*thick*) and thermal (*thin*) energy densities at the same times. CR energy densities are higher than thermal when the gas densities peak (but still generally less than turbulent energy densities).

discussed in detail in Su et al. (2017, 2018), but the stochasticity during the early evolution can wash out such effect.

Starburst galaxy

The **Starburst** model is designed to reach high SFRs and gas densities, which are transient phenomena since strong stellar feedback after the starburst will disrupt the galaxy and reduce the gas density. Thus, our **Starburst** run reaches SFR peaks of $\sim 5\,{\rm M}_{\odot}\,{\rm yr}^{-1}$ with highest central gas densities $\sim 100\,{\rm cm}^{-3}$ or (edge-on) surface densities $\sim 0.1\,{\rm g\,cm}^{-2}$ ($\sim 500\,{\rm M}_{\odot}\,{\rm pc}^{-2}$) (compare Fig. 4.6 and Weiß et al. 2001), which last $\sim 10\,$Myr. Between starbursts the galaxy has lower SFR and gas densities, with correspondingly longer hadronic loss times, so CRs can escape more easily.

Fig. 4.6 shows that CR energy densities during starburst phases are around 100 eV$/$cm^3 with slow transport, similar to the value inferred from modeling the observed γ-ray spectra of e.g. M82 (L11 and Yoast-Hull et al. 2016). Although these are high relative to the MW, and a factor of several higher than the thermal (or magnetic) energy densities, they are lower than the pressure

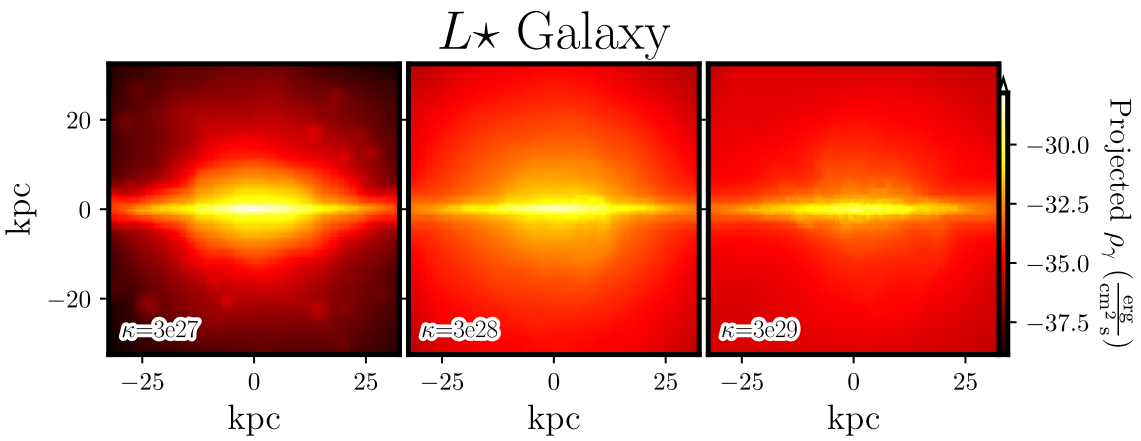

Figure 4.7: Projected pionic γ-ray surface brightness ($E_\gamma > 1\,\mathrm{GeV}$) with different isotropic diffusion coefficients in $L\star$ **Galaxy** at $t = 500\,\mathrm{Myr}$. γ-ray emission is stronger and more compact for lower κ.

required for hydrostatic balance ($\pi G \Sigma_{\mathrm{g}} \Sigma_{\mathrm{g}} \sim 10^{3-4} \mathrm{eV}/\mathrm{cm}^3$), which is primarily comparable to the kinetic energy density in these galaxies (with turbulent velocity dispersions similar to those observed, $\sim 50 - 100\,\mathrm{km\,s^{-1}}$). Our findings are therefore consistent with earlier claims by Lacki et al. (2010), L11, and others who showed that CRs are dynamically unimportant at least in the cores of the starbursts, but they might be more important away from the central dense region.

4.5.2 Pionic γ-ray emission as a measure of CR propagation

Owing to the lack of direct measurements of primary and secondary CRs at low ($\sim$GeV) energies from extra galactic sources, pionic γ-ray emission is one of the few observables that constrain CR propagation outside of the MW. CRs interact with nuclei and produce pions that decay into pionic γ-rays. While there is a substantial amount of pionic γ-ray emission with energy < 1 GeV, it is difficult to isolate it observationally owing to contamination by leptonic emission. For γ-rays with energies $>$ 1 GeV, the leptonic emission is less than one tenth of the pionic emission (for CRs with a spectrum consistent with our default model assumptions; see calculations by Pfrommer et al. 2017b). We will ignore additional potential channels of $>$ 1 GeV γ-ray production, e.g. pulsars or dark matter annihilation. Hence, in the following, we assume all

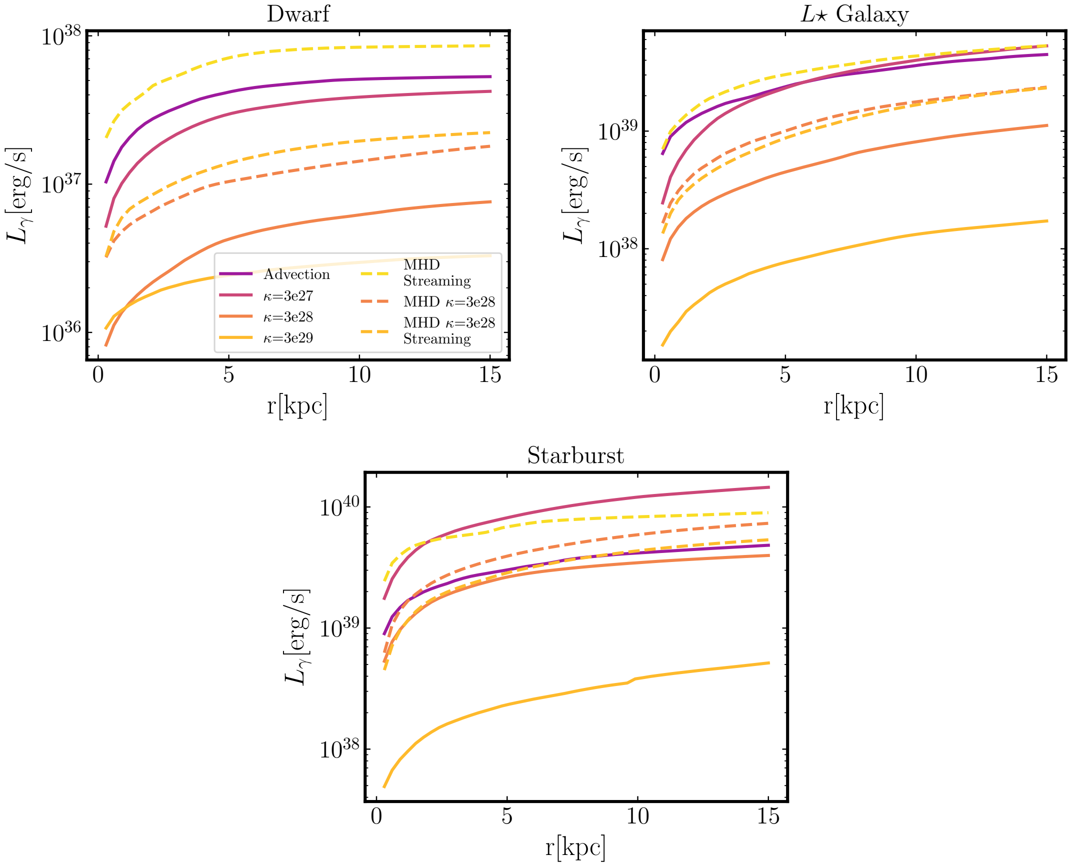

Figure 4.8: Cumulative pionic γ-ray luminosity ($E_\gamma > 1$ GeV) as a function of spherical radius (averaged over t = 400 - 500 Myr) in **Dwarf** (*upper*), *L*⋆ **Galaxy** (*middle*) and **Starburst** (*lower*). The γ-ray luminosity has a spatial extent of a few kpc in dwarf galaxies and more than 10 kpc in $L_\star$ galaxies.

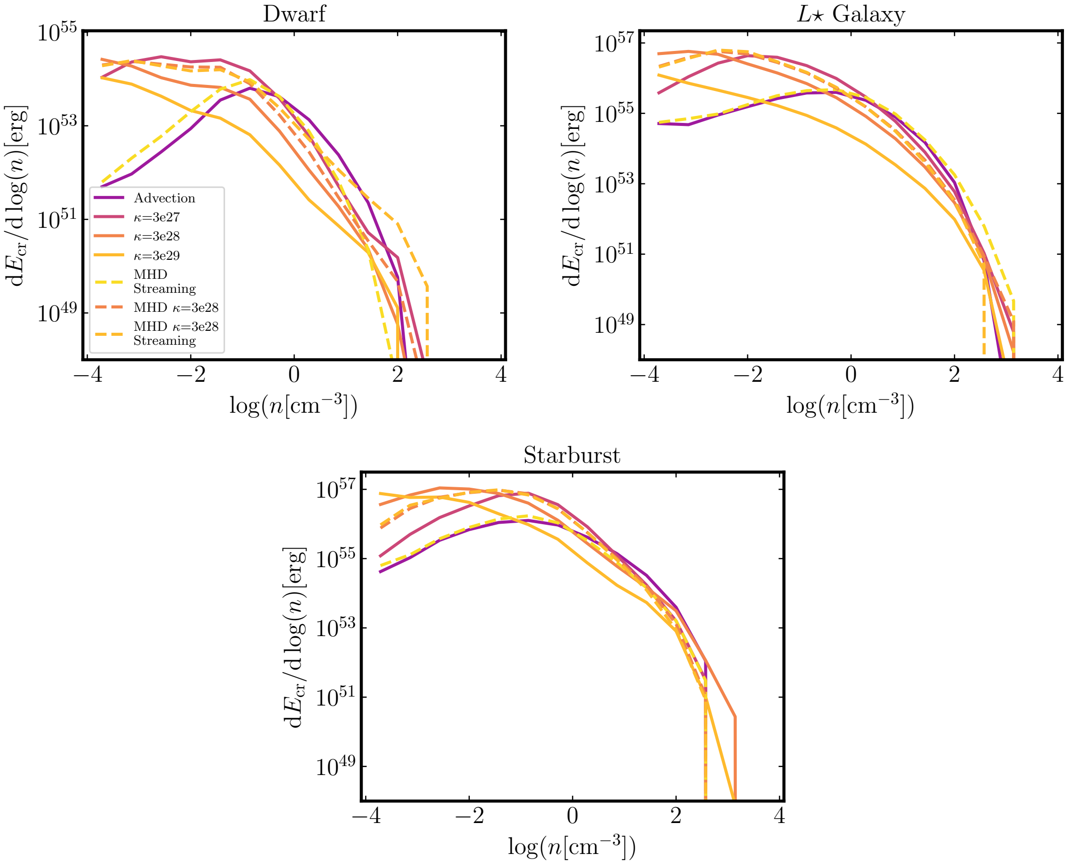

Figure 4.9: The CR energy distribution as a function of local ISM or CGM density (at $t =$ 500 Myr), in different galaxies and CR propagation models (Table 4.2). CR energy is less concentrated at high densities (e.g. within the thin disk, and in dense clouds where SNe explode) when diffusivities are larger, as expected. This reduces the γ-ray luminosity.

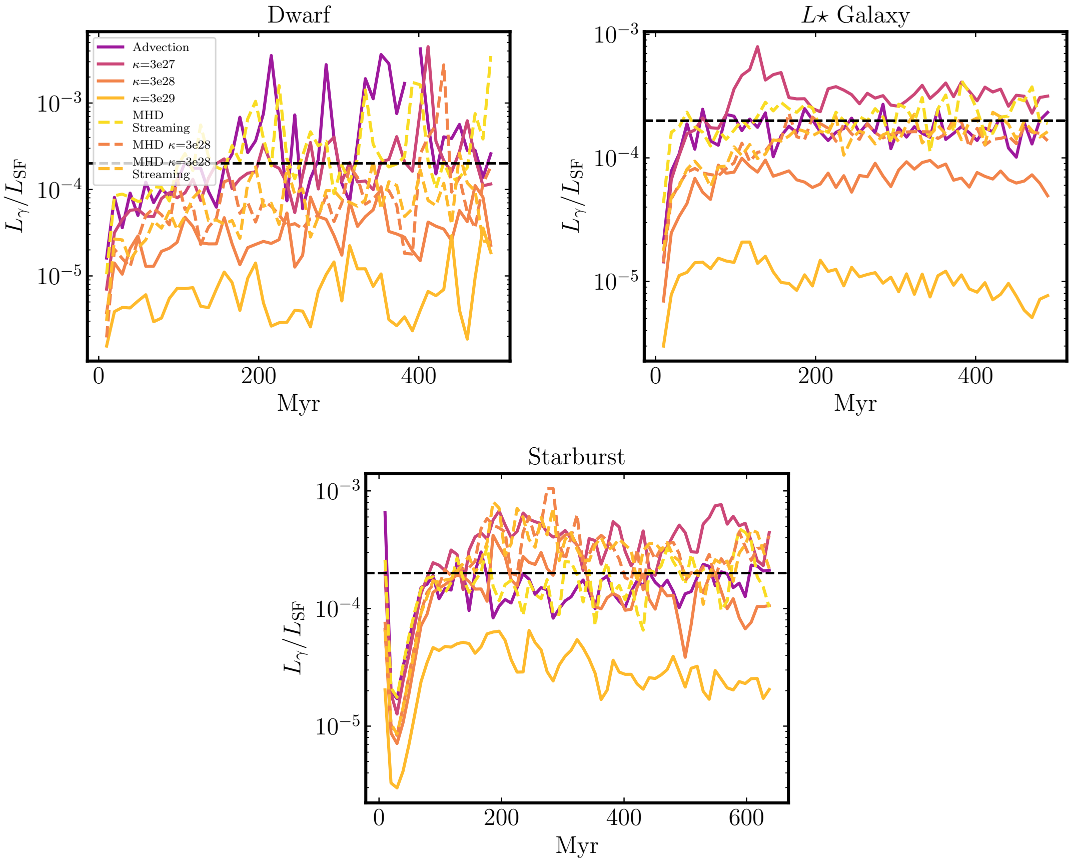

Figure 4.10: Ratios between pionic γ-ray luminosity, $L_\gamma(E_\gamma > 1\,\mathrm{GeV})$, integrated within $< 0.1\,R_{\rm vir}$, and total star formation luminosity (estimated from the SFR averaged over the last 10 Myr at each time). Dashed horizontal lines show the calorimetric limit, i.e. CRs cannot escape galaxies and are lost immediately to collisions without gains (see the caveats in the main text). The ratio reaches a steady value after ~ 100 Myr and is lower with higher CR diffusion coefficients.

> 1 GeV γ-rays are pionic (if there is substantial pulsar contamination, the pionic γ-ray emission is lower, and higher diffusivities κ are required).

The > 1 GeV γ-ray luminosity for γ-rays $L_\gamma(\geq \mathrm{GeV})$ can be calculated as:

$$L_\gamma(\geq \mathrm{GeV}) \approx \sum_i \frac{1}{3} \beta_\pi \tilde{\Lambda}_{\mathrm{cr,had}}\, e_{\mathrm{cr}}\, n_{\mathrm{n}} \Delta V_i, \tag{4.8}$$

where we sum over gas particle i with volume ΔV_i. First, the most of the hadronic loss ($\tilde{\Lambda}_{\mathrm{cr,had}}\, e_{\mathrm{cr}}\, n_{\mathrm{n}}$ in Eq. 4.6) is responsible for the pion production. Second, only one third of the pions (π^0) produce γ-rays. Third, $\beta_\pi (\approx 0.7)$ is the fraction of the pionic γ-rays with energy above GeV(Lacki et al., 2011), which is calculated with the GALPROP pionic cross sections (Moskalenko & Strong, 1998; Strong & Moskalenko, 1998; Strong et al., 2000) built on Dermer (1986), assuming the CR spectrum (between 1 GeV and 1 PeV) follows E^{-p}, where E is the CR proton energy and $p\ (= 2.2)$ is the spectral index.

If CRs can propagate fast enough that a significant fraction can leave galaxies without interacting with ISM, the γ-ray emission will be relatively weak, compared to the expectations from the CR injection. We follow Thompson et al. (2007) and L11 and quantify this by comparing the pionic γ-ray luminosity L_γ (above > 1 GeV) with the bolometric "star formation luminosity" L_{SF} (UV/optical/IR luminosity ultimately contributed by stellar radiation from massive stars, estimated assuming a time-constant SFR and the same stellar IMF as in our simulations), since the CR injection is proportional to SN injection rate and thus to the SFR. If the SFR is constant and we are in the "proton calorimetric limit" (all CR protons instantly lose their energy to collisional processes, without any other processes influencing their energies or spatial distribution, assuming the same time-constant SFR), then the ratio $L_\gamma / L_{\mathrm{SF}}$ is approximately constant.

The value of L_γ in the calorimetric limit is derived as follows. If the SFR is constant, the

SNe rate is dominated by Type-II events, and the CR injection rate is:

$$\frac{\dot{E}_{\rm cr,SN}}{[{\rm erg/s}]} = \varepsilon_{\rm cr}\frac{E_{\rm SN}}{[{\rm erg}]}\frac{[{\rm M}_\odot]}{< m_* >}\xi(m_* > 8{\rm M}_\odot)\frac{\rm SFR}{3.2\times10^7[{\rm M}_\odot/{\rm yr}]}, \tag{4.9}$$

where $\varepsilon_{\rm cr}(=0.1)$ is the fraction of SNe energy going into CRs (constant by assumption in our simulations), $E_{\rm SN}(=10^{51}$ erg) is the energy from one supernova (also constant by assumption), $\xi(m_* > 8{\rm M}_\odot)(=0.0037)$ is fraction of stars that end as supernovae, and $< m_* > (= 0.4\,{\rm M}_\odot)$ is the mean stellar mass, both calculated for the same (Kroupa, 2002) IMF used in our simulations. If this injection rate of CRs is balanced by collisional losses without any other energy gain/loss processes, i.e. $\dot{E}_{\rm cr,SN} = e_{\rm cr}\tilde{\Lambda}_{\rm cr}$, then the pionic γ-ray luminosity is

$$L_\gamma(\geq {\rm GeV})^{\rm calor} \approx 6.7\times10^{39}\frac{\rm SFR}{[{\rm M}_\odot/{\rm yr}]}\ {\rm erg/s}. \tag{4.10}$$

The corresponding “star formation luminosity” $L_{\rm SF}$ for a constant SFR assuming again the same Kroupa (2002) IMF adopted in our simulations is

$$L_{\rm SF}^{\rm constant} \approx 3.5\times10^{43}\frac{\rm SFR}{[{\rm M}_\odot/{\rm yr}]}{\rm erg/s}, \tag{4.11}$$

where the prefactor is calculated with STARBURST99[13] (Leitherer et al., 1999; Vázquez & Leitherer, 2005; Leitherer et al., 2010, 2014).[14] So in the constant-SFR, calorimetric limit, we would expect $L_\gamma/L_{\rm SF} \approx 2\times10^{-4}$ (Thompson et al., 2007).

Pionic γ-ray emission

Figure 4.7 shows the projected pionic γ-ray surface brightness of the $L\star$ **Galaxy** run, for different values of κ. γ-rays mostly originate from galactic disk, i.e. where gas and CR densities

---

[13] `http://www.stsci.edu/science/starburst99/docs/default.htm`

[14] L11 adopted a different conversion factor because they assumed a Salpeter IMF (Salpeter, 1955) (following Kennicutt 1998). But the ratio $L_\gamma/L_{\rm sf}$ in L11 is only higher by $\sim 10\%$ since the SNe rate is also adjusted accordingly.

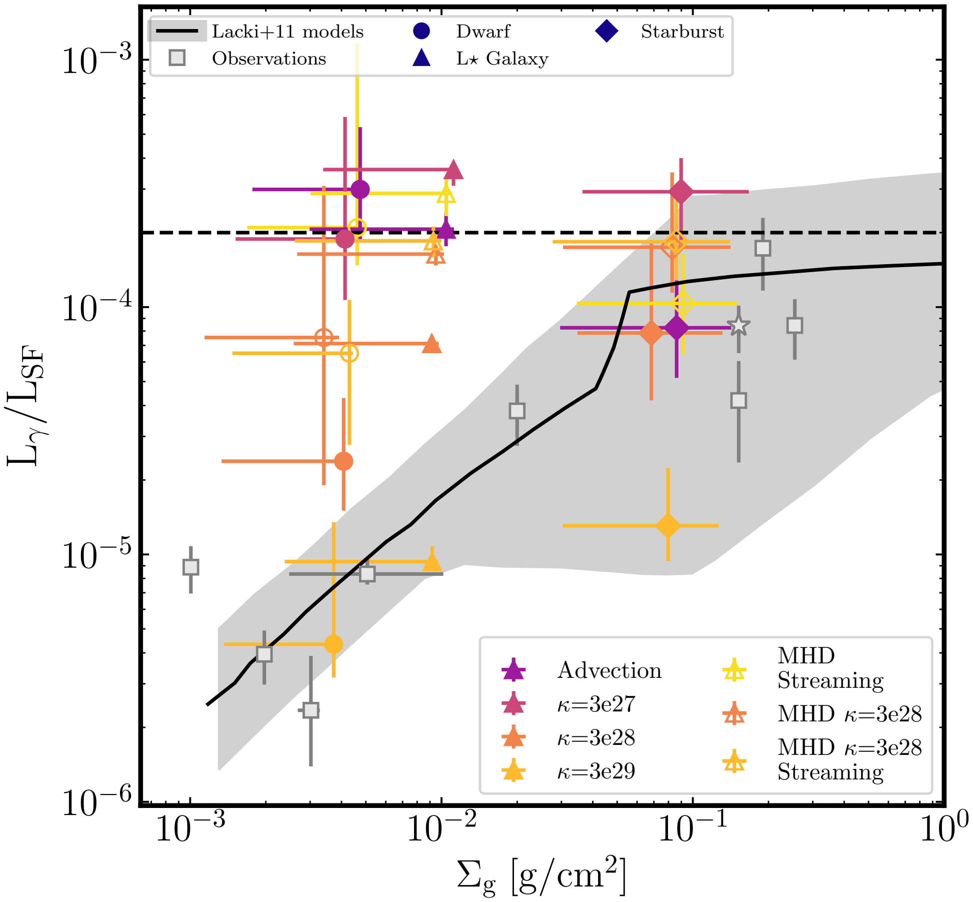

Figure 4.11: Ratio of pionic γ-ray luminosity (L_γ; $E_\gamma > 1\,$GeV) to SF luminosity (L_{SF}) as a function of gas surface density (Σ_g, averaged over inclination). We compare our **Dwarf** (circle), $L\star$ (triangle), and **Starburst** (diamond) galaxy models, with different CR transport models (colors; Table 4.2). Dashed line is calorimetric (Fig. 4.10). Points+error bars indicate median and $\pm 1\sigma$ range of values over the time range $\sim 400-500\,$Myr (smoothed on 10Myr timescales). In order to compare with "active" starbursts, in our **Starburst** runs we only consider snapshots that reach $\Sigma_g > 0.08\,\mathrm{g\,cm^{-2}}$ for at least one inclination during an extended t=250-650 Myr interval (L_{SF} and L_γ are averaged on 5 Myr timescales). Grey squares show observed values compiled in L11 (left-to-right: M31, LMC, SMC, MW, NGC1068, NGC253, NGC4945, M82; star is the NGC253 core). Solid line and shaded range shows the range of "successful" models considered in L11 which simultaneously fit the available observational constraints on CR γ-ray emission, spectra, and Milky Way constraints. The simulations of low surface density galaxies are consistent with observations for $\kappa \sim 3\times 10^{29}\,\mathrm{cm^2\,s^{-1}}$, while lower effective κ might be preferred in **Starburst** runs (but note that typical gas densities in **Starburst** model are lower than in observed starbursts, so here we use only a handful of snapshots that reach highest central gas densities). Lower gas densities Σ_g, or higher diffusivity κ, produce lower L_γ/L_{SF}.

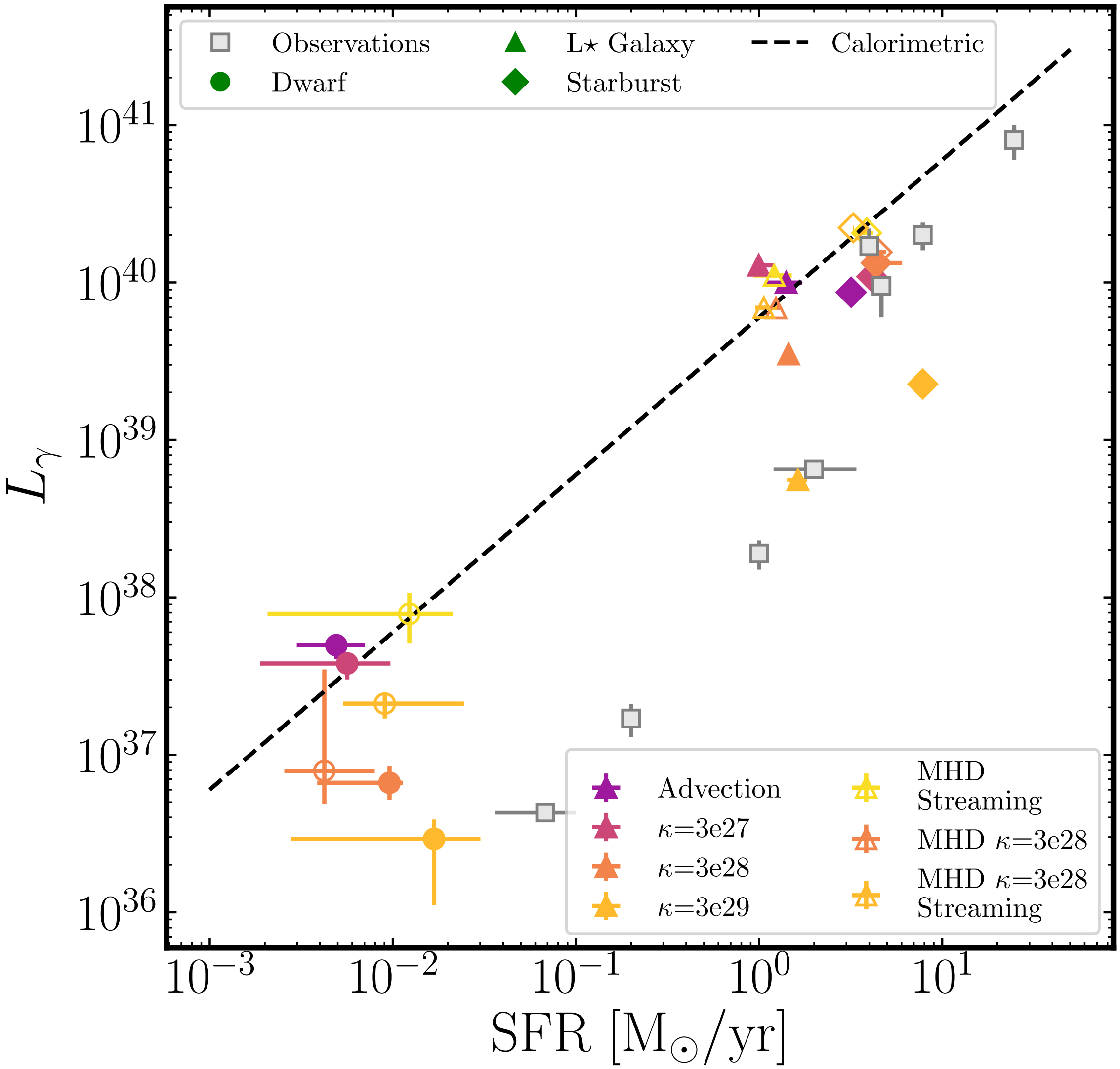

Figure 4.12: Pionic γ-ray luminosity ($E_\gamma > 1\,\mathrm{GeV}$) vs SFR (averaged over $\sim 10\,\mathrm{Myr}$) from our simulations and observations (as in Fig. 4.11). For the **Starburst** models we restrict to times "during starburst" ($\mathrm{SFR} > 3\,\mathrm{M}_\odot\,\mathrm{yr}^{-1}$) and take 5-Myr averaged SFR. Trends are similar to Fig. 4.11: high-SFR galaxies have L_γ close to calorimetric (dashed), while low-SFR galaxies have much lower L_γ, indicating efficient CR escape. Again $\kappa \sim 3\times10^{29}\,\mathrm{cm}^2\,\mathrm{s}^{-1}$ matches the observations in low SFR galaxies.

are the highest. The γ-ray surface brightness drops by over an order of magnitude a few kpc away from the disk plane. For higher-κ, the emission is dimmer but more spatially extended (reflecting the CR energy distribution).

Fig. 4.8 quantifies the distribution of the γ-ray luminosity within spheres of increasing radii for all of our runs with cosmic rays. Consistent with the discussion above, γ-ray emission is much weaker for large κ.[15] For our $L\star$ **Galaxy**, half of the γ-ray luminosity originates from the inner 5-7 kpc. The half-luminosity radius is smaller for our dwarf galaxy, as expected, since the galaxy itself (gas and stellar) is smaller.

Fig. 4.9 breaks down the distribution of CR energy as a function of local gas density, which (since $L_\gamma \propto e_{\rm cr}\, n_{\rm gas}$) effectively determines L_γ. With low-κ (or with advection/streaming only), CRs reside longer in the high-density regions where they are injected. If the density (on some scale ℓ of the cloud or disk) is larger than $\sim 10\,{\rm cm^{-3}}\,(\ell/{\rm kpc})^{-2}\,(\kappa/10^{29}\,{\rm cm^2\,s^{-1}})$, then the collisional loss time of CRs becomes shorter than the diffusion time, so the CRs decay close to their injection. This means L_γ is lower at higher κ, even when the SFR (injection rate) is higher, because the bulk of the CR energy is at lower $n_{\rm n} < 0.1\,{\rm cm^{-3}}$.

$L_\gamma/L_{\rm SF}$ ratio and scalings

Fig. 4.10 shows the time evolution of $L_\gamma/L_{\rm SF}$. With a lower κ ("**Advection**" or "$\kappa = 3$e27"), the galaxies are closer to the calorimetric limit (as expected).[16] But the "$\kappa = 3$e29" runs are lower than the calorimetric limit by more than an order of magnitude in our **Dwarf** and $L\star$ runs.

Turning around our argument from § 4.5.2 above, if CRs are injected in a structure of size ℓ and gas density n with an isotropically-averaged diffusivity $\kappa \lesssim 10^{28}\,{\rm cm^2\,s^{-1}}\,(\ell/{\rm kpc})^2\ (n/{\rm cm^{-3}})$, the collisional loss time becomes shorter than the escape time, so we expect near-calorimetric

---

[15] As with the CR energy density, we note that sometimes the runs with finite-but-low κ exhibit slightly higher L_γ even than the "**Advection**" runs owing to non-linear effects discussed in § 4.6.2.

[16] Note there are periods where $L_\gamma/L_{\rm SF}$ exceeds calorimetric – this is perfectly allowed. Usually it occurs because of short-timescale drops in the SFR and hence $L_{\rm SF}$, where the CRs take somewhat longer to decay so L_γ is $\sim$ constant. But it can also owe to adiabatic compression increasing CR energy, or the contribution of SNe Ia's, or smoothly declining SF histories, all of which violate the assumptions used to derive the calorimetric limit.

$L_\gamma/L_{\rm SF}$. On the other hand, at larger $\kappa \gg 10^{28}\,{\rm cm}^2\,{\rm s}^{-1}$ in the limit where CRs do escape, if we assume the galaxy gas structure is otherwise similar, then the ratio of escape time to loss time (proportional to the fraction of CR energy lost in escaping, and therefore $L_\gamma/L_{\rm SF}$) should scale $\propto \kappa^{-1}$.

In § 4.6.2, we will show that adiabatic processes are of secondary importance relative to diffusion in reducing L_γ in runs with high-κ, but in runs with low-κ (e.g. "$\kappa = $3e27"), they boost L_γ considerably.

As expected, anisotropic diffusion tends to suppress the isotropically-averaged κ by factors $\sim 1.5 - 3$, and correspondingly increase $L_\gamma/L_{\rm SF}$. Streaming slightly increases the escape and dissipates CR energy through streaming loss, so decreases $L_\gamma/L_{\rm SF}$, but the effect is very small (and streaming alone produces near-calorimetric results). This is because (as discussed in § 4.5.1 above) the streaming escape time is much longer than the diffusive escape time, even for relatively low κ, but with the caveat that we do not consider the decoupling between CRs and gas in the cold ISM due to the low ionization fraction and ion-neutral damping (Farber et al., 2018), which could significantly reduce γ ray emission from dense gas.

For the same CR propagation model, galaxies with higher gas densities and larger sizes (effectively larger column densities of dense gas with which CRs must interact to escape) have a larger $L_\gamma/L_{\rm SF}$, which can be seen in Fig. 4.10.

Comparison to observations

We now compare the simulations to observational estimates of $L_\gamma/L_{\rm sf}$ as a function of either central gas surface density in galaxies ($\Sigma_{\rm g}$) or SFR, as compiled in L11. Most of the observed data is described in L11, but we also include the SFR of the SMC (0.036 $\rm M_\odot/yr$ from Wilke et al. 2004). We add two extra starburst galaxies in Figs. 4.11-4.12 (NGC 1068 and NGC 4945; which are listed in Table 2 of Lacki et al. 2011 but not in their figures). The SFRs of starburst galaxies (NGC1068, NGC253, NGC4945, M82) are obtained with the Kennicutt (1998)

IR to SFR conversion formula, assuming the Kroupa IMF (Their IR luminosities are also listed in Table 2 of Lacki et al. 2011).

γ-ray observations of nearby galaxies are limited in spatial extent due to energy resolution and contamination from the diffuse backgrounds and foregrounds (Abdo et al., 2010b,d,c). Hence, we only consider γ-ray emission within 3 kpc for **Dwarf**, matched approximately to that used for the SMC. This choice reduces the γ-ray luminosity by a factor of two compared to using an infinitely large aperture. For **Starburst** and $L\star$ **Galaxy**, we take 10 kpc apertures (which only reduces L_γ by tens of percent compared to an infinitely-large aperture), matched to those used for e.g. M31, NGC1068, and M82. See Fig. 4.8 for how this scales with size.

We measure the gas surface densities $\Sigma_{\rm g}$ (averaged over viewing angles) of **Starburst** within 250 pc, $L\star$ **Galaxy** with 4 kpc, and **Dwarf** within 2 kpc – chosen to be twice the sizes of the active star-forming region in **Dwarf** and $L\star$[17] and about equal in **Starburst** (similar to the choice in Kennicutt 1998 and L11).

Figs. 4.11-4.12 compare our simulations with the observations (compare to Figure 2 of L11). As expected based on our discussion above, $L_\gamma/L_{\rm SF}$ is high and close to the calorimetric limit for **Dwarf** and $L\star$ **Galaxy** with slow CR transport, i.e. for "**Advection**", "$\kappa = $ 3e27", and "**MHD Streaming**". These values are clearly well above the observationally inferred $L_\gamma/L_{\rm SF}$.

With larger diffusion coefficients, $L_\gamma/L_{\rm SF}$ decreases as expected. For isotropic diffusion, the observations in dwarf and $L\star$ galaxies appear to require $\kappa_{\rm isotropic} \sim 10^{29}\,{\rm cm^2\,s^{-1}}$. Out of the options tested $\kappa = 3\times10^{29}\,{\rm cm^2\,s^{-1}}$ provides the best match but the range of data allows for a slightly lower value as well.

For anisotropic diffusion, L_γ is somewhat larger owing to suppressed isotropic-averaged diffusivity, as discussed above, so values of the *parallel* diffusivity $\kappa_\parallel > 10^{29}\,{\rm cm^2\,s^{-1}}$ are favored.

For galaxies with high gas surface densities and SFRs, i.e. **Starburst**, we found κ has to be less than $3\times10^{29}{\rm cm^2/s}$. On the face value, this implies that CR transport is effectively

---

[17] This choice is smaller than the optical radii that Kennicutt (1998) and L11 used, but the gas surface densities are similar in both choices.

slower in high gas surface density regions or during starburst. However, in our **Starburst** runs, for the highest diffusion coefficient tested, we did not include MHD and anisotropic diffusion that, depending on the magnetic field configuration, could slow down the transport of CRs out of high density regions. The models also have gas configurations and typical gas densities that are not an excellent match to observed starburst galaxies, and our analysis only includes brief time intervals when central gas density reaches the values similar to observed starbursts.

Many observations, e.g. Ackermann et al. (2012a) and Rojas-Bravo & Araya (2016), considered L_γ with $0.1\mathrm{GeV} < E_\gamma < 100\mathrm{GeV}$, instead of $E_\gamma > 1\mathrm{GeV}$. Therefore, in Appendix 4.C, we compare $L_{0.1-100\,\mathrm{GeV}}$ from simulations with observations, and we find that the same high diffusion simulations provide the best match to the observed γ ray emission from galaxies.

It is interesting to compare the results from the simple leaky-box model of L11, as well as more detailed models of CR transport in the MW, with our findings. L11 predicts L_γ/L_{SF} as a function of gas surface density by assuming the Kennicutt-Schmidt law and a one-zone leaky box model with CR diffusion (see Lacki et al. 2010 for details), with an isotropically-averaged $\kappa = 3\times 10^{28}\,\mathrm{cm^2\,s^{-1}}$. The broad contours of their prediction for L_γ/L_{SF} as a function of Σ_{g} or SFR are similar to our simulations, suggesting – as they argued – that CR escape is required to reproduce the observed trend of L_γ/L_{SF}.

In the MW, much more detailed propagation models have been tested (see e.g. Trotta et al. 2011 and reference in § 4.2). We again caution that our "$L\star$" model is not an exact MW analogue, since it has higher gas surface density and lacks a central gas deficiency like the MW (Moskalenko et al., 2002), both of which could affect L_γ.

Note that at "face value", both MW and L11 constraints might appear to favor slightly-lower $\kappa \sim 3-6\times 10^{28}\,\mathrm{cm^2\,s^{-1}}$ compared to the best-match here ($\kappa \sim 3\times 10^{29}\,\mathrm{cm^2\,s^{-1}}$), but this is a relatively small offset and completely expected if we account for the points below. (1) The MW observations and L11 models assume relatively small halos out of which the CRs escape instantly, while we assume a constant κ everywhere, meaning that our effective halo size is large

($\sim 10-30\,\mathrm{kpc}$). Recall (§ 4.2 and § 4.3.6), the inferred κ in the observations increases with the halo height. (2) The gas in the simulations is clumpy where CRs are injected, slightly increasing L_γ (Boettcher et al., 2013), compared to the smooth mass profiles assumed in those studies (requiring larger κ by a factor $\sim 1.5-2$). (3) L11 did not consider galactic winds and adiabatic losses/gains in their fiducial models; the MW constraints did not account for galactic winds in a self consistent manner (i.e. they do not consider CR-driven winds and the radial/temporal variations of the winds). In our anisotropic runs, we also find that the isotropically-averaged κ (what is nominally constrained by the L11 study, for example) is a factor $\sim 2-3$ lower than the parallel κ. Accounting for all of these facts, our favored coefficients appear to be consistent with other state-of-the-art constraints on CR propagation in the MW from e.g. Trotta et al. 2011, and references in § 4.2.

4.6 Discussion

4.6.1 Comparisons to previous studies

Suppression of star formation by cosmic rays

In our idealized non-cosmological simulations, we find that SF can be suppressed by CR feedback in simulations with either advection or streaming only, or very low diffusivities $\kappa \lesssim 10^{28}\,\mathrm{cm^2\,s^{-1}}$, consistent with many previous findings, e.g. Booth et al. (2013); Salem & Bryan (2014); Pfrommer et al. (2017a). However, such slow transport severely violates constraints from observed γ-ray emission, and at best results in modest SFR suppression (factor $\sim 1.5-2$). For larger transport speeds required to reproduce the observed γ-ray emission, CRs have only a weak effect on SF.

Interestingly, Jubelgas et al. (2008) found that while CRs reduce SFRs in dwarf galaxies, they have almost no effect in MW mass galaxies. Their conclusion was likely due to their "local equilibrium" assumption, namely that CR injection ($\propto$ SFR $\propto \rho^{1.5}$ in their model) is balanced by collisional losses ($\propto \rho$) locally (like in the calorimetric limit), in an isothermal-like ISM, so in their models the CR energy density is proportional to $\rho^{1/2}$ while thermal energy densities are proportional to ρ: as a result, CR energy was always sub-dominant to thermal energy in their models at gas densities $n > 0.2\,\mathrm{cm}^{-3}$. In contrast, in our simulations, CRs can propagate far from their injection sites, so local equilibrium is not valid and we find that the ratio of CR pressure to gas thermal or turbulent pressure for low κ can be significant even at moderate ISM densities, providing mild suppression of the star formation (similar arguments were presented in Socrates et al. 2008; Booth et al. 2013). For our favorite, large κ values CRs escape from the ISM, resulting in practically no effect on the star formation in both our **Dwarf** and $L\star$ **Galaxy** simulations.

However, we caution that because our simulations are non-cosmological, they do not account for the effect of CRs on the CGM and IGM (the source of fuel for galaxies). As CRs escape the *galaxies* more efficiently with the favored larger κ, we have shown they have proportionally much higher energy density/pressure in the CGM, which means they could (in principle) be important for the long-term cosmological evolution and accretion onto galaxies. This is likely most important in more massive galaxies that build quasi-hydrostatic halos whose late-time cooling influences galaxy growth. We will explore this in cosmological simulations in future work (Hopkins et al., in preparation).

γ-ray emission

Our results are in line with L11: when matching the observed γ-ray emission, starburst galaxies (with effective isotropic diffusivities $\kappa < 3 \times 10^{29}\mathrm{cm}^2/\mathrm{s}$) are nearly proton calorimeters, while galaxies with lower gas surface density or SFRs (with $\kappa \sim 3 \times 10^{28-29}\mathrm{cm}^2/\mathrm{s}$) are not proton calorimeters (most CR protons escape).

Salem et al. (2016) also studied hadronic γ-ray emission with simulations of MW-mass galaxies and argued for isotropically-averaged coefficients $\kappa \sim 3 \times 10^{28}\,\mathrm{cm}^2\,\mathrm{s}^{-1}$; but they only considered the γ-ray emission in the CGM and they did not include hadronic/collisional losses in the simulations, which led to some unphysical results. For example, their predicted pionic γ-ray luminosity significantly exceeded the CR injection rate at lower κ. Moreover, as noted by Jacob et al. (2018), neglecting collisional CR losses allows CRs to build up in dense gas or the disk midplane without being rapidly lost (as they should), which artificially enhances the strength of CR-driven winds. Nevertheless, we broadly agree on the preference for a relatively high κ.

Recently, Pfrommer et al. (2017b) also investigated γ-ray emission with idealized galaxy simulations, assuming CR transport via either advection-only or advection+anisotropic diffusion with $\kappa = 10^{28}\,\mathrm{cm^2\,s^{-1}}$. They argued they could (a) reproduce the FIR-γ-ray correlation and (b) explain the low L_γ in non-starburst galaxies primarily by adiabatic losses.

But there are several caveats:

(1) Their favored model still over-predicted $L_\gamma/L_{\rm SF}$ by a factor of a few or more in non starburst galaxies, e.g. dwarf and MW-mass galaxies. For their actual simulated points (see their Fig. 3) without diffusion, the predicted $L_\gamma/L_{\rm SF}$ is larger than the SMC, LMC, MW, and M33 (not shown therein, but see L11).

They claimed to match the observed FIR-L_γ correlation, only if an empirical FIR-SFR conversion relation (Kennicutt, 1998) is assumed. However, as they acknowledged, this conversion relation over-predicts $L_{\rm FIR}$ in dwarfs, due to much lower dust opacity/absorption/reddening. Their FIR-L_γ relation might deviate from observations after taking this correction into account.[18]

(2) We do not consider the same CR models and the same range of γ ray energy. They consider $L_\gamma(0.1-100\,\mathrm{GeV})$, i.e. including all CRs from $0.1-100\,\mathrm{GeV}$, instead of the choice here and in L11, which is restricted to $L_\gamma(>1\,\mathrm{GeV})$. They also assumed a shallower CR spectrum ($\propto E^{2.05}$, as compared to $\propto E^{2.2}$ here and in L11). Together with this, our L_γ can differ from theirs by a factor of $\sim 2-3$. However, even if these differences are considered, their $L_\gamma/L_{\rm SF}$ are still

---

[18] Because both the $L_\gamma/L_{\rm SF}$ and $L_{\rm FIR}/\mathrm{SFR}$ ratios drop in dwarfs, a roughly-linear $L_{\rm FIR}-L_\gamma$ relation can still maintain in our simulations (directly related to the "conspiracy" which maintains the FIR-radio correlation; for discussion see e.g. Bell 2003; Lacki et al. 2010).

greater than the observed dwarfs.

They suggested their over-prediction of $L_\gamma/L_{\rm SF}$ might be reconciled with simulations that could resolve the multi-phase ISM, since CRs may preferentially spend time in low density regions, which dominate the volume. We do have the multi-phase ISM here, but predict similar results in our advection-only or low-κ runs. A possible explanation for the discrepancy is that the observed low γ-ray luminosities require high diffusion coefficients $\kappa \sim 3\times 10^{28-29}\,{\rm cm^2\,s^{-1}}$ as favored by our study here and the modern MW constraints (Trotta et al., 2011).

(3) We will show immediately below that when κ is in the favored range, adiabatic processes are less important than CR transport in reducing L_γ, although if κ is small, adiabatic processes tend to increase L_γ.

4.6.2 CR Energetics and the Importance of Different Gain/Loss Terms

Fig. 4.13 shows the relative importances of various CR gain/loss terms in our simulations: SNe injection, collisional (hadronic+Coulomb) losses, "streaming losses" (energy loss to excitations of Alfven waves), and "adiabatic" terms ("PdV" work lost pushing gas, or CR energy gain in compression).

The initial injection from SNe is proportional to the SFR (with a few Myr delay), so it tracks the SFR and varies only by a relatively small amount in our different runs of a given galaxy model (even the highest/lowest SFR runs differ by at most a factor ~ 2).

Collisional losses are important loss terms (within the galaxies) – and we have already discussed these extensively as they are the origin of the γ-ray emission. Since they scale $\propto e_{\rm cr}\,n_{\rm n}$ they decrease with "faster" CR transport (higher κ) as CRs reach lower-density gas faster.[19] Streaming losses are comparatively small.

The "adiabatic" term $\dot{E}_{\rm Ad}$ can be comparable to injection or collisional terms, but can

---

[19] The (weak) exception to this rule is the $\kappa = 3\times 10^{27}\,{\rm cm^2\,s^{-1}}$ run in our $L\star$ and **Starburst** models, where collisional losses are slightly larger than in the corresponding "**Advection**" runs. This is caused by the slightly stronger adiabatic compression term boosting $e_{\rm cr}$ in dense gas.

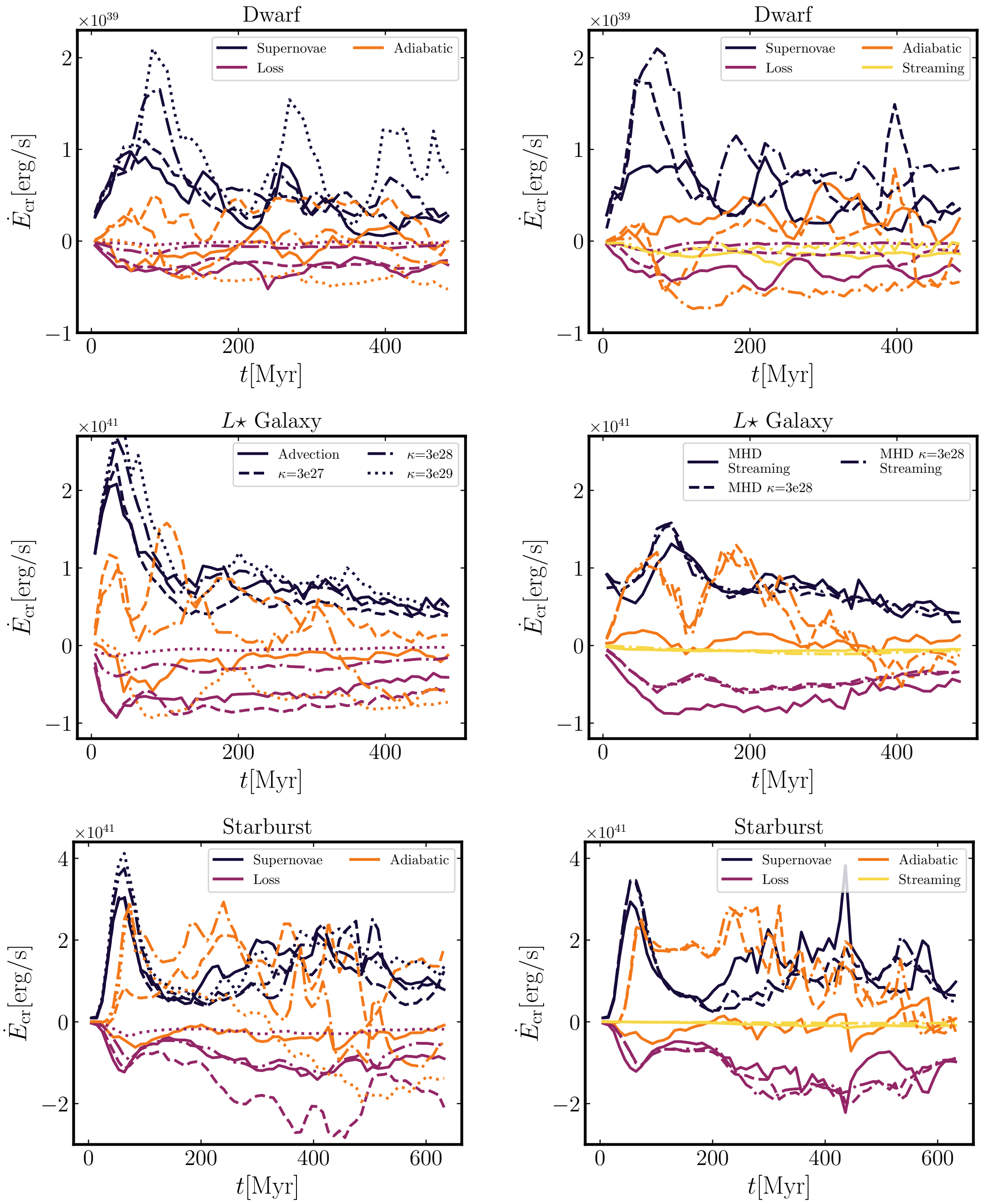

Figure 4.13: Rate-of-change of total CR energy $\dot{E}_{\rm cr}$ (integrated over the box and averaged in ~ 50 Myr intervals) in each simulation (labeled), owing to different gain (positive) or loss (negative) processes (see § 4.3). Left panels show runs without magnetic fields, whereas right panels show runs with magnetic fields. "Supernovae" (red) indicates injection from SNe. "Loss" includes the hadronic+Coulomb losses ($\Gamma_{\rm cr}$), "Streaming" the streaming loss term ($\Gamma_{\rm st}$). "Adiabatic" indicates the adiabatic ("PdV") work term (includes work done by CRs on gas, and by gas on CRs; can be positive or negative). Faster transport (larger κ) means CRs spend less time in dense gas, reducing losses. While adiabatic terms are non-negligible, they rarely exceed SNe injection so do not boost L_γ beyond a factor of ~ 2; they are also usually positive when κ is low and CRs are trapped in dense gas (while they become negative at high κ).

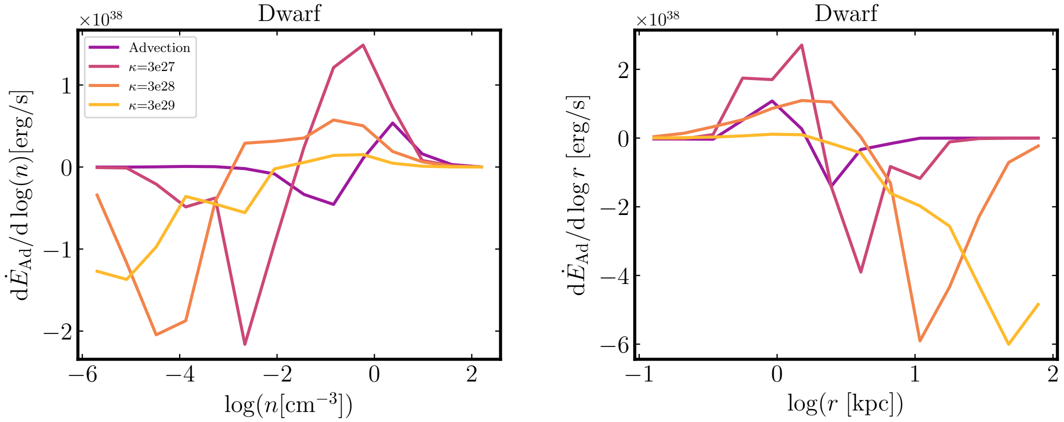

Figure 4.14: Contribution of CR energy at different local gas densities n (*top*) or at different galacto-centric radii r (*bottom*) to the total adiabatic work term in Fig. 4.13 (calculated for **Dwarf** at $t = 500\,$Myr). Gas at high-n ($\gtrsim 0.01\,\mathrm{cm}^{-3}$) and low-$r$ ($\lesssim 5\,$kpc), i.e. within the disk, is primarily contracting, so the "adiabatic term" boosts CR energy (increasing e_{cr} and L_{γ}). Gas at low-n_{ISM} and high-r is primarily expanding so the adiabatic work decreases e_{cr}. In simulations with an explicitly-resolved multi-phase ISM like those here, CRs must *first* escape dense gas and the disk midplane, before adiabatic terms can significantly reduce e_{cr} or L_{γ}.

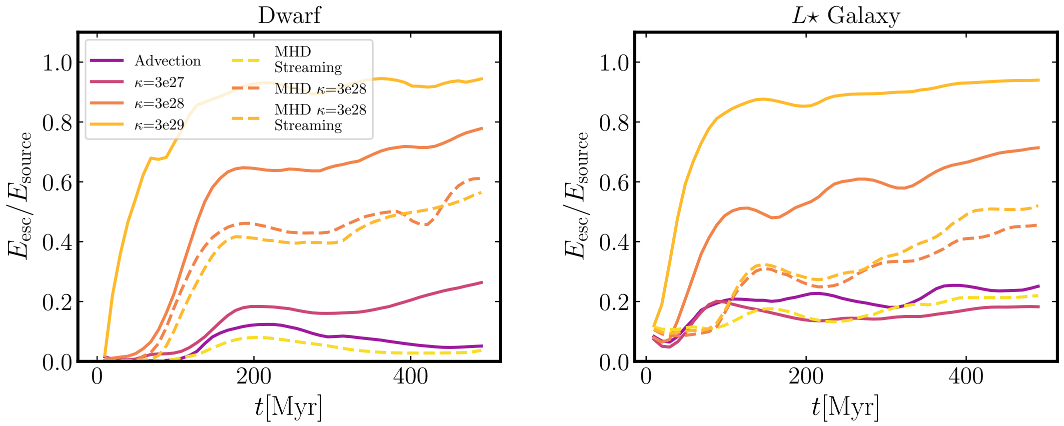

Figure 4.15: Ratio between the cumulative CR energy escape (E_{esc}) from the central region and the cumulative CR energy input in the central region (E_{source}). The CR escape fraction, $E_{\mathrm{esc}}/E_{\mathrm{source}}$, increases with CR propagation speed: more than 90% of CR energy leaves the central region for high κ, compared to only $\sim$10-20% that leave for simulations with advection-only.

be a gain or loss process. To better understand where the gains and losses occur, Fig. 4.14 shows the contribution to the total $\dot{E}_{\rm Ad}$ from gas with different densities n or at different galactocentric radii n. For CRs at low ambient n (or large r), $\dot{E}_{\rm Ad}$ tends to be a loss term (i.e. CRs are expanding or losing energy in rarefactions). For CRs in high ambient $n_{\rm ISM}$ and small r, it tends to be a gain (CRs are being compressed in converging flows). Recall, the "adiabatic" term is *defined* (Eq. 4.2) by $-\int d^3\mathbf{x} P_{\rm cr}\,(\nabla\cdot\mathbf{v}) = -(\gamma_{\rm cr}-1)\int dE_{\rm cr}\,\nabla\cdot\mathbf{v}$ (where $\mathbf{v}$ is the gas velocity). So, combined with Fig. 4.14, this simply means that at high gas densities within galaxies, more of the ISM is collapsing/converging or being compressed (in e.g. shocks), while at low densities outside galaxies, more the gas is expanding in outflows. Whether one or the other term dominates depends on where most of the CR energy resides (shown in Fig. 4.9).

So, unsurprisingly in Fig. 4.13, our runs with the most efficient CR escape to large-r and low-n (all the highest $\kappa \sim 3\times10^{29}\,{\rm cm^2\,s^{-1}}$ runs, or most of the **Dwarf** runs with even intermediate κ) show net $\dot{E}_{\rm Ad} < 0$, since CRs rapidly migrate to the expanding regions. In contrast, those with the least efficient escape (e.g. all the **Starburst** runs and the $L\star$ runs with lower isotropically-averaged κ) show net $\dot{E}_{\rm Ad} > 0$.[20]

For either advection-only or low-κ ($\sim 10^{28}\,{\rm cm^2\,s^{-1}}$), the qualitative behaviors of $\dot{E}_{\rm Ad}$ in both dwarf and MW-mass systems in Pfrommer et al. (2017b) are similar to what we find here.

However, for the reasons discussed in § 4.6.1, our results do not support their conclusion that adiabatic losses are the dominant factor for the low $L_\gamma/L_{\rm SF}$ in dwarfs. At very low κ, $\dot{E}_{\rm Ad}$ is primarily a gain term. But even at higher κ where $\dot{E}_{\rm Ad} < 0$ is a loss term, it is insufficient (in itself) to explain the very low $L_\gamma/L_{\rm SF}$ observed in the SMC/LMC without significant CR leakage (the adiabatic+SNe terms are not enough to explain the loss terms in the top right panel of Fig. 4.13). More importantly, the adiabatic losses arise only after the CRs have already escaped the dense gas, i.e. the regions which produce most of L_γ.

---

[20] Interestingly, if CRs do not preferentially stay in regions where the adiabatic term is mostly negative or positive, then the $\dot{E}_{\rm Ad}$ term will be relatively small, since adiabatic gains compensate adiabatic losses, as occurs in a couple of our "**Advection**" runs.

To explicitly show that CR leakage is significant, in Fig. 4.15 we plot the fraction of CR energy that escapes the central galactic region, $E_{\rm esc}/E_{\rm source}$. We define $E_{\rm source}$ as the total cumulative CR energy input within the central 6 kpc (10 kpc) and $E_{\rm esc}$ as the CR energy that leaves this central region in **Dwarf** ($L\star$ **galaxy**)[21]. Outside of this central region the (hadronic) dissipation time is much longer than 50 Myr. At high CR propagation speeds (e.g. high κ), most of the CR energy indeed escapes the central region, where most γ rays are produced. This shows that CR escape is the main reason for reduced γ ray emission in low-gas-density galaxies.

4.7 Conclusions

We explore the effects of CRs on galaxies, in high-resolution, idealized (non-cosmological) (magneto-)hydrodynamic simulations of dwarf, $L\star$, and sub-$L\star$ starburst galaxies, using the FIRE-2 treatment of the multi-phase ISM, star formation, and stellar feedback, accounting for CR injection from SNe, collisional (hadronic+Coulomb) losses, and CR transport via diffusion and streaming. We focus on constraining CR propagation models (e.g. diffusion and streaming coefficients) using observations of GeV γ-rays from galaxies. Our main conclusions include:

1. We adopt a newly developed two moment method for CR transport, and show that it is computationally efficient and accurate, allowing us to simulate CR transport simultaneously including diffusion and streaming with diffusivities up to $\sim 3\times 10^{29}\,{\rm cm^2\,s^{-1}}$ and $\sim$pc resolution.
2. The CR "transport parameters", in particular, the effective diffusivity $\kappa \equiv |\mathbf{F}_{\rm cr}|/|\nabla_{\parallel} e_{\rm cr}|$ (which can, microphysically, arise from a combination of streaming and diffusion), have a significant impact on galaxy properties and predicted γ-ray emission. With very slow propagation ($\kappa \lesssim 10^{28}{\rm cm^2/s}$), CRs are trapped in the disk and contribute to the mid-plane

---

[21] In practice, we calculate $E_{\rm source}$ by summing up all positive CR energy gains within the central region, including SNe, adiabatic, and the small numerical error terms mentioned in footnote 8. To calculate $E_{\rm esc}$, we sum up all CR energies outside the central region and compensate for the collisional, streaming, and adiabatic losses.

pressure gradients, so suppress SF (albeit only by modest factors $\sim 1.5-2$, *if* hadronic losses which limit the CR energy density are accounted for). However, these models are ruled out because they produce much larger γ-ray luminosities than the observed for dwarf or MW-like systems. At higher $\kappa \gtrsim 10^{28}\,\mathrm{cm^2\,s^{-1}}$, CRs form extended halos. This means they have weak effects on gas *within* the disk, but could help accelerate galactic winds or provide support via pressure gradients in the CGM.

3. The extent of the CR halo, and correspondingly the extent of the pionic γ-ray emission, increase with κ as expected. For e.g. our $L\star$ galaxy, half the CR energy is located within 10 kpc (30 kpc) for $\kappa = 3\times10^{28}\,\mathrm{cm^2\,s^{-1}}$ ($\kappa = 3\times10^{29}\,\mathrm{cm^2\,s^{-1}}$). Correspondingly only about $\sim 50\%$ of the γ-rays are emitted from the central few kpc.

4. In our sub-$L\star$ starburst galaxies, the CR energy density reaches $\sim 10^{2-3}\,\mathrm{eV\,cm^{-3}}$ throughout the burst and is larger than thermal or magnetic pressure in the ISM (for any κ), but is still much smaller than the energy density in turbulent motions or that required to maintain hydrostatic equilibrium. This leads to weak CR effects at the central region of starburst, consistent with the results in L11.

5. We constrain the average CR propagation speed/diffusivity with γ-ray ($>$ GeV) emission from galaxies. The observed $L_\gamma -$ SFR relation requires isotropically-averaged diffusivities $\kappa \sim 3\times10^{29}\mathrm{cm^2/s}$ in dwarf and $L\star$ galaxies, and $\kappa \lesssim 3\times10^{29}\mathrm{cm^2/s}$ in sub-$L\star$ starburst galaxies.

   If CRs are transported only by gas advection, or streaming only at speeds which cannot exceed modestly super-Alfvenic values, or (equivalently) low isotropically-averaged effective diffusivities $\kappa < 3\times10^{28}\,\mathrm{cm^2\,s^{-1}}$,then CRs escape galaxies too slowly and produce γ-ray luminosity close to the calorimetric limit. This over-predicts the observed γ-ray luminosities in dwarfs (e.g. the SMC, LMC, M33) and $L\star$ systems (M31, the MW) by an order of magnitude or more. However, for faster transport parameters (effective $\kappa \sim 3\times10^{28-29}\,\mathrm{cm^2\,s^{-1}}$), CRs escape the dense regions rapidly and the γ-ray luminosity (which scales $\propto e_{\rm cr}\,n_{\rm gas}$) is reduced (especially in dwarf galaxies), predicting γ-ray luminosities in good agreement with those observed as a function of either gas surface density or SFR (see Figs. 4.11 and 4.12).

6. Given the transport parameters required to reproduce the observed $L_{\gamma}/L_{\rm SF}$, we find most CR protons escape from dwarf galaxies, i.e. low-gas-surface-density systems are not proton calorimeters, while our (sub-$L\star$) starburst models are (approximate) proton calorimeters.

7. CR streaming at trans-Alfvenic speeds is relatively slow and cannot alone reduce $L_{\gamma}/L_{\rm SF}$ significantly below the calorimetric limit in our models (as required by observations), even if we allow modestly super-Alfvenic streaming (with $\sim 4\,v_{\rm A}$; see Appendix 4.A). For our favored effective κ, the equivalent streaming speed (using the fact that the CR flux is similar for a diffusivity κ or streaming speed $v_{\rm st} \sim \kappa|\nabla P_{\rm cr}|/P_{\rm cr}$) is $\sim 10-100$ times the Alfven speed.

8. “Adiabatic” effects on CR energy densities (losses in expansion, or gains in compression) can be comparable to injection or collisional loss terms, but cannot alone reduce $L_{\gamma}/L_{\rm SF}$ close to the level required by observations of the MW/SMC/LMC/M33. In dense gas within the galaxies, the net effect of these terms is primarily to increase CR energy density (and L_{γ}), while in low-density gas outside galaxies, it is primarily to decrease the CR energy via expansion in outflows. This means that CR “adiabatic losses” are significant only *after* CRs already diffuse out of the dense ISM gas (where γ-rays are produced).

Our study only scratches the surface of the rich phenomena of CRs in galaxies and leaves out many important details. For example, it is clearly important to study the effects of CRs in cosmological galaxy simulations, which can treat CRs and magnetic field evolution consistently, explore the effects of CRs on magnetic field amplification, self-consistently generate starburst systems (in e.g. mergers), and (perhaps most importantly) explore the interaction of CRs with inflows and outflows in a “live” CGM/IGM environment. We will explore such cosmological runs in future work (Hopkins et al., in preparation).

Although we briefly mentioned the effects of CRs on galactic winds (which are ubiquitous in these simulations), we have not investigated them here. It has been proposed that CR-driven winds could have very different phase structure (compared to thermally-driven winds) and strongly modify the CGM properties (Booth et al., 2013; Salem et al., 2016). Although extensive literature on this topic exists, detailed study of CR winds in (cosmological) simulations that can already self-consistently drive galactic winds with stellar feedback (Muratov et al., 2015; Anglés-Alcázar et al., 2017; Hafen et al., 2019) is largely unexplored. Our simulations provide a unique combination of a high-resolution, multi-phase ISM, with explicit treatment of local star formation in self-gravitating substructures, individually time-resolved SNe and their thermal and momentum feedback combined with CR injection and transport. It will therefore be especially interesting to explore the effects of CRs on the development of galactic winds (Chan et al., in preparation).

We also do not study another important indirect CR constraint, the radio emission from synchrotron radiation, which has been observed in many galaxies (Condon, 1992). These observations provide independent constraints on primary CRs, secondary CR electrons from CR protons, and magnetic fields. It is worth also exploring the observed FIR-radio correlation (van der Kruit, 1971, 1973) with galaxy simulations in a manner similar to our analysis of the connection between SFR and γ-ray emission. However, as mentioned in Lacki et al. (2010), these correlation requires the consideration of secondary CRs, which we plan to incorporate in the future.

Because this was an idealized parameter study, we have adapted a simple model with a constant isotropic/parallel diffusivity κ. But in essentially any physical model, this coefficient depends on local properties of the gas and CRs, in a manner which remains deeply uncertain both theoretically and observationally (see e.g. Jokipii 1966; Enßlin 2003). It would be interesting to investigate galaxy evolution and CR observables in studies where the CR transport coefficients vary dynamically and locally (see e.g. Farber et al., 2018), or with recently-developed models which attempt to actually predict the coefficients self-consistently (Thomas & Pfrommer, 2019).

4.8 ACKNOWLEDGEMENTS

We thank the anonymous referee for the detailed comments that helped to improve this manuscript. We thank Patrick Diamond, Ellen Zweibel, Michael Norman, and Todd Thompson for insightful suggestions and advice, Eve Ostriker for pointing out a typo, and Bili Dong for his help with YT. We would like to thank the Simons Foundation and the participants of the *Galactic Superwinds* symposia for stimulating discussions. TKC and DK were supported by NSF grant AST-1715101 and the Cottrell Scholar Award from the Research Corporation for Science Advancement. Support for PFH was provided by an Alfred P. Sloan Research Fellowship, NSF Collaborative Research Grant #1715847 and CAREER grant #1455342, and NASA grants NNX15AT06G, JPL 1589742, 17-ATP17-0214. EQ was supported in part by a Simons Investigator Award from the Simons Foundation and by NSF grant AST-1715070. The Flatiron Institute is supported by the Simons Foundation. CAFG was supported by NSF through grants AST-1517491, AST-1715216, and CAREER award AST-1652522, by NASA through grants NNX15AB22G and 17-ATP17-0067, and by a Cottrell Scholar Award from the Research Corporation for Science Advancement.

The simulation presented here used computational resources granted by the Extreme Science and Engineering Discovery Environment (XSEDE), which is supported by National Science Foundation grant no. OCI-1053575, specifically allocation TG-AST120025. Numerical calculations were also run on the Caltech compute cluster "Wheeler", allocations from XSEDE TG-AST130039 and PRAC NSF.1713353 supported by the NSF, and NASA HEC SMD-16-7592. This work uses data hosted by the Flatiron Institute's FIRE data hub. This work also made use of

YT (Turk et al., 2011), matplotlib (Hunter, 2007), numpy (van der Walt et al., 2011), scipy (Jones et al., 2001), and NASA's Astrophysics Data System.

4.A A comparison of different streaming parameters

In § 4.3.4, we discussed uncertainties in the parameters describing CR streaming: both the streaming speed $v_{\rm st}$ and magnitude of the streaming loss term $\Gamma_{\rm st} = -\mathbf{v}_{\rm A} \cdot \nabla P_{\rm cr}$ owing to excited and thermalized high-frequency Alfven waves (independent of streaming speed; see §4.3.4). Here we explore these more thoroughly. We consider four model variations:

1. "$v_{\rm st} = v_{\rm A}$": This is our default choice in the main text, with streaming speed equal to the Alfven speed.
2. "$v_{\rm st} = 3v_{\rm A}$": Here $v_{\rm st} = 3\,v_{\rm A}$, one of the super Alfvenic speeds considered in Ruszkowski et al. (2017).
3. "$v_{\rm st} = 4v_{\rm A}$": Here $v_{\rm st} = 4v_{\rm A}$, another super Alfvenic speed considered in Ruszkowski et al. (2017)
4. "$v_{\rm st} = v_{\rm A+c_s}$": Here $v_{\rm st} = \sqrt{v_{\rm A}^2 + c_{\rm s}^2}$, the fastest MHD wavespeed (which has no particular physical motivation but resembles what might be inferred in hydrodynamic models or observations where a plasma $\beta \sim 1$ is simply assumed).

Fig. 4.16 summarizes the results: the effects of this choice are much smaller than the variations of e.g. κ discussed in the main text. Most importantly, we see *no* difference in averaged $L_\gamma/L_{\rm SF}$ (although there are significant fluctuations due to stochasticity), implying that streaming at these speeds – even if modestly super-Alfvenic streaming is allowed – is ineffective at transporting CRs from dense regions. Of course, if we limit the "streaming losses" to scale with $\mathbf{v}_{\rm A} \cdot \nabla P_{\rm cr}$ and continue to increase $v_{\rm st}$ without limit, it will eventually become "fast enough." In fact, our Eq. 4.4

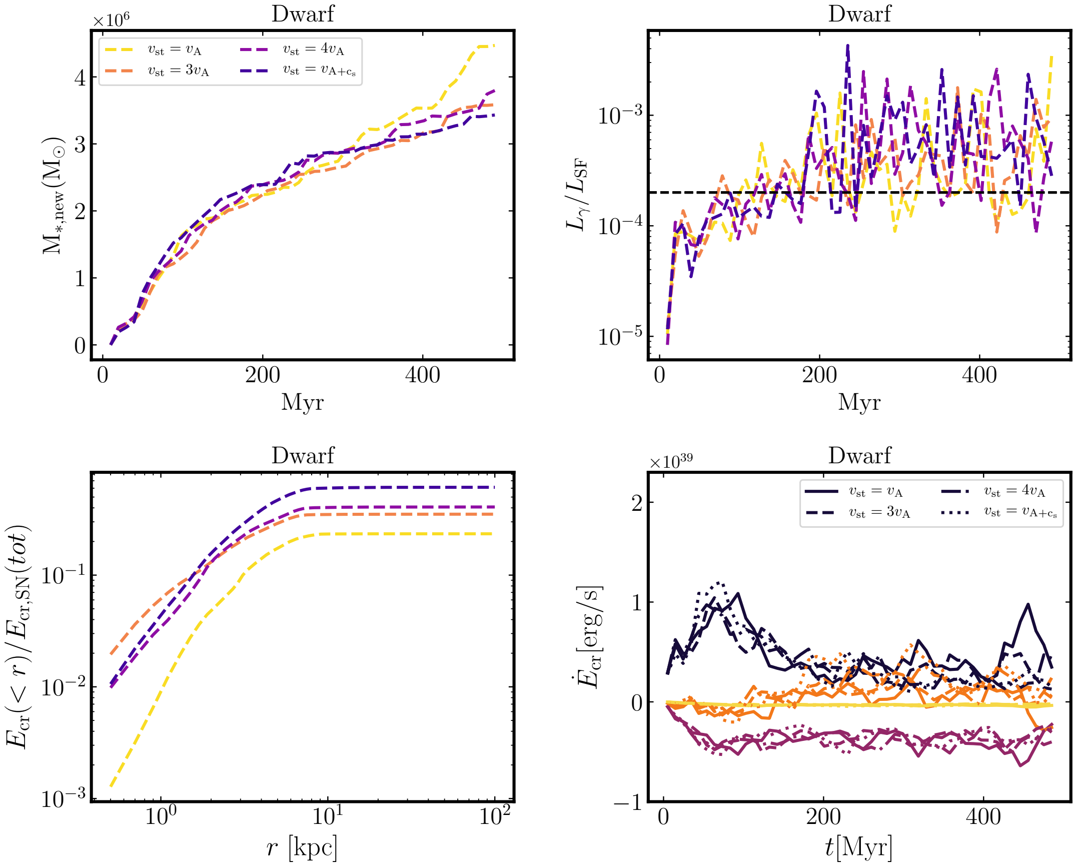

Figure 4.16: Comparison of effects of different CR streaming speeds and loss rates, described in Appendix 4.A. *Top Left:* Stellar mass vs. time (as Fig. 4.5). *Top Right:* γ-ray luminosity relative to SF luminosity (as Fig. 4.10). *Bottom Left:* Cumulative CR energy vs. radius (as Fig. 4.3). *Bottom Right:* CR energy gain/loss rate (as Fig. 4.13) via injection (black), adiabatic terms (orange), streaming losses (yellow), collisional losses (purple). There are only small differences between streaming schemes, compared to e.g. the effects of changing the diffusion coefficient κ. Most importantly, the $L_\gamma/L_{\rm SF}$ ratio is around the calorimetric limit regardless of which streaming scheme we used (here there is no additional diffusion), which means streaming – even when modestly super-Alfvenic – is not effective in transporting CRs from the galaxies.

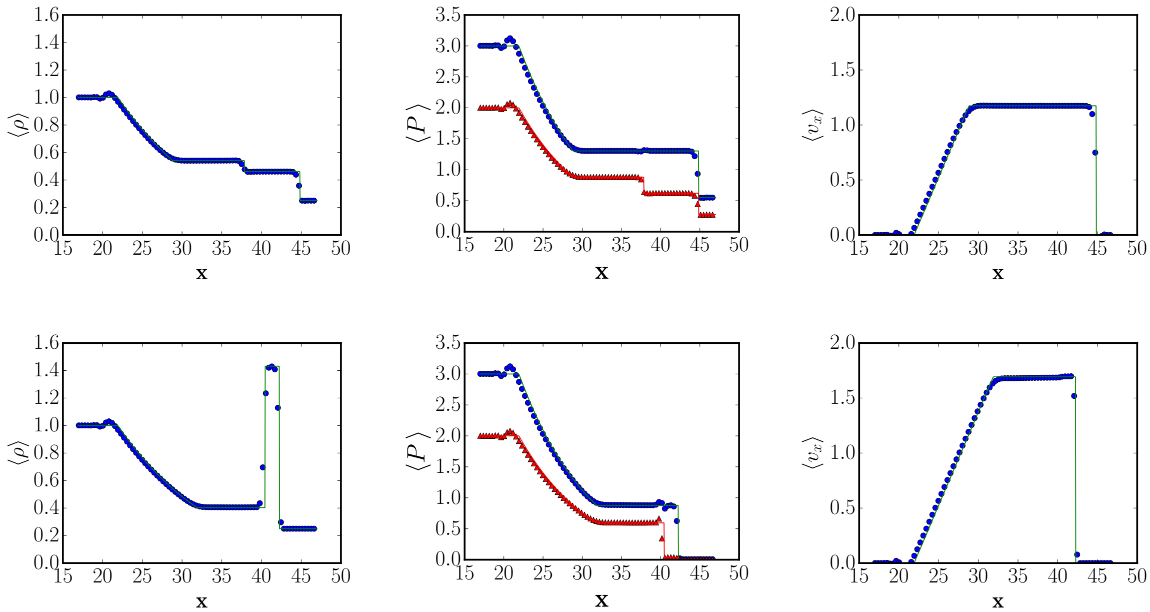

Figure 4.17: Density, pressure and gas velocity profiles of the Sod shocktubes with a composite of gas and CR (§ 4.B.1). We show a shocktube with Mach number $M = 1.5$ in the top panels and $M = 10$ in the bottom panels. In the left panels, we show the volume averaged gas densities from the analytic calculations (*green* lines; from Appendix B of Pfrommer et al. 2006) and simulations (*blue* points). In the center panels, the green lines and blue points show the analytic and simulated volume-averaged total (gas + CR) pressure, respectively. Red lines and points show analytic and simulated volume-averaged CR pressure, respectively. In the right panels, we show the volume averaged gas velocities in the x direction. The simulations are a good match to the analytic solutions.

shows that, given the manner in which we approximate CR transport numerically, κ and $v_{\rm st}$ are formally degenerate if we replace κ with $v_{\rm st} \rightarrow \kappa|\hat{\mathbf{B}}\cdot\nabla e_{\rm cr}|/(e_{\rm cr}+P_{\rm cr})$. From this, using a typical CR gradient scale length $\sim 1-10\,{\rm kpc}$ in our galaxies and favored $\kappa \sim 3\times10^{29}\,{\rm cm^{-2}\,s^{-1}}$, we see that $v_{\rm st} \sim 100-1000\,{\rm km\,s^{-1}} \gg v_{\rm A}$ (and $\gg c_s$ in most of the ISM) is required.

We have run the similar tests with our $L\star$ galaxy model (not shown) and find qualitatively identical results (with even smaller differences between streaming models).

4.B Numerical Tests

Our CR transport implementation is described in § 4.3.5. Here we present some numerical tests, including simple code validation problems, tests of the effect of the maximum CR free-streaming speed (or "reduced speed of light" $\tilde{c}$), comparison of our two-moment implementation to zeroth-moment "pure diffusion" solvers, and numerical resolution studies.

4.B.1 CR Shocktube Test

We test our code implementation of CR coupling to adiabatic and advective terms and in the MHD Riemann problem using a variation of the Sod (1978) shocktube presented in Pfrommer et al. (2006). A 3D box of of dimensions $64 \times 16 \times 16$ is full of gas (adiabatic index 7/5) and CRs. Half the box has initial $(\rho, v_x/c_s, P_{\rm gas}, P_{\rm cr}) = (1,1,1,2)$ and the other half has $(0.25, 1.5, 0.275, 0.275)$. We also consider another shocktube with $(1,1,1,2)$ and $(0.25, 10, 0.00384, 0.00384)$. In both our mass resolution is 0.004. CRs have no diffusion or streaming (just advection).

Fig. 4.17 compares with analytic solutions from Pfrommer et al. (2006) at $t = 5$. The agreement is good (despite very small shock broadening and numerical oscillations near discontinuities). The small "bumps" on the left close to x=20 are due to the slope limiter and should converge away at a higher resolution in our MFM method (see the hydrodynamic Sod shocktube test in Hopkins 2015a).

4.B.2 Idealized Diffusion Test

We now test a "diffusion" problem to validate the diffusive terms in our CR transport implementation, i.e. a problem where the gas does not move or respond to CRs (we disable the terms by which the CRs act on the gas), but the CRs are transported ($\tilde{\mathbf{F}}_{\rm cr} \neq 0$). The corresponding

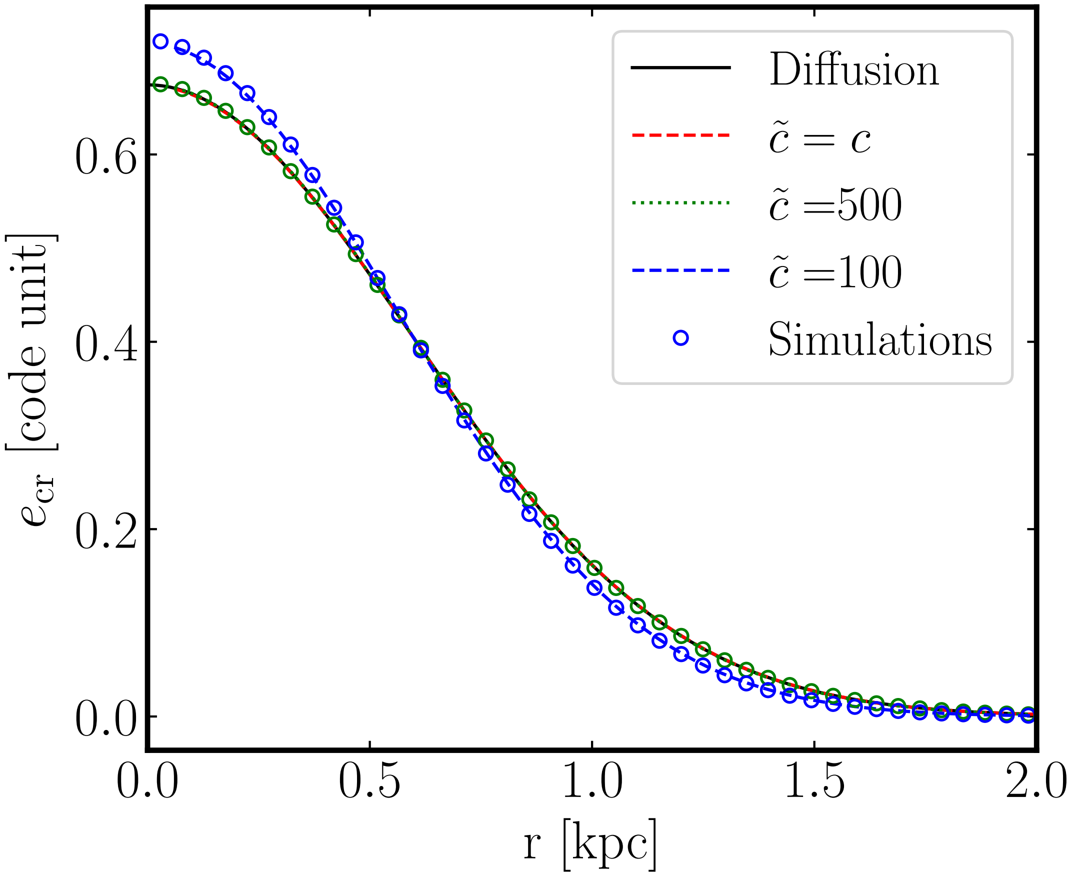

Figure 4.18: Idealized 1D CR diffusion test (§ 4.B.2), run for 5 Myr. We solve the two-moment CR transfer equation with $\tilde{c}$ given (in $\mathrm{km\,s^{-1}}$) and $\kappa = 3\times10^{27}\,\mathrm{cm^2\,s^{-1}}$ given an initial Gaussian CR energy density with $\sigma = 0.5\,\mathrm{kpc}$. Lines show analytic solutions for both finite $\tilde{c}$ and the "pure diffusion" equation, whereas points show simulation results (colors represent $\tilde{c}$). At all $\tilde{c}$ the numerical solutions agree well with the analytic result. Also, given these spatial/timescales, the difference between solutions with finite $\tilde{c} \gtrsim 500\,\mathrm{km\,s^{-1}}$, $\tilde{c} = c$, and "pure diffusion" is extremely small, and even at $\tilde{c} = 100\,\mathrm{km\,s^{-1}}$ the solutions differ by less than 10%.

"two moment" equation is

$$\frac{\partial e_{\rm cr}}{\partial t}+\frac{\kappa}{(\gamma_{\rm cr}-1)\tilde{c}^2}\frac{\partial^2 e_{\rm cr}}{\partial t^2}=\kappa\nabla^2 e_{\rm cr}, \tag{4.12}$$

which is a telegraph equation.

We initialize a 1D Gaussian distribution in $e_{\rm cr}^0 \equiv e_{\rm cr}(r, t=0)$, centered at $r=0$, with total energy $E_{\rm cr}=1$, width $\sigma=0.5\,{\rm kpc}$ at the center of a 5-kpc cube with 2048 resolution elements, set constant $\kappa=3\times10^{27}\,{\rm cm^2\,s^{-1}}$, and set $\tilde{c}=100\,{\rm km\,s^{-1}}$ or $500\,{\rm km\,s^{-1}}$, and evolve the system for 5 Myr. We do not include magnetic fields so the diffusion is isotropic. Given the symmetry of the problem, this can be solved exactly via the usual separation of modes, giving solutions of the form:

$$e_{\rm cr}(\mathbf{r},t)=\int d\mathbf{k}\,a_{\mathbf{k}}^{\pm}\exp\{i[\mathbf{k}\cdot\mathbf{r}-\omega_{\mathbf{k}}^{\pm}t]\}, \tag{4.13}$$

where $\kappa\omega_{\mathbf{k}}^2/(\gamma_{\rm cr}-1)/\tilde{c}^2+i\,\omega_{\mathbf{k}}=\kappa k^2$ and $\omega_{\mathbf{k}}^{\pm}$ are two roots of the previous equation,

$$\omega_{\mathbf{k}}^{\pm}=\frac{-i\pm\sqrt{4\kappa^2k^2/(\gamma_{\rm cr}-1)/\tilde{c}^2-1}}{2\kappa/(\gamma_{\rm cr}-1)/\tilde{c}^2}. \tag{4.14}$$

In our "diffusion" test, the initial CR flux is set to zero. Together with the initial CR energy density, we can solve for

$$a_{\mathbf{k}}^{\pm}=\frac{1}{(2\pi)^D}\frac{\exp(-\sigma^2k^2/2)}{1-\omega_{\mathbf{k}}^{\pm}/\omega_{\mathbf{k}}^{\mp}}, \tag{4.15}$$

where D is the dimension of the Gaussian packet. With Eqs. 4.14 and 4.15, the time evolution of CR energy density can then be calculated by integrating Eq. 4.13 numerically.

This problem is entirely scale-free, and we can transform to solutions with any other value of κ via suitable re-scaling. As $\tilde{c}^2\,t/\kappa\rightarrow\infty$, the solutions progressively approach the solution of the pure diffusion equation[22], which is:

$$e_{\rm CR}(\mathbf{r},t,\tilde{c}\to\infty)\to\frac{\exp\left[-\frac{r^2}{2(2\kappa t+\sigma^2)}\right]}{[2\pi(2\kappa t+\sigma^2)]^{3/2}}. \tag{4.16}$$

Fig. 4.18 shows the results of our simulation for varying $\tilde{c}$ at fixed κ and t (i.e. varying the dimensionless parameters $\tilde{c}^2 t/\kappa$ and $r\tilde{c}/\kappa$ which determine the behavior of the problem)[23]. In all cases, the agreement with the exact solution is excellent, with numerical integration errors less than one percent. This validates that our two-moment implementation correctly solves the desired diffusion problem.

Moreover, Fig. 4.18 also gives us a practical estimate – for typical units and spatial scales of our simulations – of the rate at which solutions with lower $\tilde{c}$ converge to the solution with $\tilde{c}=c$ (the speed of light). In Fig. 4.18, the test with $\tilde{c}=500\,{\rm km\,s^{-1}}$ is already effectively indistinguishable from the "pure diffusion" solution. Even at $\tilde{c}=100\,{\rm km\,s^{-1}}$, the solutions differ only by less than 10%.

Of course, in real problems with bulk *gas* flows (e.g. galactic rotation), such a slow maximum CR transport speed would mean CRs would lag advection, in an unphysical manner, which motivates our additional tests below.

4.B.3 Comparison of Zeroth and Two Moment Approximations in Galaxy Simulations

In Figure 4.19, we compare results of a full galaxy simulation using, instead of our default two-moment expansion (where we explicitly evolve the CR flux $\tilde{\mathbf{F}}_{\rm cr}$ with a finite maximum free-streaming speed $\tilde{c}$, as discussed in § 4.3), the "zeroth moment" or "pure diffusion" method

---

[22] Specifically, at this limit, the $a_{\mathbf{k}}^{-}$ term becomes exponentially small and the $a_{\mathbf{k}}^{+}$ term approaches the "pure diffusion" solution. Thus the solution to the two moment equation converges to the "pure diffusion" solution insensitive to the initial condition.

[23] We have turned off the HLL flux in the simulation to avoid small numerical diffusion.

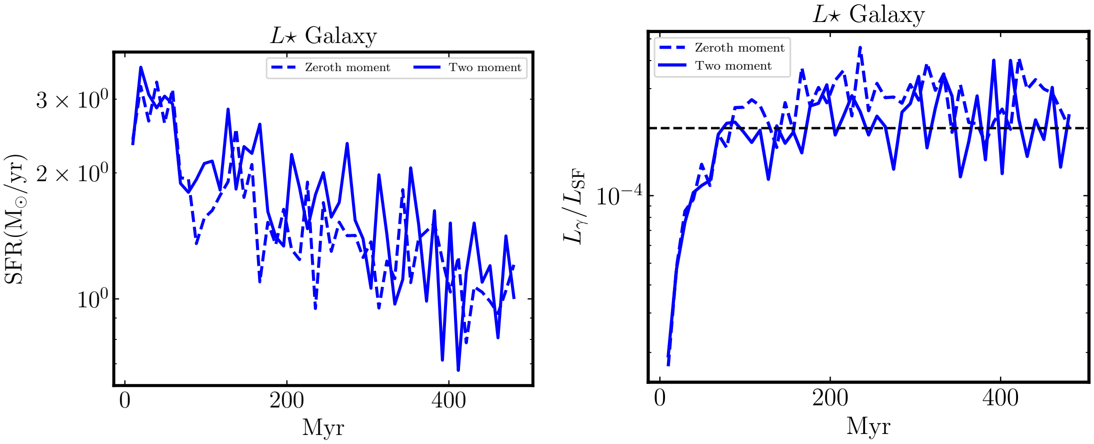

Figure 4.19: SFR and $L_\gamma/L_{\rm SF}$ as Fig. 4.23, comparing runs with $\kappa = 3\times10^{27}\,{\rm cm^2\,s^{-1}}$ using either (a) our default two-moment CR transport solver, with $\tilde{c} = 400\,{\rm km\,s^{-1}}$, or (b) the "zeroth-moment" method (solve a pure single-diffusion equation, i.e. fixing $\mathbf{F}_{\rm cr} = -\kappa\nabla e_{\rm cr}$). The "zeroth-moment" solution is mathematically equivalent to $\tilde{c}\to\infty$. We see no meaningful systematic difference (if anything, $L_\gamma/L_{\rm SF}$ is slightly higher with $\tilde{c}\to\infty$, but this owes mostly to stochastic run-to-run variations here).

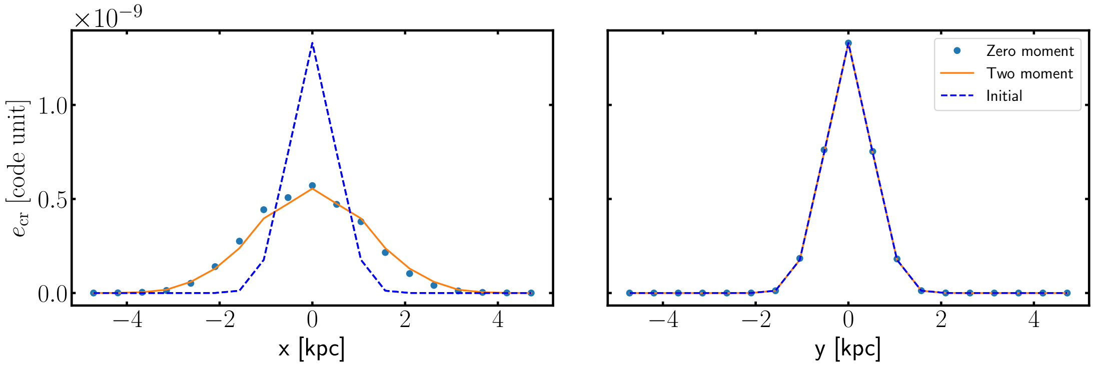

Figure 4.20: 3D anisotropic diffusion tests as described in §4.B.4. We set a uniform magnetic field along the x direction. We consider CR energy density within thin slices along the z=0 (left) and x=0 (right) planes. CRs can only diffuse along the B field direction but not perpendicular to the B field in both schemes (but see caveats in §4.B.5). The resultant CR energy densities in the two schemes are in very good agreement.

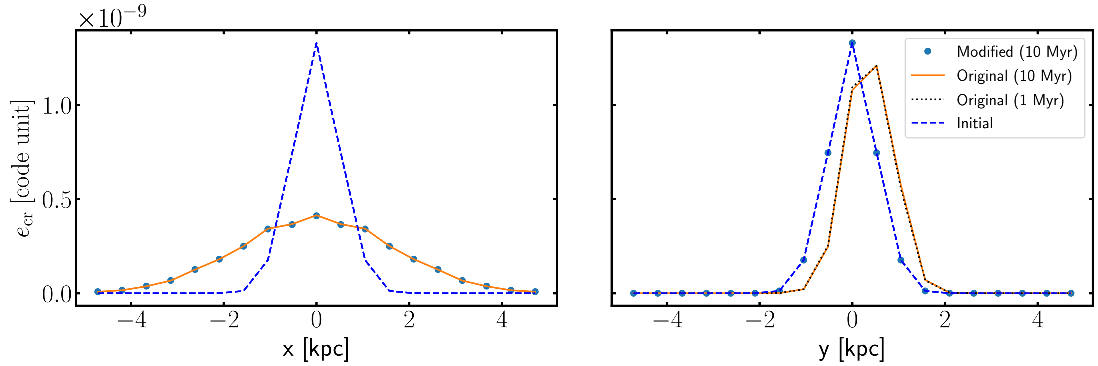

Figure 4.21: 3D anisotropic diffusion tests as described in §4.B.4 and Fig. 4.20, but with an initial CR flux pointing to the positive y direction (perpendicular to the B field, which points along the x direction; see §4.B.5) and evolved over 10 Myr, except "Original (1 Myr)", which evolved over 1 Myr only. Here we consider two implementations of anisotropic diffusion, "Original" (Eq. 4.3, default case in the main text) and "Modified" (Eq. 4.17; see the description in §4.B.5). We also show the CR energy density (black dotted) at t = 1 Myr with "Original" on the right panel. We find that while the CR energy densities in both formulations agree very well along the B field (left panel), CRs can propagate across the B field in "Original", but not in "Modified" (right panel). However, the perpendicular CR flux is small and vanishes after 1 Myr, as shown by the overlap of the "Original (10 Myr)" and "Original (1 Myr)" lines.

(for detailed tests of our pure isotropic/anisotropic diffusion solver, we refer to Hopkins 2017). In the equations of motion, the latter simply replaces the explicitly-evolved flux vector with the value $\tilde{\mathbf{F}}_{\rm cr} = -\kappa\nabla e_{\rm cr}$. This is mathematically equivalent to taking $\tilde{c} \to \infty$, and imposes a number of numerical difficulties discussed in § 4.3 (not least of which is a much smaller timestep limit). However, Fig. 4.19 shows there are only small differences in SFR and $L_\gamma/L_{\rm SF}$ between these two approaches. We find the same in all other galaxy properties studied here.

4.B.4 Anisotropic Diffusion Test

We next test our scheme with an intrinsically multi-dimensional anisotropic diffusion test. We consider an initial 3D (256 particles on a side) spherically symmetric Gaussian profile with an anisotropic diffusion coefficient $\kappa = 3\times10^{28}{\rm cm^2/s}$ and a fixed B field pointing in the x direction. We set $\tilde{c} = 1000\,{\rm km/s}$, initial $\mathbf{F}_{\rm cr} = 0$, and evolve over 5 Myr with the zeroth moment ("pure diffusion") and two moment schemes. Fig. 4.20 show the resultant CR energy densities through

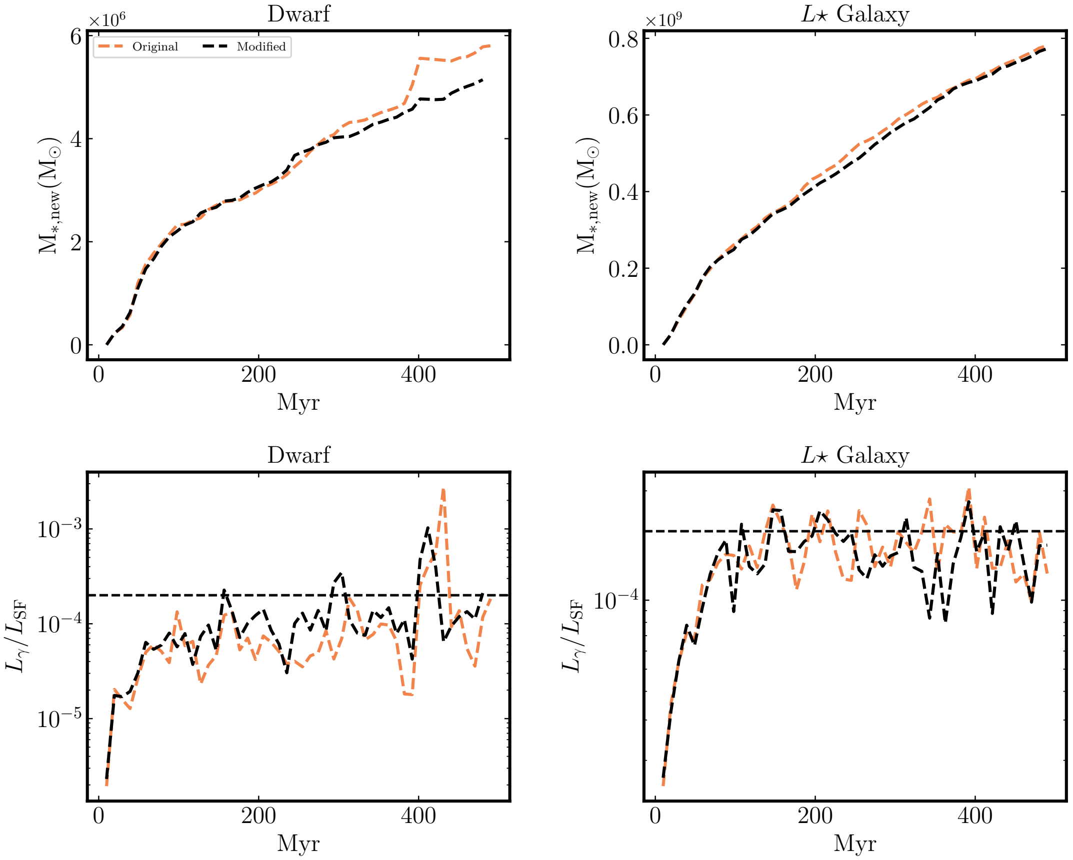

Figure 4.22: Time evolution of stellar mass accumulation (*top*) and ratio between pionic γ-ray luminosity and the total SF luminosity (*bottom*) with the "Original" (Eq. 4.3) and "Modified" (Eq. 4.17) formulations (see §4.B.5). Two formulations give similar star formation and $L_\gamma/L_{\rm SF}$, so the choice between two formulations should have negligible effects on our conclusions.

the x or y planes. We found a good agreement between two schemes and that CRs only diffuse along the B field direction (if there is no initial $\mathbf{F}_{\rm cr}$ perpendicular to the B field; see §4.B.5). We have also checked that the total CR energy is conserved (with deviations smaller than one in a thousand) in both schemes.

4.B.5 Test of a variation in the CR flux equation (Eq. 4.3)

Eq. 4.3 governs the CR flux evolution, and obviously approaches the desired anisotropic diffusion+streaming equation (with $\tilde{\mathbf{F}}_{\rm cr} \rightarrow -\kappa_{*}\,\nabla_{\parallel} e_{\rm cr}$) when $\tilde{c} \rightarrow \infty$ is large, or in local quasi-steady-state ($\partial \tilde{\mathbf{F}}_{\rm cr}/\partial t \rightarrow 0$), or on spatial scales $> \kappa/\tilde{c}$ (timescales $> \kappa/\tilde{c}^2$). However, on small spatial/time scales when out-of-equilibrium, small fluxes perpendicular to the magnetic fields can arise from either integration error or rapid small-scale fluctuations in the magnetic field direction[24]. If we divide the flux into parallel and perpendicular components $\tilde{\mathbf{F}}_{\rm cr} = \tilde{\mathbf{F}}_{{\rm cr},\parallel} + \tilde{\mathbf{F}}_{{\rm cr},\perp}$, then we see the perpendicular component obeys $\tilde{c}^{-2}\,\partial \tilde{\mathbf{F}}_{{\rm cr},\perp}/\partial t = -[(\gamma_{\rm cr}-1)/\kappa_{*}]\,\tilde{\mathbf{F}}_{{\rm cr},\perp}$ (taking $\mathbf{v} = 0$, for simplicity, though this does not change our conclusions below). So an initial $\tilde{\mathbf{F}}_{{\rm cr},\perp}$ can formally propagate but will be exponentially damped on a timescale $\sim \kappa_{*}/\tilde{c}^2$. For κ^{*} needed to match the γ ray luminosity of nearby galaxies ($\sim 10^{29}$) and $\tilde{c} \sim 1000\,{\rm km/s}$, this timescale is $\sim 0.2\,{\rm Myr}$, much shorter than the hadronic interaction time in the MW's ISM ($n_{\rm ISM} \sim 1\,{\rm cm}^{-3}$), so our γ ray constraint will not be affected with or without $\tilde{\mathbf{F}}_{{\rm cr},\perp}$ (well within the uncertainties). Likewise since this is much shorter than relevant dynamical times, essentially no effects of CR pressure and other dynamics should be altered.

If desired, we can trivially set $\tilde{\mathbf{F}}_{{\rm cr},\perp} = 0$ every timestep, and evolve only the parallel component of Eq. 4.3:

$$\frac{1}{\tilde{c}^2}\left[\frac{\partial \tilde{\mathbf{F}}_{\rm cr}}{\partial t} + \nabla\cdot\left(\mathbf{v}\otimes\tilde{\mathbf{F}}_{\rm cr}\right)\right]_{\parallel} + \nabla_{\parallel} P_{\rm cr} = -\frac{(\gamma_{\rm cr}-1)}{\kappa^{*}}\,\tilde{\mathbf{F}}_{{\rm cr},\parallel} \tag{4.17}$$

---

[24] We thank the anonymous referee pointing out this potential issue.

where $\mathbf{X}_{\|} \equiv (\hat{\mathbf{B}} \otimes \hat{\mathbf{B}}) \cdot \mathbf{X}$. We have implemented Eq. 4.17 and compare it (in Fig. 4.21) to our default Eq. 4.3 in an anisotropic diffusion test (as § 4.B.4) with an initial (intentionally erroneous) pure-perpendicular flux $\tilde{\mathbf{F}}_{\rm cr} = \tilde{\mathbf{F}}_{{\rm cr},\perp} = (2000\,{\rm km/s})e_{\rm cr}\hat{y}$. This shows that the "original" Eq. 4.3 does formally allow CRs to propagate perpendicular to the B field, although the effect is rapidly damped, while the "modified" Eq. 4.17 does not.

Fig. 4.22 compares two galaxy simulations (**Dwarf** and $L\star$ **galaxy**, with the latter at one level lower resolution than the fiducial main-text case) run with MHD (anisotropic diffusion), $\kappa_{\|}$=3e28, and either Eq. 4.3 or Eq. 4.17. We find essentially no difference in their star formation rates or gamma-ray luminosities (apart from a small stochastic deviation associated with one slightly-stronger burst in the dwarf run). This is expected given the arguments above. Moreover, note that all the differences between Eq. 4.3 and Eq. 4.17 appear on scales $\ll \kappa/\tilde{c}$; but § 4.B.3 showed that taking $\tilde{c} \rightarrow \infty$ does not change our conclusions.

Of course, CRs *can* physically propagate across mean magnetic fields due to unresolved (micro-scale) magnetic turbulence (Zweibel, 2017; Farber et al., 2018), so a small $\tilde{\mathbf{F}}_{{\rm cr},\perp}$ might not be unreasonable. But in the main text, we show that even much larger perpendicular diffusivities given by assuming *isotropic* diffusion (much larger than the fluxes that arise from the numerical or physical effects described above) do not strongly alter our conclusions regarding either the effects of CRs or the observationally-favored effective κ.

It is worth noting that several recent studies including this one and Zweibel (2017), Jiang & Oh (2018), and Thomas & Pfrommer (2019) have adopted slightly-different forms of the CR flux equation (although the CR energy equation is consistent in all cases). If we impose some desired scattering (κ_*), all of these can be written (after some algebra) in the form:

$$\frac{1}{\tilde{c}^2}\,\mathbb{D}_t\tilde{\mathbf{F}}_{\rm cr} + \nabla_{\|}P_{\rm cr} = -\frac{(\gamma_{\rm cr}-1)}{\kappa_*}\,\tilde{\mathbf{F}}_{\rm cr}, \tag{4.18}$$

where the differences are contained in the operator $\mathbb{D}_t$. For our default Eq. 4.3, $\mathbb{D}_t\tilde{\mathbf{F}}_{\rm cr} = \partial\tilde{\mathbf{F}}_{\rm cr}/\partial t +$

$\nabla\cdot(\mathbf{v}\otimes\tilde{\mathbf{F}}_{\rm cr})$. For the zeroth-moment or “pure diffusion+streaming” equation in § 4.B.3, $\mathbb{D}_t\tilde{\mathbf{F}}_{\rm cr}=\mathbf{0}$. For Jiang & Oh (2018), $\mathbb{D}_t\tilde{\mathbf{F}}_{\rm cr}=[\partial\{\tilde{\mathbf{F}}_{\rm cr}+\mathbf{v}\,(e_{\rm cr}+P_{\rm cr})\}/\partial t]_{\parallel}$, and for Thomas & Pfrommer (2019), $\mathbb{D}_t\tilde{\mathbf{F}}_{\rm cr}=\hat{\tilde{\mathbf{F}}}_{\rm cr}\,[\partial|\tilde{\mathbf{F}}_{\rm cr}|/\partial t+\nabla\cdot(\mathbf{v}\,|\tilde{\mathbf{F}}_{\rm cr}|)+\tilde{\mathbf{F}}_{\rm cr}\cdot\{(\hat{\tilde{\mathbf{F}}}_{\rm cr}\cdot\nabla)\mathbf{v}\}]=\partial\tilde{\mathbf{F}}_{\rm cr}/\partial t+\nabla\cdot(\mathbf{v}\otimes\tilde{\mathbf{F}}_{\rm cr})+(\tilde{\mathbf{F}}_{\rm cr}\cdot\nabla)\,(\mathbf{v}_{\parallel}-\mathbf{v}_{\perp})$, with $\tilde{\mathbf{F}}_{{\rm cr},\perp}=\mathbf{0}$.[25]

What is important for our purposes here is to note that all of these expressions differ only inside the term suppressed by $\tilde{c}^{-2}$. This means they all relax to the same diffusion+streaming equation in quasi-steady state and/or as $\tilde{c}\rightarrow\infty$, and differ only on scales below the CR mean free path $\sim\kappa/\tilde{c}$. To the extent that our galaxy-scale results are converged with respect to the value of $\tilde{c}$, and are not changed if we take $\tilde{c}\rightarrow\infty$ (§ 4.B.3), these differences in $\mathbb{D}_t\tilde{\mathbf{F}}_{\rm cr}$ cannot alter our conclusions. Moreover, if we adopt a “reduced speed of light” $\tilde{c}\ll c$, then by definition the flux equation does not exactly represent reality on scales $\ll\kappa/\tilde{c}$, *regardless* of the form of $\mathbb{D}_t$ (i.e. the regime where these expressions differ is exactly where they all become inexact when $\tilde{c}\ll c$ is adopted). We have explicitly verified that our conclusions are robust to these choices of flux equation, running limited galaxy-scale simulations with the forms of $\mathbb{D}_t\tilde{\mathbf{F}}_{\rm cr}$ from Jiang & Oh (2018) or Thomas & Pfrommer (2019) as defined above: the results are similar to those in Fig. 4.22.

4.B.6 Comparison of Different (Finite) Maximum CR Propagation Speeds in Galaxy Simulations

We now examine the effect of varying $\tilde{c}$ on a full simulation (our $L\star$ model). For $\tilde{c}\gtrsim 500\,{\rm km\,s^{-1}}$, which is generally faster than the bulk rotation and outflow speeds (at least those containing most of the gas) in the galaxies, Fig. 4.23 shows there is a small impact of $\tilde{c}$ on the SFR (we find the same for all other galaxy properties, not shown here). For $L_{\gamma}/L_{\rm SF}$, we find

---

[25] For Jiang & Oh (2018), we have formally taken the limit of the diffusion/interaction tensor $\mathbb{K}\equiv\kappa_{*}\,(\hat{\mathbf{B}}\otimes\hat{\mathbf{B}})+\kappa_{\perp}\,(\mathbb{I}-\hat{\mathbf{B}}\otimes\hat{\mathbf{B}})$ ($\mathbb{I}$ is the identity tensor) as $\kappa_{\perp}\rightarrow 0$. For Thomas & Pfrommer (2019), we use $\tilde{\mathbf{F}}_{\rm cr}=|\tilde{\mathbf{F}}_{\rm cr}|\,\hat{\tilde{\mathbf{F}}}_{\rm cr}=f_{\rm cr}\,\hat{\mathbf{B}}$ in their notation, and replace their scattering term $\partial f/\partial t|_{\rm scatt}$ (which explicitly attempts to account for dynamically-evolving, forward-and-backward propagating gyro-scale Alfven waves) with $-[(\gamma_{\rm cr}-1)/\kappa_{*}]\tilde{\mathbf{F}}_{\rm cr}$ for a locally-stationary κ_{*}.

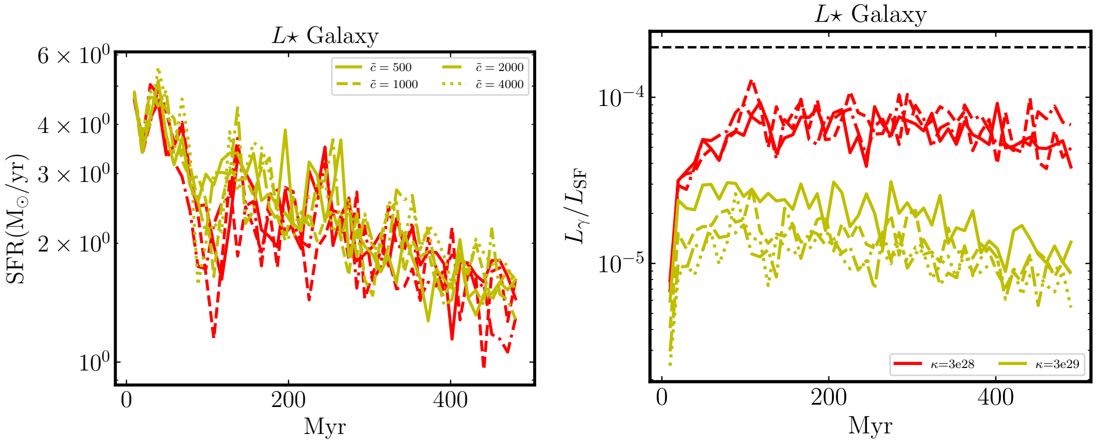

Figure 4.23: Time evolution of SFR (*top*, as Fig. 4.5) and ratio between pionic γ-ray and total SF luminosity (*bottom*, as Fig. 4.10, with different "maximum CR free-streaming speeds" $\tilde{c}$ (equivalently, "reduced speed of light" for CRs) in $\mathrm{km\,s^{-1}}$, and different κ (see § 4.B.6). We show the $L\star$ galaxy without magnetic fields or streaming (dependence on $\tilde{c}$ is smaller with these added). One $\tilde{c}$ is faster than bulk transport and diffusive CR escape velocities from the disk, the results should be independent of it, and we confirm this. For $\kappa < 10^{29}\,\mathrm{cm^2\,s^{-1}}$, we see no systematic differences for any $\tilde{c} \gtrsim 500\,\mathrm{km\,s^{-1}}$. For larger κ these same values produce no detectable difference in galaxy properties, but the "slowest" ($\tilde{c} \sim 500\,\mathrm{km\,s^{-1}}$) produces a slightly larger (factor ~ 1.4) $L_\gamma / L_{\rm SF}$ owing to slightly slower CR escape.

almost no impact of $\tilde{c}$ in simulations with $\kappa < 10^{29}\mathrm{cm^2/s}$ for any values $\tilde{c} \gtrsim 500\,\mathrm{km\,s^{-1}}$.

Because the effective "advective velocity" of CRs under pure diffusion is $\sim \kappa/\ell$ (where ℓ is some gradient scale-length), at much larger diffusion coefficients, e.g. our $\kappa = 3 \times 10^{29}\,\mathrm{cm^2\,s^{-1}}$, where *most* of the CRs escape diffusively, the value of L_γ is slightly larger for $\tilde{c} = 500\,\mathrm{km\,s^{-1}}$ compared to much-higher $\tilde{c}$ (because escape is slightly slower). But once $\tilde{c} \geq 1000\,\mathrm{km\,s^{-1}}$, we see no detectable difference. Moreover by the latter half of the time we run for, the differences even for $\tilde{c} = 500\,\mathrm{km\,s^{-1}}$ (compared to $\tilde{c} \sim 4000\,\mathrm{km\,s^{-1}}$) at $\kappa = 3 \times 10^{29}\,\mathrm{cm^2\,s^{-1}}$ are factors of ~ 1.4, not large enough to change any of our conclusions.

In tests run for shorter duration and tests of our **Dwarf** galaxy (not shown), we have also verified similar conclusions, and found that runs with magnetic fields (since these slow down the transport) and finite streaming velocities (since these dominate the transport over diffusion in some regimes) exhibit even weaker dependence on $\tilde{c}$ within the range $\tilde{c} \sim 500 - 4000\,\mathrm{km\,s^{-1}}$, even at $\kappa = 3 \times 10^{29}\,\mathrm{cm^2\,s^{-1}}$.

4.B.7 Idealized Streaming Test

Here we test our streaming implementation with an initial 1D symmetric triangular CR profile with $e_{\rm cr} = 2 - |x|$ (and $\mathbf{F}_{\rm cr} = \mathbf{v}_{\rm str} e_{\rm cr}$), where we disable the gas motion and CR streaming loss ($v_{\rm st} \cdot \nabla P_{\rm cr}$), but CRs can move across gas particles with a constant $v_{\rm st} = 1$ km/s. In the numerical test, we consider evenly spaced 2048 particles over 10 kpc, the reduced speed of light $\tilde{c} = 1000\,{\rm km/s}$, and a small diffusion coefficient 3×10^{22} cm^2/s.[26] Here, we also consider a variant test in which we relax the limiter on CR pressure gradient[27] in order to correctly capture the plateau region and also turn off the HLL flux to avoid numerical diffusion smoothing the discontinuity (so we can cleanly separate the effects of numerical dissipation, which are resolution-dependent, and the effects of the actual form of the flux equation and its implementation of streaming).[28] We also show the "original" test run with the original limiter and the HLL flux included, to illustrate the version that we used in the main text.

The analytic solution, calculated in Jiang & Oh (2018), has a flat CR distribution between $x = \pm x_{\rm m}$ and two inclined distributions for $|x| > x_{\rm m}$ & $|x| < 1$ with

$$e_{\rm cr}(x,t) = 2 + 4 v_{\rm st} t - |x|, \tag{4.19}$$

and $x_{\rm m}$ is determined from the energy conservation:

$$x_{\rm m} = \sqrt{\left(1 + \frac{4}{3} v_{\rm st} t\right)^2 + \frac{8 v_{\rm st} t}{3} - 1}. \tag{4.20}$$

Fig. 4.24 shows the analytic solution agrees well with our numerical solution at $t = 10\,{\rm Myr}$, although the "original" run has a round top rather than a plateau mainly because of the limiter on

---

[26] We include a very small diffusion coefficient to avoid potential (numerical) overflows in Eq. 4.3, i.e. when the CR pressure profile is flat or, equivalently, $\nabla P_{\rm cr}$ is huge.

[27] The limiter is necessary to avoid divergence and other numerical issues in realistic galaxy simulations.

[28] Because the exact solution to this test contains dis-continuous first derivatives, any numerically stable method will introduce some dissipation at the cusps, even at infinite resolution.

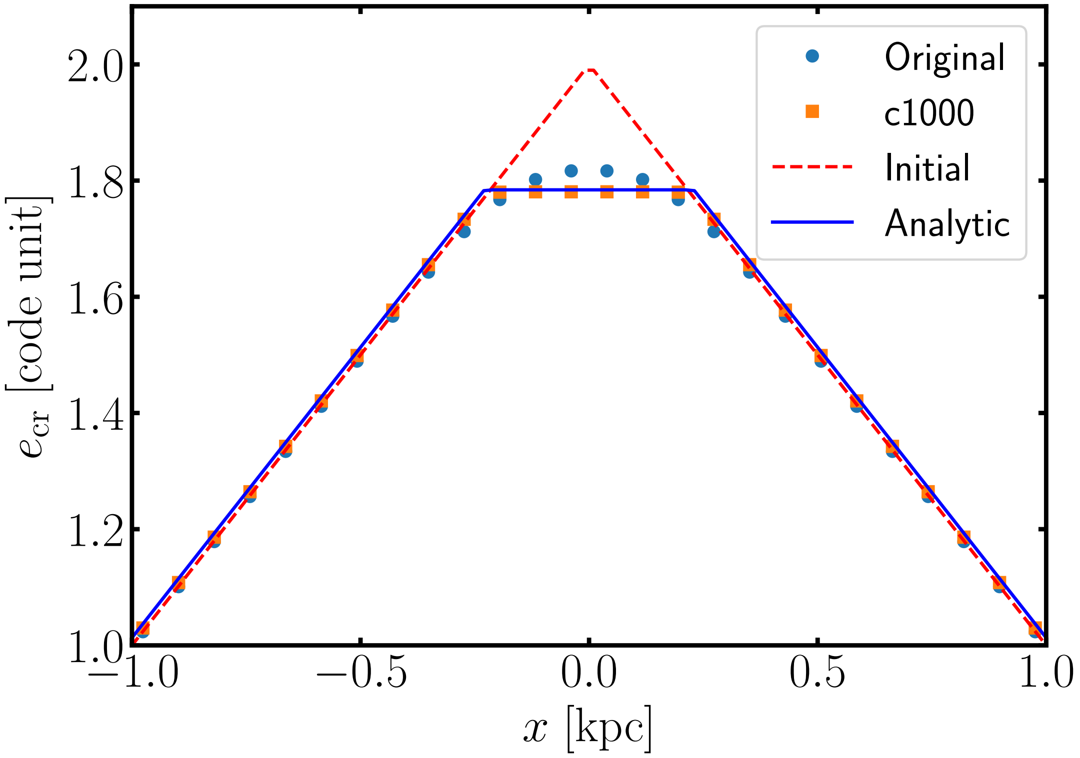

Figure 4.24: Idealized 1D CR streaming test (§ 4.B.7) with an initial triangular CR distribution evolved over 10 Myr. Red and blue lines show the analytic solutions at t = 0 Myr and t = 10 Myr respectively. Orange squares (blue circles) show the numerical results with (without) CR pressure gradient limiters and HLL flux. The analytic and numerical results agree well in overall shapes.

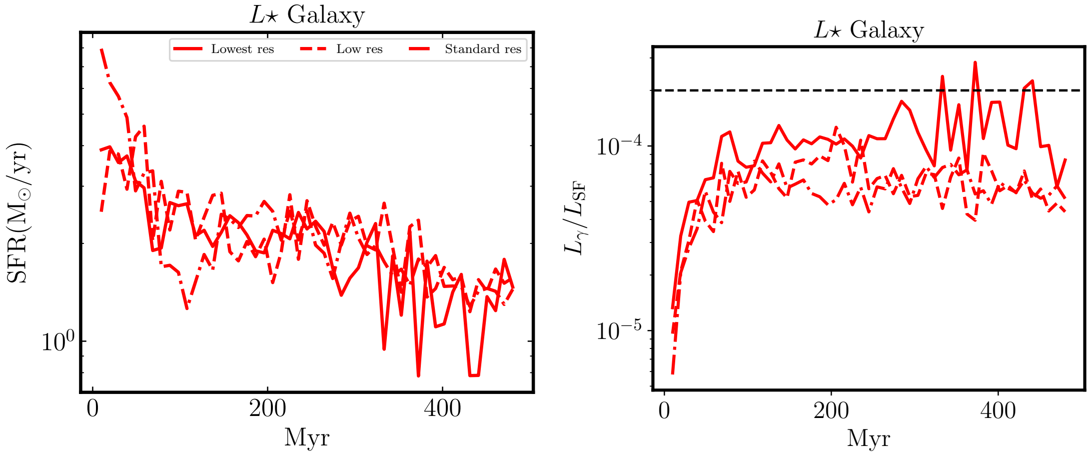

Figure 4.25: SFR and $L_\gamma/L_{\rm SF}$ as Fig. 4.23, in a resolution survey. We consider runs without magnetic fields, with $\kappa = 3\times10^{28}{\rm cm}^2\,{\rm s}^{-1}$. "Standard" (dash-dotted) is the resolution used in the main text, "Low" (dashed) is 10x poorer mass resolution, and "Lowest" (solid) is 100x poorer. Between "low" and "standard" resolution we see no difference in any property studied. Even at "lowest" resolution our qualitative conclusions are similar, although the artificially poorly-resolved ISM leads to noticeable biases in e.g. $L_\gamma/L_{\rm SF}$.

the CR pressure gradient.

4.B.8 Resolution study

In Fig. 4.25, we show the properties of $L\star$ **Galaxy** runs, at three different resolution levels. Our baseline is the fiducial resolution listed in Table 4.1, but we compare runs with 10x and 100x poorer mass resolution. Even at 10x poorer resolution, we find very similar SFRs, $L_\gamma/L_{\rm SF}$, and all other galaxy properties studied here; the same is true in the **Dwarf** runs (not shown). However systematic offsets do begin to appear at 100x poorer resolution. Other more detailed properties (e.g. phase structure of galactic winds) may require much higher resolution - this will be explored in future work.

4.C Comparison with $L_{0.1-100\mathrm{GeV}}$ observations

For completeness, we also compare our simulations with the broader, 0.1-100 GeV, observed energy range of γ rays from Ackermann et al. (2012a) and Rojas-Bravo & Araya (2016).

In the main text, we estimate the $L_{>1\mathrm{GeV}}$ following the L11 approach with the hadronic loss rate taken from Guo & Oh (2008) (see Eq. 4.8 and the related text), with an implicit assumption that all CR energy is at > 1GeV to simplify the calculation. However, to properly account for the lower energy γ rays and enable direct comparison to both the observations and simulations from Pfrommer et al. (2017b), we follow Pfrommer et al. (2017b) to calculate $L_{0.1-100\mathrm{GeV}}$.

We assume that CRs follow a power-law spectrum with a constant spectral index 2.2 (as used in the main text) and the low momentum cutoff $q = P_p/(m_p c) = 1$, where m_p is the proton mass. The normalization is determined by integrating the spectrum over energy and comparing to the local CR energy density. Then we calculate the energy-integrated γ-ray emissivity from pion decay for the energy band 0.1-100 GeV with Eq. 6 in Pfrommer et al. (2017b), and then integrate to get $L_{0.1-100\mathrm{GeV}}$. While the secondary IC emission from high energy CR electrons also contributes to γ-ray luminosity in this range, we find it is relatively unimportant compared to emission from pion decay, since (1) in high B field regions, CR electrons cool preferentially through synchrotron radiation; (2) in low B field regions, IC luminosity is only a small fraction ($<$ 20%) of the γ-ray luminosity. Thus, we simply neglect its contribution in Fig.4.26.

Fig. 4.26 shows that $\kappa \sim 1\mathrm{e}29 - 3\mathrm{e}29\ \mathrm{cm}^2/\mathrm{s}$ provides the best match to the observations for **Dwarf** and **L⋆ Galaxy** runs, consistent with our conclusions in the main text.

Chapter 4, in full, is a reformatted reprint of the material as it will appear in *Monthly Notices of the Royal Astronomical Society*, Chan, Tsang Keung; Kereš, Dušan; Hopkins, Philip F.; Quataert, Eliot; Su, Kung-Yi ; Hayward, Christopher C.; Faucher-Giguère, Claude-André, Volume 488, Issue 3, September 2019, Pages 3716-3744. The dissertation author was the primary

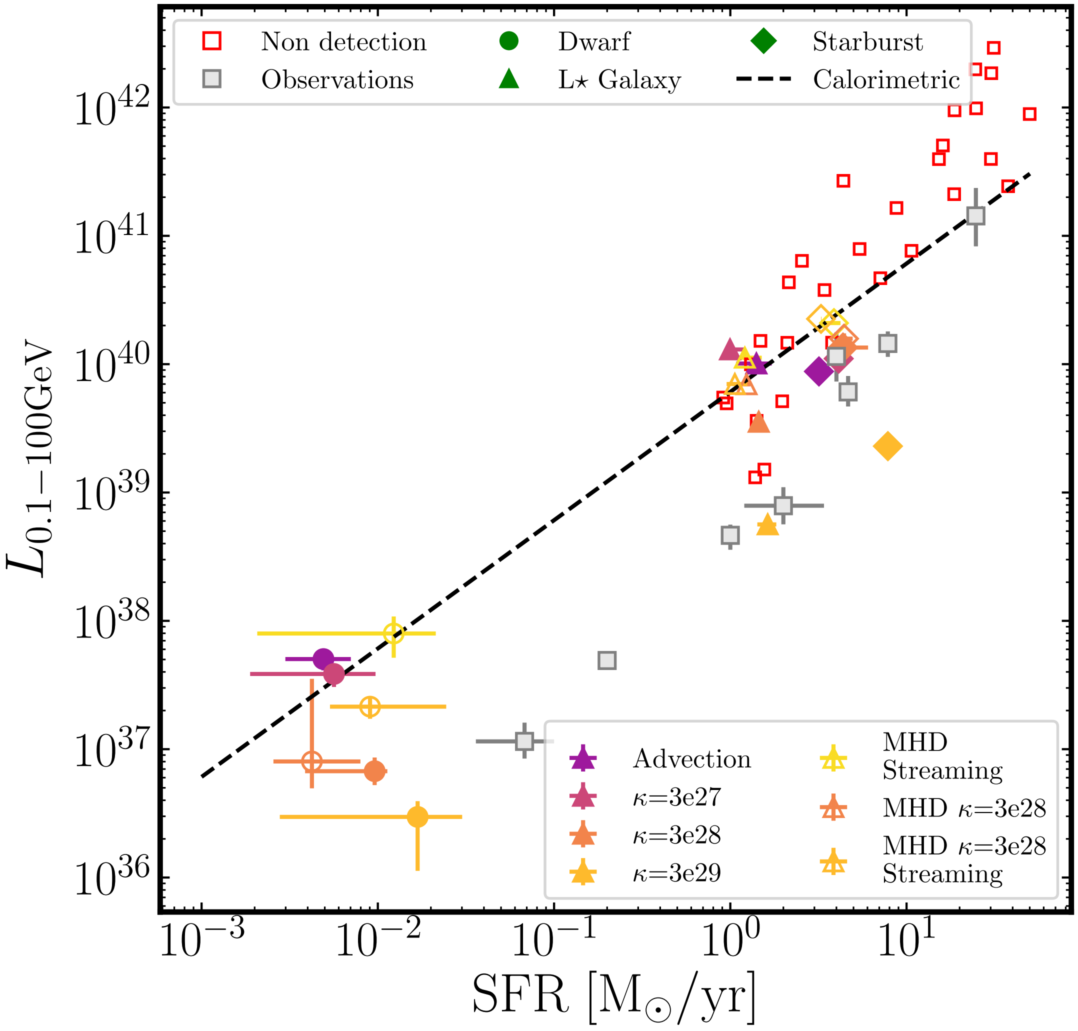

Figure 4.26: γ-ray luminosity $L_{0.1-100\mathrm{GeV}}$ ($0.1\mathrm{GeV} < E_\gamma < 100\mathrm{GeV}$) vs SFR (averaged over $\sim 10\,\mathrm{Myr}$) from our simulations, compared to observations. Grey squares show the observed $L_{0.1-100\mathrm{GeV}}$ from Ackermann et al. (2012a) but we use the SFRs described in §4.5.2. Red empty squares show the upper limits of non detection of the γ ray fluxes by Fermi LAT (galaxies without AGN), calculated in Rojas-Bravo & Araya (2016). Their SFRs were estimated with the Chabrier IMF, so we convert them assuming the Kroupa IMF to be consistent with our simulations. For the **Starburst** models we restrict to times "during starburst" ($\mathrm{SFR} > 3\,M_\odot\,\mathrm{yr}^{-1}$) and take 5-Myr averaged SFR.

investigator and author of this paper.

References

Abazajian K., 2006, Phys. Rev. D, 73, 6, 063513

Abazajian K. N., 2011, JCAP, 3, 10

Abazajian K. N., Canac N., Horiuchi S., Kaplinghat M., 2014, Phys. Rev. D, 90, 2, 023526

Abazajian K. N., Kaplinghat M., 2012, Phys. Rev. D, 86, 8, 083511

Abdo A. A., Ackermann M., Ajello M., Atwood W. B., Axelsson M., Baldini L., Ballet J., Barbiellini G., Bastieri D., Bechtol K., Bellazzini R., Berenji B., Bloom E. D., Bonamente E., Borgland A. W., Bregeon J., Brez A., Brigida M., Bruel P., Burnett T. H., Caliandro G. A., Cameron R. A., Caraveo P. A., Casandjian J. M., Cavazzuti E., Cecchi C., Çelik Ö., Charles E., Chekhtman A., Cheung C. C., Chiang J., Ciprini S., Claus R., Cohen-Tanugi J., Conrad J., Dermer C. D., de Angelis A., de Palma F., Digel S. W., Silva E. d. C. e., Drell P. S., Drlica-Wagner A., Dubois R., Dumora D., Farnier C., Favuzzi C., Fegan S. J., Focke W. B., Foschini L., Frailis M., Fukazawa Y., Funk S., Fusco P., Gargano F., Gasparrini D., Gehrels N., Germani S., Giebels B., Giglietto N., Giordano F., Glanzman T., Godfrey G., Grenier I. A., Grondin M.-H., Grove J. E., Guillemot L., Guiriec S., Hanabata Y., Harding A. K., Hayashida M., Hays E., Hughes R. E., Jóhannesson G., Johnson A. S., Johnson R. P., Johnson W. N., Kamae T., Katagiri H., Kataoka J., Kawai N., Kerr M., Knödlseder J., Kocian M. L., Kuss M., Lande J., Latronico L., Lemoine-Goumard M., Longo F., Loparco F., Lott B., Lovellette M. N., Lubrano P., Madejski G. M., Makeev A., Mazziotta M. N., McConville W., McEnery J. E., Meurer C., Michelson P. F., Mitthumsiri W., Mizuno T., Moiseev A. A., Monte C., Monzani M. E., Morselli A., Moskalenko I. V., Murgia S., Nakamori T., Nolan P. L., Norris J. P., Nuss E., Ohsugi T., Omodei N., Orlando E., Ormes J. F., Ozaki M., Paneque D., Panetta J. H., Parent D., Pelassa V., Pepe M., Pesce-Rollins M., Piron F., Porter T. A., Rainò S., Rando R., Razzano M., Reimer A., Reimer O., Reposeur T., Ritz S., Rodriguez A. Y., Romani R. W., Roth M., Ryde F., Sadrozinski H. F.-W., Sander A., Saz Parkinson P. M., Scargle J. D., Sellerholm A., Sgrò C., Shaw M. S., Smith D. A., Smith P. D., Spandre G., Spinelli P., Strickman M. S., Strong A. W., Suson D. J., Takahashi H., Tanaka T., Thayer J. B., Thayer J. G., Thompson D. J., Tibaldo L., Tibolla O., Torres D. F., Tosti G., Tramacere A., Uchiyama Y., Usher T. L., Vasileiou V., Vilchez N., Vitale V., Waite A. P., Wang P., Winer B. L., Wood K. S., Ylinen T., Ziegler M., Fermi LAT Collaboration, 2010a, ApJL, 709, L152

Abdo A. A., Ackermann M., Ajello M., Baldini L., Ballet J., Barbiellini G., Bastieri D., Bechtol K., Bellazzini R., Berenji B., Blandford R. D., Bloom E. D., Bonamente E., Borgland A. W., Bouvier A., Brandt T. J., Bregeon J., Brez A., Brigida M., Bruel P., Buehler R., Buson S., Caliandro G. A., Cameron R. A., Caraveo P. A., Carrigan S., Casandjian J. M., Cecchi C., Çelik Ö., Charles E., Chekhtman A., Cheung C. C., Chiang J., Ciprini S., Claus R., Cohen-Tanugi J., Conrad J., Dermer C. D., de Palma F., Digel S. W., Silva E. D. C. E., Drell P. S., Dubois R., Dumora D., Favuzzi C., Fegan S. J., Fukazawa Y., Funk S., Fusco P., Gargano F., Gasparrini D., Gehrels N., Germani S., Giglietto N., Giordano F., Giroletti M., Glanzman T., Godfrey G., Grenier I. A., Grondin M.-H., Grove J. E., Guiriec S., Hadasch D., Harding A. K., Hayashida M., Hays E., Horan D., Hughes R. E., Jean P., Jóhannesson G., Johnson A. S., Johnson W. N., Kamae T., Katagiri H., Kataoka J., Kerr M., Knödlseder J., Kuss M., Lande J., Latronico L., Lee S.-H., Lemoine-Goumard M., Llena Garde M., Longo F., Loparco F., Lovellette M. N., Lubrano P., Makeev A., Martin P., Mazziotta M. N., McEnery J. E., Michelson P. F., Mitthumsiri W., Mizuno T., Monte C., Monzani M. E., Morselli A., Moskalenko I. V., Murgia S., Nakamori T., Naumann-Godo M., Nolan P. L., Norris J. P., Nuss E., Ohsugi T., Okumura A., Omodei N., Orlando E., Ormes J. F., Panetta J. H., Parent D., Pelassa V., Pepe M., Pesce-Rollins M., Piron F., Porter T. A., Rainò S., Rando R., Razzano M., Reimer A., Reimer O., Reposeur T., Ripken J., Ritz S., Romani R. W., Sadrozinski H. F.-W., Sander A., Saz Parkinson P. M., Scargle J. D., Sgrò C., Siskind E. J., Smith D. A., Smith P. D., Spandre G., Spinelli P., Strickman M. S., Strong A. W., Suson D. J., Takahashi H., Takahashi T., Tanaka T., Thayer J. B., Thayer J. G., Thompson D. J., Tibaldo L., Torres D. F., Tosti G., Tramacere A., Uchiyama Y., Usher T. L., Vandenbroucke J., Vasileiou V., Vilchez N., Vitale V., Waite A. P., Wang P., Winer B. L., Wood K. S., Yang Z., Ylinen T., Ziegler M., 2010b, A& A, 523, A46

Abdo A. A., Ackermann M., Ajello M., Allafort A., Atwood W. B., Baldini L., Ballet J., Barbiellini G., Bastieri D., Bechtol K., Bellazzini R., Berenji B., Blandford R. D., Bloom E. D., Bonamente E., Borgland A. W., Bouvier A., Brandt T. J., Bregeon J., Brigida M., Bruel P., Buehler R., Burnett T. H., Buson S., Caliandro G. A., Cameron R. A., Cannon A., Caraveo P. A., Casandjian J. M., Cecchi C., Çelik Ö., Charles E., Chekhtman A., Chiang J., Ciprini S., Claus R., Cohen-Tanugi J., Conrad J., Dermer C. D., de Angelis A., de Palma F., Digel S. W., Silva E. D. C. E., Drell P. S., Drlica-Wagner A., Dubois R., Favuzzi C., Fegan S. J., Fortin P., Frailis M., Fukazawa Y., Funk S., Fusco P., Gargano F., Germani S., Giglietto N., Giordano F., Giroletti M., Glanzman T., Godfrey G., Grenier I. A., Grondin M.-H., Guiriec S., Gustafsson M., Hadasch D., Harding A. K., Hayashi K., Hayashida M., Hays E., Healey S. E., Jean P., Jóhannesson G., Johnson A. S., Johnson R. P., Johnson T. J., Kamae T., Katagiri H., Kataoka J., Kerr M., Knödlseder J., Kuss M., Lande J., Latronico L., Lee S.-H., Lemoine-Goumard M., Longo F., Loparco F., Lott B., Lovellette M. N., Lubrano P., Madejski G. M., Makeev A., Martin P., Mazziotta M. N., Mehault J., Michelson P. F., Mitthumsiri W., Mizuno T., Moiseev A. A., Monte C., Monzani M. E., Morselli A., Moskalenko I. V., Murgia S., Naumann-Godo M., Nolan P. L., Norris J. P., Nuss E., Ohsugi T., Okumura A., Omodei N., Orlando E., Ormes J. F., Ozaki M., Paneque D., Panetta J. H., Parent D., Pepe M., Persic M., Pesce-Rollins M., Piron F., Porter T. A., Rainò S., Rando R., Razzano M., Reimer A., Reimer O., Ritz S., Romani R. W., Sadrozinski H. F.-W., Saz Parkinson P. M., Sgrò C., Siskind E. J., Smith D. A., Smith P. D., Spandre G., Spinelli P., Strickman M. S., Strigari L., Strong A. W., Suson D. J., Takahashi H., Takahashi T., Tanaka T., Thayer J. B., Thompson D. J., Tibaldo L., Torres D. F., Tosti G., Tramacere A., Uchiyama Y., Usher T. L., Vandenbroucke J., Vianello G., Vilchez N., Vitale V., Waite A. P., Wang P., Winer B. L., Wood K. S., Yang Z., Ziegler M., 2010c, A& A, 523, L2

Abdo A. A., Ackermann M., Ajello M., Atwood W. B., Baldini L., Ballet J., Barbiellini G., Bastieri D., Baughman B. M., Bechtol K., Bellazzini R., Berenji B., Blandford R. D., Bloom E. D., Bonamente E., Borgland A. W., Bregeon J., Brez A., Brigida M., Bruel P., Burnett T. H., Buson S., Caliandro G. A., Cameron R. A., Caraveo P. A., Casandjian J. M., Cecchi C., Çelik Ö., Chekhtman A., Cheung C. C., Chiang J., Ciprini S., Claus R., Cohen-Tanugi J., Cominsky L. R., Conrad J., Cutini S., Dermer C. D., de Angelis A., de Palma F., Digel S. W., Silva E. D. C. E., Drell P. S., Dubois R., Dumora D., Farnier C., Favuzzi C., Fegan S. J., Focke W. B., Fortin P., Frailis M., Fukazawa Y., Fusco P., Gargano F., Gasparrini D., Gehrels N., Germani S., Giavitto G., Giebels B., Giglietto N., Giordano F., Glanzman T., Godfrey G., Gotthelf E. V., Grenier I. A., Grondin M.-H., Grove J. E., Guillemot L., Guiriec S., Hanabata Y., Harding A. K., Hayashida M., Hays E., Horan D., Hughes R. E., Jackson M. S., Jean P., Jóhannesson G., Johnson A. S., Johnson R. P., Johnson T. J., Johnson W. N., Kamae T., Katagiri H., Kataoka J., Kawai N., Kerr M., Knödlseder J., Kocian M. L., Kuss M., Lande J., Latronico L., Lemoine-Goumard M., Longo F., Loparco F., Lott B., Lovellette M. N., Lubrano P., Madejski G. M., Makeev A., Marshall F., Martin P., Mazziotta M. N., McConville W., McEnery J. E., Meurer C., Michelson P. F., Mitthumsiri W., Mizuno T., Moiseev A. A., Monte C., Monzani M. E., Morselli A., Moskalenko I. V., Murgia S., Nolan P. L., Norris J. P., Nuss E., Ohsugi T., Omodei N., Orlando E., Ormes J. F., Paneque D., Parent D., Pelassa V., Pepe M., Pesce-Rollins M., Piron F., Porter T. A., Rainò S., Rando R., Razzano M., Reimer A., Reimer O., Reposeur T., Ritz S., Rodriguez A. Y., Romani R. W., Roth M., Ryde F., Sadrozinski H. F.-W., Sanchez D., Sander A., Saz Parkinson P. M., Scargle J. D., Sellerholm A., Sgrò C., Siskind E. J., Smith D. A., Smith P. D., Spandre G., Spinelli P., Starck J.-L., Strickman M. S., Strong A. W., Suson D. J., Tajima H., Takahashi H., Tanaka T., Thayer J. B., Thayer J. G., Thompson D. J., Tibaldo L., Torres D. F., Tosti G., Tramacere A., Uchiyama Y., Usher T. L., Vasileiou V., Venter C., Vilchez N., Vitale V., Waite A. P., Wang P., Weltevrede P., Winer B. L., Wood K. S., Ylinen T., Ziegler M., 2010d, A& A, 512, A7

Abramowski A., Acero F., Aharonian F., Akhperjanian A. G., Anton G., Balzer A., Barnacka A., Becherini Y., Becker J., Bernlöhr K., Birsin E., Biteau J., Bochow A., Boisson C., Bolmont J., Bordas P., Brucker J., Brun F., Brun P., Bulik T., Büsching I., Carrigan S., Casanova S., Cerruti M., Chadwick P. M., Charbonnier A., Chaves R. C. G., Cheesebrough A., Cologna G., Conrad J., Couturier C., Dalton M., Daniel M. K., Davids I. D., Degrange B., Deil C., Dickinson H. J., Djannati-Ataï A., Domainko W., Drury L. O., Dubus G., Dutson K., Dyks J., Dyrda M., Egberts K., Eger P., Espigat P., Fallon L., Fegan S., Feinstein F., Fernandes M. V., Fiasson A., Fontaine G., Förster A., Füßling M., Gajdus M., Gallant Y. A., Garrigoux T., Gast H., Gérard L., Giebels B., Glicenstein J. F., Glück B., Göring D., Grondin M.-H., Häffner S., Hague J. D., Hahn J., Hampf D., Harris J., Hauser M., Heinz S., Heinzelmann G., Henri G., Hermann G., Hillert A., Hinton J. A., Hofmann W., Hofverberg P., Holler M., Horns D., Jacholkowska A., Jahn C., Jamrozy M., Jung I., Kastendieck M. A., Katarzyński K., Katz U., Kaufmann S., Khélifi B., Klochkov D., Kluźniak W., Kneiske T., Komin N., Kosack K., Kossakowski R., Krayzel F., Laffon H., Lamanna G., Lenain J.-P., Lennarz D., Lohse T., Lopatin A., Lu C.-C., Marandon

V., Marcowith A., Masbou J., Maurin G., Maxted N., Mayer M., McComb T. J. L., Medina M. C., Méhault J., Moderski R., Mohamed M., Moulin E., Naumann C. L., Naumann-Godo M., de Naurois M., Nedbal D., Nekrassov D., Nguyen N., Nicholas B., Niemiec J., Nolan S. J., Ohm S., de Oña Wilhelmi E., Opitz B., Ostrowski M., Oya I., Panter M., Paz Arribas M., Pekeur N. W., Pelletier G., Perez J., Petrucci P.-O., Peyaud B., Pita S., Pühlhofer G., Punch M., Quirrenbach A., Raue M., Reimer A., Reimer O., Renaud M., de los Reyes R., Rieger F., Ripken J., Rob L., Rosier-Lees S., Rowell G., Rudak B., Rulten C. B., Sahakian V., Sanchez D. A., Santangelo A., Schlickeiser R., Schulz A., Schwanke U., Schwarzburg S., Schwemmer S., Sheidaei F., Skilton J. L., Sol H., Spengler G., Stawarz Ł., Steenkamp R., Stegmann C., Stinzing F., Stycz K., Sushch I., Szostek A., Tavernet J.-P., Terrier R., Tluczykont M., Valerius K., van Eldik C., Vasileiadis G., Venter C., Viana A., Vincent P., Völk H. J., Volpe F., Vorobiov S., Vorster M., Wagner S. J., Ward M., White R., Wierzcholska A., Zacharias M., Zajczyk A., Zdziarski A. A., Zech A., Zechlin H.-S., H. E. S. S. Collaboration, 2012, ApJ, 757, 158

Acero F., Aharonian F., Akhperjanian A. G., Anton G., Barres de Almeida U., Bazer-Bachi A. R., Becherini Y., Behera B., Bernlöhr K., Bochow A., Boisson C., Bolmont J., Borrel V., Brucker J., Brun F., Brun P., Bühler R., Bulik T., Büsching I., Boutelier T., Chadwick P. M., Charbonnier A., Chaves R. C. G., Cheesebrough A., Chounet L.-M., Clapson A. C., Coignet G., Dalton M., Daniel M. K., Davids I. D., Degrange B., Deil C., Dickinson H. J., Djannati-Ataï A., Domainko W., Drury L. O. ., Dubois F., Dubus G., Dyks J., Dyrda M., Egberts K., Emmanoulopoulos D., Espigat P., Farnier C., Fegan S., Feinstein F., Fiasson A., Förster A., Fontaine G., Füßling M., Gabici S., Gallant Y. A., Gérard L., Gerbig D., Giebels B., Glicenstein J. F., Glück B., Goret P., Göring D., Hauser D., Hauser M., Heinz S., Heinzelmann G., Henri G., Hermann G., Hinton J. A., Hoffmann A., Hofmann W., Hofverberg P., Hoppe S., Horns D., Jacholkowska A., de Jager O. C., Jahn C., Jung I., Katarzyński K., Katz U., Kaufmann S., Kerschhaggl M., Khangulyan D., Khélifi B., Keogh D., Klochkov D., Kluźniak W., Kneiske T., Komin N., Kosack K., Kossakowski R., Lamanna G., Lenain J.-P., Lohse T., Marandon V., Martineau-Huynh O., Marcowith A., Masbou J., Maurin D., McComb T. J. L., Medina M. C., Méhault J., Moderski R., Moulin E., Naumann-Godo M., de Naurois M., Nedbal D., Nekrassov D., Nicholas B., Niemiec J., Nolan S. J., Ohm S., Olive J.-F., Wilhelmi E. d. O., Orford K. J., Ostrowski M., Panter M., Arribas M. P., Pedaletti G., Pelletier G., Petrucci P.-O., Pita S., Pühlhofer G., Punch M., Quirrenbach A., Raubenheimer B. C., Raue M., Rayner S. M., Reimer O., Renaud M., Rieger F., Ripken J., Rob L., Rosier-Lees S., Rowell G., Rudak B., Rulten C. B., Ruppel J., Sahakian V., Santangelo A., Schlickeiser R., Schöck F. M., Schwanke U., Schwarzburg S., Schwemmer S., Shalchi A., Sikora M., Skilton J. L., Sol H., Stawarz Ł., Steenkamp R., Stegmann C., Stinzing F., Superina G., Szostek A., Tam P. H., Tavernet J.-P., Terrier R., Tibolla O., Tluczykont M., van Eldik C., Vasileiadis G., Venter C., Venter L., Vialle J. P., Vincent P., Vivier M., Völk H. J., Volpe F., Wagner S. J., Ward M., Zdziarski A. A., Zech A., 2009, Science, 326, 1080

Ackermann M., Ajello M., Allafort A., Baldini L., Ballet J., Bastieri D., Bechtol K., Bellazzini R., Berenji B., Bloom E. D., Bonamente E., Borgland A. W., Bouvier A., Bregeon J., Brigida M., Bruel P., Buehler R., Buson S., Caliandro G. A., Cameron R. A., Caraveo P. A., Casandjian J. M., Cecchi C., Charles E., Chekhtman A., Cheung C. C., Chiang J., Cillis A. N., Ciprini S., Claus R., Cohen-Tanugi J., Conrad J., Cutini S., de Palma F., Dermer C. D., Digel S. W., Silva E. d. C. e., Drell P. S., Drlica-Wagner A., Favuzzi C., Fegan S. J., Fortin P., Fukazawa Y., Funk S., Fusco P., Gargano F., Gasparrini D., Germani S., Giglietto N., Giordano F., Glanzman T., Godfrey G., Grenier I. A., Guiriec S., Gustafsson M., Hadasch D., Hayashida M., Hays E., Hughes R. E., Jóhannesson G., Johnson A. S., Kamae T., Katagiri H., Kataoka J., Knödlseder J., Kuss M., Lande J., Longo F., Loparco F., Lott B., Lovellette M. N., Lubrano P., Madejski G. M., Martin P., Mazziotta M. N., McEnery J. E., Michelson P. F., Mizuno T., Monte C., Monzani M. E., Morselli A., Moskalenko I. V., Murgia S., Nishino S., Norris J. P., Nuss E., Ohno M., Ohsugi T., Okumura A., Omodei N., Orlando E., Ozaki M., Parent D., Persic M., Pesce-Rollins M., Petrosian V., Pierbattista M., Piron F., Pivato G., Porter T. A., Rainò S., Rando R., Razzano M., Reimer A., Reimer O., Ritz S., Roth M., Sbarra C., Sgrò C., Siskind E. J., Spandre G., Spinelli P., Stawarz Ł., Strong A. W., Takahashi H., Tanaka T., Thayer J. B., Tibaldo L., Tinivella M., Torres D. F., Tosti G., Troja E., Uchiyama Y., Vandenbroucke J., Vianello G., Vitale V., Waite A. P., Wood M., Yang Z., 2012a, ApJ, 755, 164

Ackermann M., Ajello M., Atwood W. B., Baldini L., Ballet J., Barbiellini G., Bastieri D., Bechtol K., Bellazzini R., Berenji B., Blandford R. D., Bloom E. D., Bonamente E., Borgland A. W., Brandt T. J., Bregeon J., Brigida M., Bruel P., Buehler R., Buson S., Caliandro G. A., Cameron R. A., Caraveo P. A., Cavazzuti E., Cecchi C., Charles E., Chekhtman A., Chiang J., Ciprini S., Claus R., Cohen-Tanugi J., Conrad J., Cutini S., de Angelis A., de Palma F., Dermer C. D., Digel S. W., Silva E. d. C. e., Drell P. S., Drlica-Wagner A., Falletti L., Favuzzi C., Fegan S. J., Ferrara E. C., Focke W. B., Fortin P., Fukazawa Y., Funk S., Fusco P., Gaggero D., Gargano F., Germani S., Giglietto N., Giordano F., Giroletti M., Glanzman T., Godfrey G., Grove J. E., Guiriec S., Gustafsson M., Hadasch D., Hanabata Y., Harding A. K., Hayashida M., Hays E., Horan D., Hou X., Hughes R. E., Jóhannesson G., Johnson A. S., Johnson R. P., Kamae T., Katagiri H., Kataoka J., Knödlseder J., Kuss M., Lande J., Latronico L., Lee S.-H., Lemoine-Goumard M., Longo F., Loparco F., Lott B., Lovellette M. N., Lubrano P., Mazziotta M. N., McEnery J. E., Michelson P. F., Mitthumsiri W., Mizuno T., Monte C., Monzani M. E., Morselli A., Moskalenko I. V., Murgia S., Naumann-Godo M., Norris J. P., Nuss E., Ohsugi T., Okumura A., Omodei N., Orlando E., Ormes J. F., Paneque D., Panetta J. H., Parent D., Pesce-Rollins M., Pierbattista M., Piron F., Pivato G., Porter T. A., Rainò S., Rando R., Razzano M., Razzaque S., Reimer A., Reimer O., Sadrozinski H. F.-W., Sgrò C., Siskind E. J., Spandre G., Spinelli P., Strong A. W., Suson D. J., Takahashi H., Tanaka T., Thayer J. G., Thayer J. B., Thompson D. J., Tibaldo L., Tinivella M., Torres D. F., Tosti G., Troja E., Usher T. L., Vandenbroucke J., Vasileiou V., Vianello G., Vitale V., Waite A. P., Wang P., Winer B. L., Wood K. S., Wood M., Yang Z., Ziegler M., Zimmer S., 2012b, ApJ, 750, 3

Agertz O., Moore B., Stadel J., Potter D., Miniati F., Read J., Mayer L., Gawryszczak A., Kravtsov A., Nordlund Å., Pearce F., Quilis V., Rudd D., Springel V., Stone J., Tasker E., Teyssier R., Wadsley J., Walder R., 2007, MNRAS, 380, 963

Agertz O., Teyssier R., Moore B., 2009, MNRAS, 397, L64

Amorisco N. C., Loeb A., 2016, MNRAS, 459, L51

Amorisco N. C., Monachesi A., Agnello A., White S. D. M., 2018, MNRAS, 475, 4235

AMS Collaboration, Aguilar M., Alcaraz J., Allaby J., Alpat B., Ambrosi G., Anderhub H., Ao L., Arefiev A., Azzarello P., et al., 2002, Phys. Rep., 366, 331

Anglés-Alcázar D., Faucher-Giguère C.-A., Kereš D., Hopkins P. F., Quataert E., Murray N., 2017, MNRAS, 470, 4698

Barnes J. E., 2012, MNRAS, 425, 1104

Beasley M. A., Romanowsky A. J., Pota V., Navarro I. M., Martinez Delgado D., Neyer F., Deich A. L., 2016, ApJL, 819, L20

Beasley M. A., Trujillo I., 2016, ApJ, 830, 23

Begeman K. G., 1987, HI rotation curves of spiral galaxies, Ph.D. thesis, , Kapteyn Institute, (1987)

Bell A. R., 1978, MNRAS, 182, 147

Bell A. R., 2004, MNRAS, 353, 550

Bell E. F., 2003, ApJ, 586, 794

Bellazzini M., Belokurov V., Magrini L., Fraternali F., Testa V., Beccari G., Marchetti A., Carini R., 2017, MNRAS, 467, 3751

Blandford R. D., Ostriker J. P., 1978, ApJL, 221, L29

Blanton M. R., Kazin E., Muna D., Weaver B. A., Price-Whelan A., 2011, AJ, 142, 31

Blumenthal G. R., Faber S. M., Flores R., Primack J. R., 1986, ApJ, 301, 27

Boettcher E., Zweibel E. G., Yoast-Hull T. M., Gallagher J. S. I., 2013, ApJ, 779, 12

Bolton A. S., Burles S., Koopmans L. V. E., Treu T., Gavazzi R., Moustakas L. A., Wayth R., Schlegel D. J., 2008, ApJ, 682, 964

Booth C. M., Agertz O., Kravtsov A. V., Gnedin N. Y., 2013, ApJL, 777, L16

Bothun G. D., Impey C. D., Malin D. F., 1991, ApJ, 376, 404

Bouchet P., Lequeux J., Maurice E., Prevot L., Prevot-Burnichon M. L., 1985, A& A, 149, 330

Boulares A., Cox D. P., 1990, ApJ, 365, 544

Boyarsky A., Malyshev D., Ruchayskiy O., 2011, Physics Letters B, 705, 165

Boylan-Kolchin M., Bullock J. S., Kaplinghat M., 2011, MNRAS, 415, L40

Breitschwerdt D., McKenzie J. F., Voelk H. J., 1991, A& A, 245, 79

Breitschwerdt D., McKenzie J. F., Voelk H. J., 1993, A& A, 269, 54

Broeils A. H., 1992, Ph.D. thesis, PhD thesis, Univ. Groningen, (1992)

Brook C. B., Di Cintio A., 2015, MNRAS, 450, 3920

Brook C. B., Stinson G., Gibson B. K., Roškar R., Wadsley J., Quinn T., 2012, MNRAS, 419, 771

Brooks A. M., Zolotov A., 2014, ApJ, 786, 87

Bryan G. L., Norman M. L., 1998, ApJ, 495, 80

Bullock J. S., Boylan-Kolchin M., 2017, ARA& A, 55, 1, 343

Bullock J. S., Dekel A., Kolatt T. S., Kravtsov A. V., Klypin A. A., Porciani C., Primack J. R., 2001, ApJ, 555, 240

Burkert A., 2000, ApJL, 534, L143

Burkert A., 2017, ApJ, 838, 93

Butsky I. S., Quinn T. R., 2018, ApJ, 868, 108

Caldwell N., 2006, ApJ, 651, 822

Carlson E. D., Machacek M. E., Hall L. J., 1992, ApJ, 398, 43

Chan T. K., Kereš D., Oñorbe J., Hopkins P. F., Muratov A. L., Faucher-Giguère C.-A., Quataert E., 2015, MNRAS, 454, 2981

Chan T. K., Kereš D., Wetzel A., Hopkins P. F., Faucher-Giguère C.-A., El-Badry K., Garrison-Kimmel S., Boylan-Kolchin M., 2018, MNRAS, 478, 906

Chan T. K., Kereš D., Hopkins P. F., Quataert E., Su K. Y., Hayward C. C., Faucher-Giguère C. A., 2019, MNRAS, 488, 3, 3716

Chen J., Bryan G. L., Salem M., 2016, MNRAS, 460, 3335

Condon J. J., 1992, ARA& A, 30, 575

Conroy C., Bullock J. S., 2015, ApJL, 805, L2

Conroy C., Gunn J. E., White M., 2009, ApJ, 699, 486

Courteau S., Dutton A. A., 2015, ApJL, 801, L20

Courteau S., Dutton A. A., van den Bosch F. C., MacArthur L. A., Dekel A., McIntosh D. H., Dale D. A., 2007, ApJ, 671, 203

Cox D. P., 2005, ARA& A, 43, 337

Cullen L., Dehnen W., 2010, MNRAS, 408, 669

Dalcanton J. J., Spergel D. N., Summers F. J., 1997, ApJ, 482, 659

Davé R., Spergel D. N., Steinhardt P. J., Wandelt B. D., 2001, ApJ, 547, 574

de Blok W. J. G., McGaugh S. S., 1997, MNRAS, 290, 533

de Blok W. J. G., Walter F., Brinks E., Trachternach C., Oh S.-H., Kennicutt Jr. R. C., 2008, AJ, 136, 2648

de Laix A. A., Scherrer R. J., Schaefer R. K., 1995, ApJ, 452, 495

Dekel A., Devor J., Hetzroni G., 2003, MNRAS, 341, 326

Del Popolo A., 2009, ApJ, 698, 2093

Dermer C. D., 1986, A& A, 157, 223

Di Cintio A., Brook C. B., Dutton A. A., Macciò A. V., Obreja A., Dekel A., 2017, MNRAS, 466, L1

Di Cintio A., Brook C. B., Macciò A. V., Stinson G. S., Knebe A., Dutton A. A., Wadsley J., 2014, MNRAS, 437, 415

Diemer B., More S., Kravtsov A. V., 2013, ApJ, 766, 25

Dorfi E. A., Breitschwerdt D., 2012, A& A, 540, A77

Draine B. T., 2011, Physics of the Interstellar and Intergalactic Medium

Dunstan R. M., Abazajian K. N., Polisensky E., Ricotti M., 2011, ArXiv e-prints

Durier F., Dalla Vecchia C., 2012, MNRAS, 419, 465

Dutton A. A., Conroy C., van den Bosch F. C., Prada F., More S., 2010, MNRAS, 407, 2

Dutton A. A., Macciò A. V., 2014, MNRAS, 441, 3359

Dutton A. A., van den Bosch F. C., Dekel A., Courteau S., 2007, ApJ, 654, 27

El-Badry K., Quataert E., Wetzel A., Hopkins P. F., Weisz D. R., Chan T. K., Fitts A., Boylan-Kolchin M., Kereš D., Faucher-Giguère C.-A., Garrison-Kimmel S., 2018, MNRAS, 473, 1930–1955

El-Badry K., Wetzel A., Geha M., Hopkins P. F., Kereš D., Chan T. K., Faucher-Giguère C.-A., 2016, ApJ, 820, 131

El-Badry K., Wetzel A. R., Geha M., Quataert E., Hopkins P. F., Kereš D., Chan T. K., Faucher-Giguère C.-A., 2017, ApJ, 835, 193

El-Zant A., Shlosman I., Hoffman Y., 2001, ApJ, 560, 636

Elbert O. D., Bullock J. S., Garrison-Kimmel S., Rocha M., Oñorbe J., Peter A. H. G., 2015, MNRAS, 453, 29

Enßlin T., Pfrommer C., Miniati F., Subramanian K., 2011, A& A, 527, A99

Enßlin T. A., 2003, A& A, 399, 409

Ensslin T. A., Biermann P. L., Kronberg P. P., Wu X.-P., 1997, ApJ, 477, 560

Enßlin T. A., Pfrommer C., Springel V., Jubelgas M., 2007, A& A, 473, 41

Everett J. E., Zweibel E. G., Benjamin R. A., McCammon D., Rocks L., Gallagher III J. S., 2008, ApJ, 674, 258

Farber R., Ruszkowski M., Yang H.-Y. K., Zweibel E. G., 2018, ApJ, 856, 112

Faucher-Giguère C., Kereš D., Dijkstra M., Hernquist L., Zaldarriaga M., 2010, ApJ, 725, 633

Faucher-Giguère C.-A., Feldmann R., Quataert E., Kereš D., Hopkins P. F., Murray N., 2016, MNRAS, 461, L32

Faucher-Giguère C.-A., Hopkins P. F., Kereš D., Muratov A. L., Quataert E., Murray N., 2015a, MNRAS, 449, 987

Faucher-Giguère C.-A., Hopkins P. F., Kereš D., Muratov A. L., Quataert E., Murray N., 2015b, MNRAS, 449, 1, 987

Faucher-Giguère C.-A., Kereš D., 2011, MNRAS, 412, L118

Faucher-Giguère C.-A., Lidz A., Zaldarriaga M., Hernquist L., 2009, ApJ, 703, 1416

Ferland G. J., Porter R. L., van Hoof P. A. M., Williams R. J. R., Abel N. P., Lykins M. L., Shaw G., Henney W. J., Stancil P. C., 2013, RMxAA, 49, 137

Ferrero I., Abadi M. G., Navarro J. F., Sales L. V., Gurovich S., 2012, MNRAS, 425, 2817

Fillingham S. P., Cooper M. C., Wheeler C., Garrison-Kimmel S., Boylan-Kolchin M., Bullock J. S., 2015, MNRAS, 454, 2039

Fitts A., Boylan-Kolchin M., Elbert O. D., Bullock J. S., Hopkins P. F., Oñorbe J., Wetzel A., Wheeler C., Faucher-Giguère C.-A., Kereš D., Skillman E. D., Weisz D. R., 2017, MNRAS, 471, 3547

Flores R. A., Primack J. R., 1994, ApJL, 427, L1

Garrison-Kimmel S., Boylan-Kolchin M., Bullock J. S., Kirby E. N., 2014, MNRAS, 444, 222

Garrison-Kimmel S., Rocha M., Boylan-Kolchin M., Bullock J. S., Lally J., 2013, MNRAS, 433, 3539

Gavazzi G., Donati A., Cucciati O., Sabatini S., Boselli A., Davies J., Zibetti S., 2005, A& A, 430, 411

Gentile G., Salucci P., Klein U., Vergani D., Kalberla P., 2004, MNRAS, 351, 903

Ginzburg V. L., Ptuskin V. S., 1976, Reviews of Modern Physics, 48, 161

Ginzburg V. L., Ptuskin V. S., 1985, Astrophysics and Space Physics Reviews, 4, 161

Girichidis P., Naab T., Hanasz M., Walch S., 2018, MNRAS, 479, 3042

Girichidis P., Naab T., Walch S., Hanasz M., Mac Low M.-M., Ostriker J. P., Gatto A., Peters T., Wünsch R., Glover S. C. O., Klessen R. S., Clark P. C., Baczynski C., 2016, ApJL, 816, L19

Gnedin O. Y., Kravtsov A. V., Klypin A. A., Nagai D., 2004, ApJ, 616, 16

Gnedin O. Y., Ostriker J. P., 2001, ApJ, 561, 61

Gnedin O. Y., Zhao H., 2002, MNRAS, 333, 299

González-Samaniego A., Bullock J. S., Boylan-Kolchin M., Fitts A., Elbert O. D., Hopkins P. F., Kereš D., Faucher-Giguère C.-A., 2017, MNRAS, 472, 4786

Goodenough L., Hooper D., 2009, ArXiv e-prints

Gordon C., Macías O., 2013, Phys. Rev. D, 88, 8, 083521

Governato F., Brook C., Mayer L., Brooks A., Rhee G., Wadsley J., Jonsson P., Willman B., Stinson G., Quinn T., Madau P., 2010, Nature, 463, 203

Governato F., Zolotov A., Pontzen A., Christensen C., Oh S. H., Brooks A. M., Quinn T., Shen S., Wadsley J., 2012, MNRAS, 422, 1231

Grenier I. A., Black J. H., Strong A. W., 2015, ARA& A, 53, 199

Gu M., Conroy C., Law D., van Dokkum P., Yan R., Wake D., Bundy K., Merritt A., Abraham R., Zhang J., Bershady M., Bizyaev D., Brinkmann J., Drory N., Grabowski K., Masters K., Pan K., Parejko J., Weijmans A.-M., Zhang K., 2017, ArXiv e-prints

Guo F., Oh S. P., 2008, MNRAS, 384, 251

H. E. S. S. Collaboration, Abdalla H., Aharonian F., Ait Benkhali F., Angüner E. O., Arakawa M., Arcaro C., Armand C., Arrieta M., Backes M., Barnard M., Becherini Y., Becker Tjus J., Berge D., Bernhard S., Bernlöhr K., Blackwell R., Böttcher M., Boisson C., Bolmont J., Bonnefoy S., Bordas P., Bregeon J., Brun F., Brun P., Bryan M., Büchele M., Bulik T., Bylund T., Capasso M., Caroff S., Carosi A., Casanova S., Cerruti M., Chakraborty N., Chandra S., Chaves R. C. G., Chen A., Colafrancesco S., Condon B., Davids I. D., Deil C., Devin J., deWilt P., Dirson L., Djannati-Ataï A., Dmytriiev A., Donath A., Drury L. O. C., Dyks J., Egberts K., Emery G., Ernenwein J. P., Eschbach S., Fegan S., Fiasson A., Fontaine G., Funk S., Füßling M., Gabici S., Gallant Y. A., Garrigoux T., Gaté F., Giavitto G., Glawion D., Glicenstein J. F., Gottschall D., Grondin M. H., Hahn J., Haupt M., Heinzelmann G., Henri G., Hermann G., Hinton J. A., Hofmann W., Hoischen C., Holch T. L., Holler M., Horns D., Huber D., Iwasaki H., Jacholkowska A., Jamrozy M., Jankowsky D., Jankowsky F., Jouvin L., Jung-Richardt I., Kastendieck M. A., Katarzýnski K., Katsuragawa M., Katz U., Kerszberg D., Khangulyan D., Khélifi B., King J., Klepser S., Klúzniak W., Komin N., Kosack K., Krakau S., Kraus M., Krüger P. P., Lamanna G., Lau J., Lefaucheur J., Lemière A., Lemoine-Goumard M., Lenain J. P., Leser E., Lohse T., Lorentz M., Ló pez-Coto R., Lypova I., Malyshev D., Marandon V., Marcowith A., Mariaud C., Martí-Devesa G., Marx R., Maurin G., Meintjes P. J., Mitchell A. M. W., Moderski R., Mohamed M., Mohrmann L., Moulin E., Murach T., Nakashima S., de Naurois M., Ndiyavala H., Niederwanger F., Niemiec J., Oakes L., O'Brien P., Odaka H., Ohm S., Ostrowski M., Oya I., Padovani M., Panter M., Parsons R. D., Perennes C., Petrucci P. O., Peyaud B., Piel Q., Pita S., Poireau V., Priyana Noel A., Prokhorov D. A., Prokoph H., Pühlhofer G., Punch M., Quirrenbach A., Raab S., Rauth R., Reimer A., Reimer O., Renaud M., Rieger F., Rinchiuso L., Romoli C., Rowell G., Rudak B., Ruiz-Velasco E., Sahakian V., Saito S., Sanchez D. A., Santangelo A., Sasaki M., Schlickeiser R., Schüssler F., Schulz A., Schwanke U., Schwemmer S., Seglar-Arroyo M., Senniappan M., Seyffert A. S., Shafi N., Shilon I., Shiningayamwe K., Simoni R., Sinha A., Sol H., Spanier F., Specovius A., Spir-Jacob M., Stawarz Ł., Steenkamp R., Stegmann C., Steppa C., Sushch I., Takahashi T., Tavernet J. P., Tavernier T., Taylor A. M., Terrier R., Tibaldo L., Tiziani D., Tluczykont M., Trichard C., Tsirou M., Tsuji N., Tuffs R., Uchiyama Y., van der Walt D. J., van Eldik C., van Rensburg C., van Soelen B., Vasileiadis G., Veh J., Venter C., Viana A., Vincent P., Vink J., Voisin F., Völk H. J., Vuillaume T., Wadiasingh Z., Wagner S. J., Wagner P., Wagner R. M., White R., Wierzcholska A., Wörnlein A., Yang R., Zaborov D., Zacharias M., Zanin R., Zdziarski A. A., Zech A., Zefi F., Ziegler A., Zorn J., Żywucka N., 2018, A& A, 617, A73

Hafen Z., Faucher-Giguère C.-A., Anglés-Alcázar D., Kereš D., Feldmann R., Chan T. K., Quataert E., Murray N., Hopkins P. F., 2017, MNRAS, 469, 2292

Hafen Z., Faucher-Giguère C.-A., Anglés-Alcázar D., Stern J., Kereš D., Hummels C., Esmerian C., Garrison-Kimmel S., El-Badry K., Wetzel A., Chan T. K., Hopkins P. F., Murray N., 2019, MNRAS, 488, 1, 1248

Hahn O., Abel T., 2011, MNRAS, 415, 2101

Hanasz M., Lesch H., Naab T., Gawryszczak A., Kowalik K., Wóltański D., 2013, ApJL, 777, L38

Hanasz M., Wóltański D., Kowalik K., 2009, ApJL, 706, L155

Harris W. E., Harris G. L. H., Alessi M., 2013, ApJ, 772, 82

Harten A., Lax P., Leer B., 1983, SIAM Review, 25, 1, 35

Hernquist L., 1990, ApJ, 356, 359

Hess V. F., 1912, Phys. Z., 13, 1084

Hillas A. M., Ouldridge M., 1975, Nature, 253, 609

Holman G. D., Ionson J. A., Scott J. S., 1979, ApJ, 228, 576

Hooper D., Goodenough L., 2011, Physics Letters B, 697, 412

Hooper D., Linden T., 2011, Phys. Rev. D, 84, 12, 123005

Hopkins P. F., 2013, MNRAS, 428, 2840

Hopkins P. F., 2014, ArXiv e-prints: 1409.7395

Hopkins P. F., 2015a, MNRAS, 450, 53

Hopkins P. F., 2015b, MNRAS, 450, 53

Hopkins P. F., 2016, MNRAS, 462, 576

Hopkins P. F., 2017, MNRAS, 466, 3387

Hopkins P. F., Grudic M. Y., Wetzel A. R., Keres D., Gaucher-Giguere C.-A., Ma X., Murray N., Butcher N., 2018a, MNRAS, in press, arXiv:1811.12462

Hopkins P. F., Hernquist L., Martini P., Cox T. J., Robertson B., Di Matteo T., Springel V., 2005, ApJL, 625, L71

Hopkins P. F., Kereš D., Oñorbe J., Faucher-Giguère C.-A., Quataert E., Murray N., Bullock J. S., 2014, MNRAS, 445, 581

Hopkins P. F., Raives M. J., 2016, MNRAS, 455, 51

Hopkins P. F., Wetzel A., Kereš D., Faucher-Giguère C.-A., Quataert E., Boylan-Kolchin M., Murray N., Hayward C. C., Garrison-Kimmel S., Hummels C., Feldmann R., Torrey P., Ma X., Anglés-Alcázar D., Su K.-Y., Orr M., Schmitz D., Escala I., Sanderson R., Grudić M. Y., Hafen Z., Kim J.-H., Fitts A., Bullock J. S., Wheeler C., Chan T. K., Elbert O. D., Narayanan D., 2018b, MNRAS, 480, 800

Hopkins P. F., Wetzel A., Kereš D., Faucher-Giguère C.-A., Quataert E., Boylan-Kolchin M., Murray N., Hayward C. C., El-Badry K., 2018c, MNRAS, 477, 1578

Huang S., Haynes M. P., Giovanelli R., Brinchmann J., Stierwalt S., Neff S. G., 2012, AJ, 143, 133

Hunter D. A., Ficut-Vicas D., Ashley T., Brinks E., Cigan P., Elmegreen B. G., Heesen V., Herrmann K. A., Johnson M., Oh S.-H., Rupen M. P., Schruba A., Simpson C. E., Walter F., Westpfahl D. J., Young L. M., Zhang H.-X., 2012, AJ, 144, 134

Hunter J. D., 2007, Computing in Science and Engineering, 9, 90

Impey C., Bothun G., 1997, ARA& A, 35, 267

Impey C., Bothun G., Malin D., 1988, ApJ, 330, 634

Ipavich F. M., 1975, ApJ, 196, 107

Jacob S., Pakmor R., Simpson C. M., Springel V., Pfrommer C., 2018, MNRAS, 475, 570

Jansen R. A., Franx M., Fabricant D., Caldwell N., 2000, ApJS, 126, 271

Janssens S., Abraham R., Brodie J., Forbes D., Romanowsky A. J., van Dokkum P., 2017, ApJL, 839, L17

Jiang Y.-F., Oh S. P., 2018, ApJ, 854, 5

Jokipii J. R., 1966, ApJ, 146, 480

Jones E., Oliphant T., Peterson P., et al., 2001, SciPy: Open source scientific tools for Python, [Online; accessed <today>]

Jubelgas M., Springel V., Enßlin T., Pfrommer C., 2008, A& A, 481, 33

Kadowaki J., Zaritsky D., Donnerstein R. L., 2017, ApJL, 838, L21

Kaplinghat M., Keeley R. E., Linden T., Yu H.-B., 2014, Physical Review Letters, 113, 2, 021302

Katz N., White S. D. M., 1993, ApJ, 412, 455

Kaufmann T., Mayer L., Wadsley J., Stadel J., Moore B., 2006, MNRAS, 370, 1612

Kennicutt Jr. R. C., 1998, ApJ, 498, 541

Kereš D., Hernquist L., 2009, ApJL, 700, L1

Kereš D., Katz N., Davé R., Fardal M., Weinberg D. H., 2009a, MNRAS, 396, 2332

Kereš D., Katz N., Fardal M., Davé R., Weinberg D. H., 2009b, MNRAS, 395, 160

Kereš D., Katz N., Weinberg D. H., Davé R., 2005, MNRAS, 363, 2

Kereš D., Vogelsberger M., Sijacki D., Springel V., Hernquist L., 2012, MNRAS, 425, 2027

Kim J.-h., Abel T., Agertz O., et al., 2014a, ApJS, 210, 14

Kim J.-h., Abel T., Agertz O., Bryan G. L., Ceverino D., Christensen C., Conroy C., Dekel A., Gnedin N. Y., Goldbaum N. J., Guedes J., Hahn O., Hobbs A., Hopkins P. F., Hummels C. B., Iannuzzi F., Keres D., Klypin A., Kravtsov A. V., Krumholz M. R., Kuhlen M., Leitner S. N., Madau P., Mayer L., Moody C. E., Nagamine K., Norman M. L., Onorbe J., O'Shea B. W., Pillepich A., Primack J. R., Quinn T., Read J. I., Robertson B. E., Rocha M., Rudd D. H., Shen S., Smith B. D., Szalay A. S., Teyssier R., Thompson R., Todoroki K., Turk M. J., Wadsley J. W., Wise J. H., Zolotov A., AGORA Collaboration29 t., 2014b, ApJS, 210, 14

Kirby E. N., Bullock J. S., Boylan-Kolchin M., Kaplinghat M., Cohen J. G., 2014, MNRAS, 439, 1015

Klimentowski J., Łokas E. L., Kazantzidis S., Mayer L., Mamon G. A., 2009, MNRAS, 397, 2015

Klimentowski J., Łokas E. L., Kazantzidis S., Prada F., Mayer L., Mamon G. A., 2007, MNRAS, 378, 353

Knebe A., Green A., Binney J., 2001, MNRAS, 325, 845

Knollmann S. R., Knebe A., 2009, ApJS, 182, 608

Kochanek C. S., White M., 2000, ApJ, 543, 514

Koda J., Yagi M., Yamanoi H., Komiyama Y., 2015, ApJL, 807, L2

Kroupa P., 2002, Science, 295, 82

Krumholz M. R., Gnedin N. Y., 2011, ApJ, 729, 36

Kulpa-Dybeł K., Nowak N., Otmianowska-Mazur K., Hanasz M., Siejkowski H., Kulesza-Żydzik B., 2015, A& A, 575, A93

Kulpa-Dybeł K., Otmianowska-Mazur K., Kulesza-Żydzik B., Hanasz M., Kowal G., Wóltański D., Kowalik K., 2011, ApJL, 733, L18

Kulsrud R., Pearce W. P., 1969, ApJ, 156, 445

Kulsrud R. M., 2005, Plasma physics for astrophysics, Princeton University Press, Princeton, N.J.

Lacki B. C., Thompson T. A., Quataert E., 2010, ApJ, 717, 1

Lacki B. C., Thompson T. A., Quataert E., Loeb A., Waxman E., 2011, ApJ, 734, 107

Laporte C. F. P., Peñarrubia J., 2015, MNRAS, 449, L90

Lee M. G., Kang J., Lee J. H., Jang I. S., 2017, ApJ, 844, 157

Leisman L., Haynes M. P., Janowiecki S., Hallenbeck G., Józsa G., Giovanelli R., Adams E. A. K., Bernal Neira D., Cannon J. M., Janesh W. F., Rhode K. L., Salzer J. J., 2017, ApJ, 842, 133

Leitherer C., Ekström S., Meynet G., Schaerer D., Agienko K. B., Levesque E. M., 2014, ApJS, 212, 14

Leitherer C., Ortiz Otálvaro P. A., Bresolin F., Kudritzki R.-P., Lo Faro B., Pauldrach A. W. A., Pettini M., Rix S. A., 2010, ApJS, 189, 309

Leitherer C., Schaerer D., Goldader J. D., Delgado R. M. G., Robert C., Kune D. F., de Mello D. F., Devost D., Heckman T. M., 1999, ApJS, 123, 3

Levermore C. D., 1984, J Quant Spectrosc Radiat Transf., 31, 149

Li Y., Mo H. J., van den Bosch F. C., Lin W. P., 2007, MNRAS, 379, 689

Linden T., Profumo S., Anderson B., 2010, Phys. Rev. D, 82, 6, 063529

Loeb A., Weiner N., 2011, Physical Review Letters, 106, 17, 171302

Łokas E. L., Semczuk M., Gajda G., D'Onghia E., 2015, ApJ, 810, 100

Lopez L. A., Auchettl K., Linden T., Bolatto A. D., Thompson T. A., Ramirez-Ruiz E., 2018, ApJ, 867, 44

Lovell M. R., Eke V., Frenk C. S., Gao L., Jenkins A., Theuns T., Wang J., White S. D. M., Boyarsky A., Ruchayskiy O., 2012, MNRAS, 420, 2318

Ma X., Hopkins P. F., Faucher-Giguère C.-A., Zolman N., Muratov A. L., Kereš D., Quataert E., 2016, MNRAS, 456, 2140

Ma X., Hopkins P. F., Feldmann R., Torrey P., Faucher-Giguère C.-A., Kereš D., 2017, MNRAS, 466, 4780

Macciò A. V., Dutton A. A., van den Bosch F. C., 2008, MNRAS, 391, 1940

Macciò A. V., Paduroiu S., Anderhalden D., Schneider A., Moore B., 2012a, MNRAS, 424, 1105

Macciò A. V., Stinson G., Brook C. B., Wadsley J., Couchman H. M. P., Shen S., Gibson B. K., Quinn T., 2012b, ApJL, 744, L9

Machacek M. E., Carlson E. D., Hall L. J., 1993, in Texas/PASCOS '92: Relativistic Astrophysics and Particle Cosmology, edited by C. W. Akerlof, M. A. Srednicki, vol. 688 of Annals of the New York Academy of Sciences, 681

Macias O., Gordon C., 2014, Phys. Rev. D, 89, 6, 063515

Madau P., Shen S., Governato F., 2014, ApJL, 789, L17

Makarov D. I., Sharina M. E., Karachentseva V. E., Karachentsev I. D., 2015, A& A, 581, A82

Mannheim K., Schlickeiser R., 1994, A& A, 286, 983

Mao S. A., Ostriker E. C., 2018, ApJ, 854, 89

Marigo P., Girardi L., 2007, A& A, 469, 239

Marigo P., Girardi L., Bressan A., Groenewegen M. A. T., Silva L., Granato G. L., 2008, A& A, 482, 883

Martin C., Moore A., Morrissey P., Matuszewski M., Rahman S., Adkins S., Epps H., 2010, in Ground-based and Airborne Instrumentation for Astronomy III, vol. 7735 of Proc. SPIE, 77350M

Martínez-Delgado D., Läsker R., Sharina M., Toloba E., Fliri J., Beaton R., Valls-Gabaud D., Karachentsev I. D., Chonis T. S., Grebel E. K., Forbes D. A., Romanowsky A. J., Gallego-Laborda J., Teuwen K., Gómez-Flechoso M. A., Wang J., Guhathakurta P., Kaisin S., Ho N., 2016, AJ, 151, 96

Martizzi D., Faucher-Giguère C.-A., Quataert E., 2015, MNRAS, 450, 504

Martizzi D., Teyssier R., Moore B., 2013, MNRAS, 432, 1947

Mashchenko S., Couchman H. M. P., Wadsley J., 2006, Nature, 442, 539

Mayer L., Governato F., Colpi M., Moore B., Quinn T., Wadsley J., Stadel J., Lake G., 2001, ApJL, 547, L123

McConnachie A. W., 2012, AJ, 144, 4

McConnachie A. W., Huxor A., Martin N. F., Irwin M. J., Chapman S. C., Fahlman G., Ferguson A. M. N., Ibata R. A., Lewis G. F., Richer H., Tanvir N. R., 2008, ApJ, 688, 1009

McKenzie J. F., Voelk H. J., 1982, A& A, 116, 191

Merritt A., van Dokkum P., Danieli S., Abraham R., Zhang J., Karachentsev I. D., Makarova L. N., 2016, ApJ, 833, 168

Mihos J. C., Durrell P. R., Ferrarese L., Feldmeier J. J., Côté P., Peng E. W., Harding P., Liu C., Gwyn S., Cuillandre J.-C., 2015, ApJL, 809, L21

Miralda-Escudé J., 2002, ApJ, 564, 60

Moore B., 1994, Nature, 370, 629

Moskalenko I. V., Strong A. W., 1998, ApJ, 493, 694

Moskalenko I. V., Strong A. W., Ormes J. F., Potgieter M. S., 2002, ApJ, 565, 280

Mowla L., van Dokkum P., Merritt A., Abraham R., Yagi M., Koda J., 2017, ApJ, 851, 27

Muñoz R. P., Eigenthaler P., Puzia T. H., Taylor M. A., Ordenes-Briceño Y., Alamo-Martínez K., Ribbeck K. X., Ángel S., Capaccioli M., Côté P., Ferrarese L., Galaz G., Hempel M., Hilker M., Jordán A., Lançon A., Mieske S., Paolillo M., Richtler T., Sánchez-Janssen R., Zhang H., 2015, ApJL, 813, L15

Muratov A. L., Kereš D., Faucher-Giguère C.-A., Hopkins P. F., Ma X., Anglés-Alcázar D., Chan T. K., Torrey P., Hafen Z. H., Quataert E., Murray N., 2017, MNRAS, 468, 4170

Muratov A. L., Kereš D., Faucher-Giguère C.-A., Hopkins P. F., Quataert E., Murray N., 2015, MNRAS, 454, 2691

Navarro J. F., Eke V. R., Frenk C. S., 1996, MNRAS, 283, L72

Navarro J. F., Frenk C. S., White S. D. M., 1997, ApJ, 490, 493

Nelson D., Vogelsberger M., Genel S., Sijacki D., Kereš D., Springel V., Hernquist L., 2013, MNRAS, 429, 3353

Newman A., Treu T., Ellis R. S., Sand D. J., Nipoti C., Richard J., Jullo E., 2013a, in Probes of Dark Matter on Galaxy Scales, 20302

Newman A. B., Treu T., Ellis R. S., Sand D. J., Nipoti C., Richard J., Jullo E., 2013b, ApJ, 765, 24

Oñorbe J., Boylan-Kolchin M., Bullock J. S., Hopkins P. F., Kereš D., Faucher-Giguère C.-A., Quataert E., Murray N., 2015, MNRAS, 454, 2092

Oñorbe J., Garrison-Kimmel S., Maller A. H., Bullock J. S., Rocha M., Hahn O., 2014, MNRAS, 437, 1894

Ogiya G., Mori M., 2011, ApJL, 736, L2

Ogiya G., Mori M., 2014, ApJ, 793, 46

Oh S.-H., de Blok W. J. G., Brinks E., Walter F., Kennicutt Jr. R. C., 2011, AJ, 141, 193

Oh S.-H., Hunter D. A., Brinks E., Elmegreen B. G., Schruba A., Walter F., Rupen M. P., Young L. M., Simpson C. E., Johnson M. C., Herrmann K. A., Ficut-Vicas D., Cigan P., Heesen V., Ashley T., Zhang H.-X., 2015, AJ, 149, 180

Oppenheimer B. D., Davé R., Kereš D., Fardal M., Katz N., Kollmeier J. A., Weinberg D. H., 2010, MNRAS, 406, 2325

Orr M. E., Hayward C. C., Hopkins P. F., Chan T. K., Faucher-Giguère C.-A., Feldmann R., Kereš D., Murray N., Quataert E., 2018, MNRAS

Pakmor R., Pfrommer C., Simpson C. M., Springel V., 2016, ApJL, 824, L30

Pandya V., Romanowsky A. J., Laine S., Brodie J. P., Johnson B. D., Glaccum W., Villaume A., Cuillandre J.-C., Gwyn S., Krick J., Lasker R., Martín-Navarro I., Martinez-Delgado D., van Dokkum P., 2018, ApJ, 858, 29

Papastergis E., Giovanelli R., Haynes M. P., Shankar F., 2015, A& A, 574, A113

Parker E. N., 1992, ApJ, 401, 137

Peñarrubia J., Pontzen A., Walker M. G., Koposov S. E., 2012, ApJL, 759, L42

Pei Y. C., 1992, ApJ, 395, 130

Peirani S., Kay S., Silk J., 2008, A& A, 479, 123

Peng C. Y., Ho L. C., Impey C. D., Rix H.-W., 2002, AJ, 124, 266

Peng C. Y., Ho L. C., Impey C. D., Rix H.-W., 2010, AJ, 139, 2097

Peng E. W., Lim S., 2016, ApJL, 822, L31

Peter A. H. G., Rocha M., Bullock J. S., Kaplinghat M., 2013, MNRAS, 430, 105

Pfrommer C., Pakmor R., Schaal K., Simpson C. M., Springel V., 2017a, MNRAS, 465, 4500

Pfrommer C., Pakmor R., Simpson C. M., Springel V., 2017b, ApJL, 847, L13

Pfrommer C., Springel V., Enßlin T. A., Jubelgas M., 2006, MNRAS, 367, 113

Planck Collaboration, Ade P. A. R., Aghanim N., Armitage-Caplan C., Arnaud M., Ashdown M., Atrio-Barandela F., Aumont J., Baccigalupi C., Banday A. J., et al., 2014, A& A, 571, A16

Pontzen A., Governato F., 2012, MNRAS, 421, 3464

Pontzen A., Governato F., 2014, Nature, 506, 171

Porter D. H., 1985, A study of hierarchical clustering of galaxies in an expanding universe, Ph.D. thesis, California Univ., Berkeley.

Power C., Navarro J. F., Jenkins A., Frenk C. S., White S. D. M., Springel V., Stadel J., Quinn T., 2003, MNRAS, 338, 14

Price D. J., 2008, Journal of Computational Physics, 227, 10040

Price D. J., Monaghan J. J., 2007, MNRAS, 374, 1347

Rahmati A., Pawlik A. H., Raicevic M., Schaye J., 2013, MNRAS, 430, 2427

Read J. I., Gilmore G., 2005, MNRAS, 356, 107

Read J. I., Wilkinson M. I., Evans N. W., Gilmore G., Kleyna J. T., 2006, MNRAS, 366, 429

Rocha M., Peter A. H. G., Bullock J. S., Kaplinghat M., Garrison-Kimmel S., Oñorbe J., Moustakas L. A., 2013, MNRAS, 430, 81

Rojas-Bravo C., Araya M., 2016, MNRAS, 463, 1068

Román J., Trujillo I., 2017a, MNRAS, 468, 703

Román J., Trujillo I., 2017b, MNRAS, 468, 4039

Romano-Díaz E., Shlosman I., Hoffman Y., Heller C., 2008, ApJL, 685, L105

Rong Y., Guo Q., Gao L., Liao S., Xie L., Puzia T. H., Sun S., Pan J., 2017, MNRAS, 470, 4231

Ruszkowski M., Yang H.-Y. K., Zweibel E., 2017, ApJ, 834, 208

Saitoh T. R., Makino J., 2013, ApJ, 768, 44

Salem M., Bryan G. L., 2014, MNRAS, 437, 3312

Salem M., Bryan G. L., Corlies L., 2016, MNRAS, 456, 582

Salem M., Bryan G. L., Hummels C., 2014, ApJL, 797, L18

Salpeter E. E., 1955, ApJ, 121, 161

Salucci P., Burkert A., 2000, ApJL, 537, L9

Schlickeiser R., 2002, Cosmic Ray Astrophysics, Astronomy and Astrophysics Library; Physics and Astronomy Online Library, Berlin: Springer.

Sharma P., Colella P., Martin D., 2010, SIAM Journal on Scientific Computing, 32, 6, 3564

Shi D. D., Zheng X. Z., Zhao H. B., Pan Z. Z., Li B., Zou H., Zhou X., Guo K., An F. X., Li Y. B., 2017, ApJ, 846, 26

Sifón C., van der Burg R. F. J., Hoekstra H., Muzzin A., Herbonnet R., 2018, MNRAS, 473, 3747

Sijacki D., Vogelsberger M., Kereš D., Springel V., Hernquist L., 2012, MNRAS, 424, 2999

Simha V., Weinberg D. H., Davé R., Gnedin O. Y., Katz N., Kereš D., 2009, MNRAS, 399, 650

Simpson C. M., Pakmor R., Marinacci F., Pfrommer C., Springel V., Glover S. C. O., Clark P. C., Smith R. J., 2016, ApJL, 827, L29

Skilling J., 1971, ApJ, 170, 265

Snodin A. P., Brandenburg A., Mee A. J., Shukurov A., 2006, MNRAS, 373, 643

Socrates A., Davis S. W., Ramirez-Ruiz E., 2008, ApJ, 687, 202

Sod G. A., 1978, Journal of Computational Physics, 27, 1

Somerville R. S., Davé R., 2015, ARA& A, 53, 51

Sommer-Larsen J., 2006, ApJL, 644, L1

Sparre M., Hayward C. C., Feldmann R., Faucher-Giguère C.-A., Muratov A. L., Kereš D., Hopkins P. F., 2017, MNRAS, 466, 88

Spekkens K., Giovanelli R., Haynes M. P., 2005, AJ, 129, 2119

Spergel D. N., Bean R., Doré O., et al., 2007, ApJS, 170, 377

Springel V., 2005, MNRAS, 364, 1105

Springel V., White S. D. M., Jenkins A., Frenk C. S., Yoshida N., Gao L., Navarro J., Thacker R., Croton D., Helly J., Peacock J. A., Cole S., Thomas P., Couchman H., Evrard A., Colberg J., Pearce F., 2005, Nature, 435, 629

Steinmetz M., Navarro J., 2000, in Dynamics of Galaxies: from the Early Universe to the Present, edited by F. Combes, G. A. Mamon, V. Charmandaris, vol. 197 of Astronomical Society of the Pacific Conference Series, 165

Stinson G. S., Brook C., Macciò A. V., Wadsley J., Quinn T. R., Couchman H. M. P., 2013, MNRAS, 428, 129

Strigari L. E., Kaplinghat M., Bullock J. S., 2007, Phys. Rev. D, 75, 6, 061303

Strong A. W., Moskalenko I. V., 1998, ApJ, 509, 212

Strong A. W., Moskalenko I. V., 2001, Advances in Space Research, 27, 717

Strong A. W., Moskalenko I. V., Ptuskin V. S., 2007, Annual Review of Nuclear and Particle Science, 57, 285

Strong A. W., Moskalenko I. V., Reimer O., 2000, ApJ, 537, 763

Strong A. W., Moskalenko I. V., Reimer O., 2004, ApJ, 613, 962

Su K.-Y., Hayward C. C., Hopkins P. F., Quataert E., Faucher-Giguère C.-A., Kereš D., 2018, MNRAS, 473, L111

Su K.-Y., Hopkins P. F., Hayward C. C., Faucher-Giguère C.-A., Kereš D., Ma X., Robles V. H., 2017, MNRAS, 471, 144

Swaters R. A., Madore B. F., van den Bosch F. C., Balcells M., 2003, ApJ, 583, 732

Teyssier R., Pontzen A., Dubois Y., Read J. I., 2013, MNRAS, 429, 3068

Thomas T., Pfrommer C., 2019, MNRAS, 260

Thompson T. A., Quataert E., Waxman E., 2007, ApJ, 654, 219

Tollerud E. J., Geha M. C., Grcevich J., Putman M. E., Stern D., 2015, ApJL, 798, L21

Tollet E., Macciò A. V., Dutton A. A., Stinson G. S., Wang L., Penzo C., Gutcke T. A., Buck T., Kang X., Brook C., Di Cintio A., Keller B. W., Wadsley J., 2016, MNRAS, 456, 3542

Tonini C., Lapi A., Salucci P., 2006, ApJ, 649, 591

Trotta R., Jóhannesson G., Moskalenko I. V., Porter T. A., Ruiz de Austri R., Strong A. W., 2011, ApJ, 729, 106

Trujillo I., Roman J., Filho M., Sánchez Almeida J., 2017, ApJ, 836, 191

Tully R. B., Fisher J. R., 1976, in Bulletin of the American Astronomical Society, vol. 8 of Bulletin of the American Astronomical Society, 555

Tully R. B., Fisher J. R., 1977, A& A, 54, 661

Turk M. J., Smith B. D., Oishi J. S., Skory S., Skillman S. W., Abel T., Norman M. L., 2011, ApJS, 192, 9

Uhlig M., Pfrommer C., Sharma M., Nath B. B., Enßlin T. A., Springel V., 2012, MNRAS, 423, 2374

van de Voort F., Bahé Y. M., Bower R. G., Correa C. A., Crain R. A., Schaye J., Theuns T., 2017, MNRAS, 466, 3460

van den Bosch F. C., Jiang F., Hearin A., Campbell D., Watson D., Padmanabhan N., 2014, MNRAS, 445, 1713

van der Burg R. F. J., Hoekstra H., Muzzin A., Sifón C., Viola M., Bremer M. N., Brough S., Driver S. P., Erben T., Heymans C., Hildebrandt H., Holwerda B. W., Klaes D., Kuijken K., McGee S., Nakajima R., Napolitano N., Norberg P., Taylor E. N., Valentijn E., 2017, A& A, 607, A79

van der Burg R. F. J., Muzzin A., Hoekstra H., 2016, A& A, 590, A20

van der Kruit P. C., 1971, A& A, 15, 110

van der Kruit P. C., 1973, A& A, 29, 263

van der Walt S., Colbert S. C., Varoquaux G., 2011, Computing in Science Engineering, 13, 2, 22

van Dokkum P., Abraham R., Brodie J., Conroy C., Danieli S., Merritt A., Mowla L., Romanowsky A., Zhang J., 2016, ApJL, 828, L6 van Dokkum P., Abraham R., Romanowsky A. J., Brodie J., Conroy C., Danieli S., Lokhorst D., Merritt A., Mowla L., Zhang J., 2017, ApJL, 844, L11

van Dokkum P. G., Abraham R., Merritt A., Zhang J., Geha M., Conroy C., 2015a, ApJL, 798, L45

van Dokkum P. G., Romanowsky A. J., Abraham R., Brodie J. P., Conroy C., Geha M., Merritt A., Villaume A., Zhang J., 2015b, ApJL, 804, L26

Vázquez G. A., Leitherer C., 2005, ApJ, 621, 695

Velliscig M., van Daalen M. P., Schaye J., McCarthy I. G., Cacciato M., Le Brun A. M. C., Dalla Vecchia C., 2014, MNRAS, 442, 2641

Venhola A., Peletier R., Laurikainen E., Salo H., Lisker T., Iodice E., Capaccioli M., Kleijn G. V., Valentijn E., Mieske S., Hilker M., Wittmann C., van de Ven G., Grado A., Spavone M., Cantiello M., Napolitano N., Paolillo M., Falcón-Barroso J., 2017, A& A, 608, A142

Verheijen M. A. W., 1997, The Ursa Major Cluster of Galaxies: TF-relations and dark matter, Ph.D. thesis, PhD thesis, Univ. Groningen, The Netherlands , (1997)

VERITAS Collaboration, Acciari V. A., Aliu E., Arlen T., Aune T., Bautista M., Beilicke M., Benbow W., Boltuch D., Bradbury S. M., Buckley J. H., Bugaev V., Byrum K., Cannon A., Celik O., Cesarini A., Chow Y. C., Ciupik L., Cogan P., Colin P., Cui W., Dickherber R., Duke C., Fegan S. J., Finley J. P., Finnegan G., Fortin P., Fortson L., Furniss A., Galante N., Gall D., Gibbs K., Gillanders G. H., Godambe S., Grube J., Guenette R., Gyuk G., Hanna D., Holder J., Horan D., Hui C. M., Humensky T. B., Imran A., Kaaret P., Karlsson N., Kertzman M., Kieda D., Kildea J., Konopelko A., Krawczynski H., Krennrich F., Lang M. J., Lebohec S., Maier G., McArthur S., McCann A., McCutcheon M., Millis J., Moriarty P., Mukherjee R., Nagai T., Ong R. A., Otte A. N., Pandel D., Perkins J. S., Pizlo F., Pohl M., Quinn J., Ragan K., Reyes L. C., Reynolds P. T., Roache E., Rose H. J., Schroedter M., Sembroski G. H., Smith A. W., Steele D., Swordy S. P., Theiling M., Thibadeau S., Varlotta A., Vassiliev V. V., Vincent S., Wagner R. G., Wakely S. P., Ward J. E., Weekes T. C., Weinstein A., Weisgarber T., Williams D. A., Wissel S., Wood M., Zitzer B., 2009, Nature, 462, 770

Vogelsberger M., Sijacki D., Kereš D., Springel V., Hernquist L., 2012a, MNRAS, 425, 3024

Vogelsberger M., Zavala J., Loeb A., 2012b, MNRAS, 423, 3740

Völk H. J., Aharonian F. A., Breitschwerdt D., 1996, Space Sci. Rev., 75, 279

Walker M. G., Mateo M., Olszewski E. W., Peñarrubia J., Wyn Evans N., Gilmore G., 2009, ApJ, 704, 1274

Walter F., Brinks E., de Blok W. J. G., Bigiel F., Kennicutt Jr. R. C., Thornley M. D., Leroy A., 2008, AJ, 136, 2563

Wang L., Dutton A. A., Stinson G. S., Macciò A. V., Penzo C., Kang X., Keller B. W., Wadsley J., 2015, MNRAS, 454, 83

Wang X., Fields B. D., 2018, MNRAS, 474, 4073

Watkins L. L., Evans N. W., An J. H., 2010, MNRAS, 406, 264

Webber W. R., McDonald F. B., Lukasiak A., 2003, ApJ, 599, 582

Weiß A., Neininger N., Hüttemeister S., Klein U., 2001, A& A, 365, 571

Weisz D. R., Dolphin A. E., Skillman E. D., Holtzman J., Gilbert K. M., Dalcanton J. J., Williams B. F., 2014, ApJ, 789, 147

Wentzel D. G., 1968, ApJ, 152, 987

Wetzel A. R., Hopkins P. F., Kim J.-h., Faucher-Giguère C.-A., Kereš D., Quataert E., 2016, ApJL, 827, L23

Wetzel A. R., Tinker J. L., Conroy C., van den Bosch F. C., 2013, MNRAS, 432, 336

Wetzel A. R., Tollerud E. J., Weisz D. R., 2015, ApJL, 808, L27

Wheeler C., Oñorbe J., Bullock J. S., Boylan-Kolchin M., Elbert O. D., Garrison-Kimmel S., Hopkins P. F., Kereš D., 2015, MNRAS, 453, 1305

Wheeler C., Pace A. B., Bullock J. S., Boylan-Kolchin M., Oñorbe J., Elbert O. D., Fitts A., Hopkins P. F., Kereš D., 2017, MNRAS, 465, 2420

White S. D. M., Frenk C. S., 1991, ApJ, 379, 52

Wiener J., Pfrommer C., Oh S. P., 2017, MNRAS, 467, 906

Wiener J., Zweibel E. G., Oh S. P., 2013, ApJ, 767, 87

Wilke K., Klaas U., Lemke D., Mattila K., Stickel M., Haas M., 2004, A& A, 414, 69

Wolf J., Martinez G. D., Bullock J. S., Kaplinghat M., Geha M., Muñoz R. R., Simon J. D., Avedo F. F., 2010, MNRAS, 406, 1220

Yan H., Lazarian A., 2008, ApJ, 673, 942

Yoast-Hull T. M., Everett J. E., Gallagher III J. S., Zweibel E. G., 2013, ApJ, 768, 53

Yoast-Hull T. M., Gallagher J. S., Zweibel E. G., 2016, MNRAS, 457, L29

Yoshida N., Springel V., White S. D. M., Tormen G., 2000, ApJL, 535, L103

Yozin C., Bekki K., 2015, MNRAS, 452, 937

Zahid H. J., Geller M. J., Kewley L. J., Hwang H. S., Fabricant D. G., Kurtz M. J., 2013, ApJL, 771, L19

Zirakashvili V. N., Breitschwerdt D., Ptuskin V. S., Voelk H. J., 1996, A& A, 311, 113

Zolotov A., Brooks A. M., Willman B., Governato F., Pontzen A., Christensen C., Dekel A., Quinn T., Shen S., Wadsley J., 2012, ApJ, 761, 71

Zwaan M. A., van der Hulst J. M., de Blok W. J. G., McGaugh S. S., 1995, MNRAS, 273, L35

Zweibel E. G., 2013, Physics of Plasmas, 20, 5, 055501

Zweibel E. G., 2017, Physics of Plasmas, 24, 5, 055402